Dissertation

Measurement of ν_μ-induced Charged-Current Single π^+ Production on H_2O

Submitted by

Shamil M. Assylbekov

Department of Physics

In partial fulfillment of the requirements

For the Degree of Doctor of Philosophy

Colorado State University

Fort Collins, Colorado

Summer 2015

Doctoral Committee:

Advisor: Robert J. Wilson

Walter Toki
John Harton
Bruce Berger
Alexander Hulpke

Abstract

Measurement of ν_μ-induced Charged-Current Single π^+ Production on H_2O

T2K is an international collaboration that has constructed an experiment in Japan to investigate the properties of the neutrino. It consists of two near detectors, ND280 and INGRID, and a far detector - Super-Kamiokande. ND280 has multiple sub-detectors with the π^0 detector (PØD) being of most importance to this analysis. This work describes the first measurement of neutrino cross section for charged-current single positively charged pion (CC1π^+) interaction channel on water (H_2O) using the PØD as target and detector.

The PØD detector has been taking neutrino interaction data since 2009 in configurations with and without an integrated water target. Using a statistical water-in/water-out event rate subtraction, a measurement of the ν_μ-induced CC1π^+ cross section on water is reported to be $\langle\sigma\rangle = 1.10 \times 10^{-39}\ ^{+0.39\cdot10^{-39}}_{-0.36\cdot10^{-39}}$ cm^2, where the result is provided in the form of a single-bin cross section integrated over the entire T2K neutrino energy range. The measurement is based on a sample of 2,703 events selected from beam runs of 2.64×10^{20} protons-on-target (POT) with the PØD water-in configuration, and 2,187 events selected from 3.71×10^{20} POT with the water-out configuration. The corresponding Monte Carlo simulation predicted numbers of background events to be 1,387.2 and 1,046.0 for the water-in and water-out detector configurations, respectively. The accuracy of the result is dominated by flux and cross section models uncertainties. The data favors a systematically smaller cross section when compared to the model but within the uncertainties it is consistent with the Monte Carlo simulation prediction of 1.26×10^{-39}cm^2. The result, its significance, and the strategy for future CC1π^+ measurements are discussed in conclusion.

Acknowledgements

First and foremost, I want to thank my family for their love and support. This work I dedicate to them.

I would also like to thank my advisor Robert J. Wilson for all the guidance through the years.

Most of the analysis work presented in this dissertation was carried out with tremendous help from Tomasz Wachala, who at the time was a postdoc at Colorado State University. I would like to thank Tomasz for all his help and innumerable discussions of various aspects of this analysis.

This work, of course, would not be possible without my T2K colleagues, who made this experiment happen, and the funding agencies, e.g. the Department of Energy, that paid for it. Therefore, I want to thank all my colleagues and the funding agencies.

Last, but not least, I would like to thank my Ph.D. examination committee members for their valuable inputs and support.

This dissertation is typset in LaTeX using a document class designed by Leif Anderson.

Table of Contents

List of Tables

List of Figures

CHAPTER 1

Introduction

Neutrinos are one of the least understood fundamental particles. In fact, these mysterious particles are the only elementary *fermions*[1] that are electrically neutral, i.e. don't interact through *electromagnetic* force, but only interact through the *weak* force and *gravity*.

Out of the four fundamental forces of nature (or three, in case you count weak force and electromagnetism as different manifestations of the same *electroweak* force) known to us - *strong*, *electromagnetic*, *weak*, and *gravity*, the last one is just too weak compared to the other three to play a major role in elementary particle physics. Currently, it is not well understood why gravity is so much weaker compared to the other, and how to reconcile general relativity with the principles of quantum mechanics. At present, gravitational force is not included into the *Standard Model* (SM) of particle physics. The relative strengths of these four fundamental forces of nature are shown in Table 1.1.

Theories explaining the strong, electromagnetic and weak interactions are QCD, QED amd QFD, respectively, and are combined into the SM theory of particle physics.

Table 1.1. Relative strengths of the four fundamental forces of nature, when the strong force is normalized to one for simplicity.

Field	Strength	Theory	Mediator
Strong	1	Quantum Chromodynamics (QCD)	g (gluon)
Electromagnetic	10^{-2}	Quantum Electrodynamics (QED)	γ (photon)
Weak	10^{-5}	Quantum Flavordynamics (QFD)	W and Z
Gravity	10^{-40}	General Relativity (GR)	graviton

[1] Fermions are half-integer spin particles that obey Fermi-Dirac statistics and the Pauli exclusion principle according to which two or more fermions cannot occupy the same quantum state. All quarks and leptons are elementary fermions. Protons and neutrons, the building blocks of matter, are examples of composite fermions.

Since neutrinos don't possess the *color*[2] charge, they cannot engage in strong interactions either. This leaves us with only the weak force as the primary object of neutrino data analysis scrutiny.

A short overview of the history of the neutrino physics, which serves as a foundation for modern neutrino research, is presented in Section 1.1. Neutrino flavors, masses, and mixing, are described in Section 1.2, along with a brief overview of neutrino oscillation physics formalism and some experimental results. The weak forces or weak interactions which, besides neutrino interactions, account for nuclear beta decay, the decay of the pion, the muon, and a zoo of strange particles, and other elementary particle processes are of primary interest to this analysis. The necessary basics of the neutrino weak interactions theory and the basic cross section formalism are presented in Section 1.3. Inclusive and elastic scattering cross sections are described in Sections 1.4, 1.5, and single pion production - the signal for this analysis - is covered in detail Section 1.6. An overview of the analysis strategy is presented in the conclusion of the introduction in Section 1.7.

1.1. History of Neutrino Physics

The history of neutrinos started in 1930 with Wolfgang Pauli, when he, at the age of 30, suggested the existence of a small neutral particle in order to "save the exchange theorem of statistics and the law of conservation of energy" [1] in nuclear beta decay, which at the time was incorrectly understood to be a two-body decay. Beta decay in its now accepted form is shown in Equation 1, where a neutron, n^0, decays into a proton, p^+, an electron, e^-, and an electron antineutrino, $\overline{\nu}_e$:

$$n^0 \rightarrow p^+ + e^- + \overline{\nu}_e. \tag{1}$$

[2] Color charge is a property of quarks and gluons in the theory of *Quantum Chromodynamics* (QCD). It can be red, blue or green.

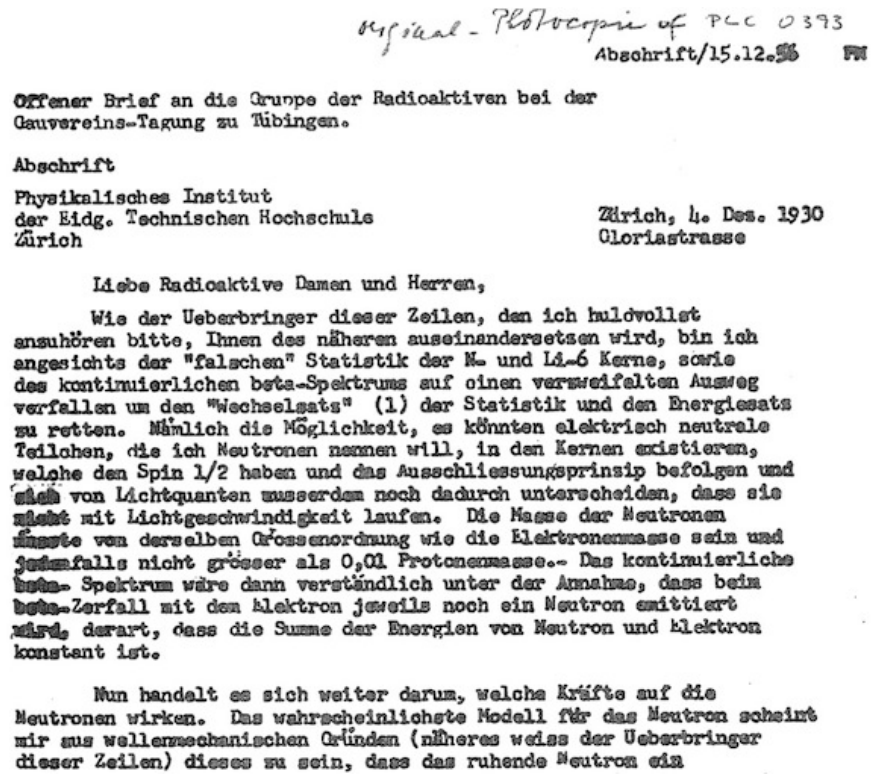

Original - Photocopie of PLC 0393
Abschrift/15.12.30 PM

Offener Brief an die Gruppe der Radioaktiven bei der Gauvereins-Tagung zu Tübingen.

Abschrift

Physikalisches Institut
der Eidg. Technischen Hochschule
Zürich

Zürich, 4. Dez. 1930
Gloriastrasse

Liebe Radioaktive Damen und Herren,

Wie der Ueberbringer dieser Zeilen, den ich huldvollst ansuhören bitte, Ihnen des näheren auseinandersetsen wird, bin ich angesichts der "falschen" Statistik der N- und Li-6 Kerne, sowie des kontinuierlichen beta-Spektrums auf einen verzweifelten Ausweg verfallen um den "Wechselsats" (1) der Statistik und den Energiesats zu retten. Nämlich die Möglichkeit, es könnten elektrisch neutrale Teilchen, die ich Neutronen nennen will, in den Kernen existieren, welche den Spin 1/2 haben und das Ausschliessungsprinsip befolgen und sich von Lichtquanten ausserdem noch dadurch unterscheiden, dass sie nicht mit Lichtgeschwindigkeit laufen. Die Masse der Neutronen müsste von derselben Grössenordnung wie die Elektronenmasse sein und jedenfalls nicht grösser als 0,01 Protonenmasse.- Das kontinuierliche beta- Spektrum wäre dann verständlich unter der Annahme, dass beim beta-Zerfall mit dem Elektron jeweils noch ein Neutron emittiert wird, derart, dass die Summe der Energien von Neutron und Elektron konstant ist.

Nun handelt es sich weiter darum, welche Kräfte auf die Neutronen wirken. Das wahrscheinlichste Modell für das Neutron scheint mir aus wellenmechanischen Gründen (näheres weiss der Ueberbringer dieser Zeilen) dieses zu sein, dass das ruhende Neutron ein

FIGURE 1.1. W. Pauli's letter in which he proposes an idea of a neutrino. Courtesy of Pauli Letter Collection, CERN.

Pauli initially called the new particle a "neutron" in line with the convention of the time, i.e. electron and proton were the only two particles known to physicists in the 1920s. However, after the discovery of the massive neutron by Chadwick in 1932, Pauli's hypothetical particle had to be renamed. Enrico Fermi helped clear up the confusion [2] in 1933 when he coined the term "neutrino". In 1934 Fermi published[3] in an Italian journal his now famous theory of beta decay, which included the hypothetical massless and electrically neutral neutrino particle He initially submitted his paper to *Nature*, but the journal rejected his submission, claiming that his theory was "too remote from reality". Yet, this is how the foundation for all modern neutrino research was laid. The theory of weak interactions was futher developed in the 1950s by Lee, Yang, Feynman, Gell-Mann, and many others. The theory acquired its

[3] Actually, in Fermi's theory of weak interactions there was only one type of neutrino, assumed to be spin $\frac{1}{2}$ massless and neutral. It wasn't known at the time that neutrinos come in three flavors/types.

present form in the 1960s when Glashow, Weinberg and Salam[4] proposed the unified theory of electromagnetic and weak interactions.

The first experiment to detect neutrinos (more specifically $\overline{\nu}_e$), now known as the Cowan-Reines neutrino experiment, resulted in a *Nature* journal publication in 1956 [3] and a 1995 Nobel Prize almost 40 years later. In that experiment, $\overline{\nu}_e$'s produced in a nuclear reactor interacted with protons in the detector target yielding neutrons and positrons as a result:

$$p^+ + \overline{\nu}_e \rightarrow n^0 + e^+ \tag{2}$$

Gamma rays (γ) produced in the annihilation of the positron with an atomic electron were detected. The final state neutron, when captured by a nucleus, also resulted in γ ray emission. These two events in coincidence - e^+e^- annihilation and neutron capture - gave a unique signature of an $\overline{\nu}_e$ interaction.

In 1962 physicists Lederman, Schwartz and Steinberger at CERN (European Organization for Nuclear Research) and BNL (Brookhaven National Laboratory) were able to show that there was more than one type or flavor of neutrinos [4]. Twenty six year later in 1988 they would get a Nobel Prize for their spectacular discovery of ν_μ's.

When the third flavor of charged lepton, denoted by the Greek letter τ, was discovered in 1975 at Stanford Linear Accelerator Center (SLAC) [5], existence of an associated neutrino (the tau neutrino or ν_τ) was inferred. First evidence of ν_τ existence came from the observation of missing energy, momentum and angular momentum in τ decays, in a way similar to how observation of missing energy in beta-decays lead to the discovery of the $\overline{\nu}_e$. The DONUT collaboration announced [6] the first experimental detection of ν_τ's in 2000.

[4] The modern weak interactions theory is sometimes called the Glashow-Weinberg-Salam (GWS) theory.

The era of neutrino cross section measurements started in 1970 with bubble chamber experiments at Argonne National Laboratory and Brookhaven National Laboratory (BNL) [7, 8, 12–14]. The first ever photograph of a neutrino event taken at ANL on November 13 1970 is shown in Figure 1.2. Other laboratories at which bubble chamber experiments were performed through out the 1970s include Fermilab and CERN.

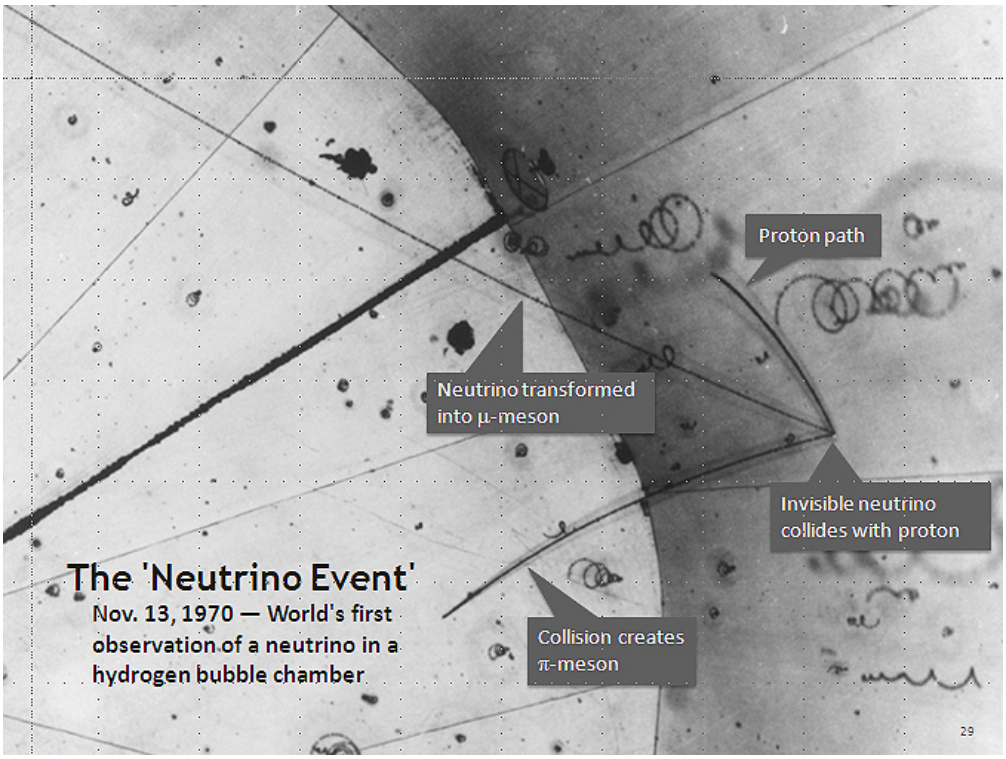

FIGURE 1.2. The first neutrino event showing a neutrino interaction vertex and three outgoing tracks: a muon (μ^-), a proton (p^+), and a positive pion (π^+). Courtesy of Argonne National Laboratory.

In the late 1960s the Homestake experiment observed [15, 16] that the flux of solar ν_e's arriving at the surface of the Earth from the Sun was significantly lower than the number predicted by the Standard Solar Model. This gave rise to the so called *Solar Neutrino Problem*, which remained unresolved for thirty years, until Sudbury Neutrino Observatory (SNO) presented the first irrefutable evidence [18] in 2001 that neutrino flavor change was responsible for the deficit in the ν_e flux. It must be noted that the Super-Kamiokande

collaboration published the first evidence for neutrino oscillation in 1998 [17], although the results were not conclusive and dealt with the atmospheric neutrinos as opposed to solar.

The phenomenon of neutrino oscillations was first suggested by Bruno Pontecorvo in 1957, who hypothesized that matter-antimatter ν-$\overline{\nu}$ oscillations may occur analogous to neutral kaon mixing [19]. In 1962 Maki, Nakagawa, and Sakata used Pontecorvo's idea as a starting point, but instead of matter-antimatter transitions (or oscillations), they proposed the theory of neutrino flavor oscillations, which was again further expanded by Pontecorvo in 1967. Gribov and Pontecorvo's paper titled "Neutrino astronomy and lepton charge" [20] was published in 1969.

In 1978 American physicist Lincoln Wolfenstein theorized that neutrino flavor oscillations can be affected by matter [21]. In 1986 Soviet physicists Stanislav Mikheyev and Alexei Smirnov expanded Wolfenstein's theory, showing that neutrino flavor oscillations must be altered when neutrinos propagate through matter. This later became known as the Mikheyev-Smirnov-Wolfenstein (MSW) effect, which helped describe neutrino propagation through a dense medium such as the Sun more precisely [22]. The first full analytic treatment of this phenomenon derived by Stephen Parke appeared later in 1986 [23]. SNO, Super-Kamiokande and other experiments have since provided irrefutable evidence of the MSW effect.

Starting in the late 1990s neutrino flavor changes were shown to exist for both atmospheric and solar neutrinos by multiple experiments, such as SNO, Super-Kamiokande and others. The beginning of the 21st century was marked by the confirmation of reactor neutrino oscillations (KamLAND experiment [24]) and the start of accelerator neutrino experiments era - the age of precision measurements of oscillation parameters and attempts to measure charge-parity (CP) violation in the lepton sector. As of 2015 active accelerator neutrino experiments include MINOS [25], NOνA [26] and MINERνA [27] in the USA, T2K [28] in Japan and

others. Experiments in planning currently include the DUNE/LBNF experiment [29] and the Hyper-K experiment [30].

TABLE 1.2. Physics Nobel Prizes awarded for neutrino-related research

Year	Laureate(s)
1988	Lederman, Schwartz and Steinberg
1995	Reines
2002	Davis and Koshiba

Over the years several Nobel Prizes in Physics were awarded for neutrino-related research. They are listed in chronological order in Table 1.2. A brief history of neutrinos is also presented in chronological order in Table 1.3 and 1.4.

Several books provide more comprehensive and complete overviews of the history of neutrino physics. Two books are worth mentioning in particular. "Neutrino Physics" by Kai Zuber [33] published in 2011 aims to outline the essential ideas of neutrino physics and provides interesting historical insights into the early development of the field. "Introduction to the Physics of Massive and Mixed Neutrinos" by Samoil Bilenky [34] gives important references to some of the pioneering neutrino papers, including the groundbreaking work by Pauli, Fermi and others. Bilenky recommends the web site by C. Giunti and M. Laveder (the Neutrino Unbound, http://www.nu.to.infn.it), which provides many references to neutrino theory and experimental literature.

1.2. NEUTRINO PROPERTIES

Neutrinos, usually denoted by the Greek letter ν, are ultrarelativistic spin-$\frac{1}{2}$ fermions, i.e. they are subject to the Pauli Exclusion Principle and occupy one of the two spin states, $|\uparrow\rangle$ (up) or $|\downarrow\rangle$ (down). As far as we know at present there are only twelve fundamental fermions in nature: six quarks $u,\ d,\ c,\ s,\ t,\ b$, and six leptons $e,\ \nu_e,\ \mu,\ \nu_\mu,\ \tau,\ \nu_\tau$. They are usually

TABLE 1.3. Brief history of neutrinos in the 20th century.

Year	Event
1930	Pauli's neutrino prediction and famous letter: "Dear radioactive ..."
1933	Fermi coins the term "neutrino," first theory of weak forces
1934	Fermi's paper lays foundation for future experimental work
1942	Ganchang proposes to use beta-capture to detect ν's experimentally
1956	First detection of $\overline{\nu}_e$ by Cowan, Reines and others
1960s	Theory of weak forces further developed by Glashow, Weinberg, and Salam
1962	Experimental detection of ν_μ by Lederman, Schwartz and others
1968	Homestake results give rise to the *Solar Neutrino Problem*
1974	Standard Model of Particle Physics acquired its modern form
1975	τ is discovered at SLAC; ν_τ existence is inferred
1978	Matter effect (MSW) is proposed by Wolfenstein
1985	IMB experiment notices a deficit in atmospheric ν_μ flux
1986	MSW effect theory is published
1987	Multiple experiments detect ν's from Supernova 1987A
1988	Kamiokande reports 40% deficit in atmospheric ν_μ flux
1989	Kamiokande - 2nd experiment to detect solar ν's; confirms the anomaly
1990	IMB confirms Kamiokande's solar ν result
1996	SK (Super-Kamiokande) detector begins operation
1997	SK confirms the deficit in flux of atmospheric and solar ν's
1997	Soudan-II experiment results agree with IMB, SK
1998	SK announces clear evidence of atmospheric ν_μ oscillations
1999	SNO experiment begins operation

grouped into three families as shown in Table 1.5, where the masses of the particles increase from left to right. Most of the matter in the known visible universe (ignoring dark matter) is composed of three particles: protons (uud), neutrons (udd), and electrons.

TABLE 1.4. Brief history of neutrinos in the 21st century.

Year	Event
2000	DONUT collaboration announces detection of ν_τ
2001	SNO publishes discovery of evidence of solar ν_e oscillations
2002	KamLAND reactor neutrino experiment starts
2005	KamLAND confirms $\overline{\nu}$ disappearance at 99.998% C.L.
2009	T2K experiment starts taking data
2010	CERN announces observation of ν_τ appearance in ν_μ beam
2011	OPERA experiment mistakenly observes superluminous ν's
2011	T2K sees indication of ν_e appearance at 2.5 σ
2012	Daya Bay experiment announces [110] a discovery that $\theta_{13} \neq 0$ at 5.2 σ
2012	RENO collaboration confirms [111] the findings of T2K and Daya Bay
2012	T2K publishes first ν_μ disappearance study with an off-axis beam
2013	T2K announces discovery of ν_e appearance in ν_μ beam
2013	T2K publishes another ν_μ disappearance result
2014	NOνA experiment with 800 km baseline starts taking data
2024	DUNE/LBNF is expected to be fully operational

Some exotic theories exist that discuss the fourth[5] family of quarks and leptons [35], but there is no experimental evidence yet to support such claims.

The neutrino is a special fermion different from other fermions mainly for two reasons:

- Neutrino masses are orders of magnitude smaller than the masses of charged leptons and quarks, which is puzzling;
- Neutrino interaction cross sections are orders of magnitude smaller than the cross sections of electromagnetic interations, since the neutrino interacts only weakly through the W and Z bosons and nothing else.

[5] Some theories suggest more than one extra family of neutrinos, i.e. sterile neutrinos that do not interact through the weak force, and are yet to be discovered experimentally.

TABLE 1.5. Three families of quarks and leptons.

u	c	t
d	s	b
e	μ	τ
ν_e	ν_μ	ν_τ

1.2.1. THREE FLAVORS. Neutrinos are known to be neutral leptons. Charged and neutral leptons are known to exist in three flavors, electron (e), muon (μ) and tau (τ), and according to the SM come in charged-neutral pairs of the same flavor which are understood as weak isospin doublet states:

$$\chi = \begin{pmatrix} e \\ \nu_e \end{pmatrix}, \begin{pmatrix} \mu \\ \nu_\mu \end{pmatrix}, \begin{pmatrix} \tau \\ \nu_\tau \end{pmatrix}. \tag{3}$$

The basic lepton properties are summarized in Table 1.6.

TABLE 1.6. A summary of lepton properties.

l/anti-l	Charge (e)	Spin	Mass (MeV/c^2)	Lifetime (s)
e^-/e^+	-1/+1	$\frac{1}{2}$	$\approxeq 0.51$	Stable
μ^-/μ^+	-1/+1	$\frac{1}{2}$	$\approxeq 105.66$	$\approxeq 2.20\times10^{-6}$
τ^-/τ^+	-1/+1	$\frac{1}{2}$	$\approxeq 1{,}776.84$	$\approxeq 2.91\times10^{-13}$
$\nu_e/\overline{\nu}_e$	0	$\frac{1}{2}$	$< 0.32 \times 10^{-6}$	Unknown
$\nu_\mu/\overline{\nu}_\mu$	0	$\frac{1}{2}$	$< 0.32 \times 10^{-6}$	Unknown
$\nu_\tau/\overline{\nu}_\tau$	0	$\frac{1}{2}$	$< 0.32 \times 10^{-6}$	Unknown

Some exotic theories propose the existence of hypothetical sterile neutrinos, which are different from their three cousins in that they don't interact via the weak force, and have vastly different masses. Currently, these theories are purely speculative, and still remain to be definitively confirmed or ruled out.

1.2.2. Helicity and Chirality. The particle helicity operator or simply H is defined as the projection of the spin S onto the direction of the momentum $\hat{p}$: $H = S \cdot \hat{p} = \frac{\hbar}{2}\sigma \cdot \hat{p}$. For massless fermions it is equivalent to the chirality operator multiplied by $\frac{\hbar}{2}$. This implies that in the small mass or massless limit, only one of two possible chiralities can be observed for a particle.

Neutrino helicity was determined experimentally at the Brookhaven National Laboratory by Goldhaber, Grodzins and Sunyar in 1957 [36]. They measured the circular polarization of gamma quanta in the following chain of reactions:

$$e^- + \mathrm{Eu} \rightarrow \nu + \mathrm{Sm}^*,\ \mathrm{Sm}^* \rightarrow \mathrm{Sm} + \gamma. \tag{4}$$

As a result of this experiment it was established with measurement uncertainty of 15% that $\sigma_\nu \cdot \hat{p_\nu} = -1$, or that neutrinos are mostly left-handed particles (and antineutrinos are right-handed).

If right-handed neutrinos and left-handed antineutrinos do actually exist, their properties would be substantially different from the neutrinos and antineutrinos observed so far experimentally. They would be either very heavy (orders of magnitude heavier than currently observed neutrinos), would be sterile (would not participate in weak processes), or both.

1.2.3. Speed. Originally neutrinos were assumed to be massless particles travelling at the speed of light $c \approx 2.9979 \times 10^8$ m·s^{-1}, which is a natural consequence of special relativity. However, since the discovery and confirmation of neutrino oscillations, and thus non-zero neutrino mass, the question of neutrino speed has risen again. As it currently stands, neutrino speed could be less than or equal to the speed of light. Some exotic theories build on top

of non-canonical variations of the theory of relativity even propose that neutrinos could be superluminous.

Since the mid-1970s [37, 38], several experiments attempted measuring the neutrino speed using neutrino beams. The typical experimental idea behind them was to measure the neutrino departure and arrival times, knowing the distance between the departure and the arrival points. The SN1987A supernova neutrino speed measurements [39–42] were exceptional in that they used a different technique and that they were the most precise measurements until 2012. All the early measurements of the neutrino speed were consistent with the speed to light within the margins of error.

The more recent experiments performed independently in the 21st century by MINOS [43], OPERA [44], ICARUS [45], Borexino [46] and LVD [47] showed that neutrino is indeed an ultrarelativistic particle with speed indiscernible from the speed of light c within the experimental uncertainties.

The OPERA collaboration is worth mentioning separately, since it was the only one that declared the "anomaly in flight time of neutrinos" [48], i.e. that neutrinos were faster than light, which later was discovered to be a mistake in the measurement due to a loose fiber-optic cable connection.

1.2.4. Mass. Very little is known about the origin of the neutrino masses, which are many orders of magnitude smaller than masses of other leptons and quarks, and which still remain to be directly measured.

According to the canonical Standard Model all leptons are assumed to have no intrinsic mass. Charged leptons, which are Dirac fermions, are assumed to get their effective mass through the coupling to the Higgs field[6], but the miniscule neutrino masses cannot be easily

[6] The standard Higgs mechanism is now part of the Standard Model, which explains how weak bosons acquire mass. The basic idea is that particles are interacting with the Higgs field, via an exchange of the Higgs

explained by this mechanism. This implies physics beyond the Standard Model. The Seesaw Mechanism (type one) [51–53] is the most favored model extending the Standard Model, which explains both why all neutrinos are left-handed (and antineutrinos are right-handed), and why neutrinos are much lighter than their corresponding charged lepton counterparts. In the Seesaw Mechanism, the neutrino is assumed to be a Majorana[7] fermion, however no experiment so far has definitively shown whether a neutrino is a Dirac or a Majorana fermion.

Over the years there have been multiple attempts at calculating and measuring the neutrino masses using a great variety of methods [54–60]. The results of the most recent neutrino mass measurements are shown in Table 1.7. A detailed summary of all neutrino mass upper limit measurements is provided [61] by the PDG. Non-zero ν mass suggests

TABLE 1.7. Measurements of the upper limits of neutrino masses.

Technique	Neutrino mass	Reference
^{3}H β decay	$m_{\bar{\nu}_e} < 2.05$ eV (95% C.L.)	[56]
^{163}Ho decay	$m_{\nu_e} < 225$ eV (95% C.L.)	[57]
$\pi^{\pm}$ decay	$m_{\nu_\mu} < 0.19$ MeV (90% C.L.)	[58]
τ^- decay	$m_{\nu_\tau} < 18.2$ MeV (95% C.L.)	[59]
Cosmological	$\sum m_\nu < 0.39$ eV (95% C.L.)	[60]

that there also might be a neutrino magnetic moment [61] estimated to be 19 orders of magnitude smaller than μ_B (Bohr magneton), which further implies that neutrinos may interact electromagnetically, however this behavior has not yet been observed experimentally. It is currently believed that neutrinos interact only through weak force and gravity, though neutrino gravity can be safely ignored at the sub-atomic scale, for it is $\sim$ 30 orders of

bosons. Particles that interacts with the Higgs field more strongly, have more mass. The existence of a particle consistent with the Higgs boson has been recently confirmed [49, 50] at the LHC.

[7] A Majorana fermion is a neutral fermion which is its own antiparticle. It is yet to be discovered experimentally. Dirac fermions are not their own antiparticles.

magnitude less strong than the weak force. However, neutrino gravity could be a major player on the cosmic distance scale.

1.2.5. Mixing and Oscillations. Neutrino oscillations are an established physical phenomenon, caused by non-zero neutrino masses and neutrino mixing, and supported by compelling evidence from experiments with solar [62, 63], atmospheric [64], reactor [65] and accelerator [66, 67] neutrinos. In this section a brief overview of neutrino mixing and oscillations is presented. Neutrino oscillations are not the main focus of this analysis, therefore, a more complete review and an exhaustive list of references on the subject can be found in the PDG review of Neutrino Mass, Mixing and Oscillations [70], updated annually.

Neutrino oscillations are a physical process that allows neutrinos to change flavor while in flight. For instance, given a neutrino produced in some weak process in a definite flavor and energy state, say $|\nu_\mu\rangle$, with energy E, at a sufficiently large distance L from the source, the probability $P(\nu_\mu \to \nu_e;\ E, L)$ to find a neutrino in a different definite flavor state, say $|\nu_e\rangle$, is not equal to zero. $P(\nu_\mu \to \nu_e;\ E, L)$ is called the $\nu_\mu \to \nu_e$ transition or oscillation probability. In this case, the probability $P(\nu_\mu \to \nu_\mu;\ E, L)$ is called the ν_μ survival probability and it is smaller than one.

In a given neutrino oscillations experiment, which, say, detects muon neutrinos, it is possible to observe the "disappearance" of muon neutrinos on the way from the source to the detector by measuring the survival rate $P(\nu_\mu \to \nu_\mu;\ E, L)$. The disappearance of solar, reactor and atmospheric neutrinos has been observed by the solar neutrino [62, 63], KamLAND [24], Daya Bay [110] and Super-Kamokande [64] experiments, respectively. Muon neutrino disappearance due to oscillations has been also confirmed by long-baseline accelerator neutrino experiments K2K [68], MINOS [69], and T2K [66, 67].

In case an experiment has the ability to detect electron neutrinos in addition to muon neutrinos, it is possible to observe the "appearance" of electron neutrinos in the muon neutrino beam by measuring the $\nu_\mu \to \nu_e$ oscillations rate $P(\nu_\mu \to \nu_e;\ E, L)$.

In June 2011 the T2K Collaboration was the first to report the indications for $\nu_\mu \to \nu_e$ oscillations, or for electron neutrino appearance in the muon neutrino beam, with a statistical significance of 2.5 σ. Later the MINOS Collaboration also obtained the results consistent with $\nu_\mu \to \nu_e$ oscillations. Mentions of other notable neutrino oscillations experimental results, e.g. from reactor-based experiments, can be found in [70].

Neutrino oscillations are a mathematical consequence of neutrino mixing, or lepton mixing, in vacuum. In the context of the Standard Model, the left-handed flavor neutrino fields ν_{lL} are linear superpositions of the fields of three (or more) neutrinos ν_j, having masses $m_j \neq 0$:

$$\nu_{lL}(x) = \sum_j U_{lj}\nu_{jL}(x),\ l = e, \mu, \tau, \tag{5}$$

where $\nu_{jL}(x)$ is the left-handed component of the field of ν_j with mass m_j. U is a unitary matrix, also known as the neutrino mixing matrix. U is also called the Pontecorvo-Maki-Nakagawa-Sakata (PMNS or MNSP) [8] or Maki-Nakagawa-Sakata (MNS) [9] mixing matrix [71].

In case of three flavor oscillations Equation 5 can be rewritten as

$$\begin{pmatrix} \nu_e \\ \nu_\mu \\ \nu_\tau \end{pmatrix} = U \cdot \begin{pmatrix} \nu_1 \\ \nu_2 \\ \nu_3 \end{pmatrix} = \begin{pmatrix} U_{e1} & U_{e2} & U_{e3} \\ U_{\mu 1} & U_{\mu 2} & U_{\mu 3} \\ U_{\tau 1} & U_{\tau 2} & U_{\tau 3} \end{pmatrix} \begin{pmatrix} \nu_1 \\ \nu_2 \\ \nu_3 \end{pmatrix}. \tag{6}$$

[8] Even though Pontecorvo came up with the first theory of neutrino oscillations, he originally assumed matter/anti-matter oscillations, and not flavor oscillations.
[9] Maki, Nakagawa and Sakata in their original paper assumed two neutrino flavor oscillations.

The PMNS matrix is mostly often parameterized by three neutrino mixing angles (θ_{12}, θ_{23} and θ_{13}) and a phase called δ_{CP}, describing the charge-parity violations in the neutrino sector. Using this parametrization the PMNS matrix can be rewritten as

$$U = \begin{pmatrix} c_{12}c_{13} & s_{12}c_{13} & s_{13}e^{-i\delta_{CP}} \\ -s_{12}c_{23} - c_{12}s_{23}s_{13}e^{i\delta_{CP}} & c_{12}c_{23} - s_{12}s_{23}s_{13}e^{i\delta_{CP}} & s_{23}c_{13} \\ s_{12}s_{23} - c_{12}c_{23}s_{13}e^{i\delta_{CP}} & -c_{12}s_{23} - s_{12}c_{23}s_{13}e^{i\delta_{CP}} & c_{23}c_{13} \end{pmatrix}, \tag{7}$$

where s_{ij} and c_{ij} denote $sin(\theta_{ij})$ and $cos(\theta_{ij})$ respectively.

Over the years most of the oscillations parameters have been measured by a variety of experiments. The CP-violating phase, however, has yet not been measured directly, and is planned to be measured by future long baseline neutrino oscillations experiments. More information on the theory of neutrino oscillations and experimental results, such as most current best fit values for the oscillation parameters, can be found in [70].

1.2.6. Sources. Neutrino sources can be split into two major categories: artificial and natural. Artificial or man-made neutrino sources include nuclear reactors, nuclear bombs and particle accelerators. Natural sources are atmospheric, solar, geological, supernovae and their remnants, and the Big Bang. The only source that is of particular interest to this analysis is the accelerator one, also known as the neutrino beam. The idea behind it is to collide the initial proton beam into a fixed target, usually a metal alloy. As a result of the occuring hadronic reactions, charged pions and kaons are created, which are subsequently magnetically focused into a forward going beam. Pions and kaons are allowed to decay in flight while passing through an evacuated decay tunnel. One of the products of pion decay is neutrinos, and that is how a neutrino beam is produced.

When neutrinos are created, usually with charged leptons involved in the process, they are produced in a definite flavor state $|\nu_l\rangle$. One such example process is a decay of a charged pion such as

$$\pi^+ \to \mu^+ + \nu_\mu,\ \pi^- \to \mu^- + \overline{\nu}_\mu, \tag{8}$$

or

$$\pi^+ \to e^+ + \nu_e,\ \pi^- \to e^- + \overline{\nu}_e. \tag{9}$$

Here the neutrino $|\nu_l\rangle$ it is coupled through the weak $W^\pm$ bosons to its charged lepton partner, $l^\pm$.

In case there were no charged leptons involved in the creation of the neutrino, for example during a rare neutral pion π^0 decay such as

$$\pi^0 \to \nu + \overline{\nu}, \tag{10}$$

it is assumed that the resulting neutrino/antineutrino are in undefined flavor state.

1.2.7. Detection. Usually, in a typical neutrino scattering experiment the direct physical observables are some kinematic properties (like momentum p or energy E) of the visible daughter particles, which are a product of a charged- or neutral-current neutrino scattering reaction

$$\nu_l + \mathcal{A} \to l^- + \mathcal{N}, \tag{11}$$

where ν represents the incoming neutrino, the lepton l is either charged or neutral, $\mathcal{A}$ is the target nucleon (or a nucleus), e.g. a proton in the oxygen in a water molecule H_2O in the detector. $\mathcal{N}$ denotes a set of outgoing particles (and the rebound nucleus). In the T2K experiment, water is the target material in the Super-Kamiokande far detector and part of the detector target mass in the PØD.

The detectable signature of neutrino charged-current events in the Super-Kamiokande is Cherenkov radiation. Cherenkov (or Cherenkov-Vavilov) radiation is a kind of electromagnetic radiation emitted by charged particles moving through matter with speeds faster than the speed of light in that material. The Cherenkov photons can be detected by photo-multiplier tubes (PMTs), and the event geometry and energy can be reconstructed. In case of the PØD detector, the observable radiation is the scintillation light emitted by the excited scintillator plastic doped with phosphorus when charged particles pass through it. The scintillator light is then absorbed and re-emitted by the wavelength-shifting (WLS) optical fibers and carried to the multi-pixel photon counter (MPPC) devices, which measure the light yield. The PØD is equipped with approximately 10,400 fiber channels which also allow the reconstruction of the neutrino event kinematics.

1.3. Introduction to Neutrino Scattering

As was mentioned earlier, it is impossible to directly observe the neutrino particle path in a detector, but it is possible to reconstruct neutrino properties by studying the properties of the secondary particles emerging from neutrino interactions. The fact that neutrino cross sections are orders of magnitude smaller than cross sections of other particles makes the study of neutrino interactions a challenging task. However, it is imperative to study

neutrino interactions with nucleons and nuclei[10] since modern precision neutrino oscillation experiments rely on accurate understanding of these interactions and the precise modeling of cross sections for background and signal estimation.

In this section an attempt is made to give a short summary overview of weak interactions and neutrino-nucleon scattering. Many particle physics textbooks provide a comprehensive in-depth description of the electroweak theory and a comparison with experiment. Two popular textbooks worth mentioning are "Introduction to Elementary Particles" by David Griffiths [72], and "Neutrino Physics" by Kai Zuber [33].

1.3.1. Weak Interactions. Just like Quantum Electrodynamics (QED) couples to electric charge, Quantum Chromodynamics (QCD) couples to color charge, electroweak force is said to be coupled to two "weak charges," which all quarks and leptons carry: weak isospin and weak hypercharge. Weak isospin (not to be confused with isospin) is a quantum number related to weak interactions and usually denoted by T. It has three components T_1, T_2 and T_3, and the third component T_3 is a conserved quantity under all interactions (weak isospin conservation law). Weak hypercharge is another quantum number $Y_W = 2(Q - T_3)$, that is dependent on the electrical charge Q of the particle and its weak isospin T_3.

The weak interaction is unique for a number of reasons. It is the only force out of the four fundamental forces of nature that can:

- change the quark flavor, e.g. from u to d;
- violate P (parity) and CP (charge-parity) symmetry.

Since the weak force is known to be mediated by the exchange of the heavy intermediate vector bosons[11], the charged $W^{\pm}$ and neutral Z^0, it is said that there are two types of weak

[10] Neutrino scattering off electrons is ignored in this analysis, since such interactions have a much lower cross section than scattering off nuclei.

[11] Bosons are integer spin particles that obey Bose-Einstein statistics, and can be either elementary or composite. As opposed to fermions that are the building blocks of matter, elementary bosons, or gauge

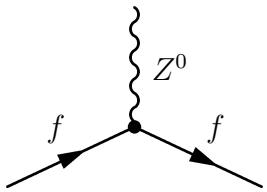

FIGURE 1.3. Feynman diagram for a fundamental neutral vertex in weak interactions.

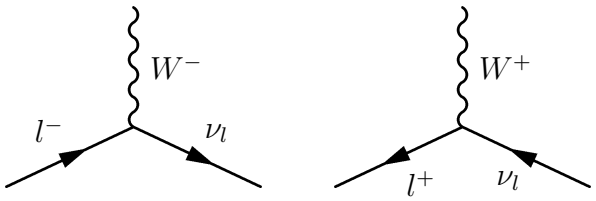

FIGURE 1.4. Feynman diagrams for fundamental charged vertices in weak interactions.

interactions, also known as vertices. These two types of fundamental weak interaction vertices are shown in Feynman diagrams[12] in Figures 1.3 and 1.4. These vertices are building blocks of more complex Feynman diagrams representing actual physical processes, which will be discussed further in the text. The W and Z bosons in these figures are intermediate, hence virtual particles. Neutrino weak interactions are said to be charged-current (CC) if the boson exchanged between a neutrino and a quark (or a system of quarks, or a whole nucleus) was a $W^{\pm}$, and neutral-current (NC) in case of the Z^0. Table 1.8 provides a summary of the properties of these bosons. The existence of the W and Z heavy bosons was experimentally confirmed in 1983. The weak charged and neutral-currents [72], which are part of the

bosons, such as photons, gluons, W and Z bosons, and the Higgs, are mediators of fundametal forces of nature.

[12] Feynman diagrams are pictorial representations of the quantum particle interactions and decays. In Feynman diagrams all particles are depicted as lines. Straight lines represent fermions, wavy lines represent bosons. All particles entering or exiting a Feynman diagram correspond to real particles. Intermediate lines depict virtual particles.

TABLE 1.8. Physical properties of the weak force bosons.

Symbol	Antiparticle	Charge	Spin	Mass (GeV/c^2)
W^-	W^+	e	1	80.4 ± 0.03
Z^0	Self	0	1	91.188 ± 0.002

Lagrangian of electroweak interactions $\mathcal{L}_{EW}$, are:

$$j_\mu^\pm = \bar{u}\tfrac{-ig_W}{2\sqrt{2}}\gamma^\mu(1-\gamma^5)u, \qquad j_\mu^0 = \bar{u}\tfrac{-ig_Z}{2\sqrt{2}}\gamma^\mu(g_V - g_A\gamma^5)u, \tag{12}$$

where $\bar{u}$ and u are Dirac spinors, γ^μ are Dirac gamma-matrices, and g_W and g_Z are coupling strengths. The couplings of these two interactions are related to the weak mixing angle θ_W, such that $\theta_W = g_W/g_Z$. The Standard Model does not predict the values of these parameters, therefore they had to be measured experimentally [19]: $\theta_W = 28.7°$, $g_W = 0.653$.

After the electroweak symmetry breaking[13] the Lagrangian can be written in the following form:

$$\mathcal{L}_{EW} = \mathcal{L}_K + \mathcal{L}_{NC} + \mathcal{L}_{CC} + \mathcal{L}_H + \mathcal{L}_{HV} + \mathcal{L}_{WWV} + \mathcal{L}_{WWVV} + \mathcal{L}_Y, \tag{13}$$

where $\mathcal{L}_K$ is the kinetic term, which contains all the quadratic terms, and the mass terms, $\mathcal{L}_{NC}$ and $\mathcal{L}_{CC}$ are the neutral- and charged-current terms, respectively, $\mathcal{L}_H$ and $\mathcal{L}_{HV}$ are the Higgs terms, $\mathcal{L}_{WWV}$ and $\mathcal{L}_{WWVV}$ are the gauge self-interaction terms, and $\mathcal{L}_Y$ is the Yukawa term. It is outside of the scope of this dissertation to write down the expressions spelling out all the Lagrangian terms, and more information about them and about the rest of the

[13] Electroweak symmetry breaking, also known as the Higgs mechanism, is a spontaneous symmetry breaking induced by the Higgs field as a result of which the weak bosons gain mass and the weak field is distinguished from the electromagnetic field. In the SM at high enough temperatures the electromagnetic and weak forces are unified into a single electroweak force: all the electroweak bosons have the same - or "symmetric" - zero mass.

theory of weak interactions can be found in a great number of widely available textbooks and scholarly articles dedicated to the subject.

1.3.2. Neutrino Cross Section. Neutrinos are often used as the probes of nuclear structure via neutrino-nucleon scattering, a special case of lepton-nucleon scattering. They allow for a precise determination of various interesting electroweak parameters, and, to perform high-statistics studies, artificial high-intensity neutrino beams are utilized.

This section gives a short summary of accelerator-based neutrino scattering cross section measurements, based on the review [73] of the field by Zeller. A more complete and comprehensive review [74] of neutrino cross sections, including neutrino-electron scattering, can be found in a review of the subject by Formaggio and Zeller.

In particle physics, a scattering cross section, σ, is defined as an area (m^2) that expresses the likelihood of interactions between particles. Because the size of the neutrino cross section is so incredibly small, a sufficiently high neutrino event rate $R = N/t$ ($\frac{\text{events}}{\text{s}}$) in the detector is required. Therefore, neutrino detectors need to be large. For instance, the Super-K detector contains 50 kilotons of water, and the PØD detector mass is 5 tons in total, with 2 tons being the water targets. High-intensity I ($\frac{\nu}{\mathrm{cm}^2\mathrm{s}}$) neutrino beams and detectors with large target mass T (nucleons) have to be employed:

$$R = T \cdot \sigma \cdot I, \tag{14}$$

where σ (cm^2) is the appropriate neutrino-nucleon cross section.

After integrating Equation 14 over time t, the following expression for an experimentally measurable cross section can be obtained:

$$\sigma = \frac{N}{T \cdot \Phi}, \tag{15}$$

where $\Phi = \int I(t)dt$ (cm^{-2}) is the integrated incident neutrino flux.

1.3.3. Simulation of ν Interactions. Monte Carlo simulations of neutrino interactions play an essential role in both theoretical and experimental neutrino physics. They are useful not just for modeling the signal and background event rates and distributions in a particular neutrino experiment, but are a theoretical frontier [14] of nuclear science. These simulation libraries are often called neutrino event generators. They provide concrete implementations of a multitude of models that cover neutrino scattering off electrons, nucleons, quarks, etc.

Historically, it has been the case that most earlier neutrino scattering experiments developed their own simulation packages. For example, the Soudan 2 experiment developed NEUGEN [87], MiniBooNE developed NUANCE [83], Super-Kamiokande developed NEUT [85], etc. These different simulations were often crafted for a specific detector technology and incoming neutrino energy range, and they were tuned to better agree with the available data. The exact details of model implementations vary among the simulations, which often makes it difficult to compare the results of the same model in different simulation libraries. This issue is known in the neutrino physics community, and attempts are being made at unifying the simulation software for the benefit of everyone.

The T2K experiment uses NEUT [85] and GENIE [86] neutrino event generators to simulate neutrino events. The scattering models include various neutrino and antineutrino CC and NC reactions important for the T2K neutrino energy range, including but not limited to deep inelastic scattering (Section 1.4), charged-current quasi-elastic and neutral-current elastic (Section 1.5), CC resonant and coherent pion production (Section 1.6), etc. After the initial interaction in the primary vertex, the final state particles such as nucleons and

[14] Neutrinos are the smallest probes available to test the nuclear models. In fact, early neutrino scattering experiments helped confirm the quark structure of the nucleons.

pions experience significant rescattering in the nucleus, so called final state interactions (FSI). Both NEUT and GENIE have extensive FSI models, both theoretical and phenomenological, implemented in them. More about the models can be read in Section 1.6.

1.4. Inclusive Scattering

The total inclusive neutrino and antineutrino cross sections for neutrino-nucleon scattering have been measured by many experiments over the years (Figure 1.5). Assuming muon neutrino beams, typically these experiments measured the total charged-current (CC) and neutral-current (NC) cross sections of the following processes:

$$\begin{aligned} &\nu_\mu + \mathcal{A} \to \mu^- + \mathcal{N}, \quad \bar{\nu}_\mu + \mathcal{A} \to \mu^+ + \mathcal{N}, \quad \text{(CC)} \\ &\nu_\mu + \mathcal{A} \to \nu_\mu + \mathcal{N}, \quad \bar{\nu}_\mu + \mathcal{A} \to \bar{\nu}_\mu + \mathcal{N}. \quad \text{(NC)} \end{aligned} \tag{16}$$

The total CC neutrino-nucleon cross section as a function of incident neutrino energy E_ν was determined to high precision by CCFR and CDHS. Above 30 GeV the total cross section rises linearly with energy, as can be seen from Figure 1.5. This behavior is expected for point-like scattering of neutrinos from quarks, but it breaks down at lower energies. It can be seen in Figure 1.5 that in the 0 - 1 GeV energy range the inclusive cross section is not precisely understood.

To add information to the picture, differential cross sections in the muon momentum-angle (p, θ) phase-space have been reported. NuTeV [75] reported the cross section on iron, ArgoNeuT [76] reported one at lower energies on argon, and T2K [77] on carbon. Such differential cross section measurements are usually less model-dependent than the cross section versus E_ν measurements.

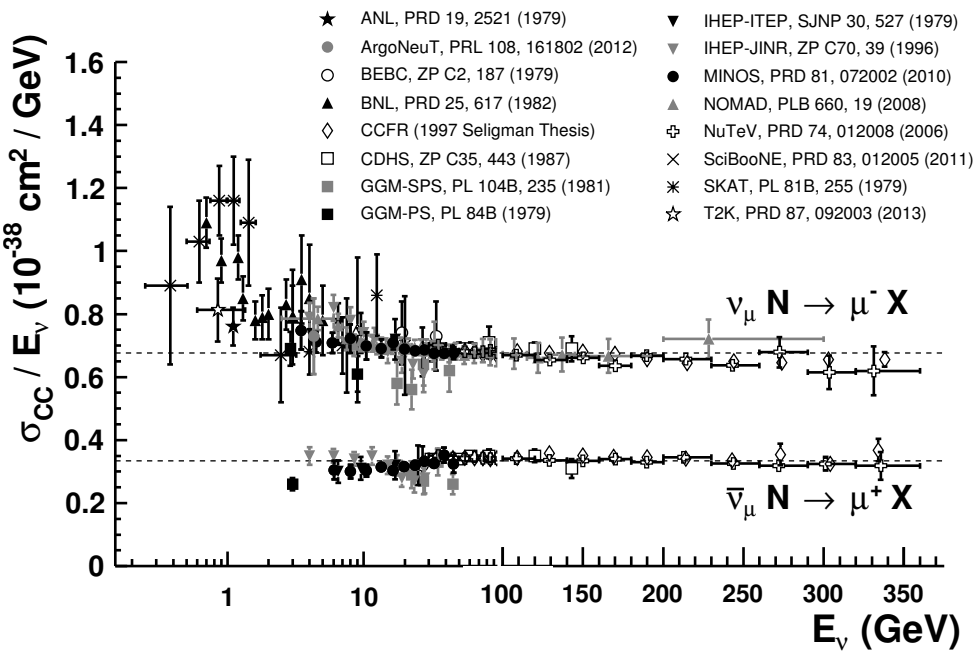

FIGURE 1.5. Measurements of ν_μ and $\bar{\nu}_\mu$ charged-current $\sigma^{CC}_{total}/E_\nu$ as a function of incident neutrino energy E_ν. Note the transition between logarithmic and linear scales occurring at 100 GeV. The error bars include both statistical and systematic uncertainties. This figure and its description were taken from the PDG [73].

At high energies the CC inclusive neutrino scattering cross section is dominated by Deep Inelastic Scattering (DIS):

$$\nu + \mathcal{A} \rightarrow l^- + \mathcal{N} + \text{mesons}. \tag{17}$$

Several experiments measured the DIS cross sections for various final states: CHORUS [78], NOMAD [79], and NuTeV [75].

1.5. CC Quasi-Elastic and NC Elastic Scattering

At low energies ($\sim$ 1 GeV) the CC inclusive cross section is dominated by charged-current quasi-elastic (CCQE) scattering:

$$\nu_\mu + n \rightarrow \mu^- + p. \tag{18}$$

It is usually chosen as the signal channel in many neutrino oscillation experiments, in part because of its dominating cross section. The Feynman diagram for the CCQE interaction is shown in Figure 1.6. This reaction would be observed, strictly speaking, in scattering off a

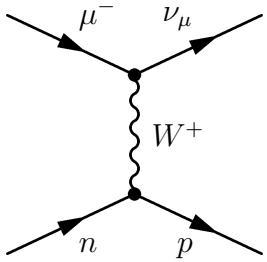

FIGURE 1.6. Feynman diagram for the ν_μ-induced CCQE interaction.

free nucleon, which is a valid approximation for smaller size nuclei, but which breaks down for larger size nuclei, where FSI or multinucleon interactions are possible.

Figure 1.7 displays the existing status of CCQE cross section measurements as a function of neutrino energy E_ν. In this plot the solid lines show the simulation prediction from the NUANCE [83] event generator. Other generators and different models exist, which sometimes yield significantly different predictions [84]. For example, the difference in CCQE cross section size after accounting for the FSI effects in NEUT [85] and GENIE [86] neutrino event generators can be on the order of 10%. Note that in many of these initial cross section measurements, which were performed with bubble chambers, light targets such as H_2 and D_2 were utilized, and the detection of a clear final state - a single muon and a single nucleon - were required. In case of heavier nuclear targets, of course, the situation is a lot more complicated: the FSI effects can and do alter the size and shape of the cross section, as well as the event kinematics and topology. Because of FSI effects, for example, it is possible to observe CCQE events with no or more than one nucleon. Therefore, care needs to be taken in defining what one means by CCQE scattering in case of nuclear targets heavier than hydrogen or deuterium.

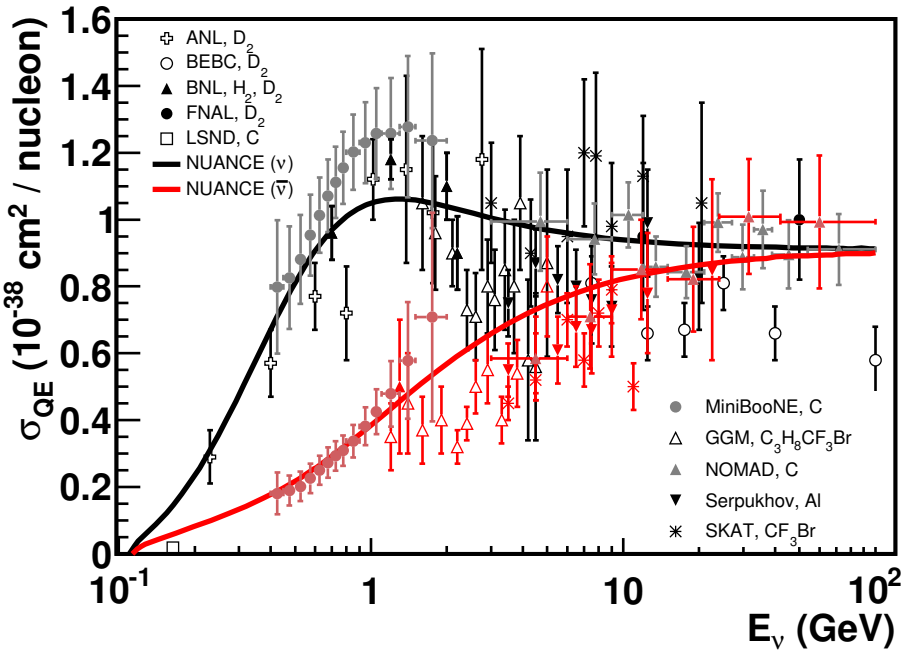

FIGURE 1.7. This figure and its description were taken from the PDG [73]: "Measurements of ν_μ (black) and $\bar{\nu}_\mu$ (red) charged-current QE cross section σ_{QE} as a function of incident neutrino energy E_ν. Data on a variety of nuclear targets are shown, including measurements from ANL [7], BEBC [80], BNL [8], FNAL [81], GGM [82], etc. Solid lines are the QE free nucleon scattering prediction from NUANCE [83] assuming $M_A = 1.0$ GeV. This prediction is significantly altered by nuclear effects in case of neutrino-nucleus scattering. Although plotted together, care should be taken in interpreting measurements performed on targets heavier that D_2 due to possible differences in QE indentification and kinematics."

The neutral-current elastic (NCE) intraction is mediated by a neutral Z^0 boson and can in general be described by the following reaction:

$$\nu + \mathcal{A} \rightarrow \nu + \mathcal{A}. \tag{19}$$

In an NCE interaction event, a neutrino can scatter off either a proton or a neutron, and as a result the nucleon recoils intact. The Feynman diagram for NCE scattering off a proton is shown in Figure 1.8. Published NCE measurements include those from BNL E734 [88], and

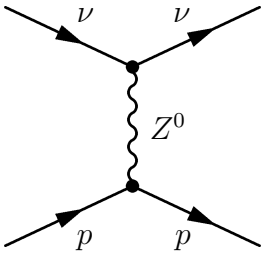

FIGURE 1.8. Feynman diagram for the NCE scattering off a proton.

MiniBooNE [89]. A more recent NCE measurement from T2K can be found in the Ph.D. thesis of D. Ruterbories [90].

1.6. CC SINGLE PION PRODUCTION

At low energies ($\sim$ 1 GeV) the second most dominant cross section after CCQE is the CC resonant single pion (CC1π) production, occuring when a neutrino scatters inelastically producing a short-lived baryonic resonance, which most often decays to a nucleon and a single pion. The relative size of the CCQE, resonant pion production, and DIS cross sections can be seen in Figure 1.9. In addition to resonant production, neutrinos can also scatter

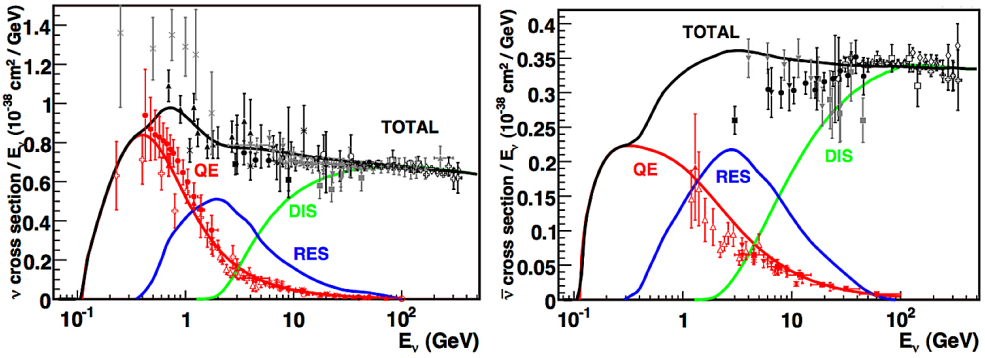

FIGURE 1.9. This figure is taken from [74]. The neutrino-nucleon (left) and antineutrino-nucleon (right) cross sections plotted as a function of (anti)neutrino energy [74]. Example predictions for each are provided by the NUANCE generator [83]. The processes that contribute to the total cross section (shown by the black lines) are: quasi-elastic (QE, red lines) scattering; resonance production (RES, blue lines); and deep inelastic scattering (DIS, green lines).

coherently off the entire nucleus, leaving the recoiled nucleus un-shattered and in the same

state as prior to the collision, however the coherent pion production cross section is small compared to resonant pion production.

In this work a ν_μ-induced charged-current single π^+ (CC1π^+) production channel is chosen as the signal of interest. The physics contributing to the signal is discussed next in Section 1.6.1. Existing CC1π^+ measurements are covered in Section 1.6.2. The Rein-Sehgal model of single pion production, which is widely used in Monte Carlo event generators, is discussed in Section 1.6.3. The Monte Carlo simulation of CC1π^+ events in T2K is presented in Section 1.6.4. The motivation for the measurement of CC1π^+ on water in T2K is discussed in Section 1.6.5.

1.6.1. CC1π^+ AS A SIGNAL. In a neutrino cross section analysis signal and background categories can be defined in a variety of ways, and care needs to be taken in being clear what definitions and conventions are used in the analysis. Some analyzers could chose to define signal and background in terms of before-FSI event categories, i.e. primary interaction models before the initial particles have a chance to reinteract. This approach works well for small nuclear targets, i.e. H_2 or D_2, but breaks down for larger targets due to FSI effects which alter the original topology.

On the other side of the spectrum the signal can be defined in terms of completely reconstructed quantities, e.g. all low energy neutrinos that produce events below the reconstruction threshold could automatically be ignored or considered background.

For the purposes of this analysis the signal defined to be an observed, or after-FSI (or post-FSI), ν_μ-induced CC1π^+ event, i.e. with one μ^- and one π^+ exiting the struck nucleus after hadronic reinteractions, however no requirements are set on event reconstruction. Also, it is required that there are no other mesons than the single π^+ that exit the nucleus, however no restrictions on the number of nucleons (protons and neutrons) are set. This exclusive CC1π^+

production channel definition is identical to the MiniBooNE CC1π^+ signal definition [91]:

$$\nu_\mu + (n \text{ or } p) \rightarrow \mu^- + \pi^+ + (\text{any number of } n \text{ or } p), \tag{20}$$

but is substantially different from the CC1π^+ definition used in the ANL and BNL measurements [7, 8], where exactly three final state particles were required: μ^-, π^+ and p.

1.6.2. Previous CC1π^+ Measurements. Over the decades there have been many CC1π^+ measurements performed on a variety of targets utilizing a number of different detector technologies. Bubble chamber experiments produced several CC1π^+ results employing light targets (H_2 or D_2) and requiring both the detection of final state μ and a single $\pi^\pm$ [19] [7] [12]. These experiments were able to measure the CC1π^+ cross section or a CC1π^+/CCQE cross section ratio on individual nucleons, commonly as a function of MC-truth neutrino energy, and confirm early neutrino-nucleon interation models. It was also verified [98] that most of the pion production is of baryonic resonance nature and occurs mainly through the production of Δ resonances. The results of these early neutrino cross section experiments are summarized in Figure 1.10.

Experimental knowledge of the single pion production cross section in the low neutrino energy range, i.e. from 100 MeV to 2 GeV, is sparse, coming solely from the ANL [7] and BNL [12] bubble chamber experiments with low statistics. Moreover, there exists a longstanding disagreement between the measurements of $\nu_\mu + p \rightarrow \mu^- + p + \pi^+$ - the leading single pion production process - by ANL and BNL. The data from the 12 ft bubble chamber at ANL and the 7 ft bubble chamber at BNL for this process differ in normalization by 30 - 40%. This disagreement, sometimes called the "ANL-BNL Puzzle", for a long time was not well understood. Recently, however, an attempt was made to revisit the ANL and

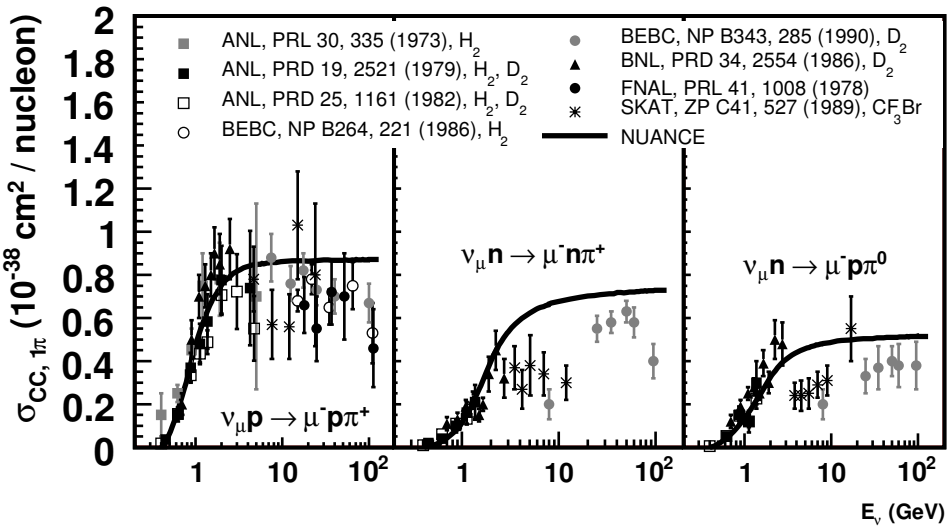

FIGURE 1.10. This figure and its caption were taken directly from Figure 49.3 of the Review of Particle Physics [19]: "Historical measurements of ν_μ resonant single-pion production. The data appear as reported by the experiments; no additional corrections have been applied to account for differing nuclear targets or invariant mass selections. The free scattering curve from NUANCE assumes $M_a = 1.1$ GeV [83]. Note that other absolute measurements have been made by MiniBooNE [91, 95] but cannot be directly compared with this historical data - such modern measurements are more inclusive and have quantified the production of pions leaving the target nucleus rather than specific π + N final states as identified at the neutrino interaction vertex".

BNL datasets to look for possible consistency by researchers at University of Sheffield and University of Rochester [9]. In their paper, ratios of event rates for different processes, e.g. CC1π^+ to CCQE, in the ANL and BNL datasets are considered, in which normalization uncertainties cancel. Subsequently, the obtained event rate ratios are multiplied by an independent measurement of the cross section in the denominator, e.g. CCQE, and the single pion cross sections are extracted as a result. The authors conclude that there is good agreement between ANL and BNL for the ratio of $\sigma_{\nu_\mu+p\to\mu^-+p+\pi^+}/\sigma_{CCQE}$, which indicates that the "ANL-BNL puzzle" results from discrepancies in the flux predictions. This is consistent with previous analyses of the same data [10] [11], which found that the ANL and BNL measurements agree within their published flux uncertianties.

All of the modern experiments utilize heavier nuclear targets in order to have significantly higher event rates. MiniBooNE has recently published a high statistics CC1π^+ differential cross section measurement [91] on mineral oil (CH_2). MINERνA experiment has also recently published two papers on the single pion production on hydrocarbon at $\langle E \rangle = 4$ GeV [92, 93]. However it is difficult to compare the MiniBooNE and other modern results to the earlier

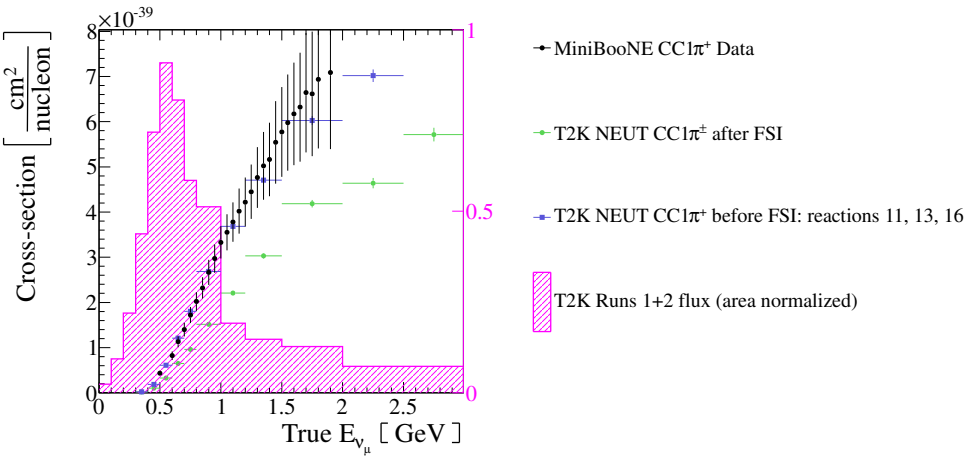

FIGURE 1.11. The MiniBooNE result (black dots) compared with NEUT predictions for the before and after FSI CC1π^+ cross sections on water. MiniBooNE cross section was measured using mineral oil and calculated per average target CH_2, NEUT prediction are calculated per H_2O molecule. No corrections were applied to account for the difference in the nuclear targets.

bubble chamber experiments, which dealt with light targets, due to FSI effects, which alter both the shape and size of the cross section as well as the observed event topology, and which are not very well known at the moment.

A comparison of MiniBooNE data to the T2K NEUT MC is shown in Figure 1.11. It can be clearly seen from that figure that MiniBooNE data does not agree well with T2K NEUT MC predictions for the after-FSI signal definition, but instead favors the before-FSI NEUT.

A review of the recent weak single pion production data is presented in a paper by J.T. Sobczyk and J. Zmuda, where they try to compare the MiniBooNE and MINERνA

results against the NuWro event generator prediction [94]. As a result they find that both normalization and shape of the ratio of the measured differential cross sections in the pion kinetic energy are different from the MC predictions. The normalization discrepancy between the data and MC is as large as a factor of 1.49. Additionally, it must be noted that there is a significant discrepancy between the MiniBooNE and MINERνA data measurements themselves in both normalization and shape.

An up-to-date detailed review of most modern and historical CC1π^+ measurements can be found in the latest version on the Review of Particle Physics [19] and [96].

1.6.3. Rein-Sehgal Model. The famous single pion production paper by Dieter Rein and Lalit M. Sehgal titled "Neutrino-Excitation of Baryon Resonances and Single Pion Production" was published [98] in the Annals of Physics 1981. It is the theoretical foundation of the single pion production models implemented in the NEUT and GENIE neutrino event generators. This section of the thesis is an attempt to give a short outline and summary of the Rein-Sehgal paper, which is important to this analysis.

The Rein-Sehgal model describes the production of baryonic resonances in NC and CC neutrino interactions with the restricted hadronic invariant mass $W < 2$ GeV. It employs the relativistic quark model of Feynman, Kislinger and Ravndal (FKR) [99], which provides the wavefunctions for the resonances as excited states of a 3-quark system in a relativistic harmonic oscillator potential with SU(6) spin-flavor symmetry. Rein and Sehgal consider 1-π production to be mediated by 18 interfering resonances below 2 GeV, with an additional simple noninterfering, nonresonant background of isospin $\frac{1}{2}$. According to Rein and Sehgal, the nature of this added background is purely empirical: "we have represented the background by a resonance amplitude of P_{11} character (like the nucleon), with the Breit-Wigner factor

replaced by an adjustable constant. The corresponding cross section is added incoherently to the resonant cross section."

Their model makes an attempt at explaining the energy levels of the excited 3-quark systems, the hadronic widths of the resonances, and the matrix elements describing the transitions between the ground state and the excited states induced by weak and electromagnetic currents. In their paper a systematic analysis of all existing data on neutrino production of pions at the time (ANL and BNL datasets) is performed, and the final state is essentially treated as a superposition of resonances.

The Rein-Sehgal model focuses on the description of inelastic neutrino-nucleon scattering where the final hadronic state is selected to consist of a nucleon and a single pion. The ν_μ- and $\bar{\nu}_\mu$-induced 1-π production reactions that are considered include 6 CC channels

$$\begin{aligned} &\nu_\mu + p \to \mu^- + p + \pi^+, \quad \bar{\nu}_\mu + n \to \mu^+ + n + \pi^-, \\ &\nu_\mu + n \to \mu^- + p + \pi^0, \quad \bar{\nu}_\mu + p \to \mu^+ + n + \pi^0, \\ &\nu_\mu + n \to \mu^- + n + \pi^+, \quad \bar{\nu}_\mu + p \to \mu^+ + p + \pi^-, \end{aligned} \tag{21}$$

and 8 NC channels

$$\begin{aligned} &\nu_\mu + p \to \nu_\mu + p + \pi^0, \quad \bar{\nu}_\mu + p \to \bar{\nu}_\mu + p + \pi^0, \\ &\nu_\mu + p \to \nu_\mu + n + \pi^+, \quad \bar{\nu}_\mu + p \to \bar{\nu}_\mu + n + \pi^+, \\ &\nu_\mu + n \to \nu_\mu + n + \pi^0, \quad \bar{\nu}_\mu + n \to \bar{\nu}_\mu + n + \pi^0, \\ &\nu_\mu + n \to \nu_\mu + p + \pi^-, \quad \bar{\nu}_\mu + n \to \bar{\nu}_\mu + p + \pi^-. \end{aligned} \tag{22}$$

According to Rein-Sehgal, "all these reaction amplitudes are expected to be dominated by nucleon resonances as long as the pion-nucleon invariant energy does not exceed about 2 GeV," and the bulk of single pion production at the neutrino energies below 1-1.5 GeV is expected to

occur via the delta resonances. An example Feynman diagram for a resonant π^+ production through a Δ^{++} resonance is shown in Figure 1.12.

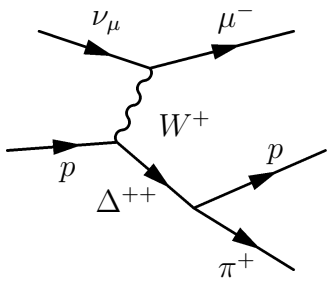

FIGURE 1.12. Feynman diagram for the ν_μ-induced CC1π^+ production occuring through the delta resonance, where the delta quickly decays to a proton and a π^+.

At the time of its publication, the Rein-Sehgal model accurately reproduced the total cross sections, cross section ratios and W-distributions at low and high energies, and gave predictions where data were lacking. The original work assumes the mass of the leptons to be negligible, but it was later expanded [100] to include finite lepton mass effects. However, this model has problems [101, 102] explaining the π electroproduction on protons in the data collected at the Jefferson lab (JLab) [103], and disagrees with some of the more modern models in both the size and the shape of the cross section [101, 102, 104–106]. It must be noted that the newer models disagree among themselves as well. Further theoretical and experimental study of the single pion production channels is therefore needed.

1.6.4. SIMULATION OF CC1π^+ IN T2K. The T2K experiment uses NEUT [85] and GENIE [86] neutrino event generators, concrete implementations of neutrino-nucleus scattering models. NEUT is T2K's primary neutrino event generator. It was originally developed for use by the Kamiokande experiment. For the purposes of this analysis NEUT is used as a primary simulation.

GENIE is a more modern universal neutrino event generator which is currently being used not only by T2K, but also NOνA, MINERνA, MicroBooNE, ArgoNEUT, LBNE, IceCUBE

and others. It is used in this cross section analysis mostly for validation and comparison purposes, but not in the final results.

Both NEUT and GENIE are two-step generators. First, a neutrino interaction per individual nucleon in the nucleus is modeled, producing final state particles at the primary interaction vertex. In the second stage of the simulation process the primary particles are propagated through the nuclear medium, where hadronic reinteractions, e.g. pion absorption, are possible.

Particles escaping the nucleus are passed on by NEUT (GENIE) to the GEANT4 detector simulation [97], where they are propagated through the detector materials and where mesons and nucleons can undergo so called Secondary Interactions (SI), which further alter event topology.

1.6.4.1. *CC1π^+ Cross Section Models.* In the first step of neutrino scattering event generation, the incident neutrino is assumed to interact with an individual quark in a nucleon (unless the reaction is occurring via a coherent production channel). New models of $2p2h$ (2 protons 2 holes) processes are now being incorporated into both generators, but are not used in the NEUT/GENIE version used in this analysis. The well-established Rein-Sehgal [98] model is adopted in NEUT (as well as GENIE) to simulate single π, K, and η resonant and coherent production final states at the primary interaction vertex. This model is what simulates most of the signal in this analysis. CC interaction modes that are relevant to this analysis, i.e. contribute most to either the signal or background event categories, are summarized in Table 1.9. NEUT interaction modes 11, 13 (resonant π^+ production) and 16 (coherent π^+ production), which contribute the most to the signal event category, are shown in Figure 1.13 along with the T2K area-normalized flux.

TABLE 1.9. Charged-current before-FSI NEUT interaction modes contributing to both signal and background. The rows are sorted in the order of increasing NEUT mode number.

NEUT mode	Reaction name	Reaction
1	Charged-current quasi-elastic (CCQE)	$\nu + n \rightarrow l^- + p$
11	Resonant π^+ production	$\nu + p \rightarrow l^- + p + \pi^+$
12	Resonant π^0 production	$\nu + n \rightarrow l^- + p + \pi^0$
13	Resonant π^+ production	$\nu + n \rightarrow l^- + n + \pi^+$
16	Coherent π^+ production	$\nu + N \rightarrow l^- + N + \pi^+$
21	Multiple π production	$\nu + (n\|p) \rightarrow l^- + (n\|p) + \text{multi-}\pi$
22	Single η^0 from Δ resonance	$\nu + n \rightarrow l^- + p + \eta^0$
23	Single K^+ from Δ resonance	$\nu + n \rightarrow l^- + \Lambda + K^+$
26	Deep inelastic scattering	$\nu + (n\|p) \rightarrow l^- + (n\|p) + \text{mesons}$

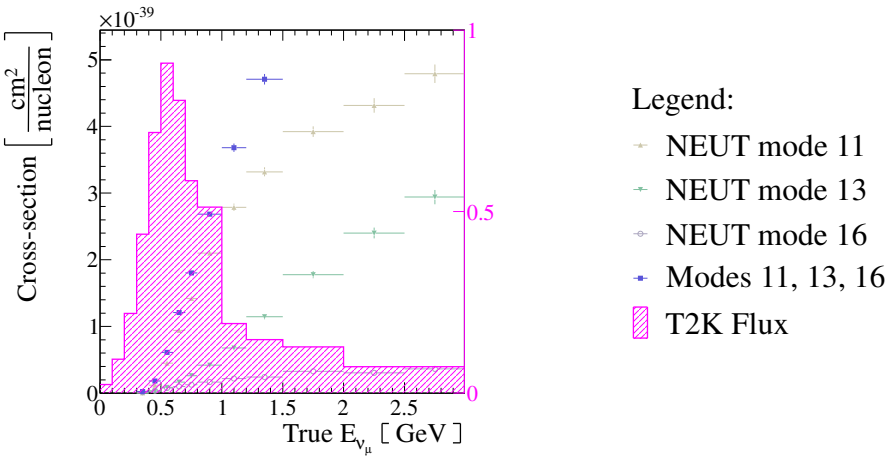

FIGURE 1.13. NEUT nucleon-level ν_μ-induced CC cross sections on oxygen. Reactions 11, 13 and 16 (description of interaction codes is in Table 1.9) are shown along with the area-normalized flux. Vertical error bars are due to MC statistical uncertainties. Horizontal error bars represent the width of the MC-truth neutrino energy bins for which the central values were calculated. The binning is described in Table 4.29.

Note that in this analysis events that have no or more than one π^+ exiting the nucleus are considered background. For example, NEUT reactions 11, 13 and 16 that have no π^+ escaping the nucleus due to either pion absorption or charge exchange effects (collectively known as FSI) would be labeled CCQE-like, etc. and considered background. The after-FSI

CC1π^+ signal definition is favored over the generator level interaction mode definition in this analysis, since we cannot directly measure intra-nuclear processes in our detectors and see what is happening directly at the nucleon level. Observed, post-FSI and after-FSI CC1π^+ names will be used throughout the text interchangeably.

Observed CC1π^+ events can come from various underlying before-FSI interaction modes, e.g. resonant or coherent single π production ($\sim$83%), multi-π production ($\sim$6%), CCQE ($\sim$4%), etc. All of the various physics contributions to the signal category according to NEUT Monte Carlo simulation are summarized in Table 1.10 and Figure 1.14, where the signal events occupy the rightmost two vertical slices. It is clear from Figure 1.14 that the biggest

TABLE 1.10. NEUT predictions for after-FSI signal physics before any analysis cuts. Rows are sorted in the order of decreasing percentage. Percentages presented here signify fractions of the total post-FSI signal category. Considered were all MC signal events in the fiducial volume of the PØD for Run 1 water-in NEUT MC.

NEUT Mode	Reaction	Fraction (%)
11	$\nu_\mu + p \to \mu^- + p + \pi^+$	55.86
13	$\nu_\mu + n \to \mu^- + n + \pi^+$	14.18
16	$\nu_\mu + N \to \mu^- + N + \pi^+$	13.11
21	$\nu_\mu + (n\|p) \to \mu^- + (n\|p) + \text{multi-}\pi$	5.65
1	$\nu_\mu + n \to \mu^- + p$	3.79
12	$\nu_\mu + n \to \mu^- + p + \pi^0$	3.54
26	$\nu_\mu + (n\|p) \to \mu^- + (n\|p) + \text{mesons}$	3.51
22	$\nu_\mu + n \to \mu^- + p + \eta^0$	0.35

background before cuts is the after-FSI CCQE with one μ^- and one p leaving the nucleus, since the nucleon-level before-FSI CCQE (NEUT mode 1) has the largest cross section around the T2K neutrino energy peak. NEUT predictions for the flux-averaged after-FSI single bin CC1π^+ cross sections on oxygen and water are $1.11 \cdot 10^{-39}$ cm^2 and $1.26 \cdot 10^{-39}$ cm^2

respectively. MC predictions for the T2K absolute flux-averaged cross sections, $\langle\sigma_{\nu_\mu}\rangle_\Phi$, for reactions 11, 13 and 16, are shown in Table 1.11. Systematic uncertainties associated with NEUT reaction/interaction modes that are important to this analysis are propagated through the measurement in Section 4.6.2.

TABLE 1.11. NEUT predictions for the nucleon-level before-FSI ν_μ-induced CC1π^+ cross sections on oxygen calculated using MCP5E (Monte Carlo Production 5 Re-spin E) Runs 1 and 2 and 11b v3.2 flux tuning.

NEUT mode	Reaction	$\langle\sigma_{\nu_\mu}\rangle_\Phi$ on O $\left[\frac{\text{cm}^2}{\text{nucleon}}\right]$
11	$\nu_\mu + p \to \mu^- + p + \pi^+$	$1.22 \cdot 10^{-39}$
13	$\nu_\mu + n \to \mu^- + n + \pi^+$	$0.42 \cdot 10^{-39}$
16	$\nu_\mu + N \to \mu^- + N + \pi^+$	$0.12 \cdot 10^{-39}$
11, 13, 16		$1.76 \cdot 10^{-39}$

1.6.4.2. *Final State Interactions.* During the second stage of the simulation process NEUT adopts a semiclassical approach to simulate hadronic reinteraction in the nucleus, commonly referred to as Final State Interactions or FSI. FSI effects are of significance to this analysis due to the fact that they can alter the observed event topology and kinematics, e.g. a charged-current single π^+ production event (interaction modes 11 and 13 in Table 1.9 and Figure 1.14) could be observed as a CCQE-like event if π^+ gets absorbed by the nucleus and only μ^- and p exit it. This scenario can be seen happening in Figure 1.14. Thus, it is important to note that care needs to be taken in defining what is the CC1π^+ signal for a particular analysis. Systematic uncertainties associated with these effects are evaluated in Section 4.6.3 of this dissertation.

1.6.5. MOTIVATION FOR THE MEASUREMENT OF CC1π^+ ON H_2O. Recently there has been a considerable increase of interest in neutrino cross section measurements on nuclear targets, due to the need for accurate signal and background event rate predictions in neutrino

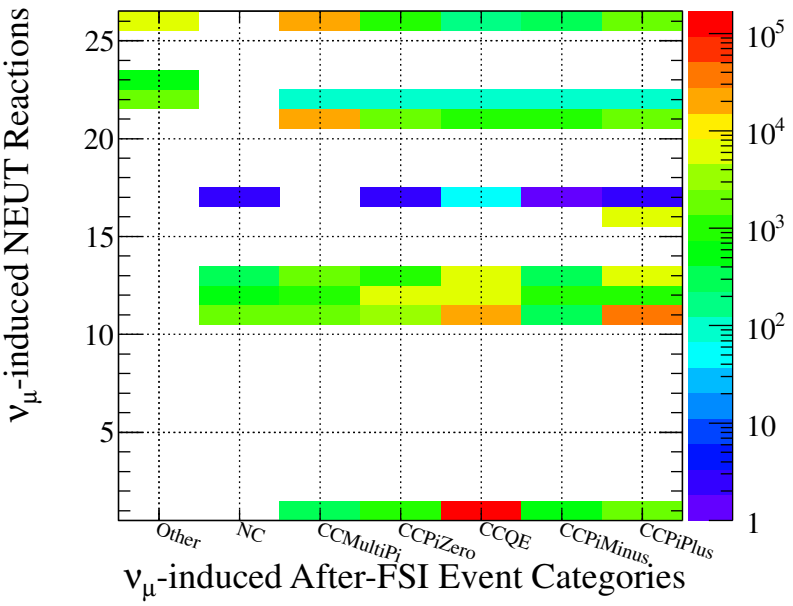

FIGURE 1.14. Mapping between before-FSI NEUT reaction modes (y axis), explained in Tab. 1.9, and after-FSI event categories (x axis) for all ν_μ-induced CC vertices in the PØD fiducial volume. Z axis is in log scale.

oscillation experiments. In the T2K experiment in particular, the Super-Kamiokande (SK) far detector [17] is a Cherenkov radiation detector with water for the target medium. In the T2K neutrino oscillation measurements [66] [67] CCQE single-Cherenkov-ring events are selected as signal with one type of background being Charged-Current Single π^+ events, when the π^+ is either below the Cherenkov energy threshold or not reconstructed as a second ring.

The primary goal of this analysis is to measure a single bin flux-integrated absolute ν_μ-induced CC1π^+ cross section on water as a target, $\langle\sigma_{\nu_\mu \mathrm{CC1}\pi^+}\rangle_\Phi$, for it is important to constrain the uncertainty on this particular channel to improve the CC1π^+ background prediction in the T2K neutrino oscillation analyses. This can be achieved by the means of an ND280 near detector based CC1π^+ measurement on water via an event rate subtraction method.

1.7. Overview of Analysis Strategy

This section briefly describes the ν_μ-induced CC1π^+ cross section analysis strategy utilizing data collected with the PØD detector, which is part of the ND280 detector complex (see Chapter 2, Section 2.4 and Chapter 3). The entire analysis with all details is described in Chapters 4 and 5.

Several probable CC1π^+ event topologies were considered in this analysis, and analysis cuts were developed and optimized to select two-track events with a single μ^- candidate track and a single π^+ candidate track. Both PØD-fully-contained and PØD-partially-contained events were considered in this analysis for better phase space coverage. The PØD-fully-contained signal candidate events have both tracks starting and ending in the PØD and are mostly induced by lower neutrino energies (less than 1 GeV). The PØD-partially-contained events have the muon candidate track exit the PØD detector in the direction of the TPCs, and the pion candidate track contained in the PØD.

CC1π^+ events could also be reconstructed as one (when all but one particle are below the reconstruction threshold or overlap), three (when μ^-, π^+ and p are all visible/reconstructed) and more (high proton track multiplicity, reconstruction error or overlap with a second event) track events, however these selections are outside the scope of this analysis, though these additional topologies could be used in future versions on the analysis.

Section 4.2 contains a detailed description of the event selection cuts implemented to select CC1π^+-enriched samples for PØD water-in and water-out T2K running periods, which are used further in the analysis.

Section 4.3 describes the cross section on water calculation methodology, how the two samples are used, including background subtraction, efficiency correction and the event rate subtraction formulae.

Sections 4.4, 4.5 and 4.6 contain full information about the statistical and systematic uncertainties associated with this analysis.

CHAPTER 2

T2K Experiment

T2K [28, 112] is an international collaboration with more than 400 members from 58 institutions in 11 countries working on a neutrino oscillation experiment situated in Japan. The T2K experiment began the commissioning of the beam and the detectors in April 2009 and started taking physics data in January 2010. As of March 2015 it is an ongoing experiment with the integrated proton beam exposure of $\sim 10^{21}$ protons on target (POT).

The science goals and design merits of T2K are discussed in Section 2.1. The Japan Proton Accelerator Research Complex (J-PARC) facility where the T2K neutrino beam is produced is described in Section 2.2. The T2K experiment has two near detectors, ND280 and INGRID, and a far detector - Super-Kamiokande (SK or Super-K). A description of Super-K is provided in Section 2.3. ND280 has multiple sub-detectors with the π^0 detector (PØD) being of interest to this analysis. The ND280 and INGRID detectors are described in Section 2.4. The PØD detector is covered in detail in Chapter 3.

2.1. Statement of Purpose

This section provides a brief overview of the T2K statement of purpose and is largely based on the T2K letter of intent [107] published in 2007.

The broad scientific purpose of the T2K experiment is to explore the physics beyond the Standard Model, that is to perform precision measurements of the neutrino oscillation parameters. More specifically its goals include:

- discovery of the electron neutrino appearance in the muon neutrino beam ($\nu_\mu \rightarrow \nu_e$);
- precision measurement of oscillation parameters in the muon neutrino disappearance experiment ($\nu_\mu \rightarrow \nu_\mu$);

- search for sterile neutrinos in the ν_μ dissapearance mode, analyzing neutral-current events;
- measurement of neutrino-nucleus scattering cross sections for various target materials, e.g. scintillator plastic, water, lead, etc.

The special emphasis of T2K is on measuring the mixing angle θ_{13} by observing the subdominant $\nu_\mu \rightarrow \nu_e$ oscillation. It must be said that most of the original T2K science goals - the measurements of neutrino oscillation parameters including θ_{13} - have already been achieved. Some of the important T2K neutrino oscillations results can be found in [66, 67, 108].

It must also be noted that the first θ_{13} measurements came from the reactor-based experiments, detecting antineutrinos as opposed to neutrinos. The Double CHOOZ experiment was the first to announce a measurement when in 2011 they reported an indication of $\overline{\nu}_e$ disappearance, concluding that $\theta_{13} \neq 0$ at 1.7 σ [109]. Later in 2012, Daya Bay reported a 5.2 σ discovery of $\overline{\nu}_e$ disappearance [110], which was promptly followed by a RENO experiment measurement [111] confirming the findings of the previous experiments.

The T2K experiment was unique when it first started operating in that it was the first off-axis long baseline neutrino oscillations experiment with the goal to measure the appearance of ν_e in the ν_μ beam.

The main goals of the near detectors - ND280 and INGRID, which include the measurement of the T2K neutrino flux and cross sections have also been mostly achieved. The T2K neutrino flux prediction is described in detail in the PRD publication [114]. As of March 2015 four neutrino cross section channel measurements were published [116–119]. Many other cross section measurements are work in progress.

For the full list of T2K publications and for more information on the T2K science goals, the readers are directed to [28] and [107].

FIGURE 2.1. The bird's eye view of the J-PARC high-intensity proton accelerator complex.

2.2. JAPAN PROTON ACCELERATOR RESEARCH COMPLEX

J-PARC [113] is a particle physics, material, and life science research lab located in Tokai on the east coast of Japan. It utilizes high-intensity proton beams to produce secondary beams of various particles, among them neutrinos. J-PARC's particle accelerator complex consists of three main parts:

- A 400 MeV proton linear accelerator (LINAC);
- A 3 GeV rapid cycling synchrotron (RCS);
- A 30 GeV main ring synchrotron (MR).

A bird's eye view of the proton accelerator complex on the east coast of Japan is shown in Figure 2.1.

In the T2K experiment an intense beam of neutrinos produced at J-PARC is sent 295 km underground across Japan to the Kamioka mine, where the Super-K far detector is situated (Figure 2.2).

The neutrino beam is produced as a result of collisions between the proton beam extracted from the Main Ring and a graphite target (Figure 2.3). These collisions result in hadronic interactions, which produce mostly pions and kaons. The charged pions and kaons are focused into a forward-going beam directed towards the INGRID near detector (Section 2.4.1) with

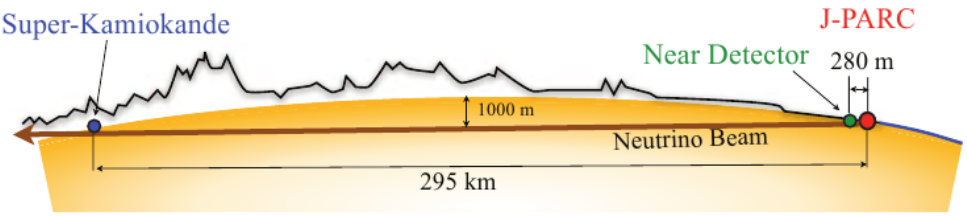

FIGURE 2.2. A schematic view of the T2K experimental setup showing the path of the neutrino journey from J-PARC through out the near detectors (green dot), and then 295 km underneath the main island of Japan to Super-Kamiokande far detector. Figure taken from the T2K NIM paper [112].

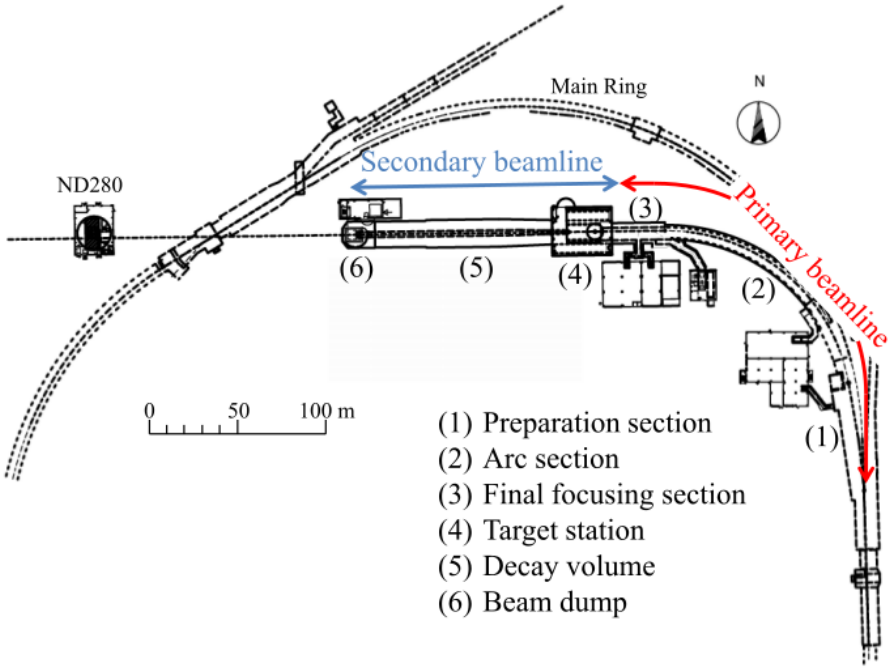

FIGURE 2.3. Overview of the T2K neutrino beamline. Figure taken from [114].

the powerful horn magnets [115]. Afterwards the pions and kaons quickly decay to mostly muons and muon neutrinos, after which the neutrino beam is heading through the ND280 off-axis detector to Super-Kamiokande.

It must be noted that both Super-K and ND280 are located 2.5° off-axis, which gives the advantage of a narrower neutrino energy peak[15], and the INGRID near detector is located on

[15] T2K off-axis energy spectrum peaking sharply at 600 MeV is a result of pion decay kinematics. At 2.5° off-axis pions of different energies (1 - 10 GeV) decay, and produce neutrinos with energies primarily less than 1 GeV.

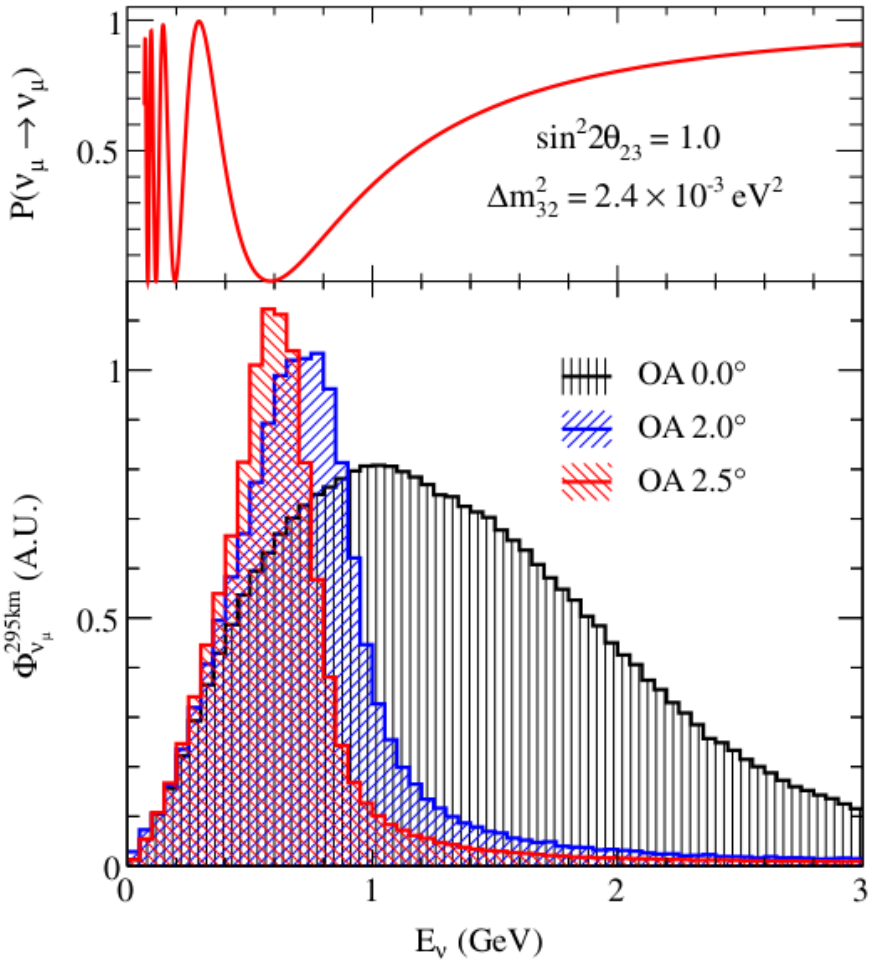

FIGURE 2.4. The T2K flux at 295 km for different off-axis angles and ν_μ survival probability. Figure taken from [114].

the beam axis. The on-axis and off-axis fluxes are shown in Figure 2.4. The T2K neutrino flux predictions for SK far detector and ND280 near detector broken down by parent particle type are shown in Figure 2.5, where it can be seen than below 2 GeV the ND280 ν_μ flux is dominated by pion parents.

The T2K experiment was unique when it first started operating in 2010 in that it was the first off-axis long baseline neutrino oscillations experiment. More details about the T2K beamline and the neutrino flux can be found in the T2K flux prediction publication [114].

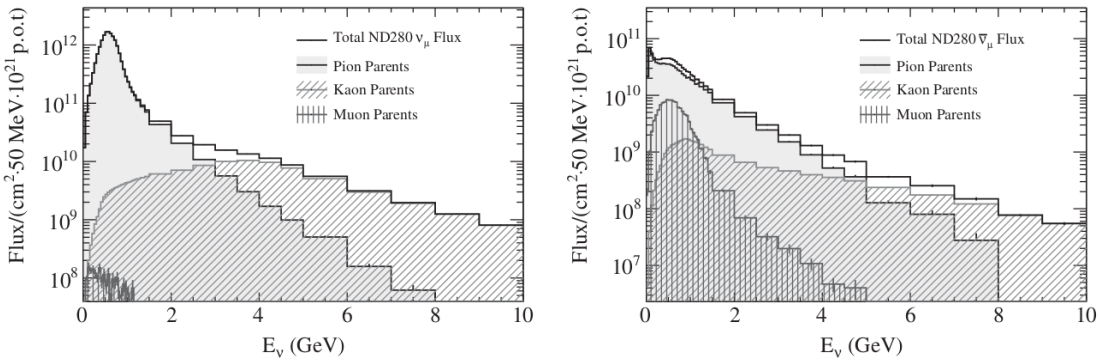

FIGURE 2.5. The T2K unoscillated ν_μ flux prediction for the ND280 near detector broken down by the parent particle type. Figure taken from [114].

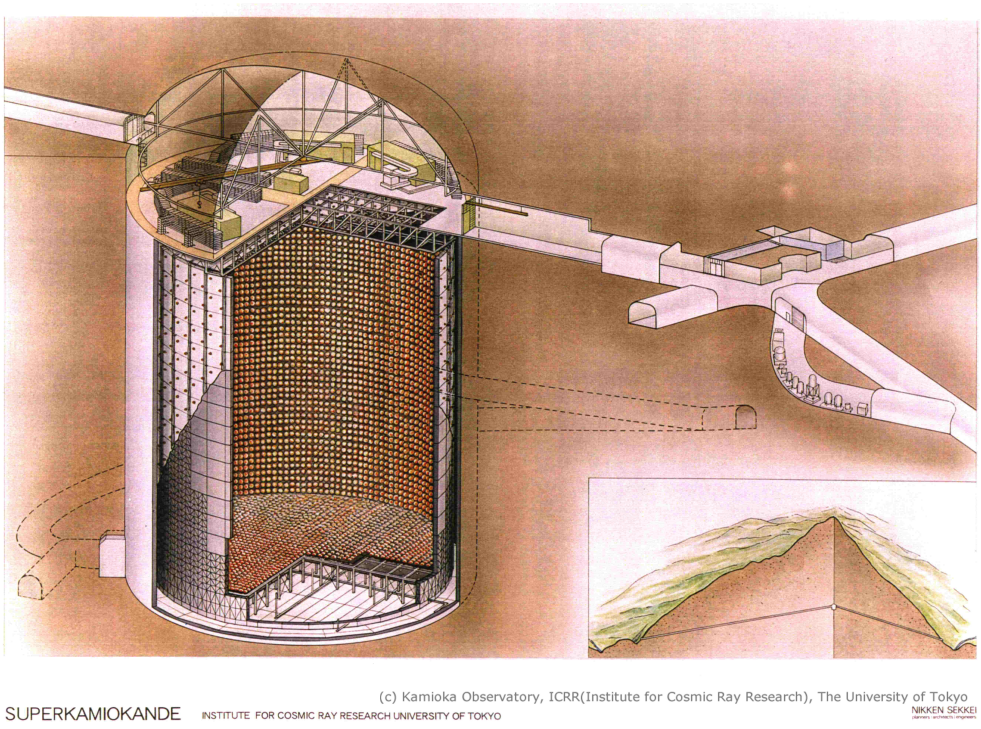

FIGURE 2.6. The drawing of the Super-Kamiokande detector, courtesy of Institute for Cosmic Ray Research, University of Tokyo.

2.3. SUPER-KAMIOKANDE FAR DETECTOR

Super-Kamiokande (Super-K or SK) [120] is a Cherenkov radiation detector located approximately 1000 m underground in the Kamioka mine near the city of Hida, Gifu Prefecture,

Japan (Figure 2.6). Super-K was built in place of an earlier experiment, Kamiokande[16], which was a proton decay[17] experiment. Super-K was originally designed for the study of solar and atmospheric neutrinos, but is also used for the study of supernovae neutrinos, proton decay and accelerator neutrinos. SK was the far detector in the K2K (KEK-to-Kamioka) neutrino oscillations experiment [68], the predecessor of T2K. It currently serves as a far detector in the T2K neutrino oscillations experiment, where it is registering the ν_μ and ν_e neutrinos originating from J-PARC.

The Super-K detector consists of a large cylindrical stainless steel tank, 39.3 m in diameter and 41.4 m in height, filled with 50 kilotons of ultra-pure water. Figure 2.6 shows the drawing of the Super-K detector in the Kamioka mine. The water tank is divided by a stainless steel structure into the inner detector (ID) region that is 33.8 m in diameter and 36.2 m in height and the outer detector (OD). Photo-sensors known as photo-multiplier-tubes (PMTs) are mounted on this steel structure. Approximately 11,000 20-inch PMTs face into ID region, and $\sim$ 2,000 8-inch PMTs face into the OD region. The OD region PMTs allow a veto of neutrino interactions that occur outside the ID, or are not contained in the ID.

Two example SK neutrino event displays[18] are shown in Figures 2.8 and 2.9. Each dot in the central part of these displays represents one of the 11,129 PMTs hit with the Cherenkov light. The color of the dots respresents the amount of light registered in that PMT. As is evident from these event displays, muons are distinguished from electrons according to the shape and fuzziness[19] of the Cherenkov rings. The shape and size of the rings, along with

[16] Kamiokande was one of the few detectors that observed the neutrinos from the SN1987A supernova, which was observed in the Large Magellanic Cloud in February 1987.
[17] Super-K has set a new lower limit on the proton lifetime of 5.9×10^{33} years [121].
[18] A neutrino interaction registered in a detector is called a neutrino event. Hence, a neutrino event display is a 2-D or a 3-D image showing the propreties (deposited charge, timing, etc.) of the hits and tracks of the charged particles resulting from the neutrino interaction in the detector. The incident neutrino itself is not visible.
[19] Electron rings are usually fuzzier than muon rings, since electrons experience multiple scattering, and produce electromagnetic showers.

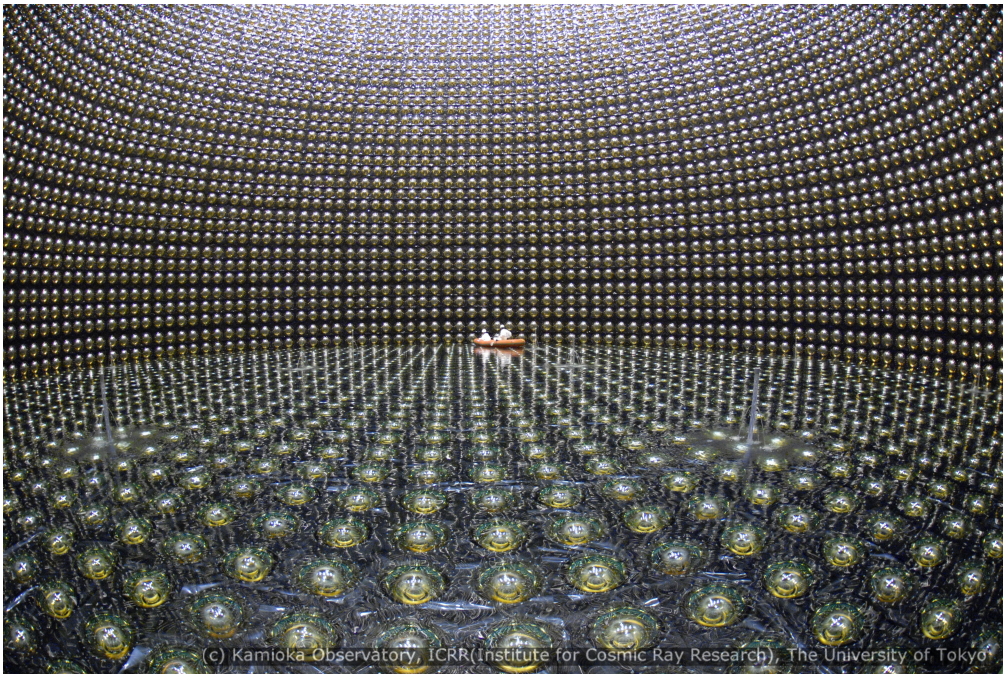

FIGURE 2.7. Photo of the inside of the Super-Kamiokande detector, showing PMTs attached to the walls. Courtesy of Institute for Cosmic Ray Research, University of Tokyo.

the PMT hit timing, allows for the reconstruction of the neutrino interaction vertex, the kinematic properties of the particles involved, and, thus, the reconstruction of the incident neutrino flavor and energy.

More information about the Super-K experiment and its publications, along with more event displays, can be found on the Super-Kamiokande webpage [120].

2.4. Near Detector Complex

The near detector complex located 280 m downstream from the target consists of an on-axis detector INGRID [122], and an off-axis detector ND280 [123]. Both of them are shown in Figure 2.10, which depicts the ND280 near detector cylindrical pit 37 m deep and of 17.5 m in diameter.

Different ND280 sub-detectors include Fine-Grained Detectors (FGDs) [124], Time Projection Chambers (TPCs) [125], Side Muon Range Detector (SMRD) [126], π^0-Detector

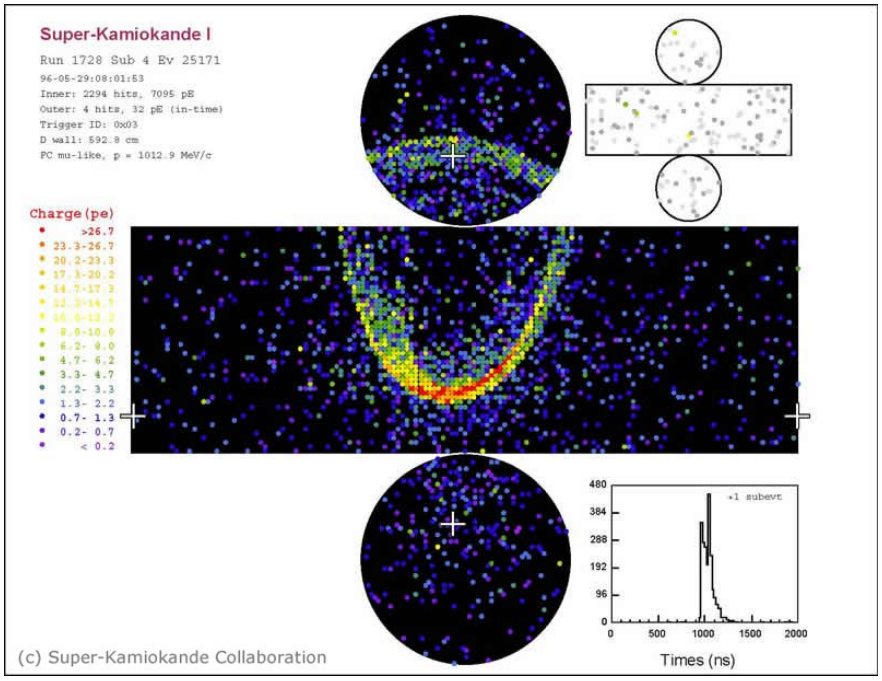

FIGURE 2.8. SK neutrino event display showing a Cherenkov ring resulting from a ν_μ CC interaction with water in the fiducial volume of the detector. This sharp Cherenkov ring has the signature of the charged muon passing through water with speed greater than the speed of light in water. The outer detector has few hits in the right-upper display. Courtesy of the Super-Kamiokande collaboration.

(PØD) [127], and Electromagnetic Calorimeters (ECALs) [128]. The emphasis of this dissertation is on the PØD detector [127], which is desribed in detail in Chapter 3.

In this chapter the INGRID detector is briefly discussed in Section 2.4.1. The ND280 detector overview is presented in Section 2.4.2. The ND280 software, which is the foundation of the work presented in this dissertation, is briefly discussed in Section 2.4.3.

More information about INGRID and ND280 near detectors can be found in several NIM publications [112, 122, 124–128]. Also, in-depth reviews of ND280 and INGRID can be found in several Ph.D. dissertations on the T2K thesis page[20].

2.4.1. INGRID NEAR DETECTOR. INGRID (Interactive Neutrino Grid) [122] is a T2K near detector positioned directly on the neutrino beam axis, which serves the purpose of

[20] http://www.t2k.org/docs/thesis

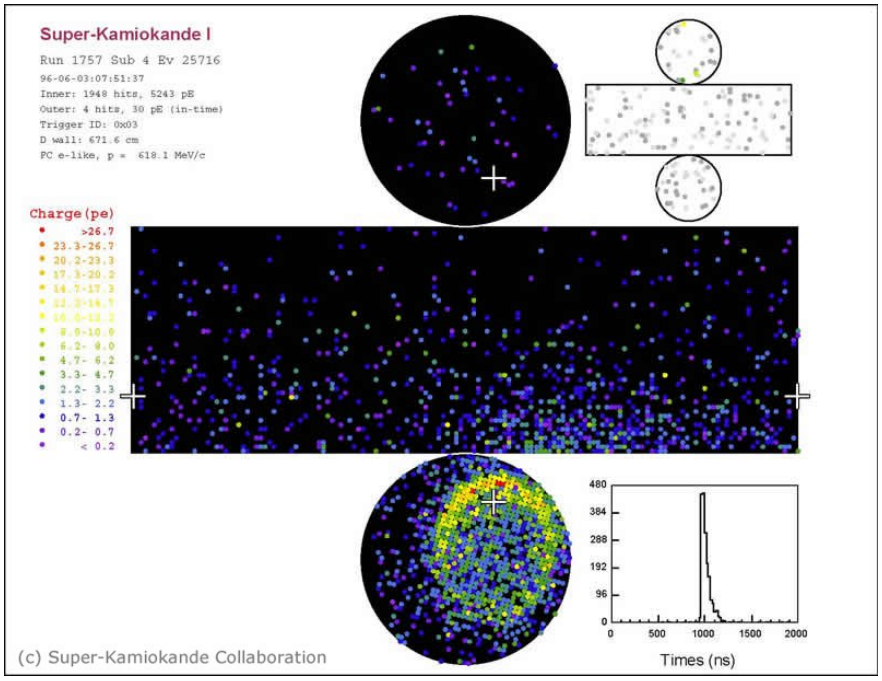

FIGURE 2.9. SK neutrino event display showing a Cherenkov ring resulting from a ν_e CC interaction with water in the fiducial volume of the detector. This fuzzy Cherenkov ring has the signature of the electron passing through water with speed greater than the speed of light in water. The outer detector has few hits in the right-upper display. Courtesy of the Super-Kamiokande collaboration.

monitoring the on-axis part of the neutrino beam. It is designed to monitor the beam direction, intensity and energy with high statistics.

INGRID is assembled out of 16 identical modules arranged in horizontal and vertical arrays around the center of the beam (Figure 2.11). The modules have a layered structure of iron plates and scintillator plastic trackers. It measures the beam direction with an accuracy better than 0.4 mrad from the beam center. The normalized event rate is measured with 4% precision.

More information about the INGRID detector design and performance can be found in the INGRID NIM paper [122].

2.4.2. ND280 NEAR DETECTOR. The ND280 off-axis near detector is a magnetized tracking detector (Figure 2.12). The elements of the detector are contained inside the UA1

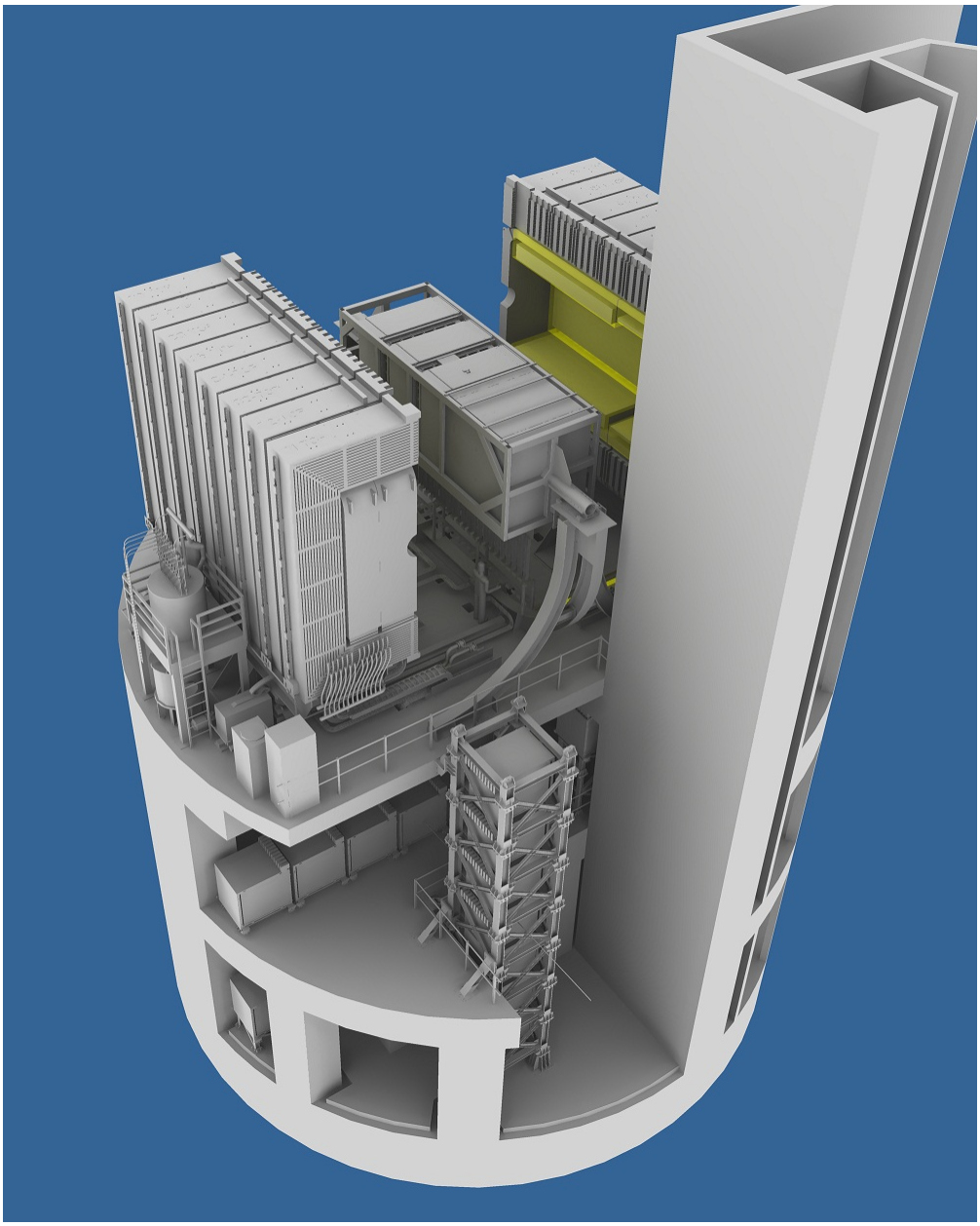

FIGURE 2.10. The drawing of the near detector complex. The off-axis detector ND280 and the magnet are located on the upper level. The horizontal INGRID modules are located on the level below. The vertical INGRID modules span the bottom two levels of the near detector pit.

magnet previously used by the UA1 and NOMAD experiments at CERN. The PØD detector, which sits at the upstream end of the magnet, consists of tracking planes of scintillating plastic bars alternating with either water target and brass foil or lead. The Tracker detector is located downstream of the PØD, and consists of three TPCs and two FGDs. The FGDs are

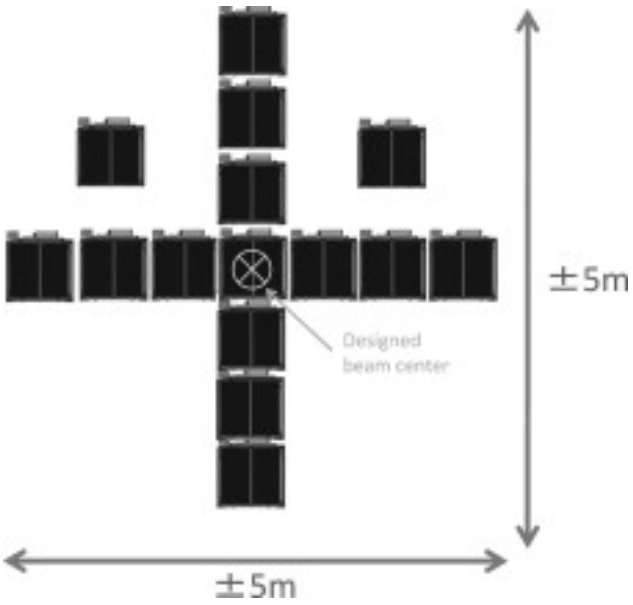

FIGURE 2.11. The INGRID detector. The 16 identical modules sample the neutrino beam in a transverse section of 10 m × 10 m. The vertical row locates upstream of the horizontal row. The center of the cross, where the center module of the vertical row and that of the horizontal row are installed along the beam direction, corresponds to the designed neutrino beam center. Figure taken from the INGRID NIM paper [122].

made out of layers of finely segmented scintillating plastic bars. The PØD, TPCs, and FGDs are surrounded by ECals. The return yoke of the magnet is also equipped with scintillator bars, which collectively are called the SMRD detector. All of the ND280 detectors allow for both independent and collective data aquisition and analysis. In this analysis only PØD data are used, and other detectors are ignored.

Figure 2.12 is a schematic drawing of all the components of the ND280 detector. Figures 2.13 and 2.14 show actual photographs of the magnet open and closed, respectively.

2.4.3. ND280 SOFTWARE. The ND280 software is a library of packages dealing with the tasks of ND280 detector data calibration, simulation, reconstruction and analysis. It is a collaborative effort of hundreds of physicists, and is mostly written in the C++ programming language. The code is based on the ROOT data analysis framework [129], making use of a

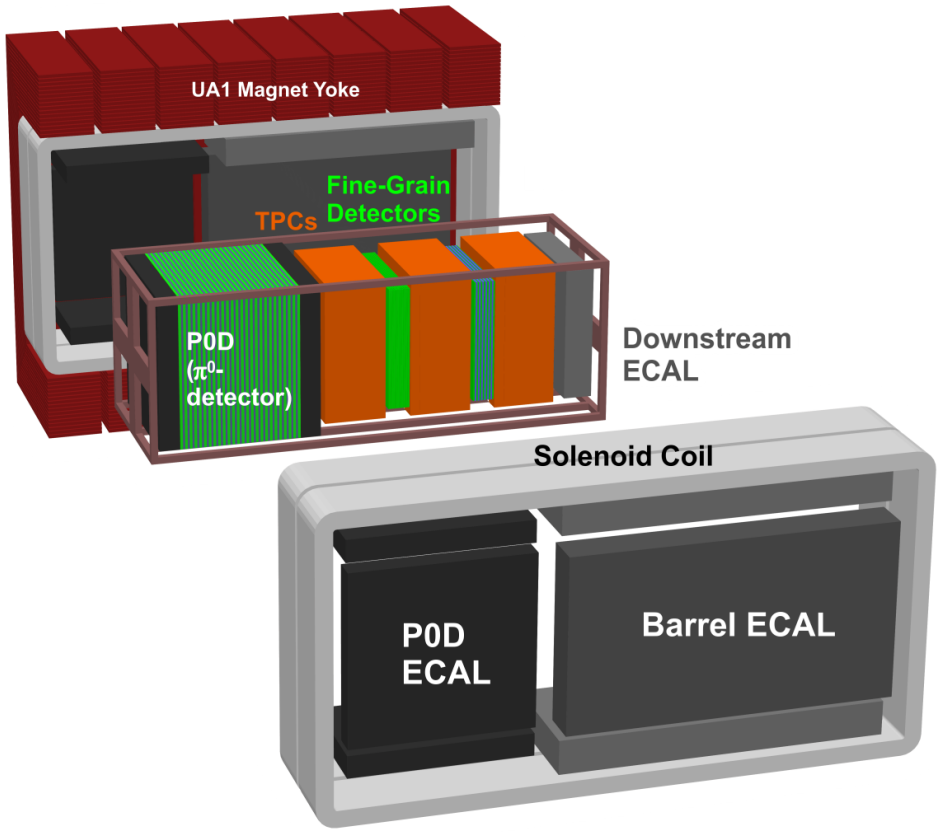

FIGURE 2.12. The drawing of the magnetized ND280 detector showing all of the individual components.

variety of ROOT classes. ND280 software is centered around neutrino event data, build in an object-oriented way using container classes to store event information.

The first stage of real data processing (RDP) is the ND280 calibration stage, during which the calibration constants for the raw ND280 data[21] collected from the detector electronic readout are generated and applied. For example, in the case of the PØD detector approximately 10,400 readout channels require calibration constants to ensure a uniform detector response. The calibration constants are a function of many different variables, such environment temperature, readout electronics power supply voltage, even time of day, etc. The calibration process ensures that the data is well calibrated and consistent. In addition to

[21] The raw ND280 data is collected through the ND280 MIDAS-based data acquisition (DAQ) system, and is in the binary MIDAS[130] file format.

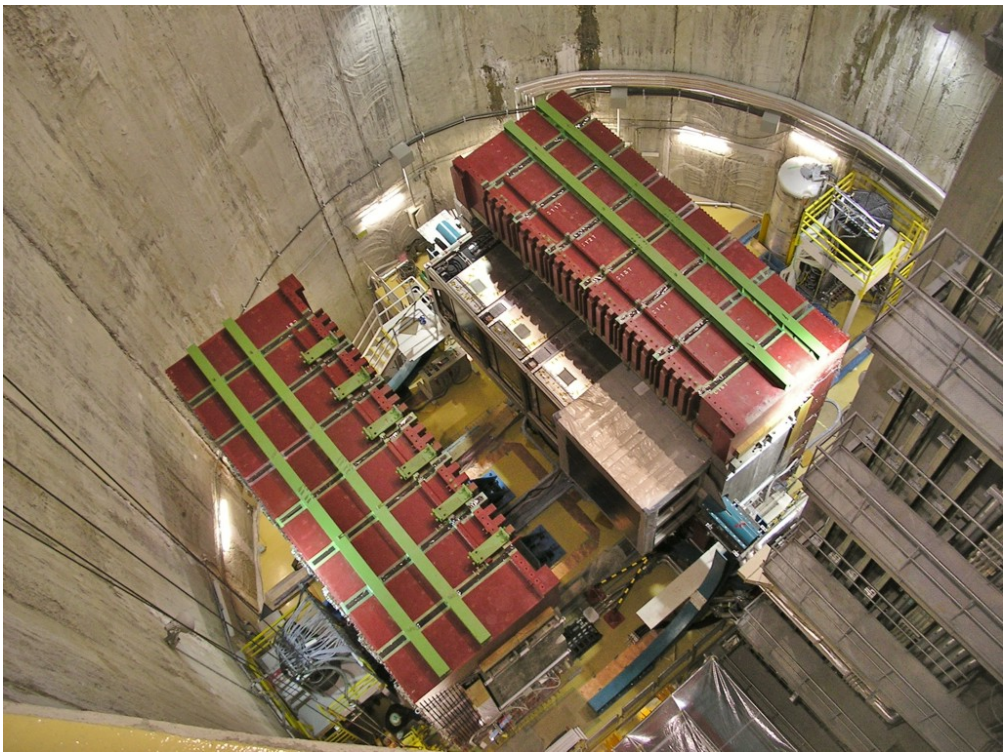

FIGURE 2.13. The ND280 Magnet open.

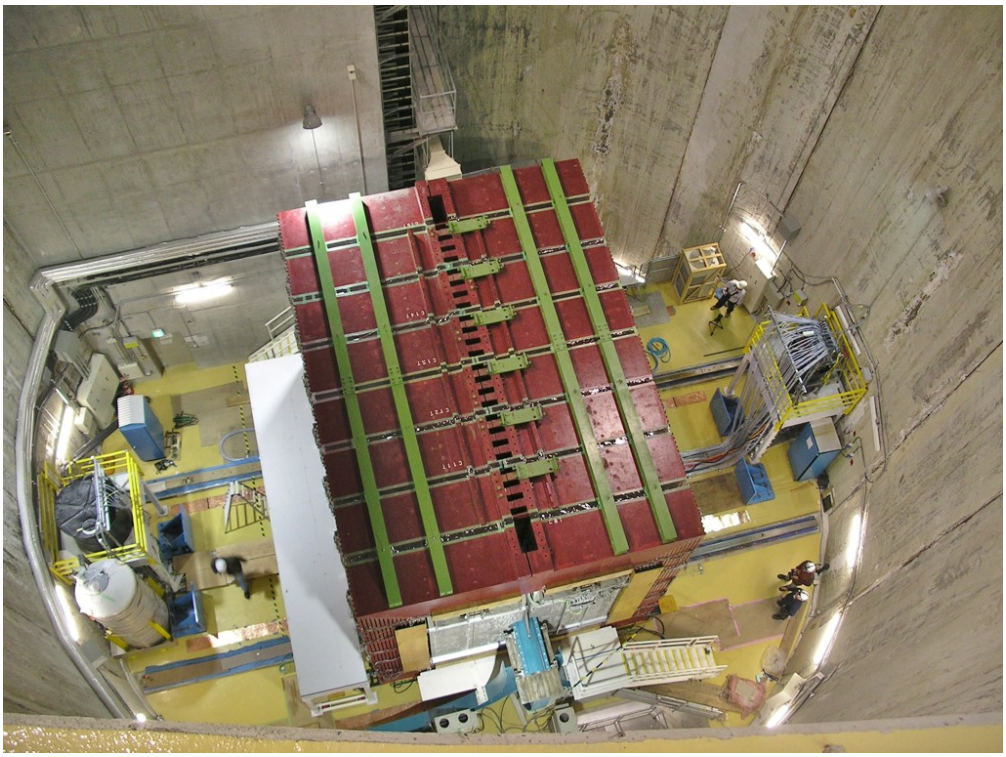

FIGURE 2.14. The ND280 Magnet closed.

data calibration, the data quality (DQ) assessment is also part of the first step of real data processing.

The ND280 simulation software handles the first stage of Monte Carlo Production (MCP). It performs the simulation of ND280 detector geometry, particle interactions in the detector, particle propagation through the detector, energy deposition, etc. Data structures specific to the ND280 simulation software are simulated MC vertices (sometimes called "true" vertices) and particle trajectories, which store information about all the MC-truth particles associated with the neutrino event. Simulated data does not require calibration in contrast to real data.

The second stage of both RDP and MCP is event reconstruction. Event reconstruction software is centered around hit pattern recognition, fits to tracks, clustering, etc. This stage is the same for both simulated MC and real data. There are a great number of distinct complex algorithms employed at this stage of data processing, such noise hit cleaning, track finding, vertex finding, likelihood fitting, etc. The exact details of reconstruction algorithms differ between detectors, and are tuned to a particular detector geometry and technology. Typical data structures at this stage are reconstructed vertices, detector hits, particle tracks and showers, hit clusters, etc. An instance of a reconstructed event class is generally a container that stores all the calibration and reconstruction algorithm results for a particular neutrino interaction event. The PØD detector data reconstruction is performed by the p0dRecon package, which handles finding tracks, showers, clusters and vertices in the PØD. Some relevant details of the p0dRecon package are discussed in Section 3.4.

After the data has been processed and MC has been produced, the next stage is the data analysis. Event analysis software is also detector specific. During this stage the relevant event selection cuts are applied to the data in order to select a particular category of events. This software is usually implemented by individual analyzers for the purposes of a particular

analysis. Indeed, the code that applies cuts to the data, and only selects events that fit the description, would be different for different analyses. The analysis uncertainties, both statistical and systematic, are usually handled during the data analysis stage as well. CC1π^+ analysis code relevant to this work is discussed in Chapter 4.

ND280 software is described in several extensive T2K internal documents, and an overview of the code base can be found in several Ph.D. dissertations [131–133].

CHAPTER 3

PØD Detector

One of the main goals of the T2K experiment is to measure the θ_{13} mixing angle using the electron neutrino appearance channel at SK. One dominant background in the search for ν_e at SK is the single neutral pion, π^0, production from neutral-current interactions, which can mimic an electron-like Cherenkov ring. The main original purpose of the π^0-detector, or PØD, was to measure this π^0 production channel, hence the name, and to be able to distinguish well between various NC and CC interaction channels.

The PØD detector is a tracking detector, also known as a sampling tracking calorimeter. The PØD consists of alternating active tracking and passive target layers. The active parts measure the energy deposited in them, while the passive targets, e.g. water layers, are essentially dead material, where the energy deposit is not directly measurable. The energy deposited in the passive targets, or invisible energy, can be inferred from the energy deposited in the active parts, and has to be accounted for via energy calibration methods. Energy calibration methods include putting a detector in a test beam with known parameters, or using cosmic ray particles such as muons for the minimum ionizing particle (MIP) energy scale calibration. Other methods include the derivation of the absolute energy scale from a well-reconstructed high-purity sample of neutrino interactions, for example using the π^0 invariant mass peak.

For the PØD, a test beam was not used, and the relevant calibration constants are derived either from cosmics, or in case of the π^0 analysis from the π^0 invariant mass. An ND280 event display showing a cosmic MIP track going from right to left through the SMRD, then the PØD and into the Tracker is shown in Figure 3.1.

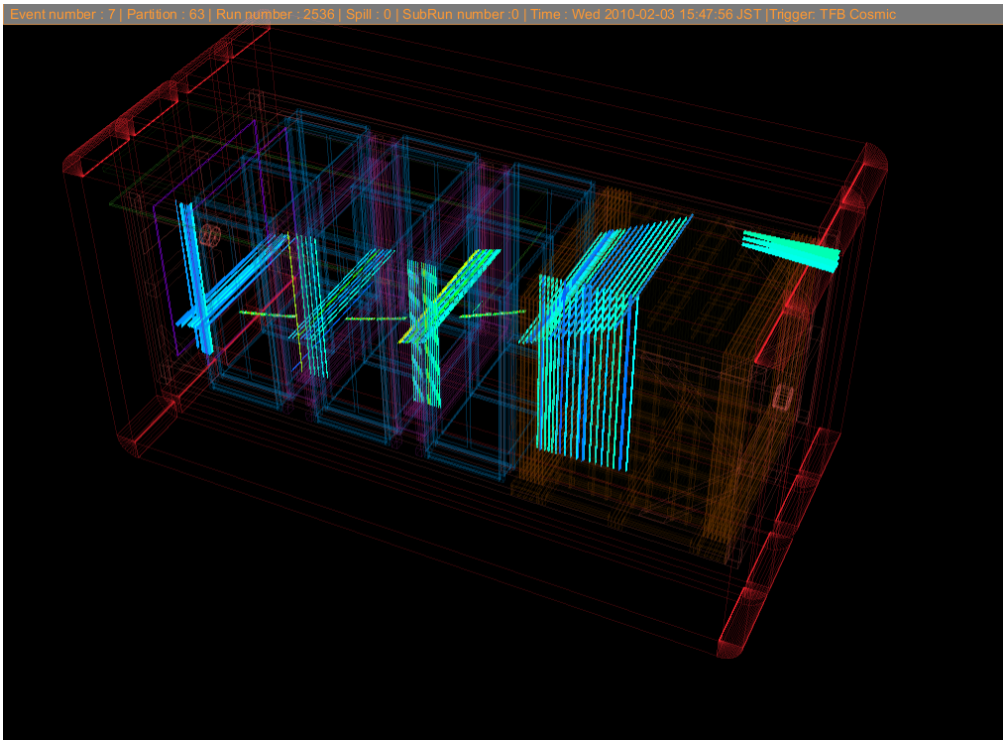

FIGURE 3.1. ND280 cosmic track.

In this chapter, the mechanical design of the PØD is presented in Section 3.1. The electronics used to read out all 10,400 channels of the PØD is discussed in Section 3.2. The PØD Light Injection (LI) calibration and monitoring system developed collaboratively at Colorado State University and the University of Pittsburgh is covered in Section 3.3. For a detailed description of the PØD detector the readers are directed to the PØD NIM publication [127]. A short review of the PØD event reconstruction software, p0dRecon, is presented in Section 3.4.

3.1. MECHANICAL DESIGN

The PØD detector design is shown in a schematic 3-D drawing in Figure 3.2. It is roughly a 2.5 m cube, with the horizontal z axis roughly along the neutrino beam direction (2.5° off-axis), the vertical y axis, and a horizontal x axis perpertidular to z. The readout electronics and the supporting auxillary systems are visible surrounding the PØD detector along the x-z

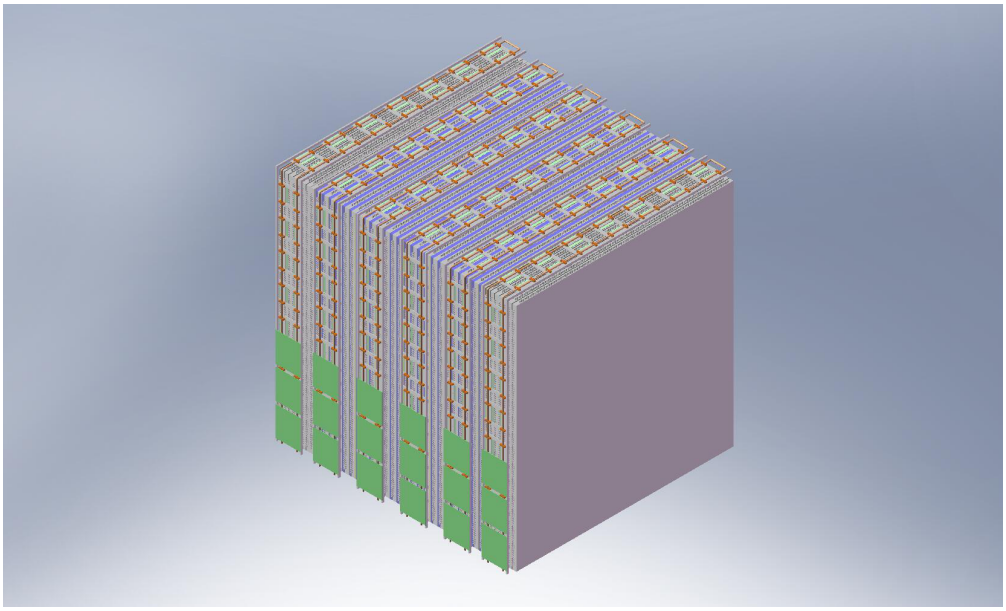

FIGURE 3.2. The 3-D drawing of the approximately 2.5 m cube PØD outside of the ND280 detector basket. Downstream face of detector shown. Figure taken from the PØD NIM paper [127].

and the y-z sides, i.e. the top and the left sides. Figure 3.3 shows an x-z (or y-z) projection of the PØD. The central region of the PØD, composed of the Upstream Water Target (USWT) and Central Water Target (CWT), is made from alternating scintillator planes, water bags, and brass sheets. The front and rear sections, the Upstream Electromagnetic Calorimeter (USECal) and Central Electromagnetic Calorimeter (CECal) respectively, use alternating scintillator planes and lead sheets. There are a total of 40 scintillator modules in the PØD [127]. Each PØD module, or PØDule, has two orthogonal arrays of triangular scintillator bars, forming an x-y 2-D scintillator plane. The 2-D scintillator tracking planes collectively measure the two-dimensional projections of a particle trajectory. The x-z and y-z projections of the trajectories are measured by the alternating x-z and y-z planes. A complete 3-D picture can be reconstructed by combining the 2-D projections.

Per PØDule there are 134 horizontal bars (2,133 mm long) and 126 vertical bars (2,272 mm long). Each bar is 17.25 cm high and 33.5 cm wide at the base. The entire PØD contains

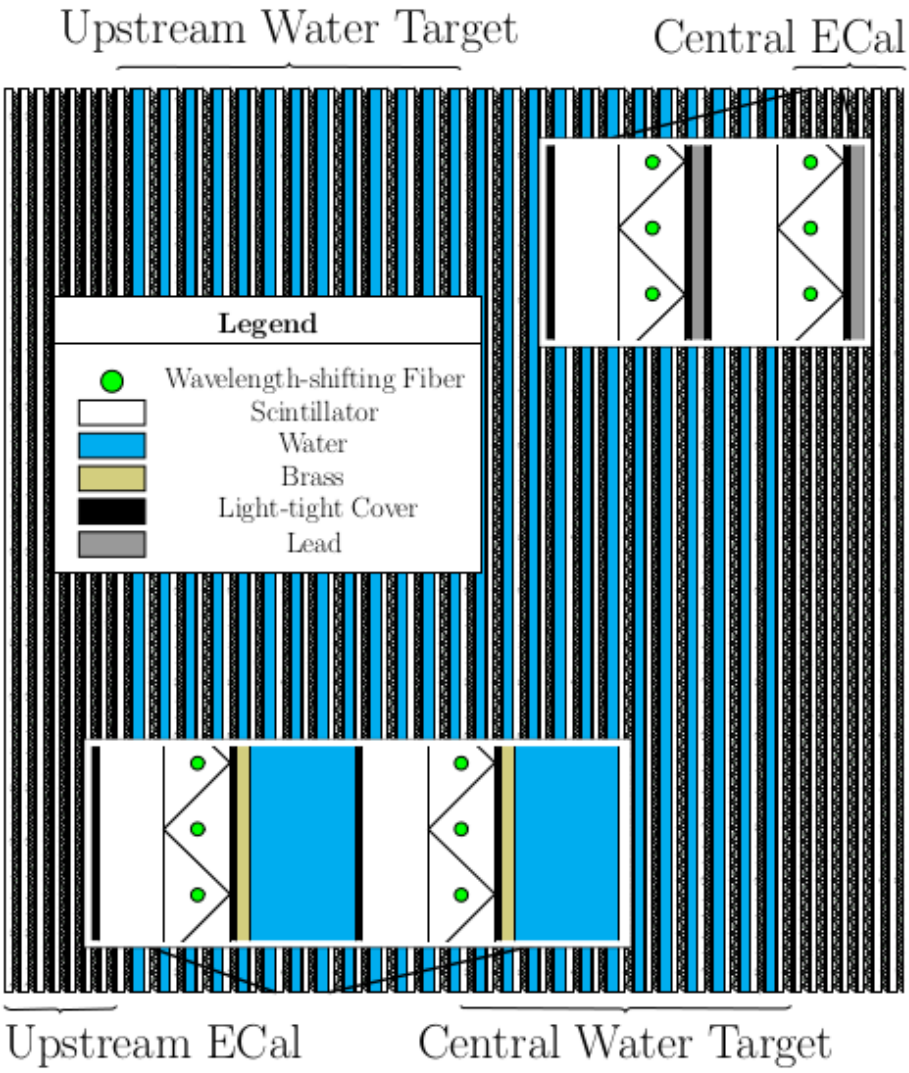

FIGURE 3.3. The schematic view of the PØD detector [127]. The four Super-PØDules as installed in the detector are shown. Beam direction is from left to right.

10,400 scintillator bars, which correspond to x-z, and y-z electronic readout channels. A drawing of a PØDule is shown in Figure 3.4. Each bar has a coaxial hole running the full length of the bar, which houses the Kurarai Y-11 wavelength-shifting (WLS) optical fiber (green dots in Figure 3.3). The fibers have a mirrored aluminum coating applied on one end (to increase the light yield), while the other end is optically coupled to a photosensitive device - a Hamamatsu multi-pixel avalanche photo diode, also known as a Multi-Pixel Photon

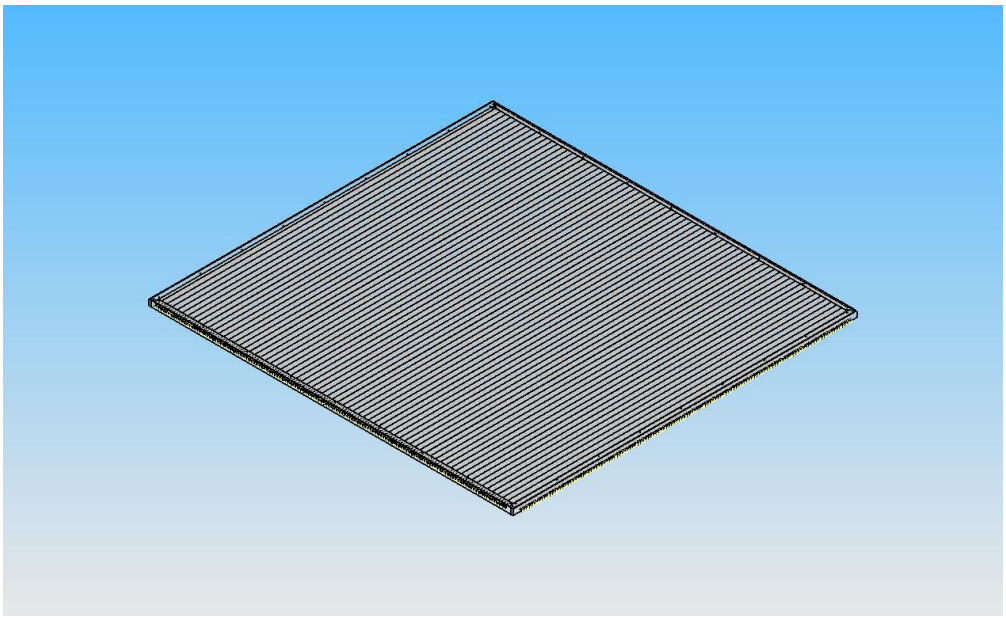

FIGURE 3.4. The schematic drawing of a single PØDule.

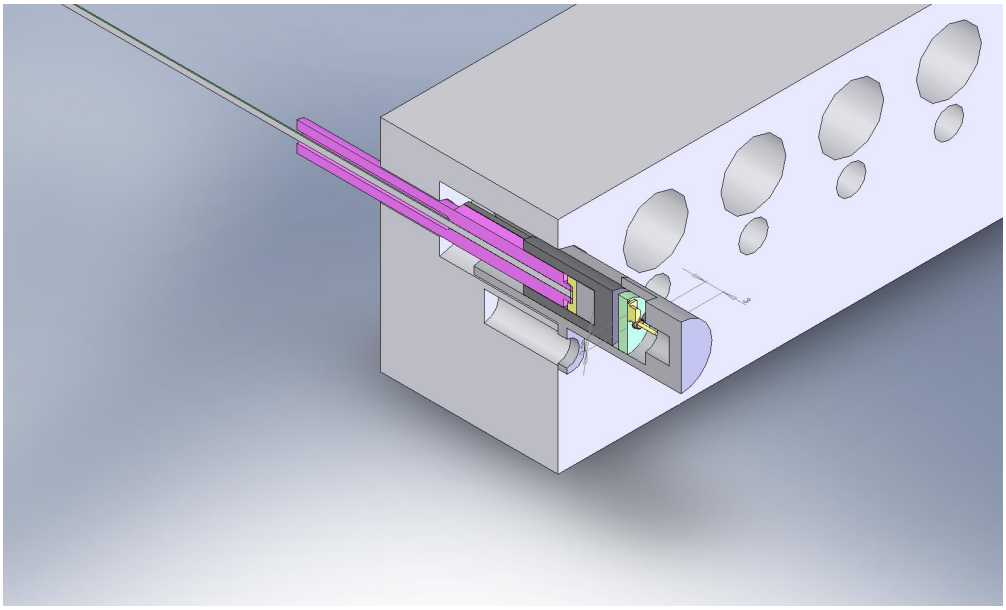

FIGURE 3.5. A close-up view of the edge of a PØDule showing how the WLS fibers exit the scintillator bars and couple to the MPPCs.

Counter (MPPC). The scintillation light generated by the charged particles passing through the scintillator bars is collected by the fibers and is measured by the MPPCs ($+x$ and $+y$ sides). Each MPPC is read out with Trip-t front-end electronics (Section 3.2). The close-up view of the fiber readout is shown in Figure 3.5.

The PØDules were assembled into four units called Super-PØDules: two ECals - USECal and CECal, and two water-targets - USWT and CWT. The two ECals each consist of a sandwich of seven PØDules alternating with seven stainless steel-clad lead sheets (4.5 mm thick). The upstream water-target USWT consists of 13 PØDules alternating with 13 water bag layers (28 mm thick), 13 brass sheets (1.28 mm thick). The central water target CWT consists out of 13 PØDules alternating with 12 water bag layers and 12 brass sheet layers. Each of the water bag layers has two water bags mounted vertically side by side and supported by a high-density polyethylene frame.

The dimensions of the entire PØD are 2,103 mm $\times$ 2,239 mm $\times$ 2,400 mm (width $\times$ height $\times$ length). The mass of the detector with and without water is 15,800 kg and 12,900 kg respectively. The PØD detector is supported inside the magnet by the basket structure, which also supports the FGDs and TPCs.

The PØD design and construction was funded by the US Department of Energy (DOE), and was a collaborative effort of eight US universities. The testing of MPPCs, partial construction and assembly of the PØD, and partial development of the LI system was completed at Colorado State University. The final assembly and testing of the PØD before shipment to Japan was performed at Stony Brook University.

3.2. Readout Electronics

The PØD detector, like the SMRD, ECal, and INGRID detectors, uses the Trip-t-based front-end electronics to read out all the 10,400 MPPC photosensors. The 32-channel Trip-t ASIC chip was originally developed at Fermilab for the Visible Light Photon Counter (VLPC) readout in the DØ experiment. Each Trip-t frontend board (TFB) contains four Trip-t chips, and can instrument up to 64 MPPCs. The TFBs are read out and controlled through

the Readout Merger Module (RMM) board, which provides communication with the data acquisition system (DAQ).

More information about the Hamamatsu MPPCs and front- and back-end electronics can be found in the PØD NIM paper [127]. Documentation of the RMM, CTM, and MCM boards is in development by the T2K electronics group and will be made available to the public later.

3.3. PØD Light Injection System

The PØD Light Injection System (LIS) is a calibration and monitoring system capable of illuminating all 10,400 PØD optical fiber channels simultaneously with the fast UV (∼400 nm) LED pulses. It has been developed for the PØD component of the T2K long-baseline neutrino oscillation experiment under a tight schedule, and with limited funding. It is capable of spanning over two orders of magnitude in light intensity, which allows for monitoring of the MPPC photosensor response over the full range of energy deposition expected for neutrino interactions in the PØD. The author co-developed and tested several prototypes of the PØD, and achieved the main design goals: a range of 10 - 1000 photons per channel, a uniform light intensity across all channels in a constrained geometry. The main design challenge of the LIS was the geometrical constraint that it must be embedded within the 3 cm × 4 cm × 220 cm PØDule layer support frame for each of the 80 scintillator planes. Each PØDule support frame which houses the mirrored end of the WLS fibers has a cavity which exposes 5 mm segments of WLS fibers to light produced by the LIS (Figure 3.6).

The LIS uses 80 pairs of fast-pulsed UV LEDs as precision light sources with each pair illuminating a cavity in a single PØDule support frame. LEDs exhibit minimal pulse-to-pulse fluctuations in intensity, i.e. in the number of photons, so the response of an MPPC

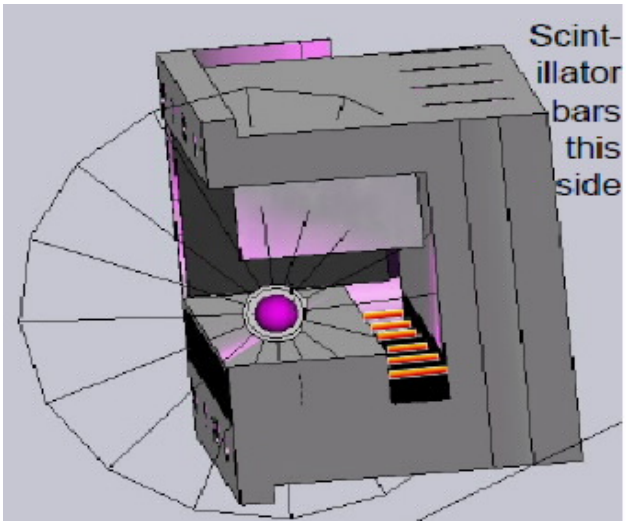

FIGURE 3.6. A cross section view of the LIS cavity cut in a PØDule frame.

photosensor is dominated by photoelectron statistics. Their light intensity can be changed by software providing a necessary dynamic range from single photons to hundreds of photons. LEDs have a fast response time and a long lifetime, which in addition to other necessary physical properties makes them a perfect match for the PØD LIS.

The LEDs are driven by electronics originally designed for the MINOS experiment light injection system [134]. The LIS electronics consists of 4 pulser boxes, a control box, a distribution box and a power supply. Each pulser box holds 2 LED driver boards, a controller board and an LVDS[22] to TTL converter board. Each driver board has 10 channels driving a pair of LEDs connected in parallel.

The pulser boxes are mounted on the sides on the PØD in close proximity of the LEDs. In the original MINOS design communication with each pulser box was done via an RS232 serial connection. For the purposes of the PØD the RS232 serial connection had to be converted to Ethernet because of long travel distances of the signal. External triggering and monitoring of the pulser boxes is provided through the fan in/out distribution box.

[22] LVDS - low voltage differential signal

The LI system has the capacity to simultaneously illuminate all 10,400 channels of the PØD and can be read out in bursts of 20 Hz interspersed with other trigger types (beam, cosmics, etc.). The current settings give the LI system an effective flash rate of 1.5 Hz.

More information about the LI system can be found in the PØD NIM paper [127]. The PØD LIS NIM publication is a work in progress.

3.4. PØD Neutrino Event Reconstruction

The neutrino data presented in this work were collected with the PØD detector. In this section, a short description of the PØD reconstruction algorithm results is presented. In total there are at least two dozen reconstruction algorithms, and describing all of them is outside the scope of this dissertation. A good review of many p0dRecon algorithms can be found in L. Trung's dissertation [133]. A full description of the PØD reconstruction software will be provided in the T2K internal note 172, which is still in preparation [135]. An attempt is made here to describe only the basic necessary details of the PØD reconstruction.

The p0dRecon event reconstruction steps - a chain of algorithms acting as filters - and the results of the algorithms relevant to this analysis and the event selection process are (in the order as they occur in the event reconstruction algorithm chain):

(1) Initial noise hit cleaning algorithm;

(2) Hit collections, track seeding, clustering, 2-D tracking algorithms;

(3) 3-D tracking algorithms (2-D track matching, Kalman filter, etc.);

(4) Track fit quality assessment algorithms;

(5) Delayed hit cluster finding algorithms (Michel tagging);

(6) Electromagnetic (EM) Shower finding algorithms;

(7) Vertexing.

In the first stage of the p0dRecon event reconstruction, the 2-D track segments, `TP0DTracks`, are found from the cleaned detector hits (`THitCollection` contains `THit` objects). Initial tracking is performed using the Hough Transform (a general track finding algorithm) in the x-z and y-z projections. Short track segments are then joined together via the road following algorithm forming longer two-dimensional track candidates. 2-D tracks from two different projections are then matched together into 3-D tracks. If the matching of 2-D tracks into 3-D object fails then the object is treated as 2D. Any clusters of hits not associated with tracks are indentified with the cluster finding algorithms.

In the next step of the reconstruction, the good track candidates are fitted using the Kalman Filter algorithm. In the cases when the Kalman Filter algorithm fails (when the track is very short or steep) a parametric fitting algorithm (global straight line fit) is used. It must be noted that the exact implementations of the fitting algorithms vary between the data processing versions. For example, the parametric track fits present in Production 5 version of the data and MC files were substituted by a different clustering algorithm in Production 6. This analysis uses Production 5 code and files.

The minimum number of planes that a candidate track needs to intersect in order to be fitted with a Kalman Filter is six, which is equivalent to 3 PØDules. The container class that holds the algorithm results coming out of the first two steps of the reconstruction is called `TP0DTrackRecon`. The common primary vertex for the tracks is found by the `TP0DPairwiseVertex` algorithm. `TP0DPairwiseVertex` uses a simple closest-approach strategy to find vertices. Both the `TP0DTrackRecon` and `TP0DPairwiseVertex` algorithm results are used in this analysis.

After the last step of the tracking stage the reconstructed objects are passed to the shower reconstruction stage where they are identified by the particle identification algorithm, as

either showers, `TP0DShower`, or tracks, `TP0DTrack`. For showers, a dedicated reconstruction algorithm is run after the tracking stage. The shower reconstruction results are not used in this analysis due to various issues with the track versus shower discrimination algorithms, which introduce a significant loss in the selection efficiency for this analysis. Therefore the detailed description of these steps is omitted from this dissertation.

When all standard reconstruction steps are completed the Michel electron tagging algorithm is run. There are two Michel tagging algorithms in the PØD reconstruction chain. Both of them use time and position clustering of hits to associate reconstructed objects, e.g. vertices and tracks, with Michel electron candidates. One of these algorithms called `TP0DTagMuonDecay` (developed in Stony Brook University) is used in this analysis, to discriminate between pions and protons.

CHAPTER 4

CC1π^+ Cross Section Analysis

In this chapter of the dissertation, the data and Monte Carlo samples used in the analysis are discussed in Section 4.1. The details of the event pre-selection and selection of CC1π^+ interactions in the PØD to achieve a signal-enriched event selection are covered in Section 4.2. The details of the calculation of the flux-integrated CC1π^+ cross section on water are described in Section 4.3. The propagation of measurement uncertainties is discussed in Section 4.4. The calculation of statistical uncertainties is covered in Section 4.5. Systematic uncertainties are discussed in Section 4.6. The final results are presented in Section 4.7.

4.1. Datasets and MC simulation

The datasets used in this analysis contain full T2K beam Runs 1, 2, 3c (called from now on run 3) and 4. During T2K Run 1, the PØD detector water target was filled with water (water-in mode). Run 2 covers two periods: water-in and water-out, while in run 3 PØD was in the water-out mode. Run 4 includes two modes of PØD operation: water-in and water-out. Throughout the document the terms water-out and air-in will be used interchangeably, since they refer to the same configuration.

To ensure the proper data quality, the standard set of cuts, recommended by the ND280 Data Quality group, have been applied. More information about the data quality cuts can be found in Section 4.2.2. Table 4.1 contains the summary of the number of protons on target (POT) of the data samples used in the analysis after applying data quality pre-selection cuts, i.e. requiring good data quality. Accumulated POT numbers for T2K Runs 1 through 5 as a function of time are shown in Figure 4.1. Run 5 was not included in this analysis since it was an antineutrino run. The Monte Carlo sample used in the analysis is the full magnet

TABLE 4.1. Data sets used in the CC1π^+ analysis and their POT.

	water-in ($\times 10^{20}$ POT)	water-out ($\times 10^{20}$ POT)	Years
Run 1	0.295628	-	2010
Run 2	0.697883	0.359124	2010 - 2011
Run 3	-	1.35522	2012
Run 4	1.64683	1.77557	2012 - 2013
All	2.64034	3.48992	

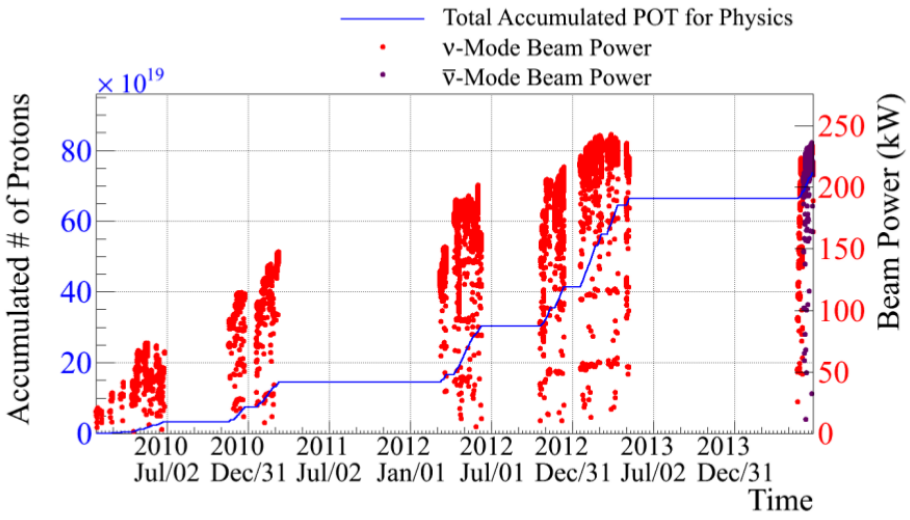

FIGURE 4.1. Accumulated POT for T2K Runs 1 - 5 as a function of time. The long inactivity gap between Run 2 and Run 3 during 2011 - 2012 corresponds to the Great East Japan Earthquake, when the beamline was damaged, and required extensive repairs. Run 5 was an antineutrino run and was not used in this analysis.

simulation that was produced with the neutrino interaction vector files generated by the NEUT neutrino event generator. A GENIE Monte Carlo sample is used for some comparisons as well. The Monte Carlo is divided into four runs and different PØD detector configurations, similar to the data. Due to a mistake in Production 5 there is no ND280 run4-air Monte Carlo sample, so only Run 2 and 3 air MC samples are used for the comparisons with water-out data. Table 4.2 shows all magnet MC samples and their POTs. The neutrino beam flux

TABLE 4.2. Monte Carlo sets used in the CC1π^+ analysis and their POTs.

	water-in ($\times 10^{20}$ POT)	water-out ($\times 10^{20}$ POT)
Run 1	5.51	-
Run 2	7.335	9.745
Run 3	-	16.105
Run 4	48.295	-
All	61.14	25.85

(provided by the T2K Beam Group) used in this Monte Carlo simulation was v11a. For the final result, the flux 11b v3.2 tunning weights were applied.

It's necessary to mention that neutrino interactions in the hall as well as in the sand surrounding the detector pit are not simulated in the magnet MC. A separate set of the simulated sand muon interactions has been used in some of the systematic studies and the details of these samples can found be in the Table 4.3. Both data and Monte Carlo samples

TABLE 4.3. Sets of Monte Carlo sand muons used in the systematic error studies for CC1π^+ analysis.

water-in ($\times 10^{20}$ POT)	water-out ($\times 10^{20}$ POT)
11.9925	11.99

are the result of the Production 5 data processing, which used the v10r11p17 version of the ND280 software. Data was processed with respin G (RDP5G), magnet MC with respin E (MCP5E), sand muons MC with respin D (water-out) and F (water-in). All data and MC sets used in the analysis are officially suggested as the samples for the physics analyses in ND280.

4.2. CC1π^+-enriched Event Selections

The CC1π^+ event selection procedure presented in this chapter is largely based on the analysis work described in the T2K internal document [136] written by the author together with T. Wachala and under the guidance of R.J. Wilson.

4.2.1. Pre-selection Cuts. In this section, the pre-selection conditions that need to be satisfied by the neutrino-induced ND280 events to be accepted into the selection are discussed. This includes the Data Quality (DQ) criteria, and in the beam timing cuts in order to select the events in time with the beam.

4.2.1.1. *Data Quality Assessment.* In the first step of the event pre-selection the standard ND280 data quality cuts are applied. Both the PØD detector and the magnet are required to have good data quality. When all of the PØD and magnet systems are functioning properly, the data collected during that time period are flagged as good. In case any critical system malfunctions, e.g. glitches in the readout electronics, power supply failure, etc., the data are incomplete or bad and have to be rejected.

The following cuts are applied to the real data:

(1) Require good PØD and magnet data quality flags;

(2) Require good beam data summary status.

The second cut is necessary to get the valid POT information for each event. This information is provided by the T2K Beam Group and is incorporated into the headers of data files. MC simulation, by definition, has no data quality flags, and is not subject to the data quality cuts.

4.2.1.2. *Beam Spill Structure.* The T2K pulsed neutrino beam has a timing structure. The beam comes in spills that each contain 8 beam bunches (6 in the Run 1). Each beam

bunch is 58 ns wide, and is separated by 580 ns from the next one. More timing details of the spill structure as seen in the PØD can be found in the Table 4.4.

TABLE 4.4. Bunch time buckets in nanoseconds (ns) relative to the ND280 beam trigger time, used in the CC1π^+ analysis.

Bunch number	1	2	3	4	5	6	7	8
Min (ns)	2,600	3,240	3,800	4,400	5,005	5,550	6,150	6,700
Max (ns)	3,140	3,700	4,300	4,880	5,450	6,050	6,600	7,200

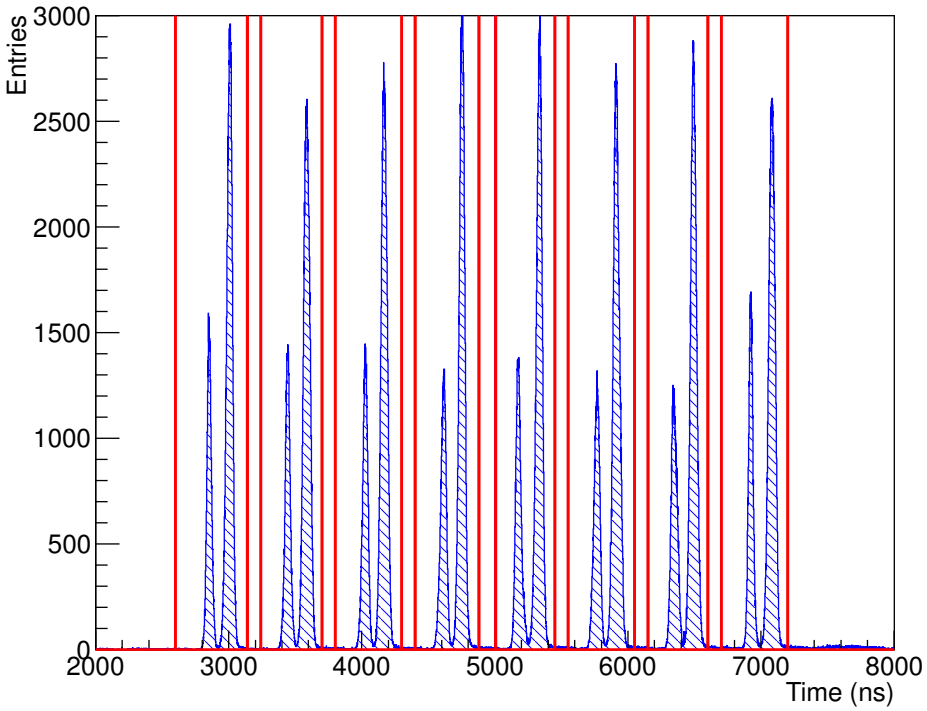

FIGURE 4.2. Timing of the reconstructed vertices in the PØD and the boundaries of the timing buckets used in CC1π^+ analysis in the T2K Run 2 data. The vertical lines show the edges of the timing buckets.

In the PØD detector, readout electronics integration cycles are synchronized with the accelerator beam spills. Each integration cycle, or bucket, is 480 ns wide, with a reset time of 100 ns. This allows for the containment of the 58 ns wide beam bunches in the electronics integration windows.

The example timing histograms for the data and Monte Carlo events in the PØD contained within the ∼500 ns wide bunch timing buckets (red lines) are shown in Figures 4.2. and 4.3.

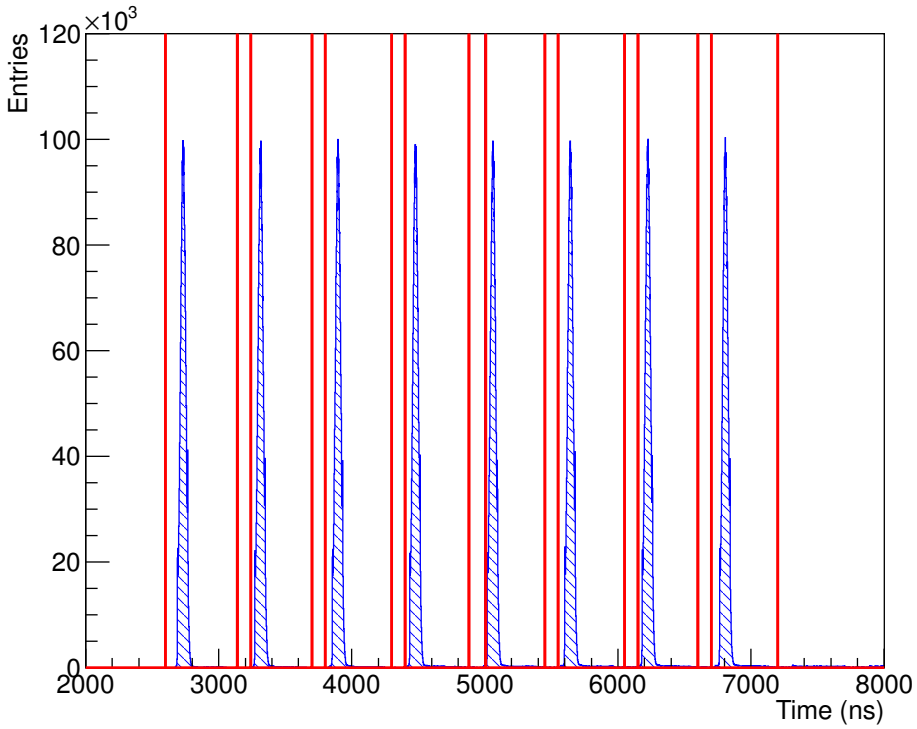

FIGURE 4.3. Timing of the reconstructed vertices in the PØD and the boundaries of the timing buckets used in CC1π^+ analysis in the T2K Run 2 MC. The vertical lines show the edges of the timing buckets.

The second step of the event pre-selection is dividing the events according to the neutrino beam structure. Each ND280 event is equivalent to a T2K beam spill, which in turn consists of a set of bunches. During this initial step, the ND280 events are split into individual bunch events, according to the timestamps of the reconstructed objects (tracks, vertices). Reconstructed objects are stored in the proper time bucket containers. The time window boundaries have been selected to be wide enough to cover Monte Carlo as well as the data from different ND280 running periods (including a timing shift in Run 2). Timing is an important aspect of the PØD detector calibration and any electronics clock shifts, which

could be as high as several dosen ns, need to be accounted for in order to be able to analyze beam events.

4.2.2. Selection Cuts. In this section the core of the PØD-based CC1π^+ selection is discussed. An event selection, in general, is a set of subsequent data cuts applied to the event variables in order to achieve a desired event sample, e.g. to select signal and reject background. The plots of the physical quantities related to each cut, before applying the cut, are shown throughout the section. These plots are an important analysis tool which help show the performance of the selection cuts and higlight any difference between data and Monte Carlo. The full CC1π^+ selection procedure can be divided into two major steps:

(1) Select events with one vertex and two tracks;

(2) Apply particle ID to both tracks.

Furthermore, one can create different sub-selections for different topologies of neutrino interactions. In this analysis, the two major topologies of CC1π^+ interactions in the PØD were considered:

(1) **Selection One**: Muon exiting through the downstream face of the PØD and entering TPC1, and pion fully-contained within the PØD;

(2) **Selection Two**: Both muon and pion contained in the PØD.

Other possible topologies include one track events, three or more track events, shower-like events, two or more tracks exiting the PØD, etc., but before discussing the different topologies and selection cuts any further it is necessary to define the PØD detector fiducial volume used in this analysis.

4.2.2.1. *Fiducial Volume Definition.* The purpose of this analysis is to select the ν_μ-induced CC1π^+ interactions on the water target and to reduce the amount of external

background in our sample. Therefore, the fiducial volume is defined as a virtual box located in the geometrical center of the PØD water target region with the top, bottom, left and right edges of the box a distance of approximately 25 cm from the PØD detector edges, leaving the last 25 cm of the PØD as a veto from the outside activity.

Upstream and downstream borders of the fiducial volume go through the middle of the first upstream and last downstream PØDules of the water targets. The definition described here is adapted from the official PØD fiducial volume defined in the NC π^0 analysis described in the T2K internal document T2K-TN-56 [144]. The mentioned document contains detailed calculations of the total detector mass and the fiducial mass. The detector masses used in this analysis are discussed later in this dissertation. The details of the fiducial volume definition can be found in the Table 4.5.

TABLE 4.5. Fiducial volume definition used in the CC1π^+ analysis. The official ND280 detector coordinate system is used.

ND280 Coord.	PØD Center (mm)	Width/2 (mm)	Min (mm)	Max (mm)
x	-36	800	-836	764
y	-1	870	-871	869
z	-2116	852.5	-2969	-1264

4.2.2.2. *Selection One: One Vertex, Two Tracks, One Track Contained.* This section describes the first event selection, or Selection One, which aims to select events occuring in the PØD fiducial volume that are not fully contained in the PØD. It selects events with exactly one vertex in the fiducial volume and with a μ^- candidate track exiting the PØD and entering the TPC1, and a π^+ candidate track fully-contained within the PØD. Figure 4.4 shows an example event topology with one vertex and two tracks selected by the Selection One cuts. The longer tracks is exiting the PØD in the direction of TPC1, but TPC1 hits are not shown in the figure.

The Selection One cuts are:

(1) Require exactly one PØD reconstructed vertex in the bunch;

(2) Reconstructed vertex has to be three dimensional (quality cut);

(3) Reconstructed vertex has to be located in the PØD water target fiducial volume;

(4) There are exactly two reconstructed particles associated with the vertex;

(5) Both reconstructed particles need to be 3-D (quality cut);

(6) One of the particles exits the PØD through its downstream face (μ^- candidate);

(7) Both particles are tracks, coming from the `TP0DTrackRecon` algorithm result.

In the first step of Selection One, exactly one PØD vertex in the bunch is required. The vertex has to be 3-D in order to decide whether it is located inside the fiducial volume box. Events with more than one interaction vertex in the PØD within the same time bucket constitute a small portion of the total number of events, but need to be accounted for since their reconstruction information would be unreliable. The so-called event pile-up correction is applied to the data and is discussed later in the text.

The next cut is the standard fiducial volume cut which is applied to the reconstructed PØD vertex, and it ensures that the reconstructed vertex is inside the fiducial volume. Distributions of the x, y and z coordinates of the position of the reconstructed vertex before the fiducial volume cut are shown in Figures 4.5, 4.6, 4.7, 4.8, 4.9, and 4.10. In order to select events with μ^- and π^+ leaving the interaction vertex, exactly two good quality (3-D) particles exiting the reconstructed vertex are required. Figures 4.11 and 4.12 shows data versus MC comparison plots for the number of 3-D particles in the vertex, i.e. track multiplicity, before the two-particles cut. Figures 4.11 and 4.12 provide a necessary data versus MC track multiplicity check, showing that the MC does reproduce the real data track multiplicity quite well. However, one can notice that there is some discrepancy between data

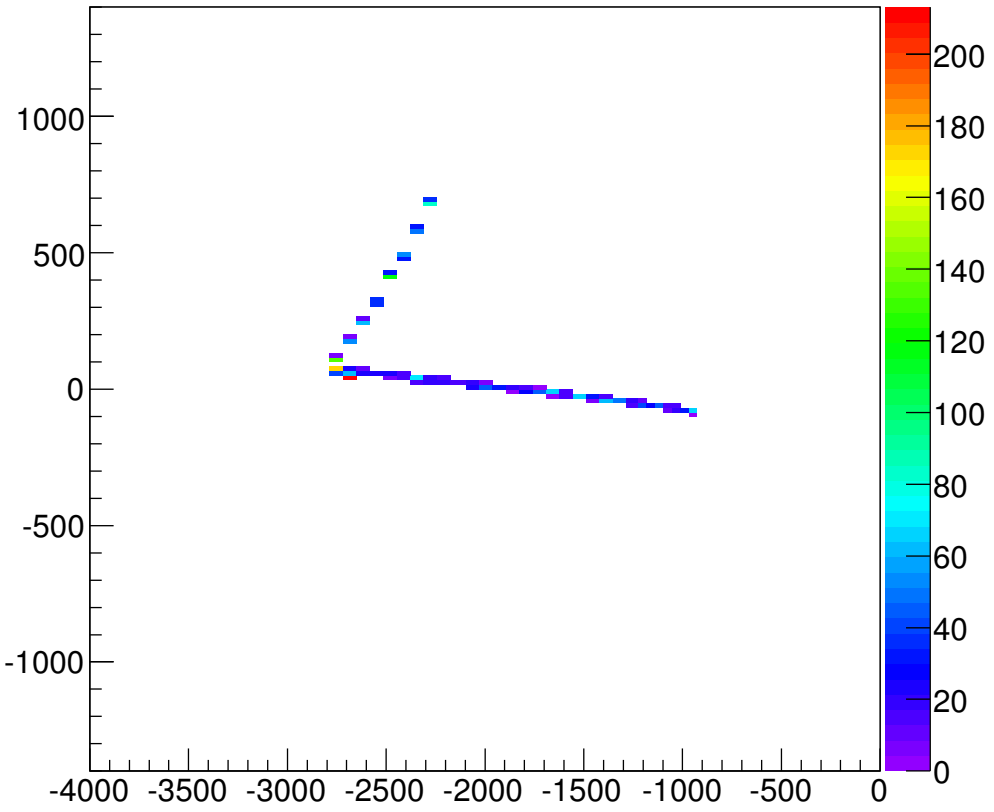

FIGURE 4.4. Selection One: a y-z view of a Run 2 water-in data event display. y (mm) is the vertical axis, z (mm) is the horizontal axis. Neutrino beam direction is from left to right. The data event has one vertex and two tracks. The longer track is exiting the PØD is the direction of TPC1. TPC1 hits are not shown. The shorter track is contained in the PØD.

and MC in the one-particle bin: MC predicts a larger number of one track events than is observed in the data. One of the possibilities that can explain this is that the FSI model is not entirely correct and that more data events with multiple nucleons ejected from the nucleus are measured than is predicted in the current FSI model. This could be resolved in the future by implementing a more accurate FSI model in MC. However, another possibility is that MC does not model well some of the actual out-of-PØD backgrounds, e.g. magnet interactions, sand muons, or interactions on lead, etc. This situation can be improved in the

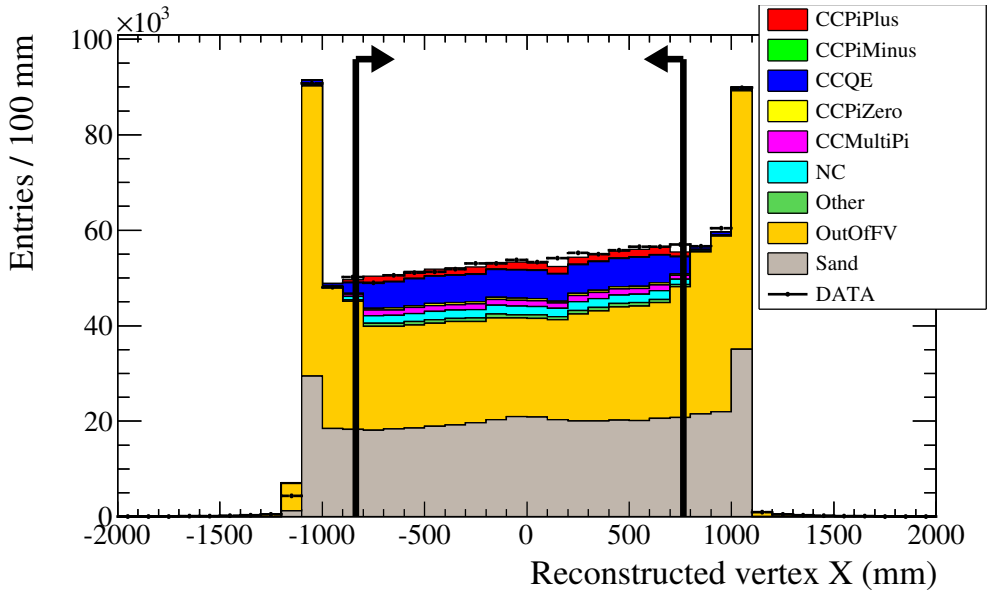

FIGURE 4.5. Selection One: Reconstructed x coordinate of the vertex position before the fiducial volume cut for the water-in data and MC. Events with $x \in (-836, 764)$ are accepted as a result of the fiducial cut.

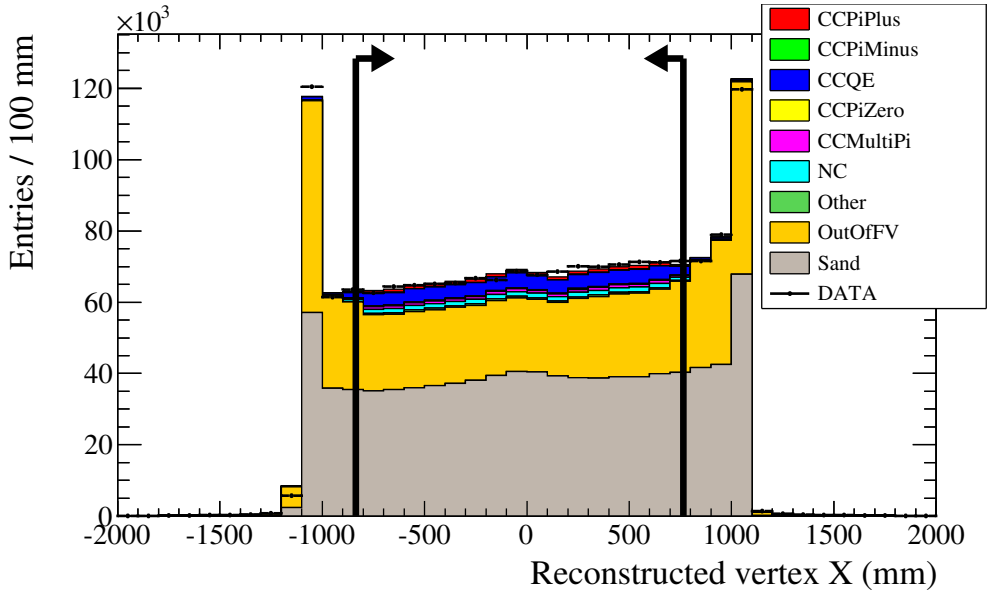

FIGURE 4.6. Selection One: Reconstructed x coordinate of the vertex position before the fiducial volume cut for the water-out data and MC. Events with $x \in (-836, 764)$ are accepted as a result of the fiducial cut.

future with more extensive out-of-PØD background studies. In order to tag the muons in Selection One, one of the particles, the muon candidate track, is required to exit the PØD

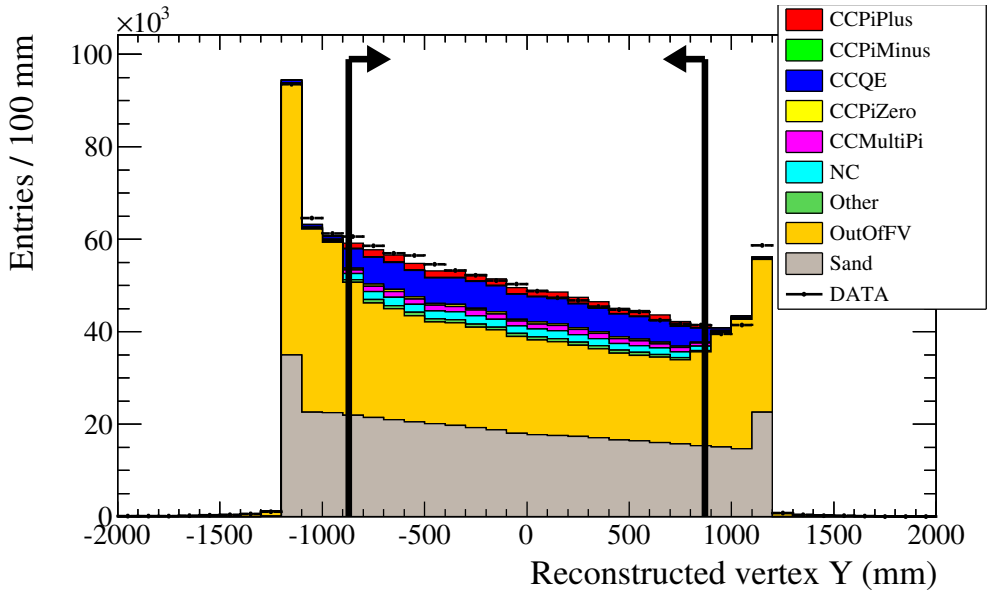

FIGURE 4.7. Selection One: Reconstructed y coordinate of the vertex position before the fiducial volume cut for the water-in data and MC. Events with $y \in (-871, 869)$ are accepted as a result of the fiducial cut.

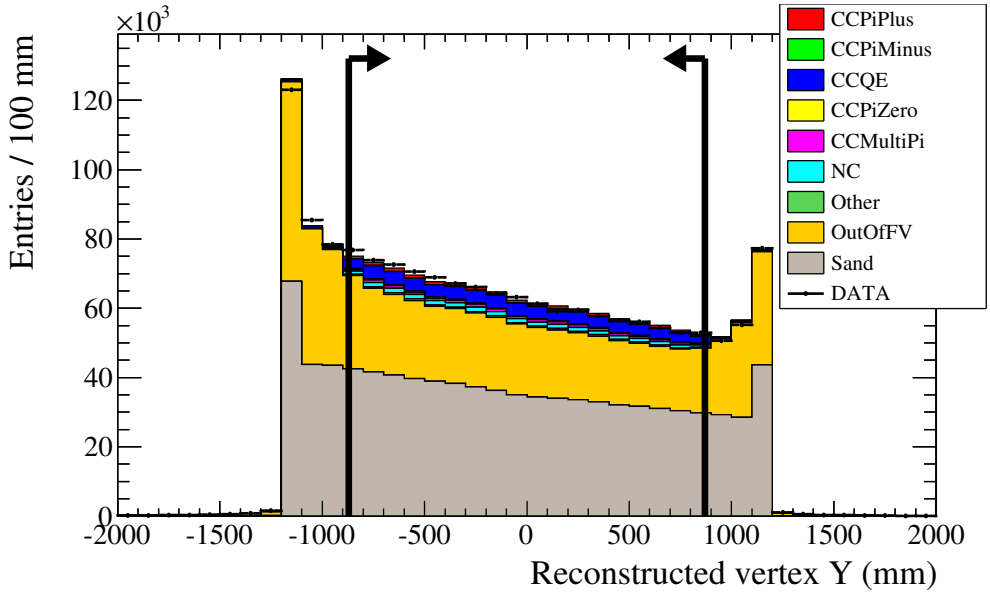

FIGURE 4.8. Selection One: Reconstructed y coordinate of the vertex position before the fiducial volume cut for the water-out data and MC. Events with $y \in (-871, 869)$ are accepted as a result of the fiducial cut.

through its downstream face into TPC1. The z position of the end of this PØD track has to be greater than -970.32 mm, and the x and y coordinates of the end of the PØD track

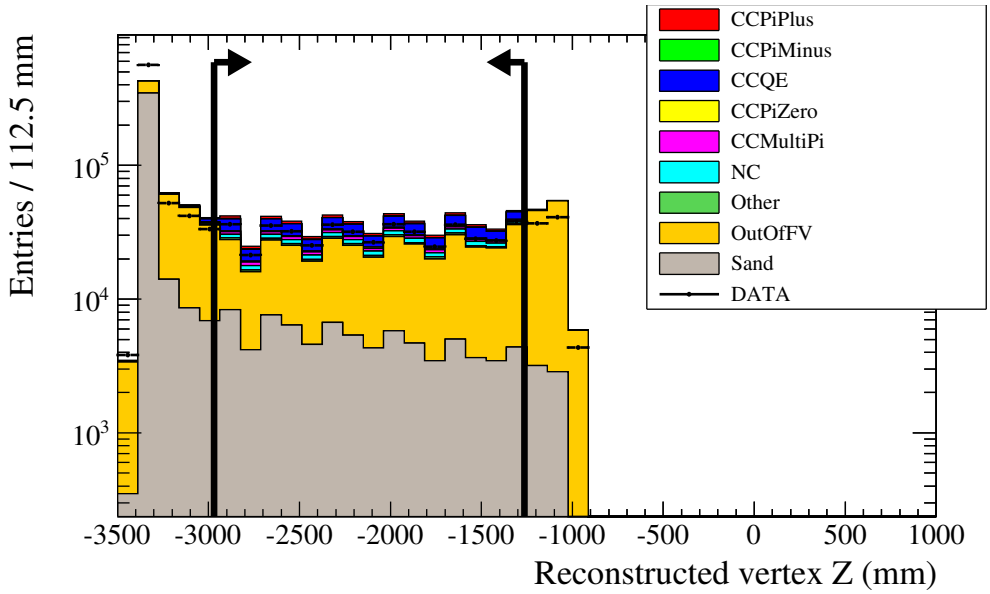

FIGURE 4.9. Selection One: Reconstructed z coordinate of the vertex position before the fiducial volume cut for the water-in data and MC. Events with $z \in (-2969, -1264)$ are accepted as a result of the fiducial cut.

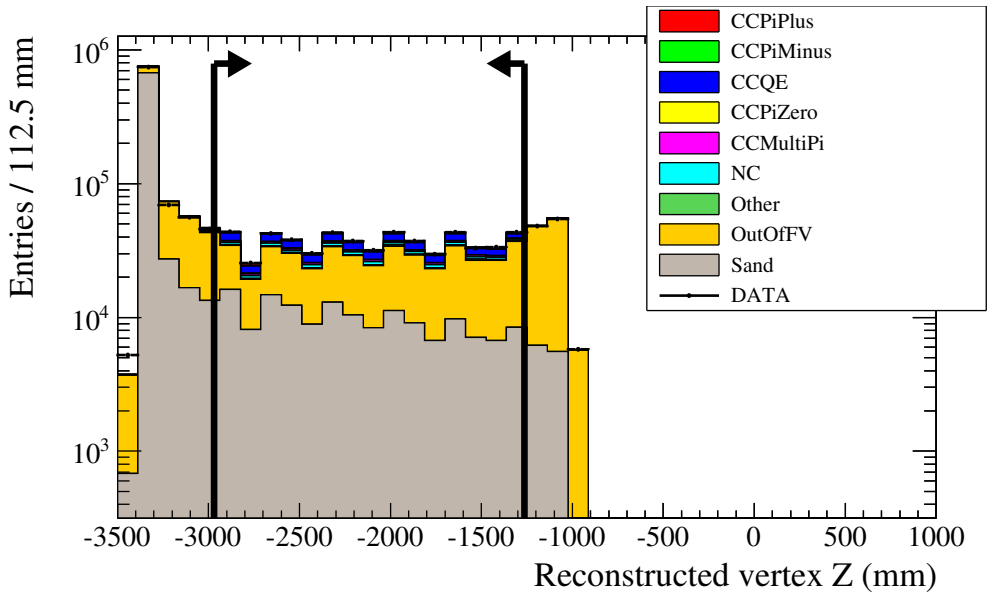

FIGURE 4.10. Selection One: Reconstructed z coordinate of the vertex position before the fiducial volume cut for the water-out data and MC. Events with $z \in (-2969, -1264)$ are accepted as a result of the fiducial cut.

extrapolated to TPC1 have to be within the TPC borders (-900 mm and 900 mm). This requirement gives a good muon purity of 86%, that is the percentage of the muon candidate

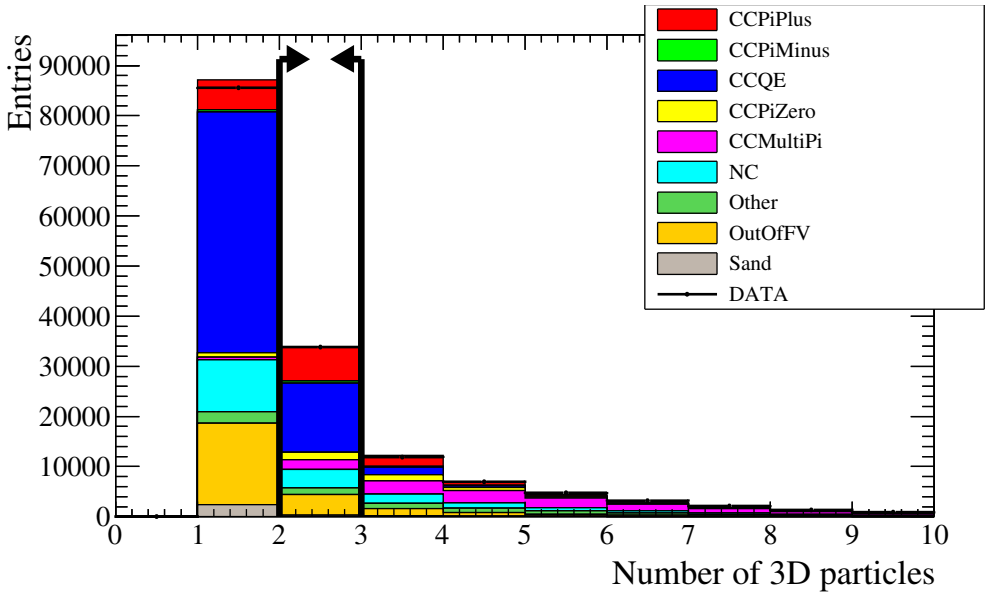

FIGURE 4.11. Number of 3-D particles in the reconstructed vertex for the water-in data (black dots) and MC (colored histogram stack). Events with exactly two particles in the reconstructed vertex are accepted. Shown in red is the CC1π^+ signal, and other colors represents different background modes.

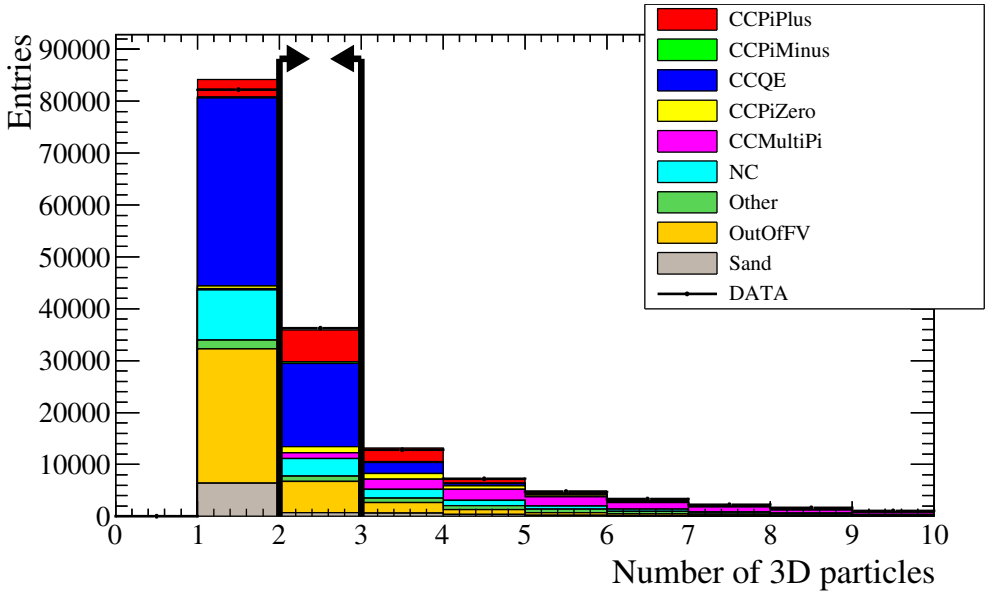

FIGURE 4.12. Number of 3-D particles in the reconstructed vertex for the water-out data and MC. Events with exactly two particles in the reconstructed vertex are accepted.

tracks that are associated with an actual MC truth muon trajectory. The requirement above means that the muon candidate has to travel a distance (minimum 30 cm which is the length

of Central ECAL along the z axis) from the PØD water target through the Central ECAL, containing lead, to the downstream face.

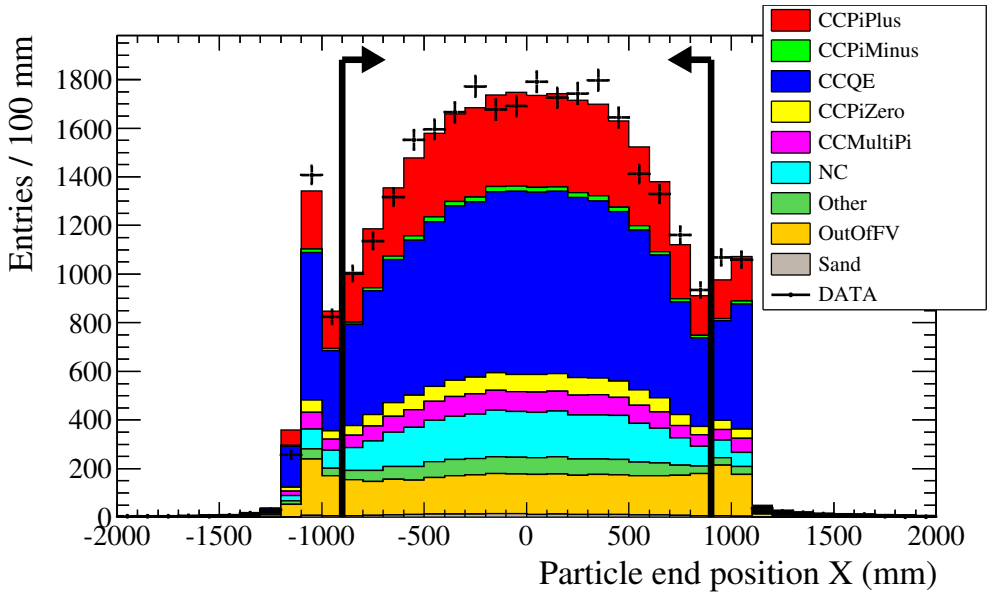

FIGURE 4.13. Selection One: the x coordinate of the end positions of the muon candidate tracks before the one-track-entering-into-TPC1 cut for the water-in data and MC.

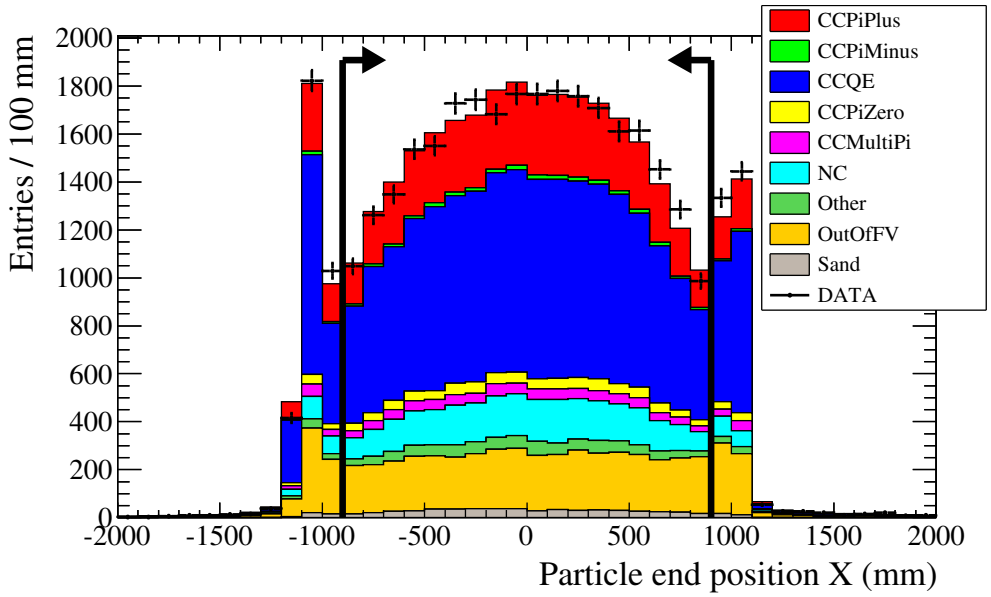

FIGURE 4.14. Selection One: the x coordinate of the end position of the muon candidate tracks before the one-track-entering-into-TPC1 cut for the water-out data and MC.

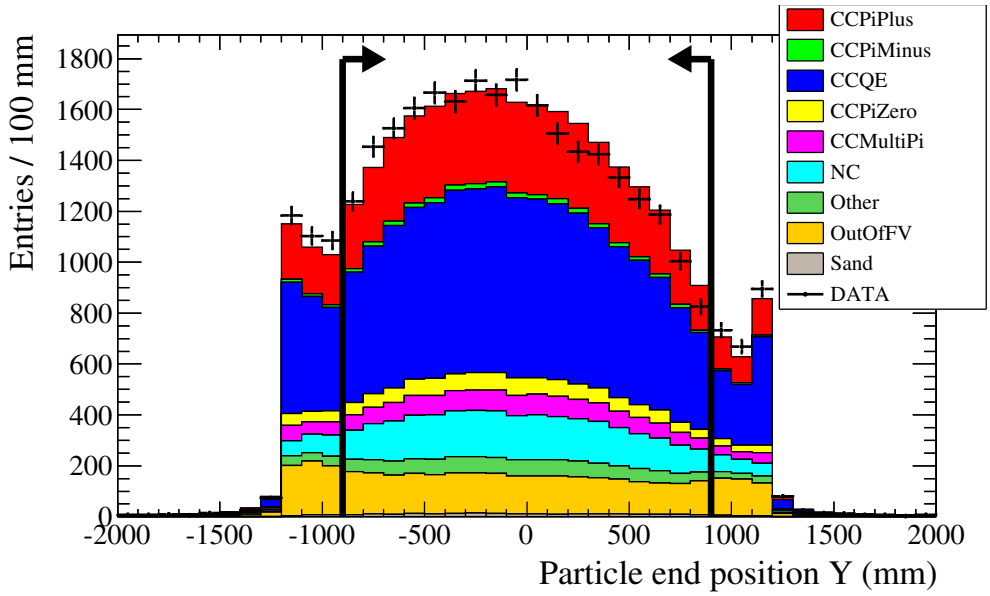

FIGURE 4.15. Selection One: the y coordinate of the end position of the muon candidate tracks before the one-track-entering-into-TPC1 cut for the water-in data and MC.

Figures 4.13, 4.14, 4.15, 4.16, and 4.17, 4.18 show a comparison of the coordinates of the end positions of the reconstructed muon candidate tracks before the cut requiring the muon candidate to enter the TPC1 volume in Selection One. The black arrows point into the region that is selected by the cuts.

The two track selection sample is mostly a mixture of two charged-current interaction channels: CCQE (in NEUT it is reaction code 1) and CC1π^+ (a small fraction of events is coming from other channels). In order to pick the CC1π^+ reactions from the two-track sample with high enough purity (at least 50% signal) more cuts, to be applied to the second track (the pion candidate track), were developed and optimized. The cuts applied on the pion candidate are as follows:

(1) Pion candidate track has to be fully contained in the PØD detector;

(2) Tracks have to start close to the reconstructed vertex (quality cut);

(3) The pull of the energy loss per unit length, dE/dx, in the muon/pion hypothesis of the pion candidate track has to be lower than 4.3 and higher than -10 for parametric tracks and lower than 15.3 and higher than -20 for Kalman tracks;

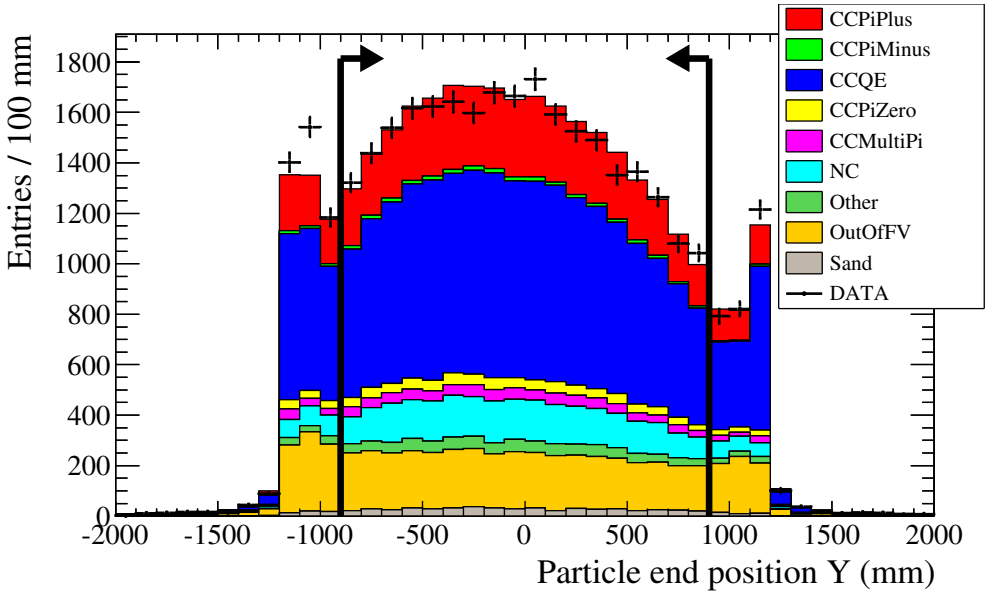

FIGURE 4.16. Selection One: the y coordinate of the end position of the muon candidate tracks before the one-track-entering-into-TPC1 cut for the water-out data and MC.

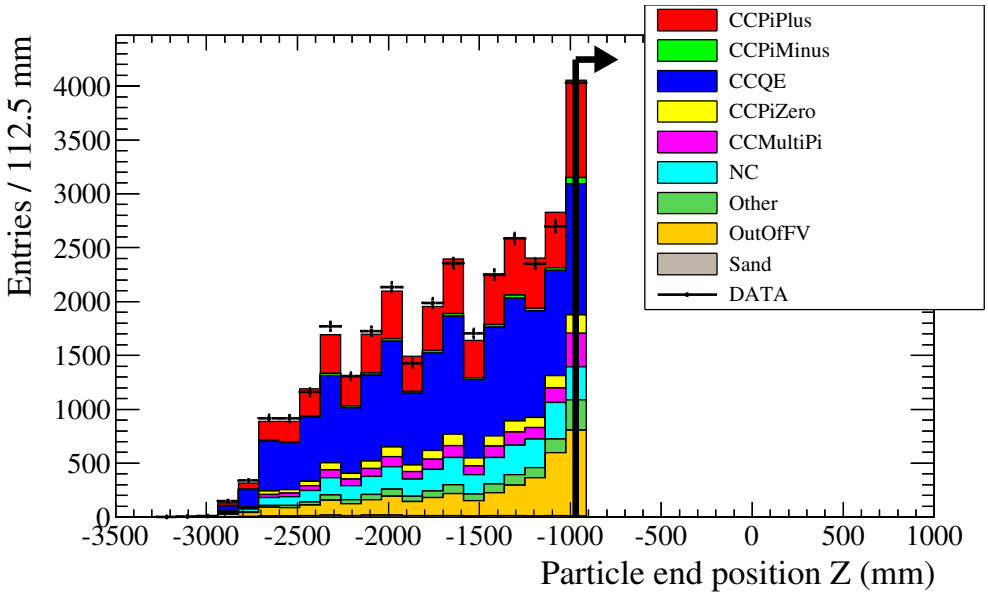

FIGURE 4.17. Selection One: the z coordinate of the end position of the muon candidate tracks before the one-track-entering-into-TPC1 cut for the water-in data and MC.

(4) If the pion candidate tracks does not pass the dE/dx cut, the event can still be selected if the number of Michel clusters is equal to one.

The pion candidate track needs to be fully contained within the PØD detector in order to be able to apply the energy loss cut. Only pion candidates that end sooner than 40 mm (width of two PØDules) from the detector edges are accepted. This requirement means that events with pion candidate tracks ending in the box - $x \in (-796, 724) \cap y \in (-831, 829) \cap z \in (-2929, -1304)$ pass the cut. Figures 4.19, 4.20, 4.21, 4.22, 4.23, and 4.24 show the coordinates of the end of the pion candidate track in Selection One before the containment cut for data and MC.

It is also necessary to require that both the muon and the pion candidate tracks start close to the vertex in order to reduce cases of vertexing algorithm failure, i.e. when the position of the reconstructed vertex happens to be a fair distance away from the first node, or the starting position, of the reconstructed tracks. Coincidentally, this cut removes some of

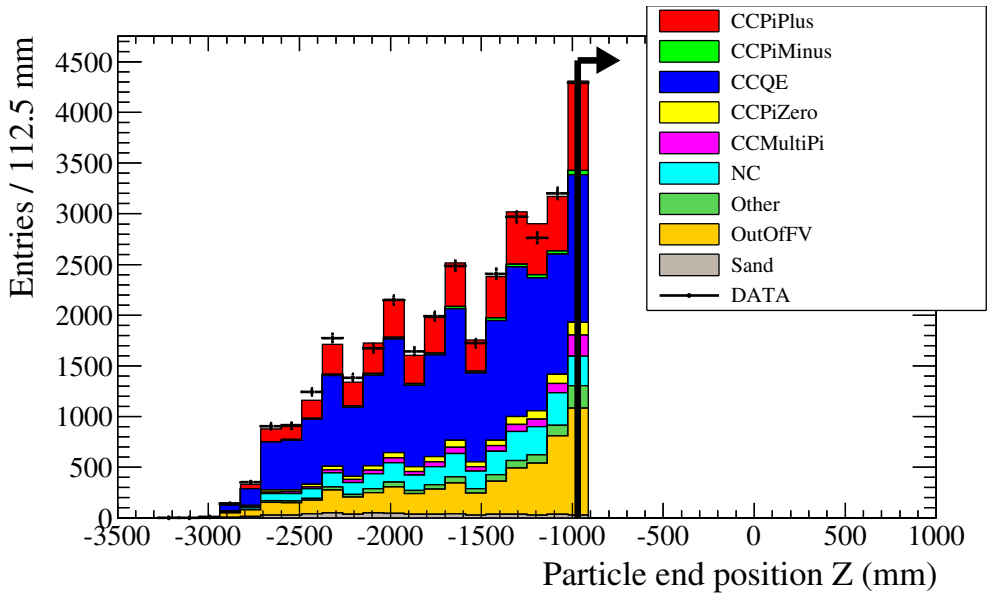

FIGURE 4.18. Selection One: the z coordinate of the end position of the muon candidate tracks before the one-track-entering-into-TPC1 cut for the water-out data and MC.

the background with neutral pions that decay into two photons, since the photons produce electromagnetic showers at some distance from the vertex.

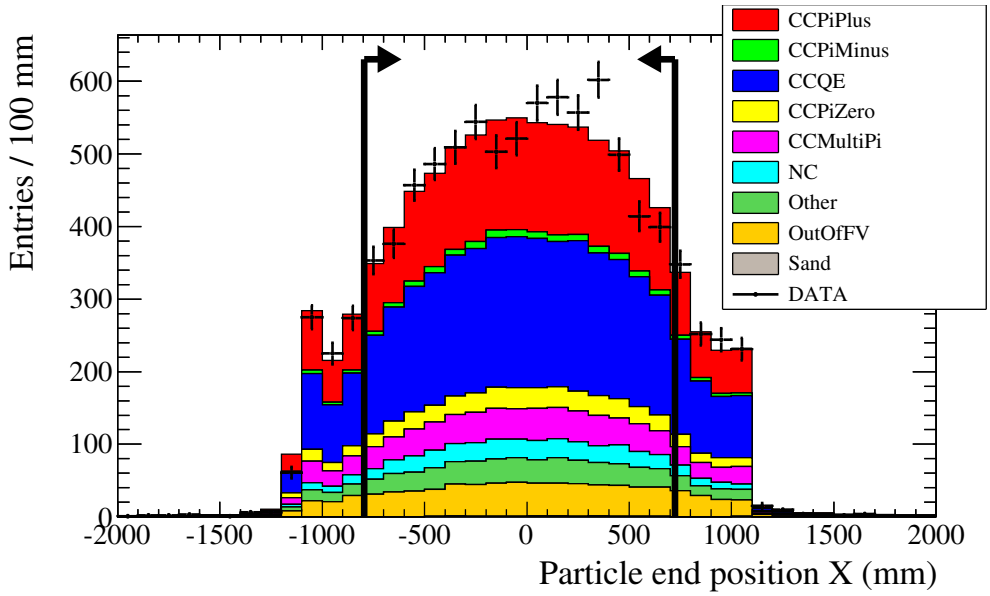

FIGURE 4.19. Selection One: the x coordinate of the end position of the pion candidate particle before the containment cut for the water-in data and MC.

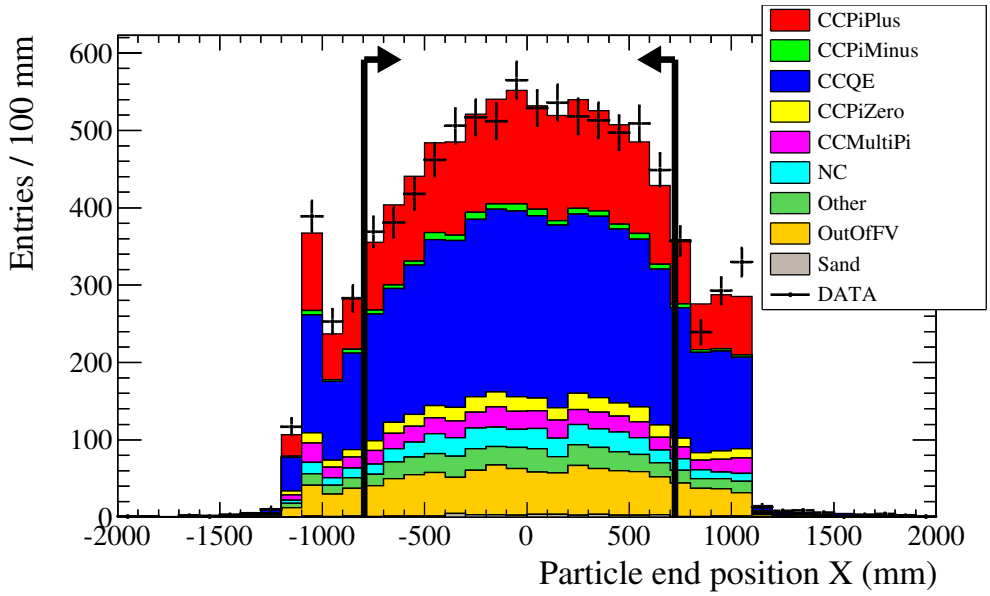

FIGURE 4.20. Selection One: the x coordinate of the end position of the pion candidate particle before the containment cut for the water-out data and MC.

Both the muon and pion candidate tracks are required to start within 80 mm from the reconstructed vertex, which is approximately equal to the width of three PØDules. This requirement allows to reject the mis-reconstructed events with two tracks, and ensures that

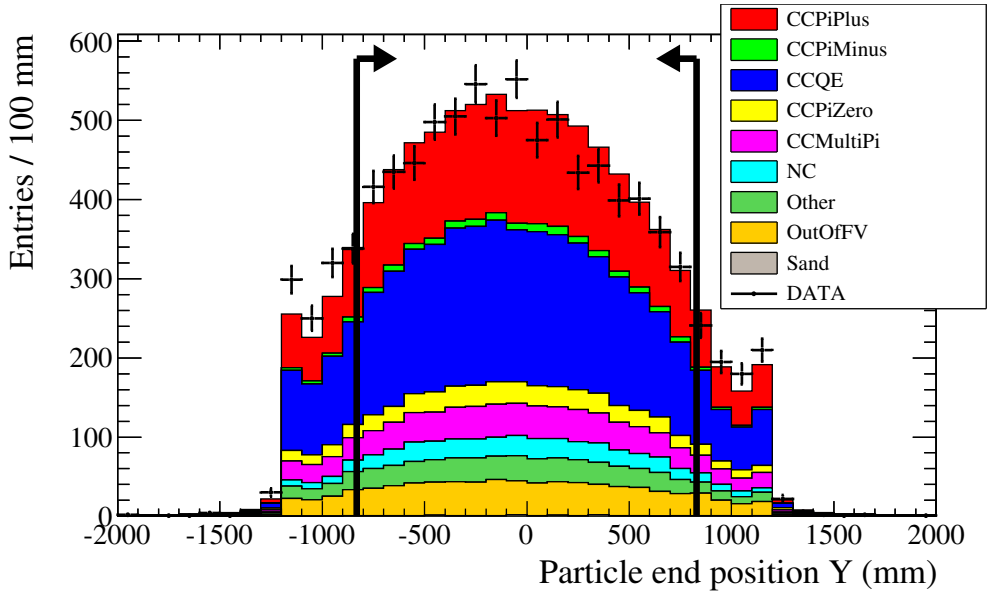

FIGURE 4.21. Selection One: the y coordinate of the end position of the pion candidate particle before the containment cut for the water-in data and MC.

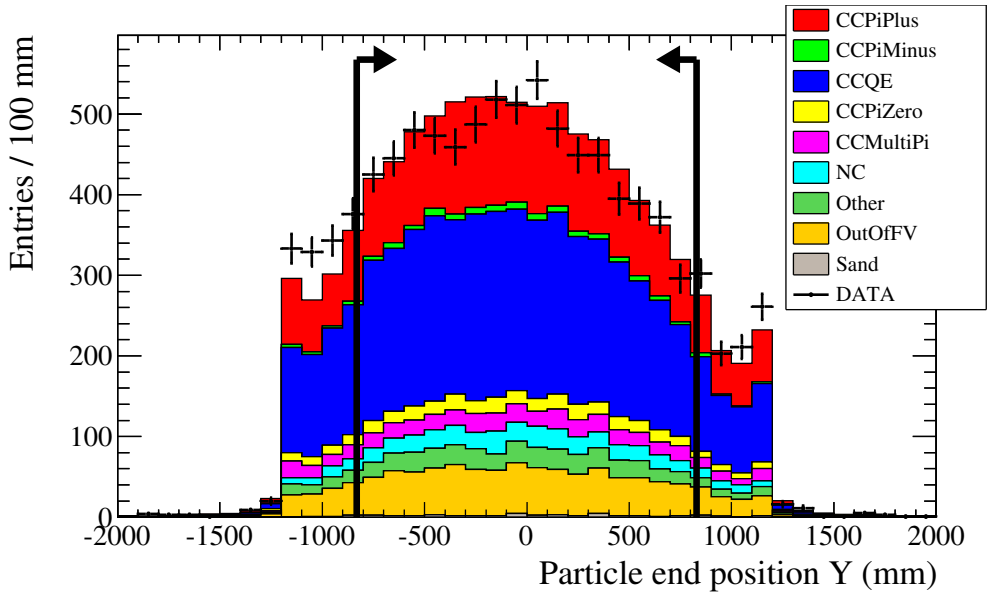

FIGURE 4.22. Selection One: the y coordinate of the end position of the pion candidate particle before the containment cut for the water-out data and MC.

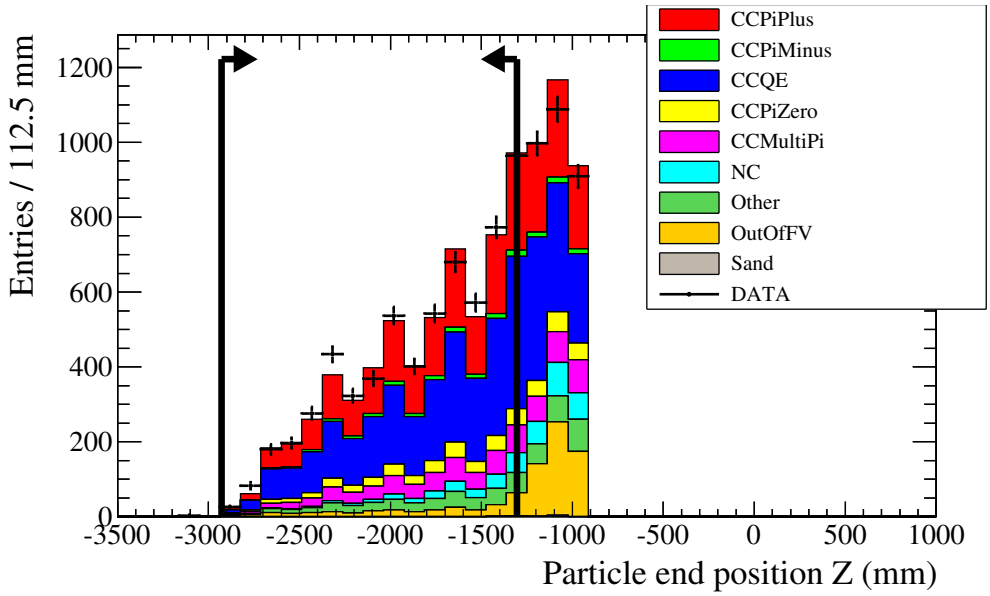

FIGURE 4.23. Selection One: the z coordinate of the end position of the pion candidate particle before the containment cut for the water-in data and MC.

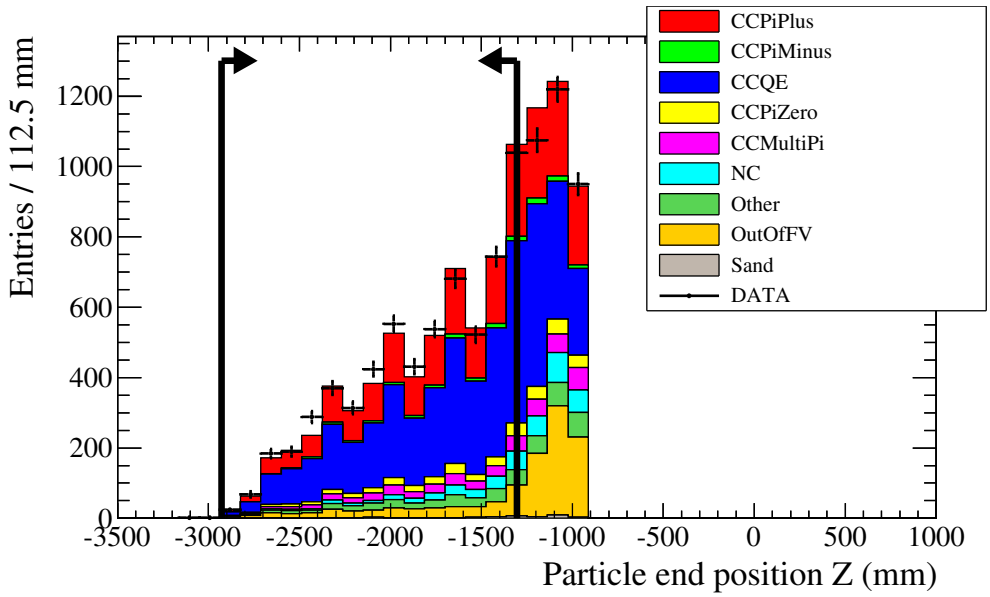

FIGURE 4.24. Selection One: the z coordinate of the end position of the pion candidate particle before the containment cut for the water-out data and MC.

both of the tracks are indeed associated with the proper vertex, and that the vertex position is accurate. The distance of 80 mm between the vertex position and the start of the track was chosen to allow at most a single skipped PØDule (with no hits) between the vertex and

the start of the track. A separation of two or more PØDules between the vertex and the start of the tracks is considered to be a signature of either signal event mis-reconstruction or a background event. Figures 4.25, 4.26, 4.27 and 4.28 show the distance between the start of the tracks and the reconstructed vertex for both the muon and pion candidate tracks.

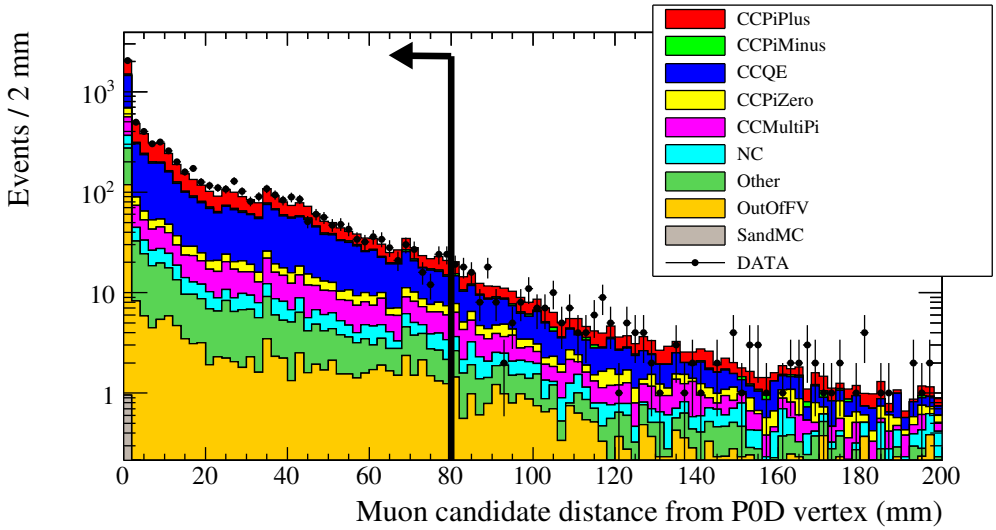

FIGURE 4.25. Selection One: the distance between the reconstructed vertex and the start of the muon candidate track for water-in data and MC. Events with distances smaller than 80 mm are accepted.

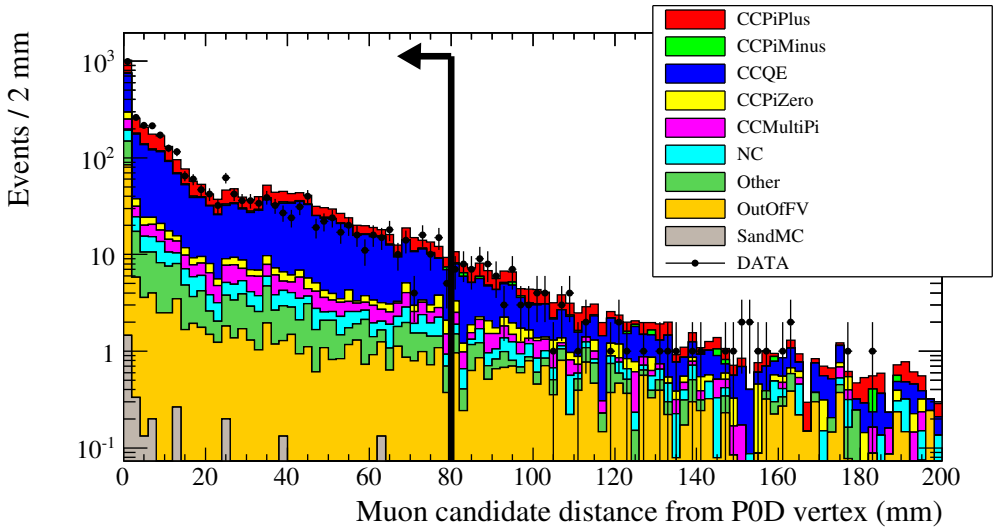

FIGURE 4.26. Selection One: the distance between the reconstructed vertex and the start of the muon candidate track for water-out data and MC. Events with distances smaller than 80 mm are accepted.

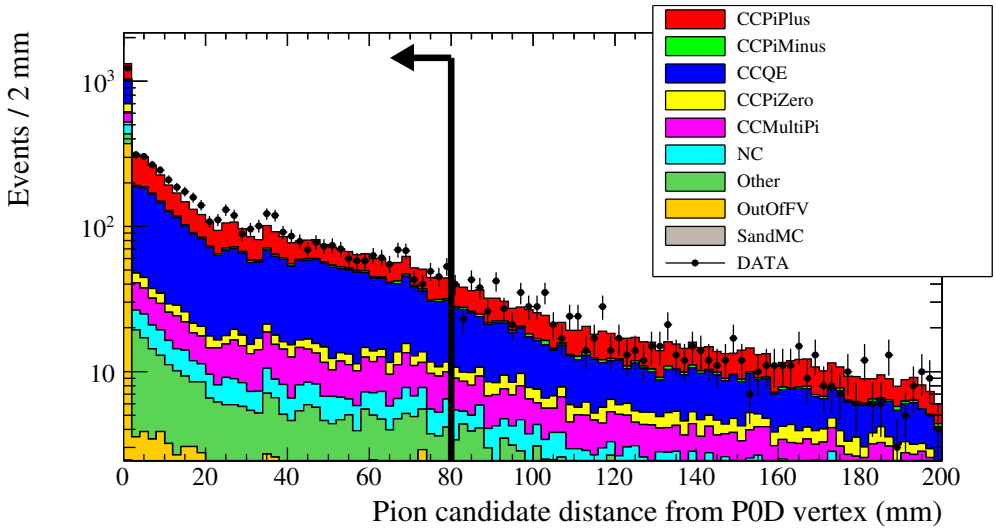

FIGURE 4.27. Selection One: the distance between the reconstructed vertex and the start of the pion candidate track for water-in data and MC. Events with distances smaller than 80 mm are accepted.

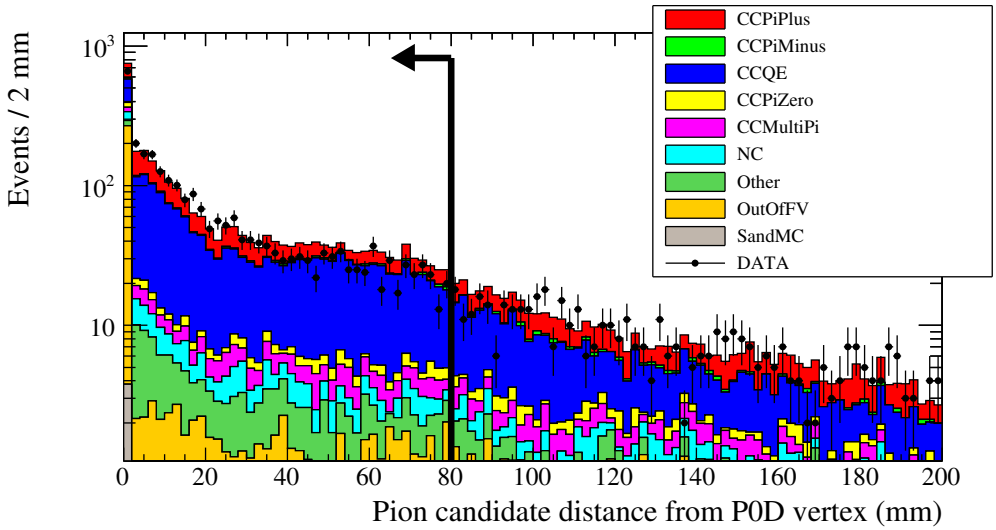

FIGURE 4.28. Selection One: the distance between the reconstructed vertex and the start of the pion candidate track for water-out data and MC. Events with distances smaller than 80 mm are accepted.

Finally, the cut on the pull of the energy loss, dE/dx, of the pion candidate track in the muon/pion hypothesis in applied. Energy loss pull, P_μ, is defined as:

$$P_\mu = \sum_{i=1}^{N} \frac{\bar{x}_i^{measured} - \bar{x}_i^{expected}}{\sigma_i}, \tag{23}$$

where the sum is calculated for six or less bins of the distance from the track length starting from the track end until the half of the total length of the track is reached. In each bin i the deviation of the most probable value of the charge $\bar{x}_i^{measured}$ from the expected value of the charge $\bar{x}_i^{expected}$ in the stopping muon hypothesis normalized to the RMS of the charge distribution (σ_i) is calculated. Bins of the distance from the end of the track have a width of 67.8 mm. Expected values of the charge and sigmas have been calculated using a sample of data sand muons stopping in the PØD detector. In each of the bins a Landau-Gaussian convoluted function has been fitted to the charge distribution; $\bar{x}_i^{expected}$ is the most probable value and σ_i is the width taken from the fit [90].

The dE/dx pull calculation and optimization code was adopted from the PØD-based NCE analysis performed by D. Ruterbories, where it was necessary to distinguish between protons and muons based on their energy deposition profile. More details about the dE/dx pull in the muon/proton hypothesis can be found in the dissertation of D. Ruterbories [90].

PØD reconstruction software (version corresponding to RDP5G and MCP5E) uses two very different algorithms to fit tracks to hits:

- a Kalman filter;
- a linear parametric fit.

Since the tracks fitted with the Kalman filter and the parametric fitter have different dE/dx distributions, different dE/dx cuts are applied to them. Distributions of the dE/dx pulls

for pion candidate tracks in this analysis are shown in Figures 4.29, 4.30, 4.31, and 4.32. The black arrows in these plots point into the area of phase space selected by the cuts. The dE/dx pull distributions have two pronounced peaks, and the cuts are designed to select the muon/pion peak around the pull value of zero, and reject the other peak, which is dominated by protons.

The dE/dx pull of the pion candidate track was required to be between 4.3 and -10 for parametric tracks and between 15.3 and -20 for Kalman tracks. These cut values were obtained as a result of a dE/dx cut optimization procedure, and correspond to the maximum value of efficiency times purity squared figure of merit, $\epsilon \times p^2$.

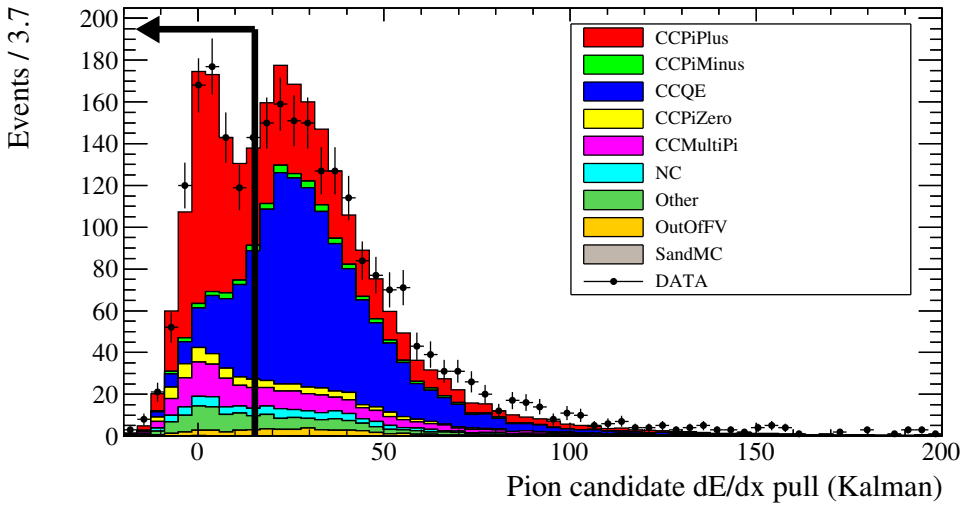

FIGURE 4.29. Selection One: dE/dx pull in the muon hypothesis of the pion candidate track fitted with a Kalman filter before the last cut for the water-in data and MC.

If a pion candidate track does not pass the appropriate dE/dx cut then the cut on the number of reconstructed Michel electron clusters in the event is applied. The Michel cluster finding algorithm searches for clusters of hits within a 35 cm radius from both the start and end of the tracks. The hits are required to be delayed by at least 100 ns with respect to the track hits but within the same integration window. These parameter values were

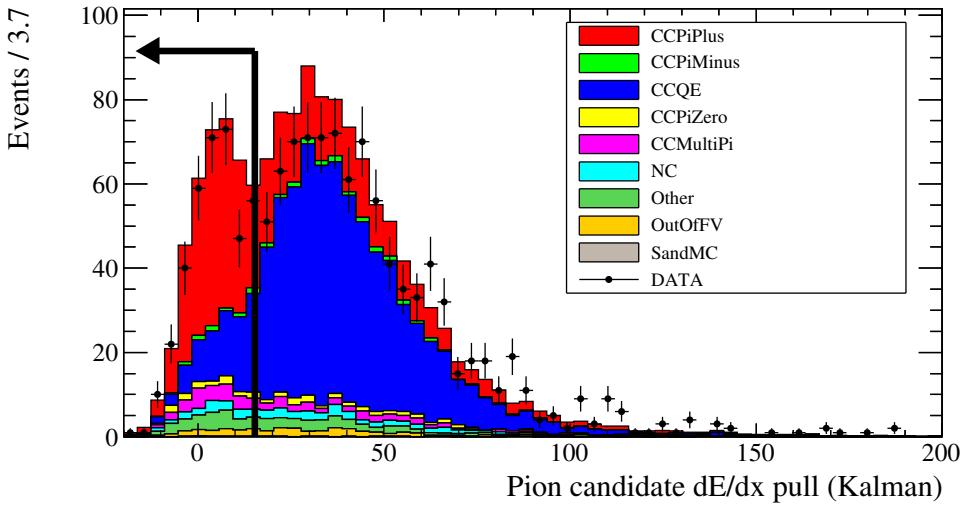

FIGURE 4.30. Selection One: dE/dx pull in the muon hypothesis of the pion candidate track fitted with a Kalman filter before the last cut for the water-out data and MC.

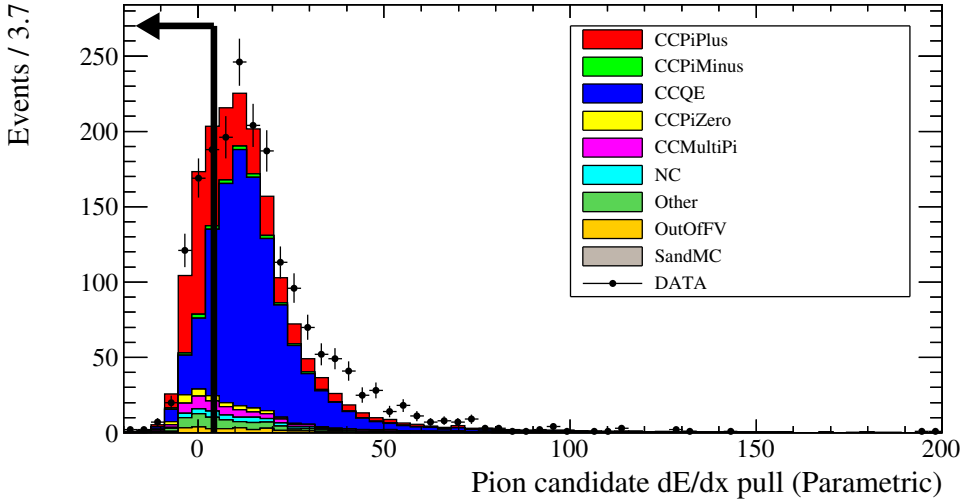

FIGURE 4.31. Selection One: dE/dx pull in the muon hypothesis of the pion candidate track fitted with a parametrtic fitter before the last cut for the water-in data and MC.

optimized by L. Trung, and details regarding the optimization procedures can be found in his Ph.D. dissertation [133]. The event is accepted if the number of clusters is exactly equal one. Applying this cut ensures that the Michel clusters from $\pi^+ \to \mu^+ \to e^+$ decay are selected. The cut on the number of Michel clusters allows for the recovery of CC1π^+ events where a

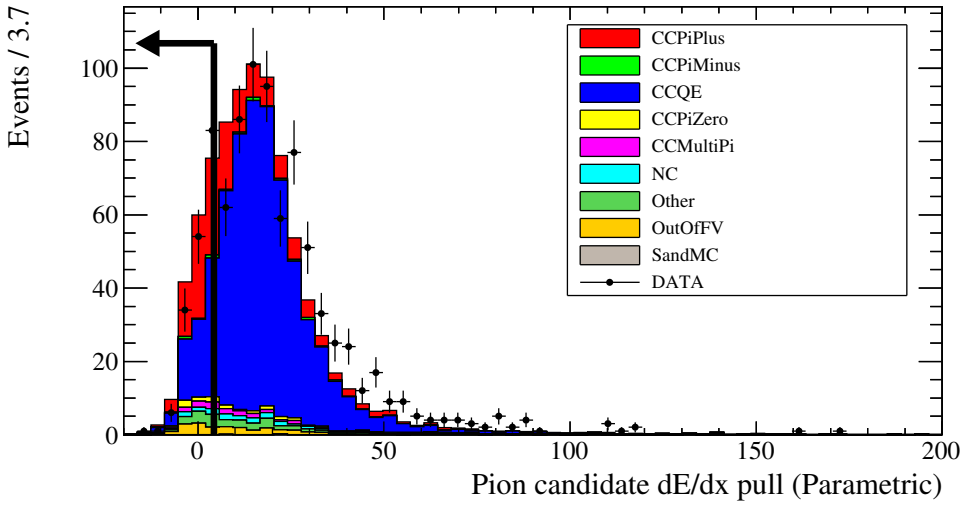

FIGURE 4.32. Selection One: dE/dx pull in the muon hypothesis of the pion candidate track fitted with a parametric fitter before the last cut for the water-out data and MC.

high momentum proton is reconstructed as pion candidate and low momentum pion (below reconstruction threshold) decays producing a Michel electron. Figures 4.33 and 4.34 show distributions of the number of Michel electron clusters per event for water-in and water-out data and MC when the dE/dx cut was not passed. Distributions of both quantities - the

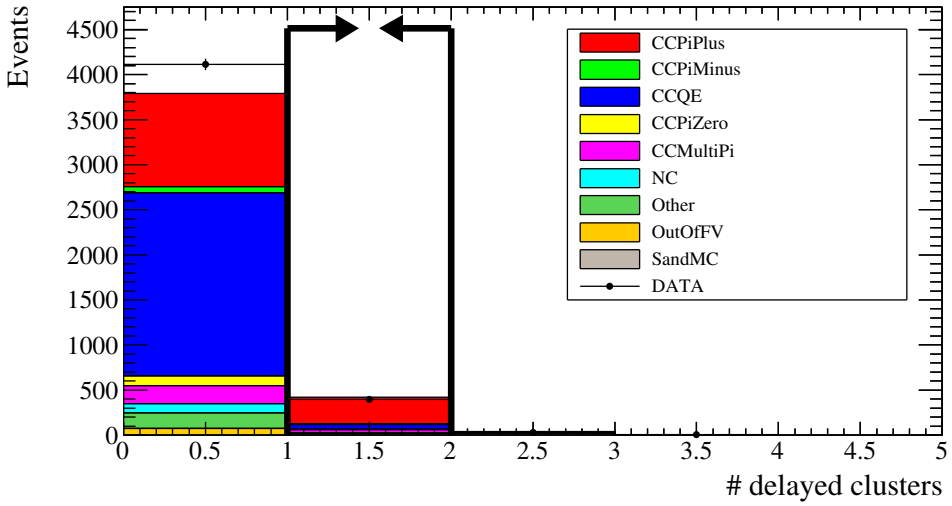

FIGURE 4.33. Selection One: the number of Michel electron clusters per event before the last cut and in case the dE/dx cut was not passed for the water-in data and MC. Events with exactly one Michel cluster are accepted.

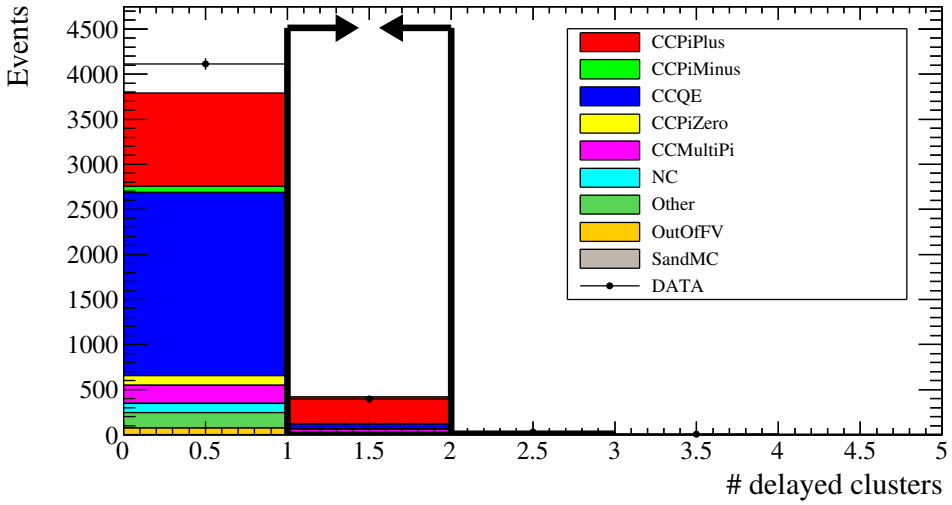

FIGURE 4.34. Selection One: the number of Michel electron clusters per event before the last cut and in case the dE/dx cut was not passed for the water-out data and MC. Events with exactly one Michel cluster are accepted.

dE/dx pull of the pion candidate track and the number of Michel electron clusters - reveal some discrepancies between data and MC. In the case of dE/dx pull the observed discrepancies might be a result of the difference between the number of protons per event in data and MC which can come from incorrect modeling of the FSI effects. In this analysis, systematic effects related to the dE/dx cut were studied, and corresponding systematic uncertainties were evaluated (Section 4.6.6.3). Data-MC discrepancies in the distributions of the number of Michel clusters are the result of the difference in the efficiency of finding Michel clusters between data and MC. A separate study and systematic uncertainty was dedicated to the Michel electron finding efficiency (Section 4.6.6.4).

4.2.2.3. *Selection Two: One Vertex, Two Contained Tracks.* The goal of Selection Two is to select CC1π^+ events with both the muon and the pion candidate tracks contained in the PØD detector. Such CC1π^+ events come from the lower neutrino energy (less than 1 GeV) range in the T2K beam spectrum. Figure 4.35 shows an example event topology with one vertex and two tracks selected by the Selection Two cuts.

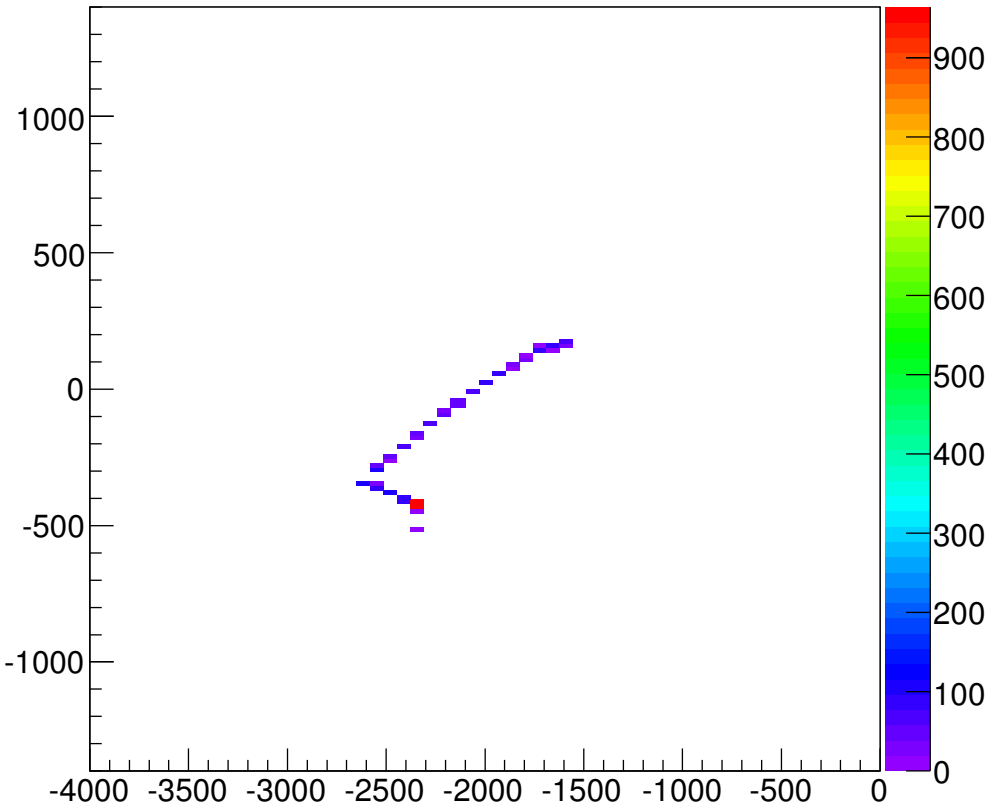

FIGURE 4.35. Selection Two: a y-z view of a Run 2 water-in data event display. y (mm) is the vertical axis, z (mm) is the horizontal axis. Neutrino beam direction is from left to right. The data event has one vertex and two tracks. Both tracks are contained in the PØD.

In Selection One (one vertex, two tracks, one track contained), the muon and pion candidate terminology was used to identify the tracks in the events. In that case it was well motivated to call the "muon candidate" the track that was exiting the PØD into the TPC1 due to the high muon selection purity (86%). In the case of Selection Two, where both tracks are contained in the PØD, this terminology is no longer valid, since both tracks have almost the same probability of being a muon or a pion (both muons and pions have very similar energy deposition signatures at low energies). Instead the terms "longer track" and "shorter track" are used in this PØD-contained selection.

Cuts for the Selection Two are similar to the Selection One cuts, and are listed below:

(1) Require exactly one PØD reconstructed vertex in the bunch;

(2) Reconstructed vertex has to be three dimensional (quality cut);

(3) Reconstructed vertex has to be located in the PØD water target fiducial volume (as defined in Section 4.2.2.1);

(4) There are exactly two reconstructed particles associated with the vertex;

(5) Both reconstructed particles need to be three dimensional (quality cut);

(6) Both particles are tracks (always true because the `TP0DTrackRecon` algorithm result is used);

(7) First particle is contained in the PØD;

(8) Second particle is contained in the PØD.

Distributions of the x, y and z coordinates of the position of the reconstructed vertex before the fiducial volume cut are shown in Figures 4.5, 4.6, 4.7, 4.8, 4.9, and 4.10.

In the two last cuts, both tracks are required to be contained in the PØD. Tracks that end before the outermost 40 mm (width of two PØDules) at the sides and at the downstream end of the PØD are accepted. Events with tracks ending in the containment box - $x \in (-796, 724)$ $\cap$ $y \in (-831, 829) \cap z \in (-2929, -1304)$ are accepted. Applying this cut makes it possible to check the dE/dx particle ID of both tracks. Figures 4.36, 4.37, 4.38, 4.39, 4.40, and 4.41 show the data-MC comparison of the coordinates of the end position of the reconstructed particles before containment cut.

After the first set of cuts, the PØD-contained charged-current two-track sample is obtained. To select CC1π^+ events the second set of cuts, particle ID, etc., is applied to both tracks. The cuts are as follows:

(1) Both tracks have to start close to the reconstructed vertex (quality cut);

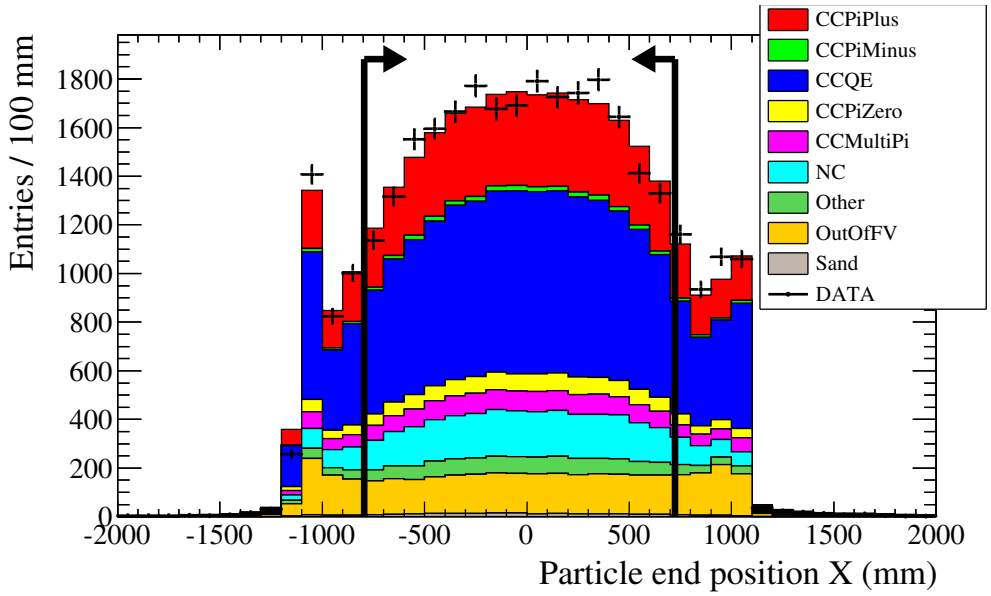

FIGURE 4.36. Selection Two: the x coordinate of the end position of the particles before the containment cuts for the water-in data and MC. Events with tracks ending in the box - $x \in (-796, 724) \cap y \in (-831, 829) \cap z \in (-2929, -1304)$ - are accepted into the selection.

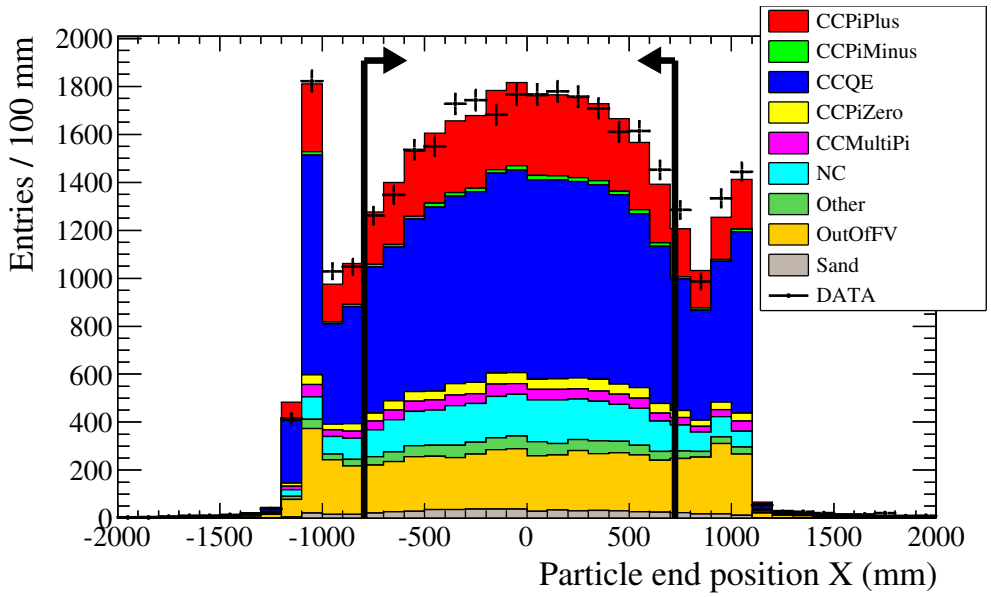

FIGURE 4.37. Selection Two: the x coordinate of the end position of the particles before the containment cuts for the water-out data and MC. Events with tracks ending in the box - $x \in (-796, 724) \cap y \in (-831, 829) \cap z \in (-2929, -1304)$ - are accepted into the selection.

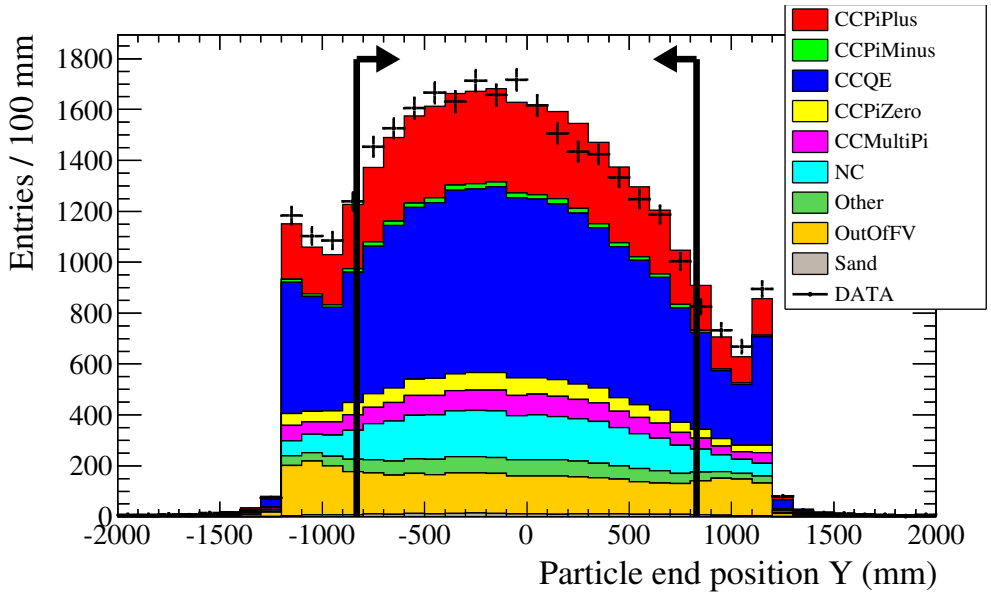

FIGURE 4.38. Selection Two: the y coordinate of the end position of the particles before the containment cuts for the water-in data and MC. Events with tracks ending in the box - $x \in (-796, 724) \cap y \in (-831, 829) \cap z \in (-2929, -1304)$ - are accepted into the selection.

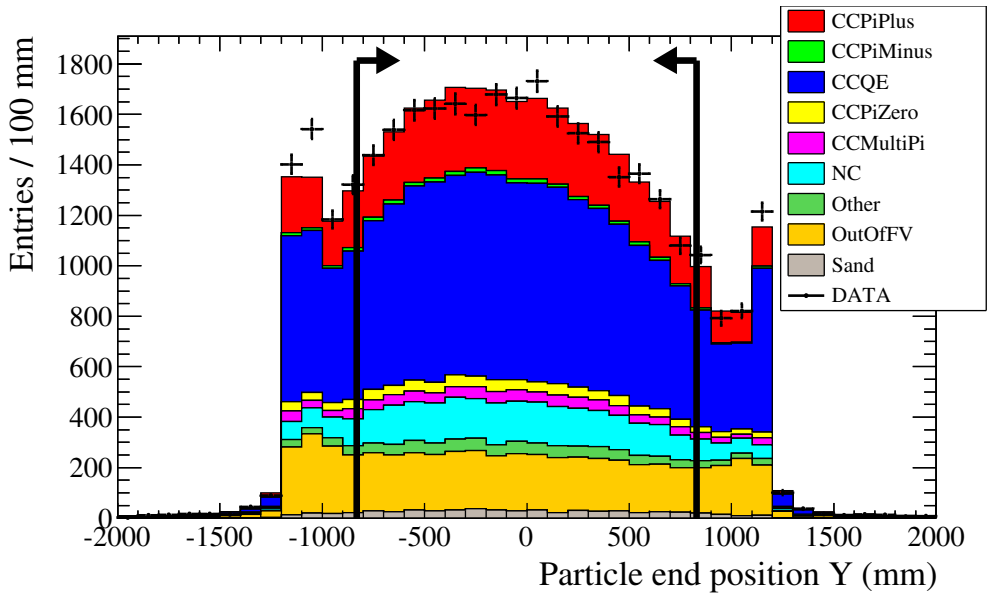

FIGURE 4.39. Selection Two: the y coordinate of the end position of the particles before the containment cuts for the water-out data and MC. Events with tracks ending in the box - $x \in (-796, 724) \cap y \in (-831, 829) \cap z \in (-2929, -1304)$ - are accepted into the selection.

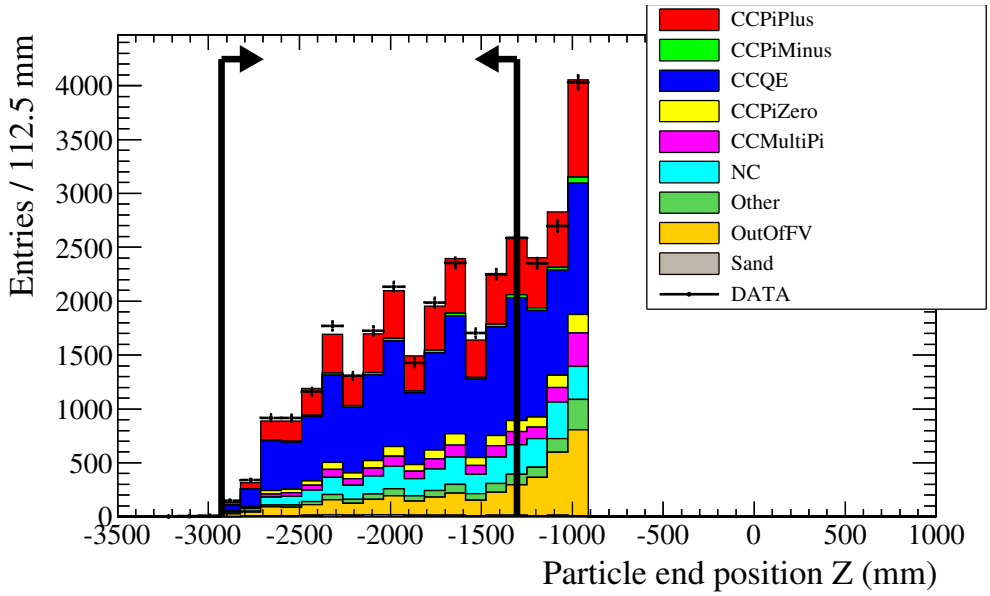

FIGURE 4.40. Selection Two: the z coordinate of the end position of the particles before the containment cuts for the water-in data and MC. Events with tracks ending in the box - $x \in (-796, 724) \cap y \in (-831, 829) \cap z \in (-2929, -1304)$ - are accepted into the selection.

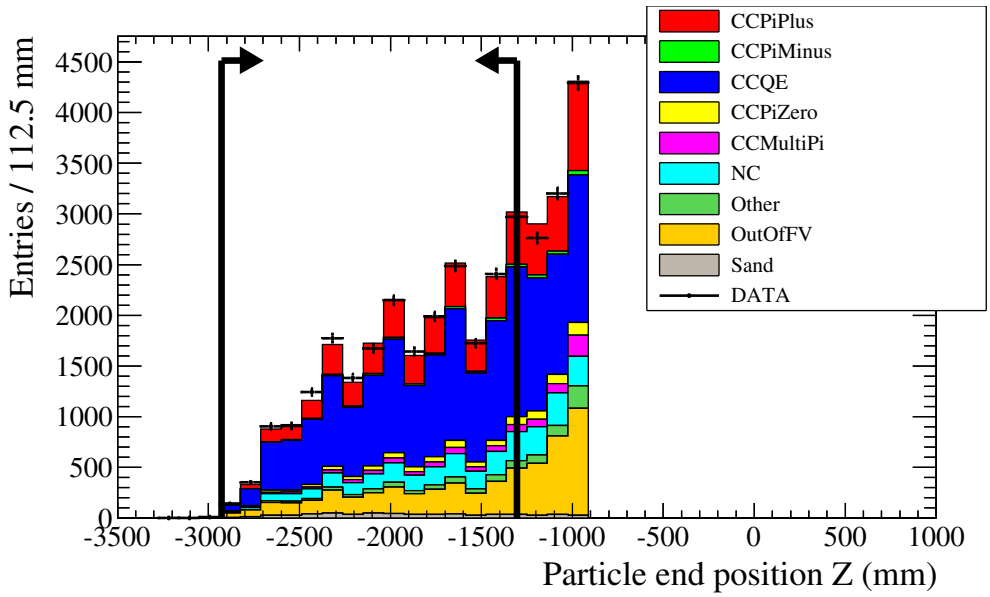

FIGURE 4.41. Selection Two: the z coordinate of the end position of the particles before the containment cuts for the water-out data and MC. Events with tracks ending in the box - $x \in (-796, 724) \cap y \in (-831, 829) \cap z \in (-2929, -1304)$ - are accepted into the selection.

(2) dE/dx pull in the muon/pion hypothesis of both tracks has to be lower than 4.3 and higher than −10 for parametric tracks and lower than 15.3 and higher than −20 for Kalman tracks;

(3) In case an event did not pass the dE/dx cut, it can be recovered if the number of Michel clusters is equal to two.

The motivation for the cut on the distance from the reconstructed vertex is the same as in the previous selection. Figures 4.42, 4.43, 4.44, and 4.45 show the plots of the distance between the track starting point and the single reconstructed vertex for both tracks, separately for the shorter and longer tracks.

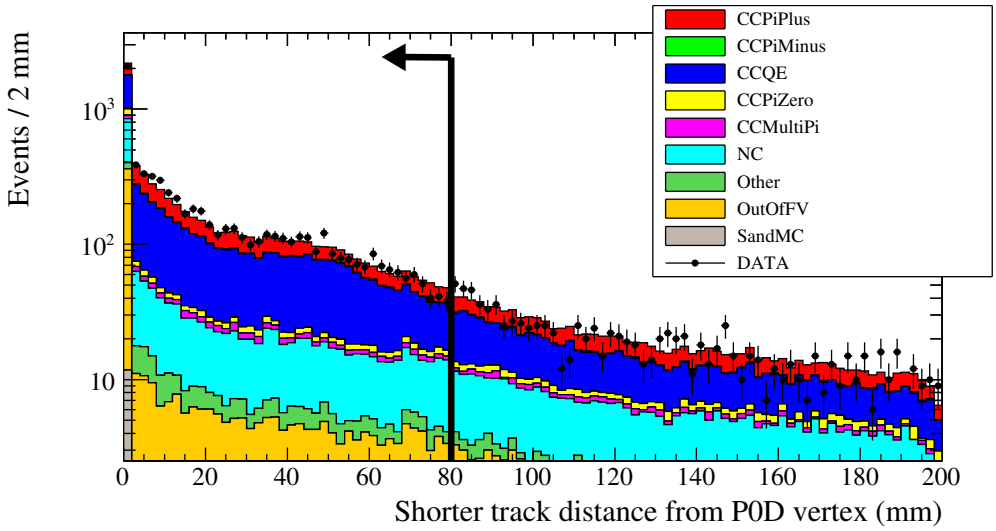

FIGURE 4.42. Selection Two: the distance between the reconstructed vertex and the start of the shorter track for the water-in data and MC. Events with distances smaller than 80 mm are accepted.

The dE/dx cut is applied to both tracks, and both tracks are required to be compatible with the stopping muon/pion hypothesis. Distributions of the dE/dx pulls of the Kalman-fit tracks are shown in Figures 4.46, 4.47, 4.48, and 4.49.

Distributions of the dE/dx pulls of the parametrically fit tracks are shown in Figures 4.50, 4.51, 4.52, and 4.53.

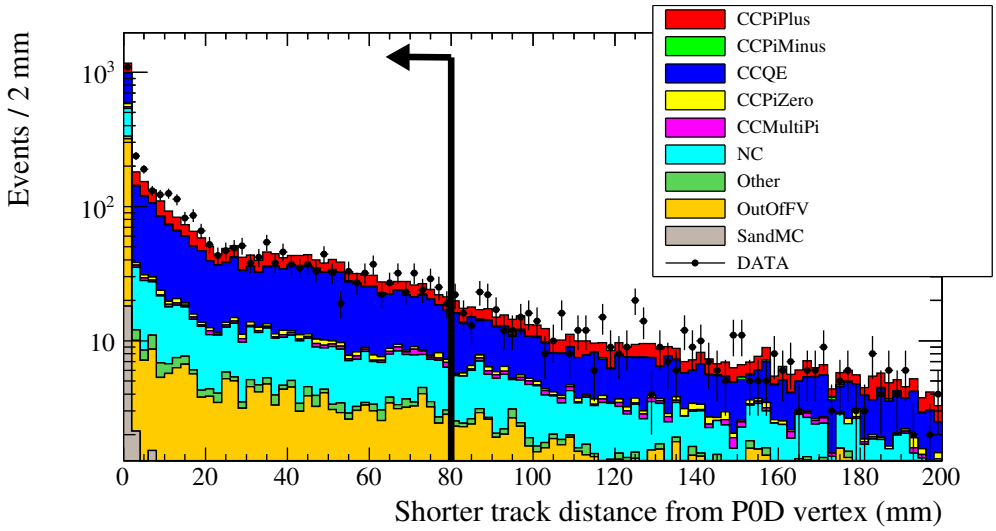

FIGURE 4.43. Selection Two: the distance between the reconstructed vertex and the start of the shorter track for the water-out data and MC. Events with distances smaller than 80 mm are accepted.

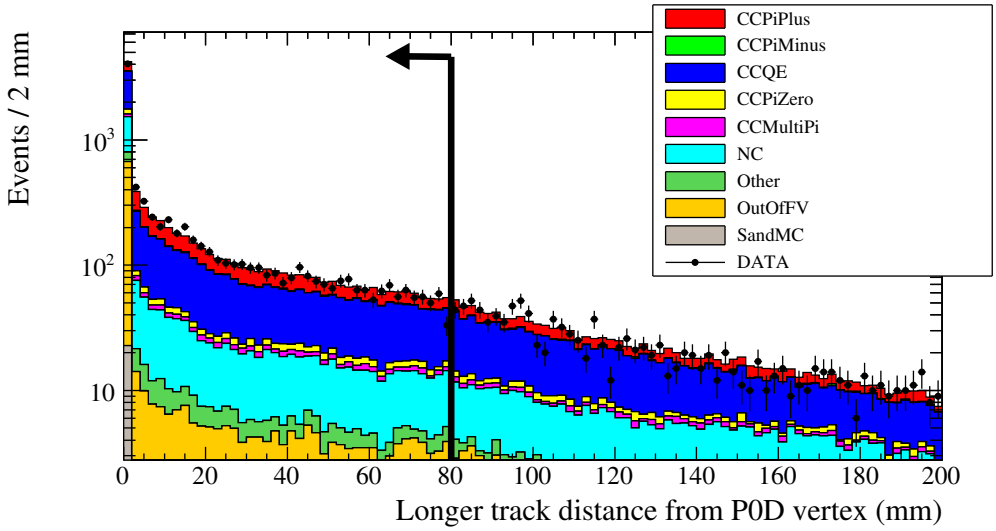

FIGURE 4.44. Selection Two: the distance between the reconstructed vertex and the start of the longer track for the water-in data and MC. Events with distances smaller than 80 mm are accepted.

In a similar way as in the Selection One, if the dE/dx cut fails, then the cut on the number of reconstructed Michel electron clusters in the event is applied. This time the event is accepted if the number of clusters is exactly equal to two: Michel clusters from both the

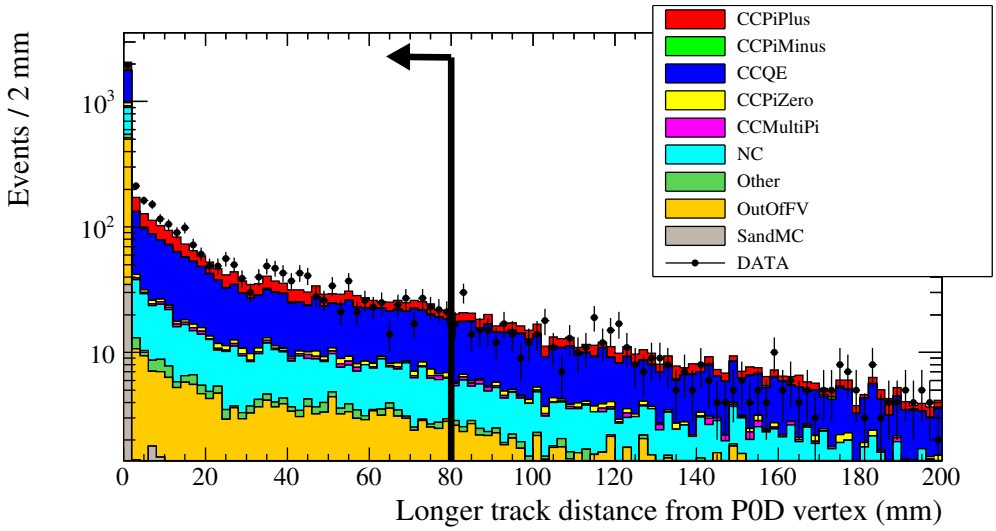

FIGURE 4.45. Selection Two: the distance between the reconstructed vertex and the start of the longer track for the water-out data and MC. Events with distances smaller than 80 mm are accepted.

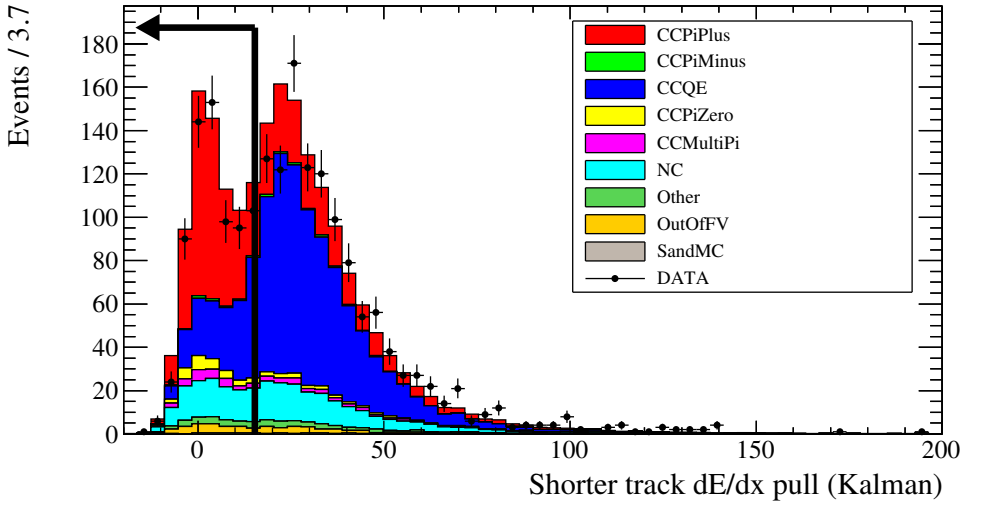

FIGURE 4.46. Selection Two: the dE/dx pull in the muon hypothesis before the last cut for shorter Kalman-fit tracks for the water-in data and MC.

muon and pion decays. Figures 4.54 and 4.55 show a distribution of the number of Michel electron clusters.

4.2.3. SUMMARY AND PERFORMANCE OF THE EVENT SELECTIONS. To evaluate the performance of the CC1π^+ event selection in the PØD, it is necessary to define the efficiency,

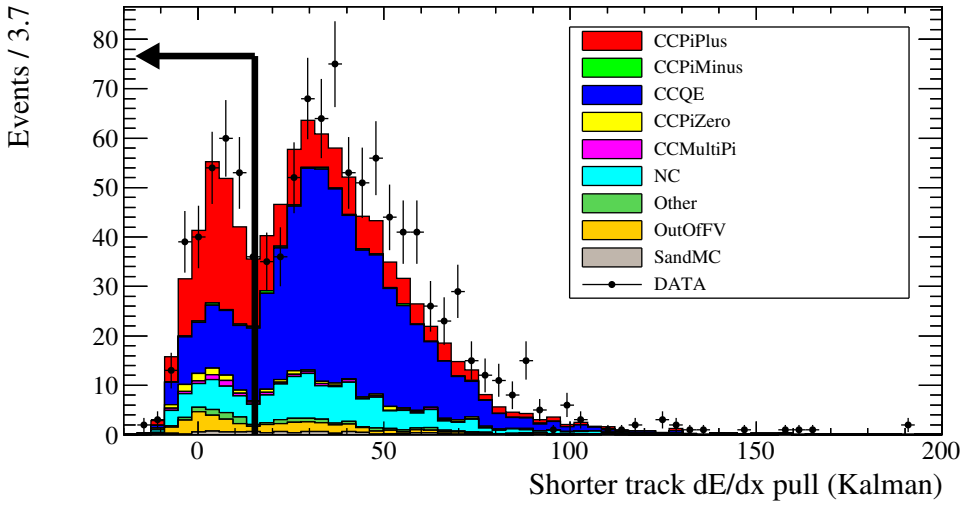

FIGURE 4.47. Selection Two: the dE/dx pull in the muon hypothesis before the last cut for shorter Kalman-fit tracks for the water-out data and MC.

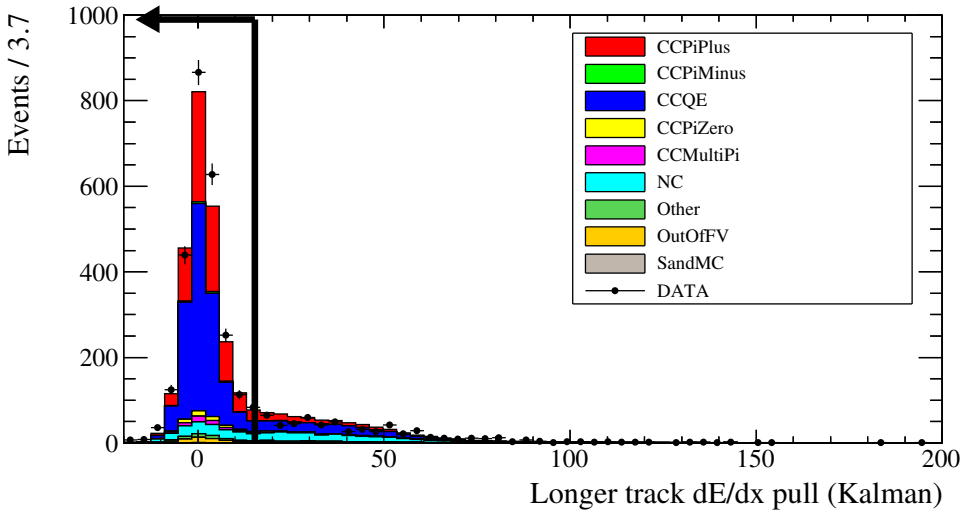

FIGURE 4.48. Selection Two: the dE/dx pull in the muon hypothesis before the last cut for longer Kalman-fit tracks for the water-in data and MC.

ϵ, and the purity, p, of an event selection:

$$\epsilon = \frac{S^{sel(\text{NEUT MC})}}{s^{gen}}, \; p = \frac{S^{sel(\text{NEUT MC})}}{N^{\text{NEUT MC}}}. \tag{24}$$

$N^{\text{NEUT MC}}$ in Equation 24 is the number of selected events in NEUT MC, $S^{sel(\text{NEUT MC})}$ is number of selected MC-truth CC1π^+ interactions with the simulated vertex in fiducial volume

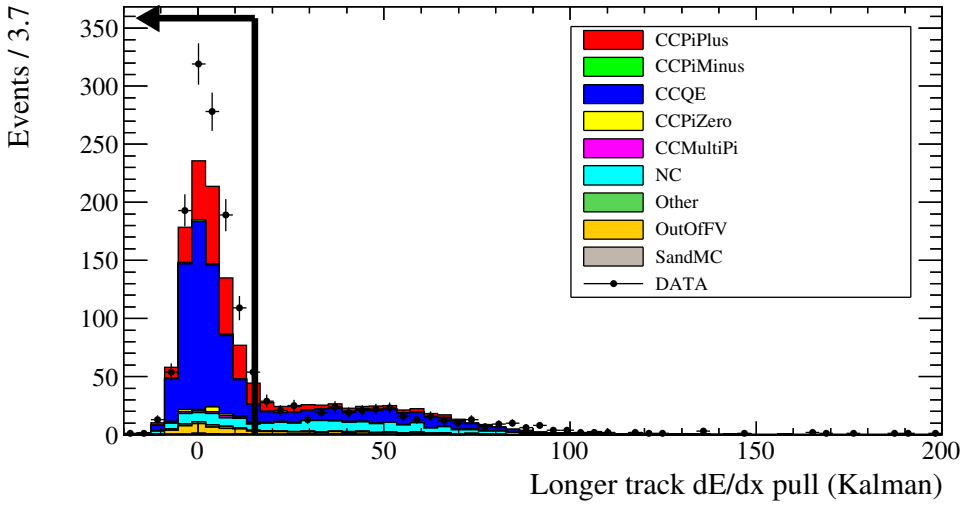

FIGURE 4.49. Selection Two: the dE/dx pull in the muon hypothesis before the last cut for longer Kalman-fit tracks for the water-out data and MC.

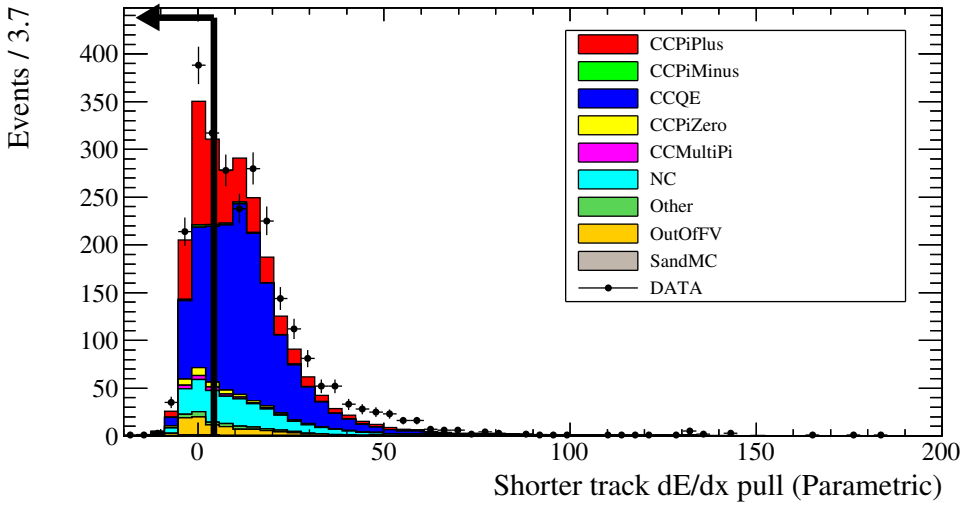

FIGURE 4.50. Selection Two: the dE/dx pull in the muon hypothesis before the last cut for shorter parametrically fit tracks for the water-in data and MC.

according to the NEUT MC, and s^{gen} is the number of all MC-truth CC1π^+ interactions before any cuts with the simulated vertex in the NEUT MC fiducial volume. The CC1π^+ interaction definition is based on the track multiplicity and content of the particles leaving the target nucleus after FSI. Events are said to be of the CC1π^+ type when there was exactly one μ^-, exactly one π^+, no other mesons and any number of nucleons leaving target nucleus.

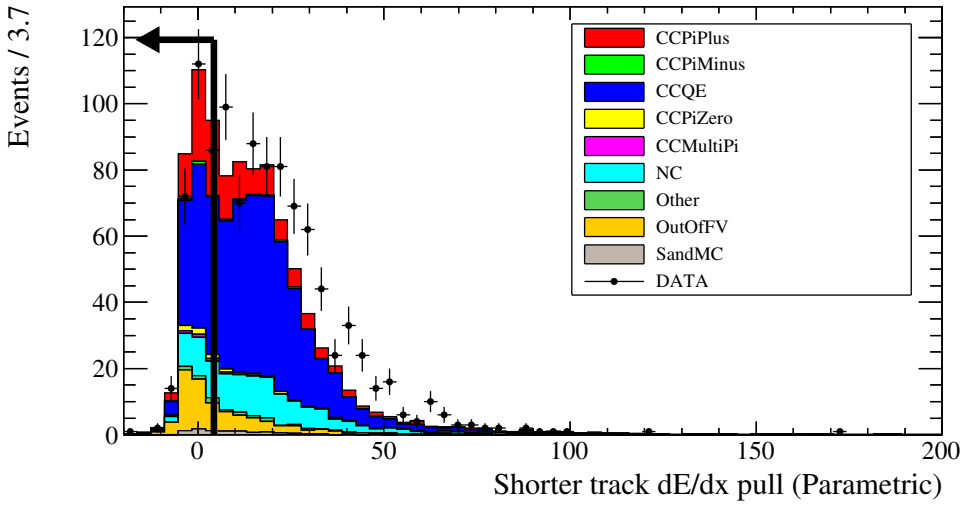

FIGURE 4.51. Selection Two: the dE/dx pull in the muon hypothesis before the last cut for shorter parametrically fit tracks for the water-out data and MC.

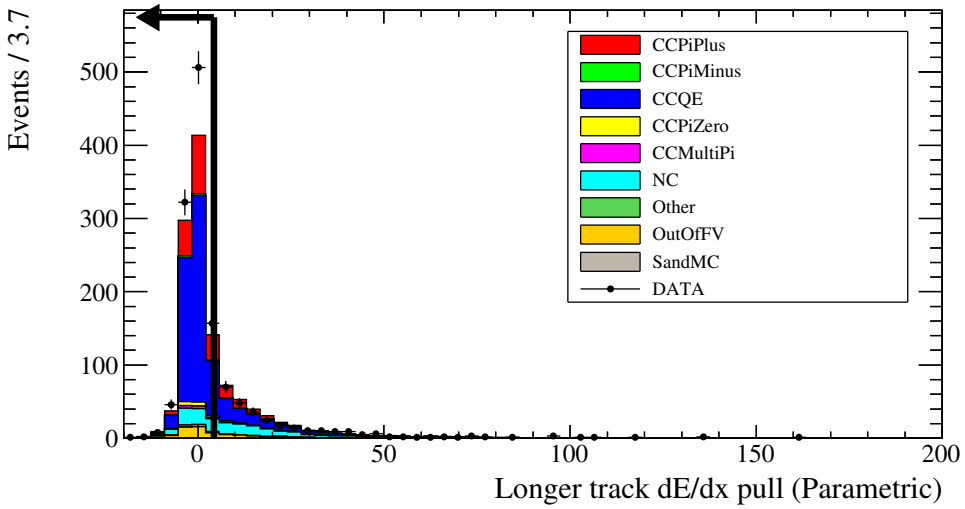

FIGURE 4.52. Selection Two: the dE/dx pull in the muon hypothesis before the last cut for longer parametrically fit tracks for the water-in data and MC.

Tables 4.6, 4.7, 4.8, and 4.9 show the event reduction and selection progression for water-in and water-out data and Monte Carlo events (Monte Carlo numbers are scaled to data POT).

Table 4.10 summarizes entire event selection (Selections One and Two combined) for data and the predictions of the simulation for water-in and water-out modes (scaled to data POT). N is the selected number of events in data, B is the number of background events predicted

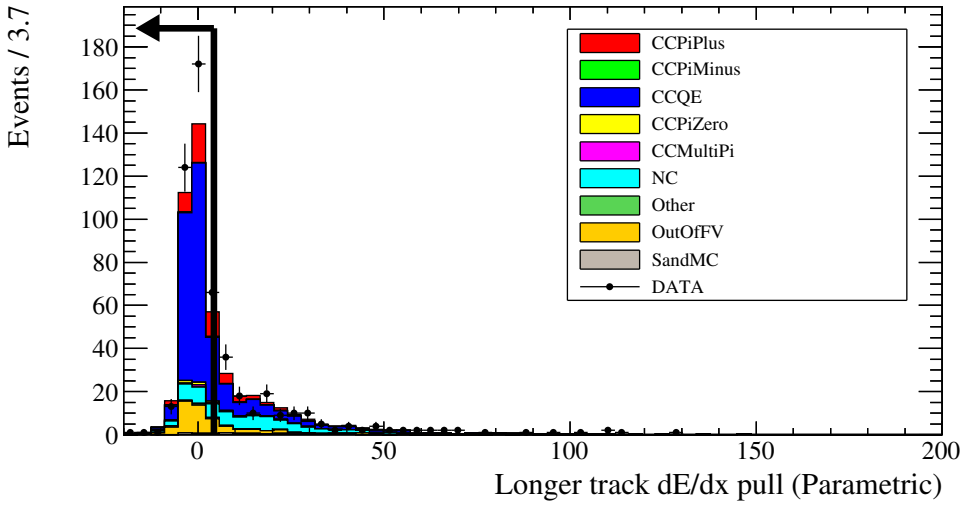

FIGURE 4.53. Selection Two: the dE/dx pull in the muon hypothesis before the last cut for longer parametrically fit tracks for the water-out data and MC.

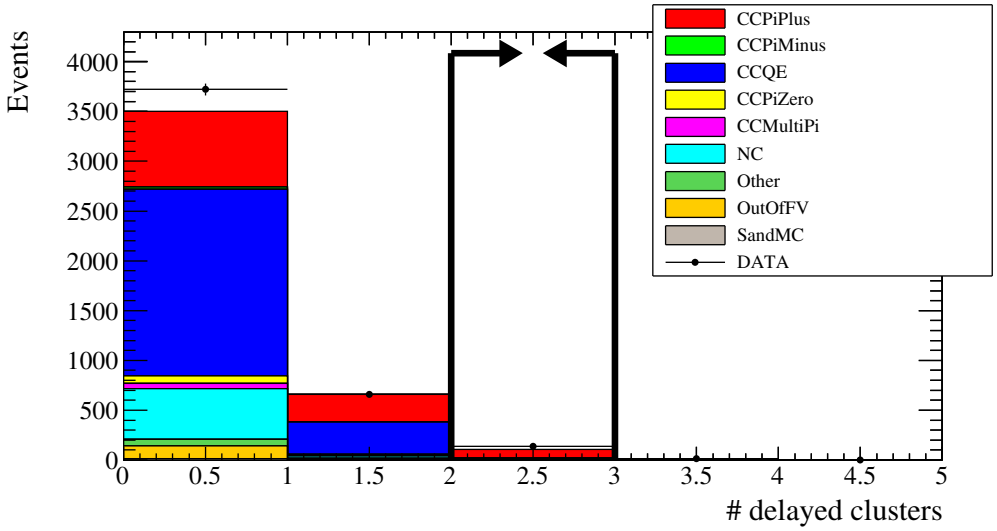

FIGURE 4.54. Selection Two: the number of Michel electron clusters in event before the last cut for the water-in data and MC. Events with exactly two Michel clusters are accepted.

by NEUT MC, ϵ and p are the efficiency and purity of the event selections.

The overall selection efficiency is low - 6 - 7%. The low efficiency is caused by two main issues. First, one should stress that only the topology with two particles in the final state is selected. From Figures 4.11 and 4.12 and Tables 4.6, 4.7, 4.8, and 4.9 it is clear that approximately 55% (water-out) to 58% (water-in) of CC1π^+ interactions are rejected by

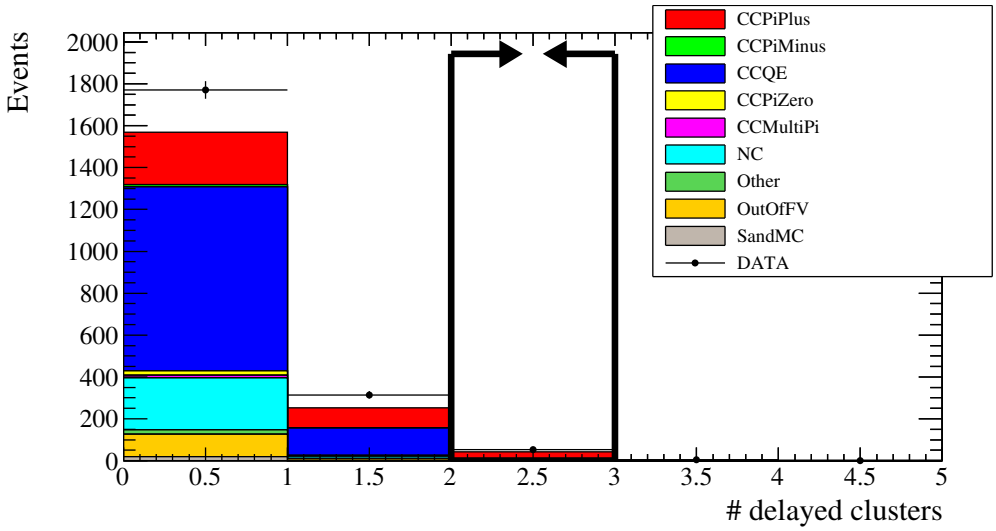

FIGURE 4.55. Selection Two: the number of Michel electron clusters in event before the last cut for the water-out data and MC. Events with exactly two Michel clusters are accepted.

TABLE 4.6. Data reduction and cut progression table for water-in-based Selection One (non-contained). MC numbers are scaled to data POT.

Cut	N_{data}	N_{NEUTMC}	ϵ (%)	p (%)
1 PØD vtx	1,398,171	656,888	98.95	2.60
3-D vtx	1,261,949	553,827	95.33	2.98
PØD fv	151,882	137,539	86.68	10.90
2 part.	35,278	32,298	36.46	19.52
2 3d part.	31,828	28,997	34.45	20.54
1 TPC-exiting part.	9,355	8,367	12.67	26.17
2 tracks	9,355	8,367	12.67	26.17
Pion cand. cont.	7,572	6,744	10.14	26.01
Vtx dist.	4,541	3,888	7.17	31.87
dE/dx & Michel	1,543	1,413	4.30	52.58

requiring exactly two particles in the event. Events which are rejected are from the "one particle" and "more than two particles" topology bins. Recovering those interactions would require defining additional selections also yielding additional systematic errors. It's certainly one of the future possible improvements which could be made to improve this analysis.

TABLE 4.7. Data reduction and cut progression table for CC1π^+ analysis for water-out-based Selection One (non-contained). MC numbers are scaled to data POT.

Cut	N_{data}	N_{NEUTMC}	ϵ (%)	p (%)
1 PØD vtx	1,872,903	850,894	99.68	1.79
3-D vtx	1,696,281	715,752	97.56	2.08
PØD fv	161,637	143,970	86.60	9.20
2 part.	39,892	36,129	39.19	16.59
2 3d part.	35,870	32,583	37.32	17.52
1 TPC-exiting part.	10,160	9025	14.35	24.31
2 tracks	10,160	9,025	14.35	24.31
Pion cand. cont.	7,887	7,134	11.16	23.83
Vtx dist.	4,768	4,130	7.31	27.07
dE/dx & Michel	1,367	1,217	4.36	54.81

TABLE 4.8. Data reduction and cut progression table for CC1π^+ analysis for water-in-based Selection Two (contained). MC numbers are scaled to data POT.

Cut	N_{data}	N_{NEUTMC}	ϵ (%)	p (%)
1 PØD vtx	1,398,171	656,888	98.95	2.60
3D vtx	126,1949	553,827	95.33	2.98
PØD fv	151,882	137,539	86.68	10.90
2 part.	35,278	32,298	36.46	19.52
2 3d part.	31,828	28,997	34.45	20.54
2 tracks	31,828	28,997	34.45	20.54
1st trk cont.	19,660	17,801	20.09	19.52
2nd trk cont.	11,501	10,460	10.64	17.59
Vtx dist.	4,528	3,904	5.99	26.51
dE/dx & Michel	1,160	1,042	2.91	48.37

In the one particle topology pions have low energy and therefore do not leave any tracks or showers in the detector. However some of the pions decay and produce Michel clusters.

TABLE 4.9. Data reduction and cut progression table for CC1π^+ analysis for water-out-based Selection Two (contained). MC numbers are scaled to data POT.

Cut	N_{data}	N_{NEUTMC}	ϵ (%)	p (%)
1 PØD vtx	1,872,903	850,894	99.68	1.79
3D vtx	1,696,281	715,752	97.55	2.08
PØD fv	161,637	143,970	86.60	9.20
2 part.	39,892	36,129	39.19	16.59
2 3d part.	35,870	32,583	37.32	17.52
2 tracks	35,870	32,583	37.32	17.52
1st trk cont.	21,013	19,046	20.40	16.38
2nd trk cont. 11,658	10,385	10.21	15.04	
Vtx dist.	4,542	3,551	4.81	20.70
dE/dx & Michel	820	684	1.97	44.15

TABLE 4.10. Summary of event selection for both sub-selections.

	N_{data}	B_{NEUTMC}	B_{sand}	ϵ (%)	p (%)
water-in	2,703	1,208	2.5	7.21	50.79
water-out	2,187	932	3.9	6.33	50.97

Looking at the number of Michel clusters can give some discrimination power against the main background, which in this analysis is the CCQE interactions. This possibility was investigated within the framework of this analysis yielding a low purity CC1π^+ sample, but there might be some reconstruction improvements and tuning that can help in the future. The main reason for CC1π^+ interactions ending in the more-than-two particles topology are pion reinteractions in the detector, and ejected protons. One can think of methods of selecting those events, however at higher track multiplicity the large CC multi-π background is a problem in this analysis.

A second issue is that the topologies where the particles exit through the sides of the PØD are missing from the selection. It would be an improvement to the analysis to expand the selection to include such events, but it would also require a lot of work to evaluate the associated systematic effects.

Analyzing Tables 4.6, 4.7, 4.8, and 4.9, one can notice that 10% - 11% of CC1π^+ events in Selection One after the pion candidate track containment cut and 10% - 11% in Selection Two after the second track containment cut are selected. This is equivalent to selecting $\sim$10% of events in the topology with one track TPC1-entering and second track contained, and another 10% events in the topology with both tracks contained. After summing up the numbers, 20% of CC1π^+ events are accepted into the intermediate selection after the containment cuts. Comparing this to the efficiency of 34% - 37% in 2 tracks topology (after the two-tracks cut, but before the containment cuts), one can see that there are 10% - 17% events to recover. To solve this issue one should also define and build additional event selections and investigate the properties of side-exiting particles. It would go on the list of future improvements of this analysis as well.

After combining both selections together one can check the region of the phase space that is the probed with the sample after cuts. The efficiency of the selection as a function of muon candidate MC-truth kinematic properties (momentum and angle with respect to the z axis) and pion candidate MC-truth kinematic properties is shown in Figures 4.56, 4.57, 4.58, and 4.59.

Figures 4.56 and 4.57 illustrates the fact that events with a wide range of muon momenta (even below 100 MeV) and angle are selected. The selection is sampling the pion momentum range from 150 MeV to approximately 1 GeV, which can be seen in Figures 4.58 and 4.59.

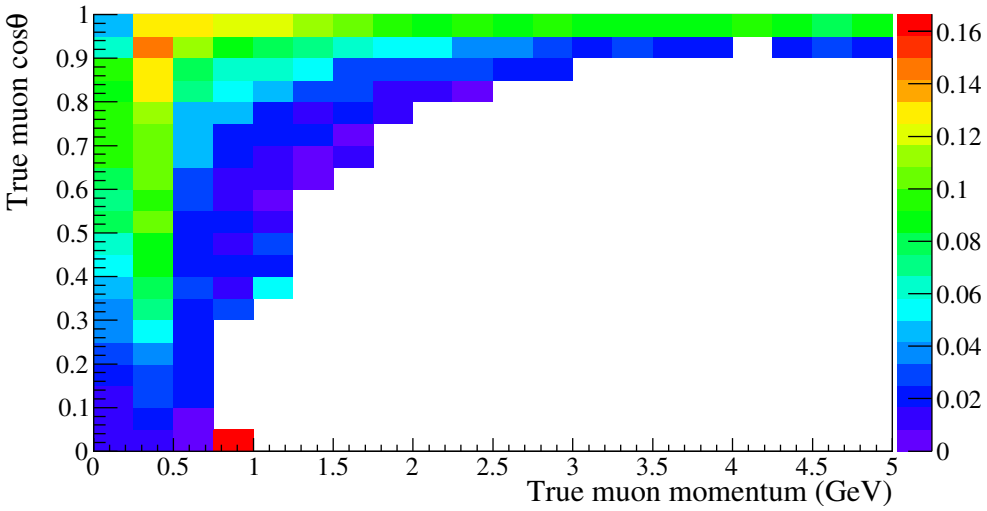

FIGURE 4.56. Overall efficiency of both selections combined as a function of the NEUT MC-truth muon momentum and cos(θ) for the water-in NEUT MC.

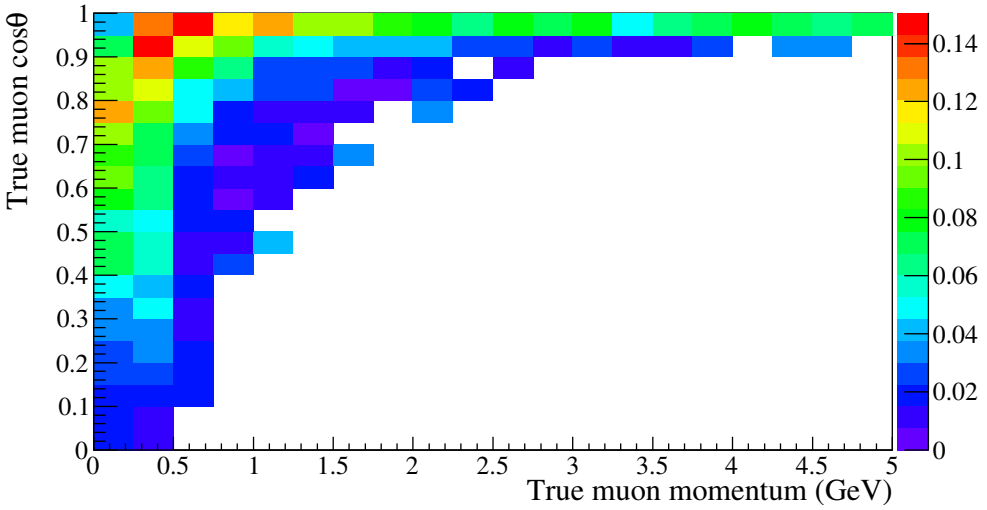

FIGURE 4.57. Overall efficiency of both selections combined as a function of the NEUT MC-truth muon momentum and cos(θ) for the water-out NEUT MC.

The selection efficiency as a function of MC-truth neutrino energy is shown in Figures 4.60 and 4.61. The efficiency of the selection, as one could expect, is low for low neutrino energies and becomes flat above ~800 MeV.

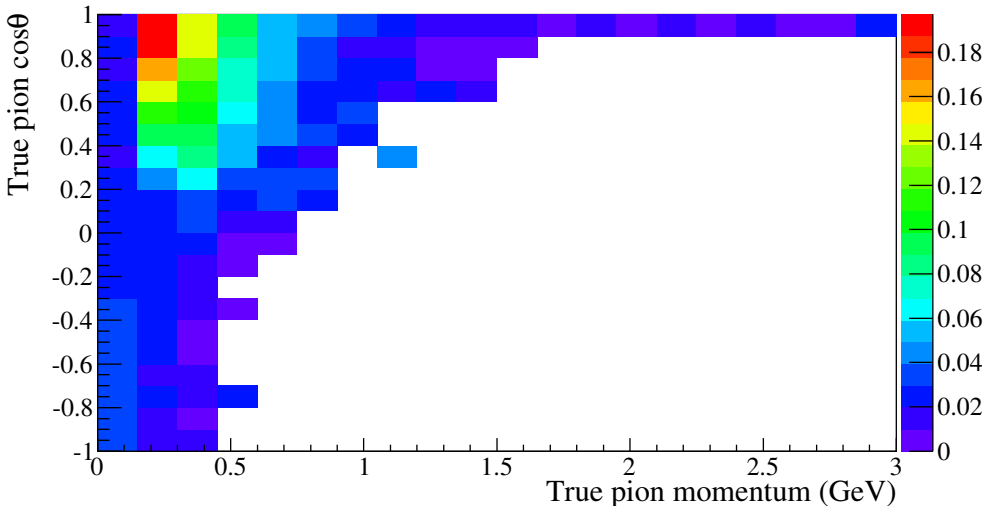

FIGURE 4.58. Overall efficiency of both selections combined as a function of the NEUT MC-truth pion momentum and cos(θ) for the water-in NEUT MC.

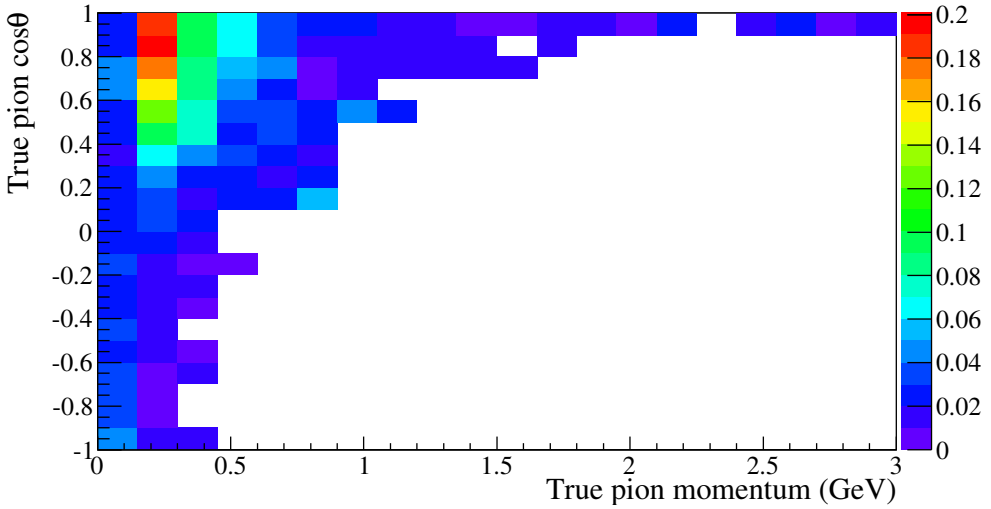

FIGURE 4.59. Overall efficiency of both selections combined as a function of the NEUT MC-truth pion momentum and cos(θ) for the water-out NEUT MC.

4.2.4. MC CORRECTIONS. During the course of this analysis several aspects of the MC simulation were identified as either lacking or wrong, which renders the simulation partially incorrect (by $\sim$ 1-3%) and requires the use of MC corrections. The MC corrections that are described here are related to MC fiducial mass and MC Out-of-Fiducial (OOF) background, e.g. sand muons. The detector fiducial mass is described in more detail in Section 4.3.3.

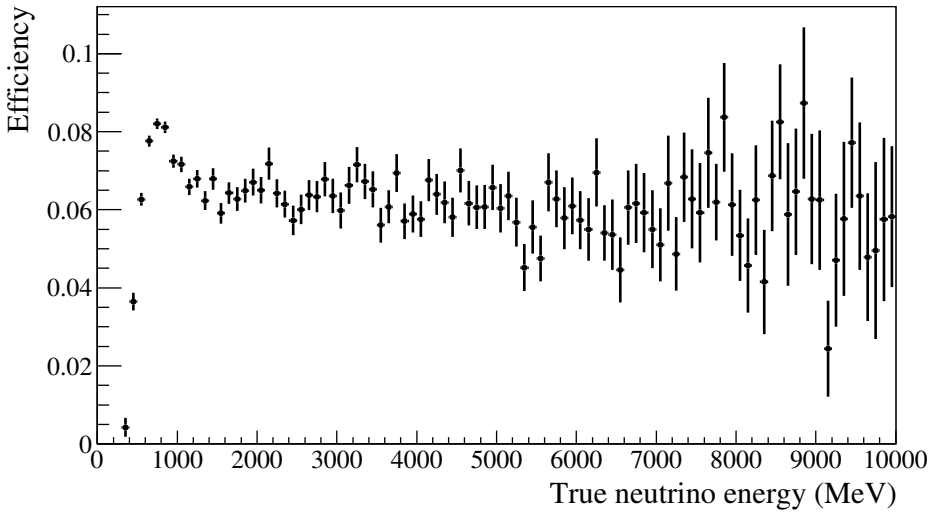

FIGURE 4.60. Overall efficiency of both selections combined as a function of MC-truth neutrino energy for the water-in NEUT MC.

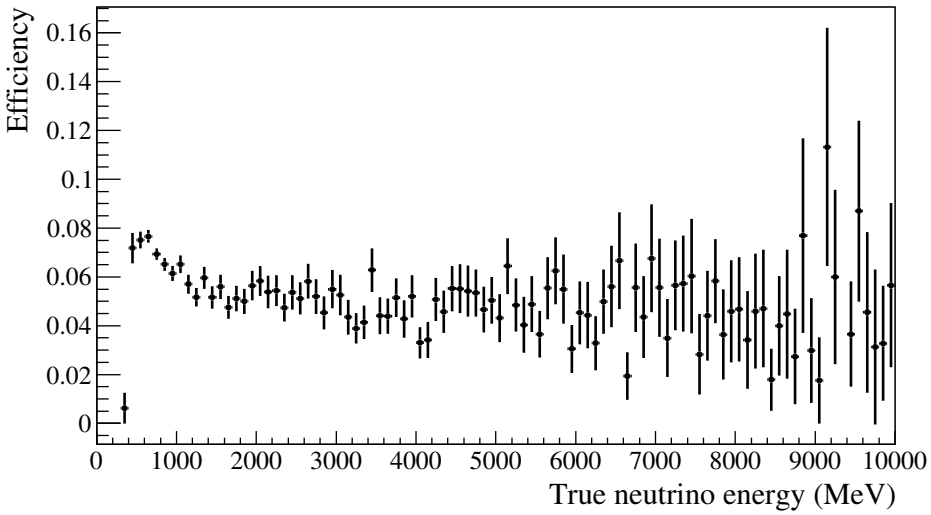

FIGURE 4.61. Overall efficiency of both selections combined as a function of MC-truth neutrino energy for the water-out NEUT MC.

Uncertainty associated with the detector mass is discused in Section 4.6.6.1. OOF background is discussed in Section 4.3.1. Systematic uncertainties associated with the OOF background are described in Section 4.6.6.2.

4.2.4.1. *PØD Fiducial Mass.* Due to a bug in Monte Carlo geometry used in MC Production 5, the MC fiducial mass of the PØD was different from the actual detector mass as

shown in Section 4.3.3. The small difference was accounted for by simple scaling correction factors shown in Table 4.11, which were adopted from the technical study dedicated to the PØD geometry and mass (T2K internal document [138]).

TABLE 4.11. Multiplicative mass correction factors C^{mass} (calculated as data/MC PØD fiducial mass ratios) used to rescale the Monte Carlo predictions [138].

Run	PØD Status	Correction Factor
1	water-in	1.013
2-4	water-in	1.016
2-4	water-out	1.031

4.2.4.2. *Interference of Sand Muons and Events in ND280.* In Production 5, sand muons (neutrino interactions in the sand surrounding ND280 near detector pit) and interactions in ND280 proper were simulated separately. Therefore, two separate Monte Carlo samples were used in this analysis:

(1) magnet MC (interactions occurring within the ND280 magnet area);

(2) sand MC (interactions outside the ND280, but detected in ND280).

One should stress that in this way the effects of the pileup, or interference, of interactions in ND280, and sand muons were not simulated. One example of such pile-up would be a sand-muon entering the front face of the PØD and interfering with a PØD neutrino interaction. Another example would be the out-of-PØD background coming from the magnet interactions induced by sand-muons. To account for this effect, an external study done for PØD-TPC CC-inclusive analysis described in T2K document [140] was utilized.

In that study, data and MC high purity CC inclusive samples were compared, i.e. a selection was geared towards selecting CC events in the PØD with an ability to tag additional through-going sand muons penetrating the PØD, either from the front or the sides. MC

correction factors were defined as data to MC event rate double ratios: a data to MC ratio of ratios of numbers of selected events before the sand-muon-veto cut and after the sand-muon-veto cut.

Because of this sand-muon interference effect, both selected signal and background numbers of events would be reduced, i.e. rejected by the fiducial volume cut. These double ratios were used as a weights to scale both the Monte Carlo background and signal selection efficiency predictions. The sand-muon interference corrections used in this analysis are listed in Table 4.12.

TABLE 4.12. Multiplicative sand muons interference correction factors C^{sp} used to scale the Monte Carlo predictions [140].

Run	PØD Status	MC Correction
1	water-in	0.988
2	water-in	0.980
2	water-out	0.978
3	water-out	0.975
4	water-in	0.972
4	water-out	0.968

4.2.4.3. *Sand Muon Background.* The sand muon MC is simulated separately from the ND280 magnet interactions and comes as a separate set of simulation files. A small number of sand muons make it past the strict analysis cuts (few sand-muon induced interactions in the magnet enter the PØD from the sides) from these files, however the rate of sand muons in data and MC is not exactly the same. To obtain the correct rate of sand muons that enter the selection as background, external studies performed by Justyna Lagoda for the ND280 tracker CC analysis were used [137]. She selected a sample of sand muons through going the PØD with a set of simple cuts. The study showed that data/MC ratio for sand muons is

1.084 ± 0.002 . This ratio was used as a correction (C^{sb}) for the Monte Carlo sand muon background prediction.

4.2.5. Data vs MC Comparison Figures. The figures in this section show the comparisons of the kinematic variables for data and NEUT MC for both selections: Selection One and Selection Two. Monte Carlo is always normalized to corresponding data POT with flux tuning 11b v3.2 and all corrections applied, unless otherwise stated.

Figures 4.62 and 4.63 show disagreement between the data and MC in the shape of the muon candidate track length for the non-contained Selection One, but the distributions are consistent within the uncertainties. Strange shape of the data distribution could be attributed to statistical fluctutations, or some unknown systematic effect, not modeled in MC.

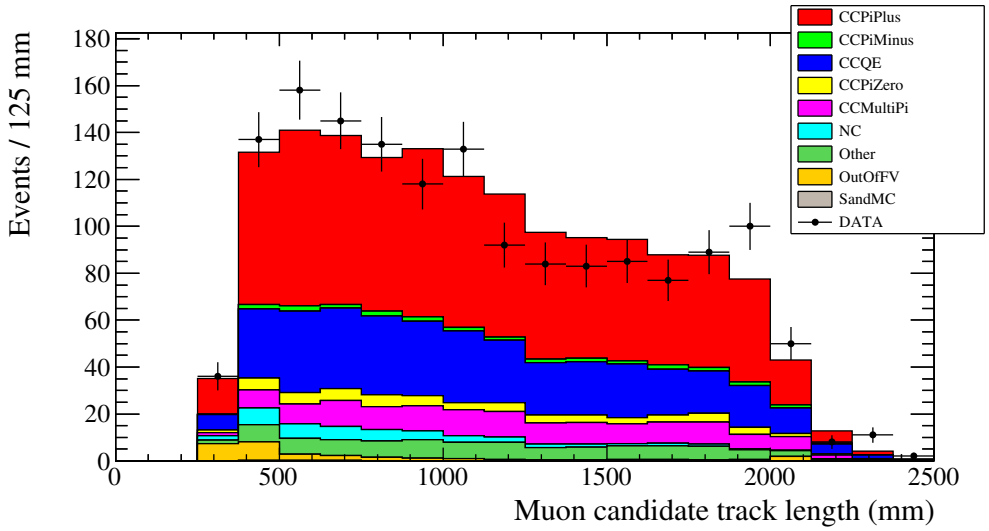

Figure 4.62. Muon candidate track reconstructed length for the Selection One, non-contained selection, for the water-in data and MC. Uncertainties shown for data are purely statistical.

There is relatively good agreement between data and MC in the $\cos(\theta)$ of the muon candidate track in Selection One, which can be seen from Figures 4.64 and 4.65. However, it can also be said that MC oversimulates the number of muons in the forward going direction, which is consistent with the hypothesis that the coherent pion production model in NEUT is

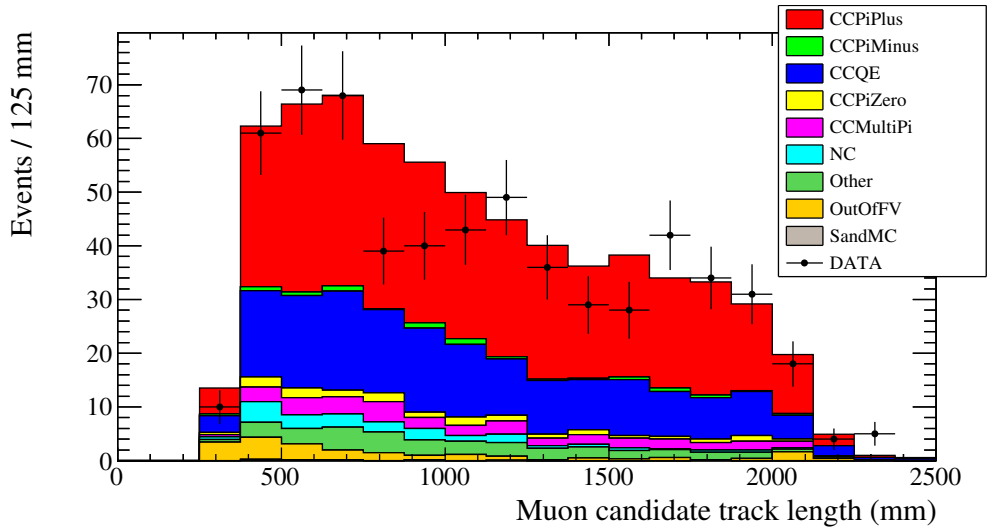

FIGURE 4.63. Muon candidate track reconstructed length for the Selection One, non-contained selection, for the water-out data and MC. Uncertainties shown for data are purely statistical.

wrong, i.e. it overestimates the coherent pion production cross section. The poor modeling of coherent pion production in the NEUT simulation (software version corresponding to RDP5G and MCP5E files) was independently confirmed in several other ND280 cross section analyses.

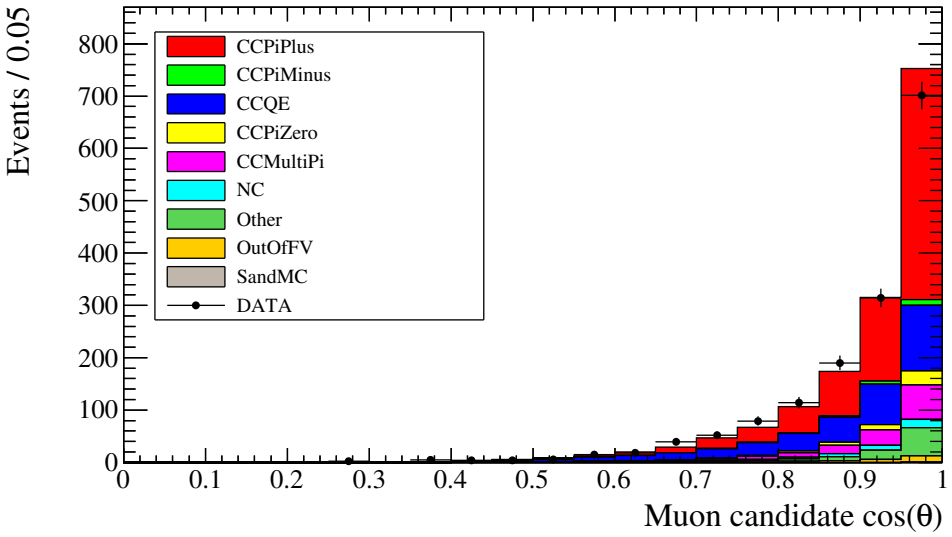

FIGURE 4.64. Muon candidate track reconstructed cos(θ) for the Selection One, non-contained selection, for the water-in data and MC. Uncertainties shown for data are purely statistical.

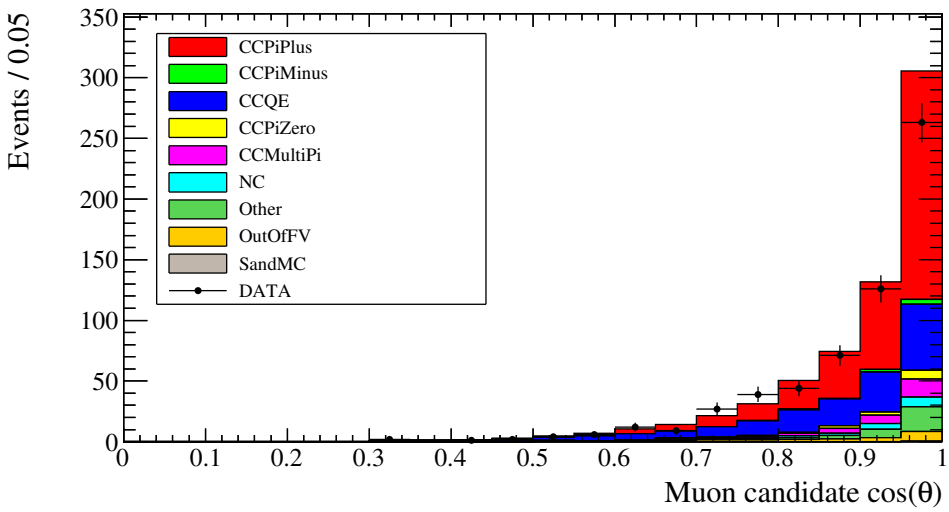

FIGURE 4.65. Muon candidate track reconstructed cos(θ) for the Selection One, non-contained selection, for the water-out data and MC. Uncertainties shown for data are purely statistical.

Figures 4.66 and 4.67 show the pion candidate track length distribution for Selection One.

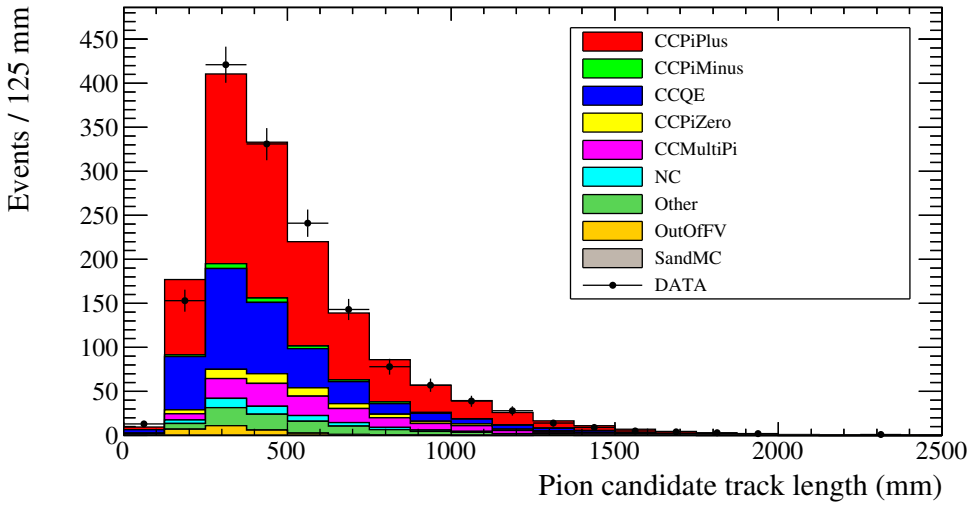

FIGURE 4.66. Pion candidate track reconstructed length for the Selection One, non-contained selection, for the water-in data and MC. Uncertainties shown for data are purely statistical.

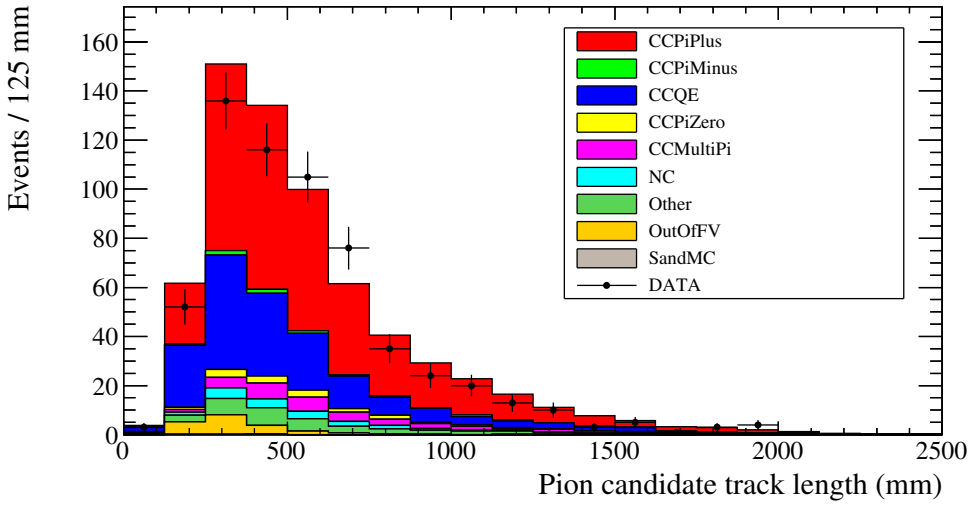

FIGURE 4.67. Pion candidate track reconstructed length for the Selection One, non-contained selection, for the water-out data and MC. Uncertainties shown for data are purely statistical.

Figures 4.68 and 4.69 show the pion candidate track cos(θ) distributions for Selection One, where some data-MC disagreement can be seen.

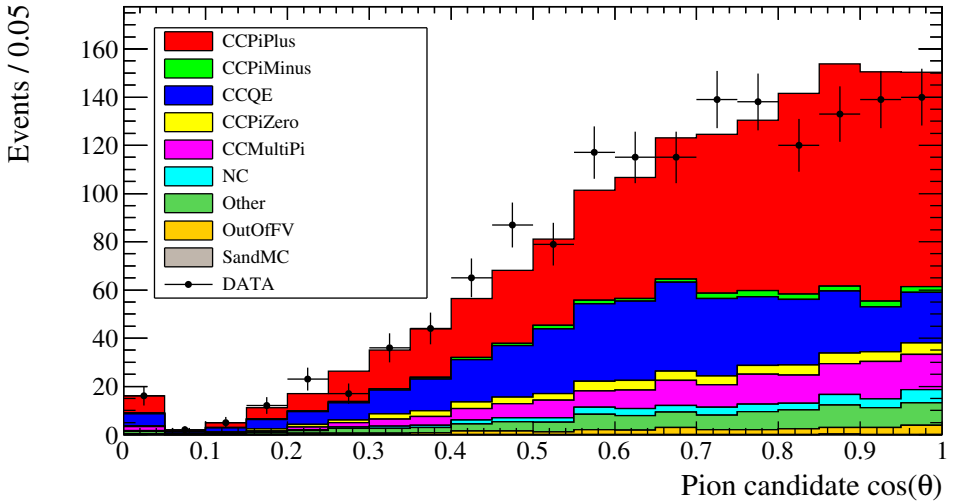

FIGURE 4.68. Pion candidate track reconstructed cos(θ) for the Selection One, non-contained selection, for the water-in data and MC. Uncertainties shown for data are purely statistical.

Figures 4.70, 4.71, 4.72, 4.73, 4.74, 4.75, 4.76, and 4.77 show kinematic distributions for Selection Two described in Section 4.2.2.3.

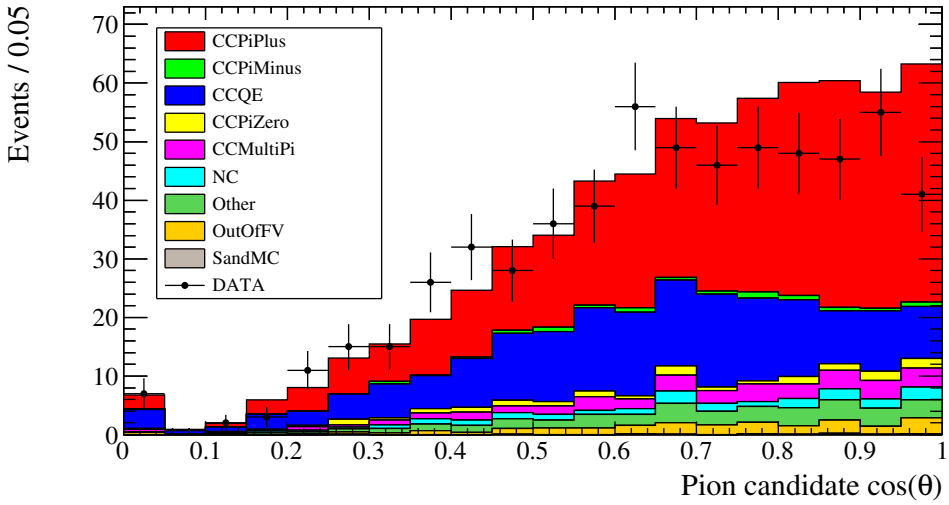

FIGURE 4.69. Pion candidate track reconstructed cos(θ) for the Selection One, non-contained selection, for the water-out data and MC. Uncertainties shown for data are purely statistical.

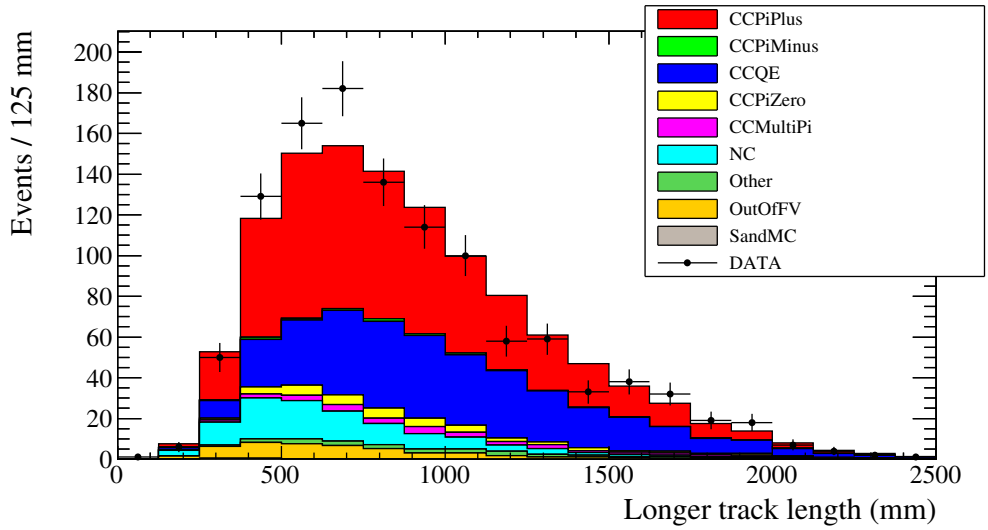

FIGURE 4.70. Reconstructed length of the longer track for Selection Two, the contained selection, for the water-in data and MC.

In summary, it can be noted that there is certainly a difference in shape of several data and MC distributions. However, taking into account the full range of uncertainties of the measurement, one can tell that there is an overall agreement between data and Monte Carlo. In order to make any definite conclusions based on the difference of data and MC shapes, the measurement uncertainties need to be reduced.

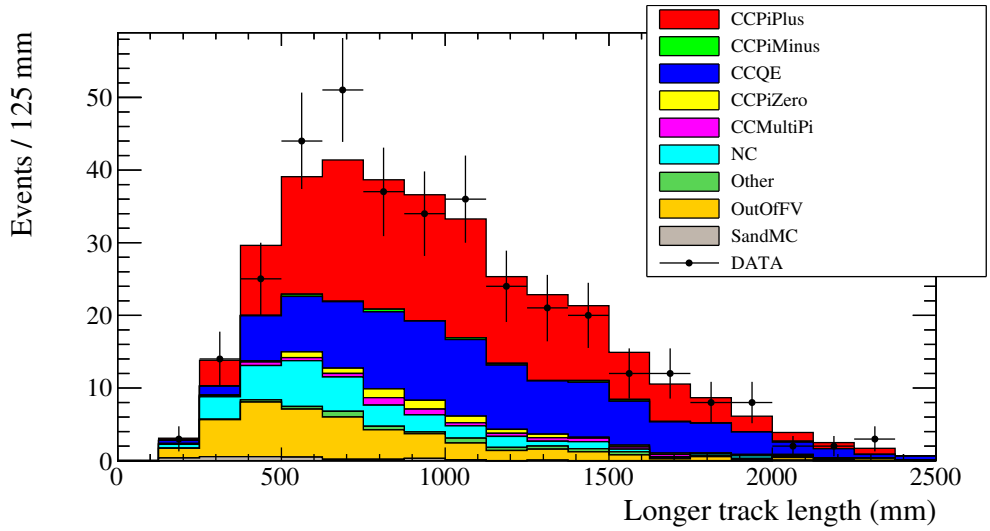

FIGURE 4.71. Reconstructed length of the longer track for Selection Two, the contained selection, for the water-out data and MC.

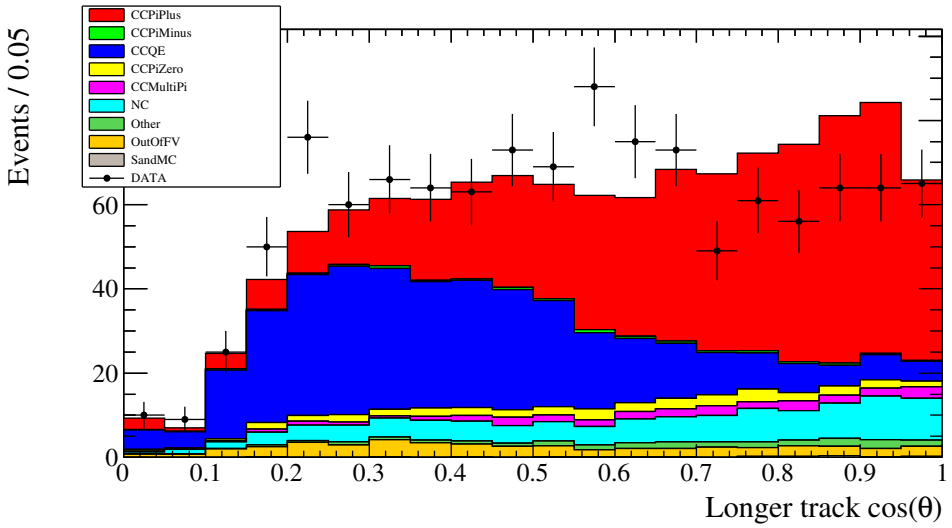

FIGURE 4.72. Reconstructed $\cos(\theta)$ of the longer track for Selection Two, the contained selection, for the water-in data and MC.

4.3. CC1π^+ Flux-integrated Cross Section on Water

For a beam of neutrinos incident on a target the true number of signal interactions, s, is generally a function of incident neutrino flux, $\Phi(E_\nu)$ $\left[\frac{\nu_\mu}{cm^2}\right]$, the signal cross section $\sigma(E_\nu)$,

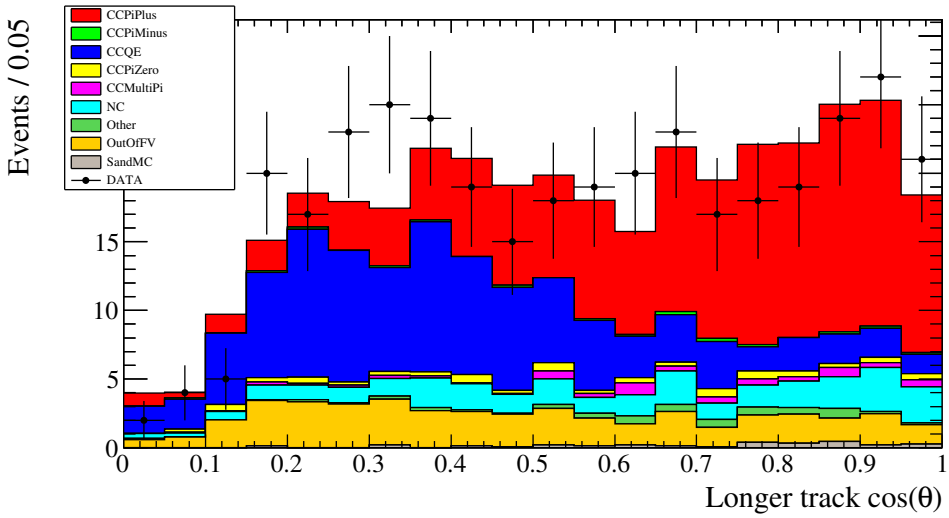

FIGURE 4.73. Reconstructed $\cos(\theta)$ of the longer track for Selection Two, the contained selection, for the water-out data and MC.

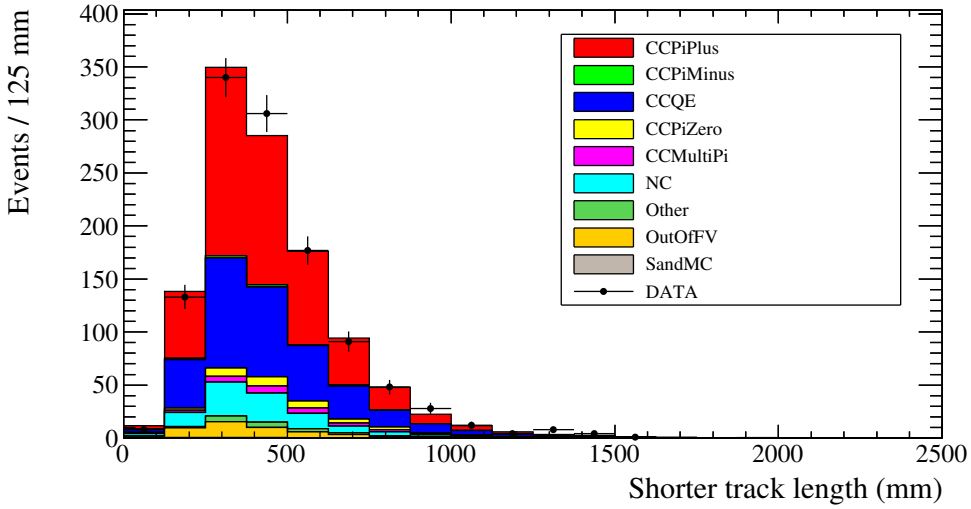

FIGURE 4.74. Reconstructed length of the shorter track for Selection Two, the contained selection, for the water-in data and MC.

and the number of interacting targets T, and is given by:

$$s = T \int \sigma(E_\nu) \frac{\partial \Phi(E_\nu)}{\partial E_\nu} dE_\nu, \tag{25}$$

where flux and cross section in general are functions of MC-truth neutrino energy E_ν. However, for the purposes of a single-bin measurement a flux-averaged cross section can be defined as

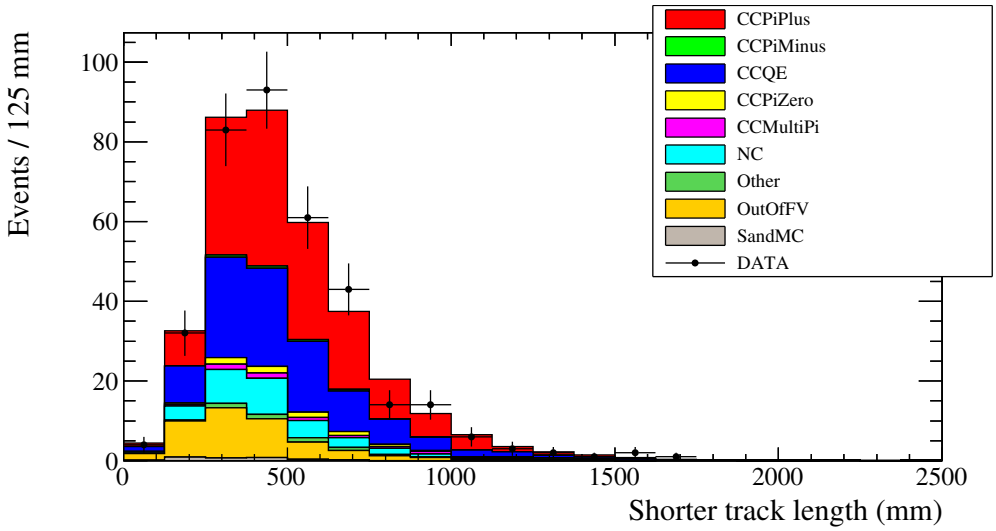

FIGURE 4.75. Reconstructed length of the shorter track for Selection Two, the contained selection, for the water-out data and MC.

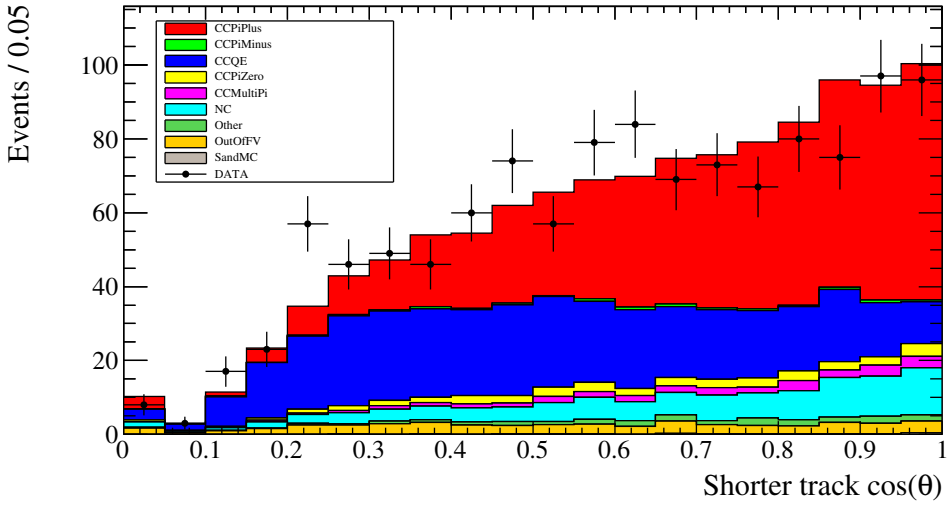

FIGURE 4.76. Reconstructed $\cos(\theta)$ of the shorter track for Selection Two, the contained selection, for the water-in data and MC.

a function of the total integrated flux Φ:

$$\langle \sigma_s \rangle = \frac{s}{T \cdot \Phi} = \frac{1}{\Phi} \cdot \int \sigma(E_\nu) \frac{\partial \Phi(E_\nu)}{\partial E_\nu} dE_\nu, \tag{26}$$

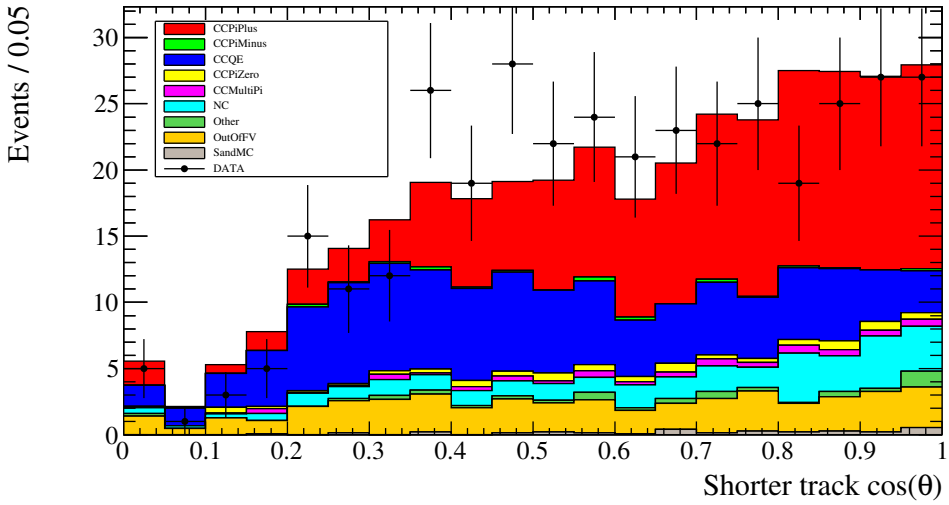

FIGURE 4.77. Reconstructed $\cos(\theta)$ of the shorter track for Selection Two, the contained selection, for the water-out data and MC.

so Equation 25 takes a simplified form:

$$s = T \cdot \langle \sigma_s \rangle \cdot \Phi, \tag{27}$$

where $\langle \sigma_s \rangle$ is the total flux-averaged signal cross section, T is the number of targets, e.g. molecules or nucleons, Φ is the total integrated neutrino flux (for a particular flavor corresponding to signal) incident into the volume containing the targets.

Thus, having measured s and given that T, Φ are also known, flux-averaged cross section $\langle \sigma_s \rangle$ can be trivially calculated. Here and throughout the document a distinction is made between s and S, where lower-case denotes total signal before any cuts, and upper-case denotes signal after analysis cuts.

4.3.1. Signal Extraction.

4.3.1.1. *Nominal MC Signal and Background Predictions.* The physics contributing to the signal after cuts is summarized in Tables 4.13 and 4.14 for water-in and water-out events respectively. It can be seen that for both the water-in and water-out samples ∼95% of the

TABLE 4.13. Fiducial ν_μ-induced post-FSI signal composition (in terms of before-FSI NEUT modes) for PØD water-in NEUT MCP5E sample after cuts for PØD both contained and non-contained selections combined. Percentages are calculated with respect to the total water-in signal in the fiducial volume. Rows are sorted in the order of decreasing percentage.

NEUT mode	Reaction	Fraction (%)
11	$\nu_\mu + p \to \mu^- + p + \pi^+$	53.25
16	$\nu_\mu + N \to \mu^- + N + \pi^+$	32.17
13	$\nu_\mu + n \to \mu^- + n + \pi^+$	9.14
21	$\nu_\mu + (n\|p) \to \mu^- + (n\|p) + \text{multi-}\pi$	2.53
1	$\nu_\mu + n \to \mu^- + p$	1.25
12	$\nu_\mu + n \to \mu^- + p + \pi^0$	1.05
26	$\nu_\mu + (n\|p) \to \mu^- + (n\|p) + \text{mesons}$	0.48
22	$\nu_\mu + n \to \mu^- + p + \eta^0$	0.13

signal events come from either resonant or coherent single charged pion production, with the remaining ∼5% of the signal coming from either before-FSI multiple or no pion production. Tables 4.15 and 4.16 show the background composition for events passing the cuts in terms of

TABLE 4.14. Fiducial ν_μ-induced post-FSI signal after-cut composition (in terms of the before-FSI NEUT modes) for PØD water-out NEUT MCP5E sample for both PØD contained and non-contained selections combined. Fractions are calculated with respect to the total water-out signal in the fiducial volume. Rows are sorted in the order of decreasing percetange.

NEUT Code	Reaction	Fraction (%)
11	$\nu_\mu + p \to \mu^- + p + \pi^+$	48.23
16	$\nu_\mu + N \to \mu^- + N + \pi^+$	36.87
13	$\nu_\mu + n \to \mu^- + n + \pi^+$	9.93
21	$\nu_\mu + (n\|p) \to \mu^- + (n\|p) + \text{multi-}\pi$	1.87
1	$\nu_\mu + n \to \mu^- + p$	1.32
12	$\nu_\mu + n \to \mu^- + p + \pi^0$	1.25
26	$\nu_\mu + (n\|p) \to \mu^- + (n\|p) + \text{mesons}$	0.50
22	$\nu_\mu + n \to \mu^- + p + \eta^0$	0.02

different neutrino flux contributions where in can be seen that most of the fiducial background comes from ν_μ-induced events.

The out-of-fiducial (OOF) background is also dominated by ν_μ which can be seen in Table 4.16. All of the backgrounds shown in Tables 4.15 and 4.16 are subject to the flux normalization uncertainty, which is described in Section 4.6.1 of this dissertation. The OOF background percentages are different for the water-in and water-out samples, however a consistent treatment of associated systematic uncertainties accounts for the difference through the OOF volume background systematic uncertainty evaluation. A more detailed

TABLE 4.15. Background composition in terms of neutrino flavors and fiducial/out-of-fiducial categories for Run 4 water-in and Run 3 water-out events after cuts. The numbers are for both contained and non-contained selections combined.

	Water-in	Water-out
Background type	Fraction (%)	Fraction (%)
Fiducial ν_μ	86.51	78.61
Fiducial $\overline{\nu}_\mu$	6.12	6.70
Fiducial ν_e	1.40	1.31
Fiducial $\overline{\nu}_e$	0.1	0.17
Out-of-fiducial	5.87	13.21

TABLE 4.16. OOF background composition in terms of neutrino flavors. Fractions are calculated with respect to the total OOF background number of events after the selections cuts, for Run 4 PØD water-in and Run 3 water-out running.

	Water-in	Water-out
OOF Background	Fraction (%)	Fraction (%)
ν_μ	95.44	94.08
non-ν_μ	4.56	5.92

ν_μ and $\overline{\nu}_\mu$ fiducial background composition is shown in Tables 4.17, 4.18, 4.19 and 4.20.

Non-ν_μ-induced backgrounds for the water-in and for the water-out samples are described in Appendix A. However, signal and background numbers of events in data and MC are not necessarily the same,

$$S^{MC} = S^{data} + \delta S, \qquad B^{MC} = B^{data} + \delta B, \tag{28}$$

where δS and δB are the discrepancies between data and MC for signal and background respectively. This could be due to statistical uncertainties, new physics or other reasons (e.g systematic bias, a bug in the MC simulation, or systematic uncertainties in the physics models). Statistical and systematic uncertainties relevant to this analysis are discussed in detail in Sections 4.5 and 4.6. MC corrections that are utilized in this analysis are discussed in Section 4.2.4.

4.3.1.2. *Background Subtraction.* The background prediction from MC, B^{MC} or simply B, with assigned statistical and systematic uncertainties, can be used to remove the background from the data, i.e. via background subtraction, and extract the sought-after signal. The total background is comprised of nominal MC background and sand muon MC background.

In this analysis, $S^{data}_{w|a,\ i}$, the number of selected signal events for T2K Run data set i, can be extracted via background subtraction, where correction factors are applied to the backgrounds:

$$S^{data}_{w|a,\ i} = N^{data}_{w|a,\ i} - C^{mass}_{w|a,\ i} C^{sp}_{w|a,\ i} B_{w|a,\ i} - C^{sb}_{w|a,\ i} B^{sand}_{w|a,\ i}, \tag{29}$$

The lower indices w and a stand for water-in and air-in (water-out) samples accordingly, $C^{mass}_{w|a,\ i}$ and $C^{sp}_{w|a,\ i}$ are MC detector fiducial mass correction and MC sand muon pile-up/interference correction correspondingly, $C^{sb}_{w|a,\ i}$ is the sand muon background normalization correction.

TABLE 4.17. Fiducial ν_μ-induced post-FSI background after cuts composition (in terms of before-FSI NEUT modes) for PØD water-in NEUT MCP5E sample for both contained and non-contained selections combined. Fractions are calculated with respect to the total water-in background. Rows are sorted in the order of decreasing percentage.

NEUT mode	Reaction	Fraction (%)
1	$\nu_\mu + n \to \mu^- + p$	38.62
11	$\nu_\mu + p \to \mu^- + p + \pi^+$	13.74
12	$\nu_\mu + n \to \mu^- + p + \pi^0$	6.99
13	$\nu_\mu + n \to \mu^- + n + \pi^+$	4.06
17	$\nu_\mu + n \to \mu^- + p + \gamma$	0.05
21	$\nu_\mu + (n\|p) \to \mu^- + (n\|p) + \text{multi-}\pi$	10.85
22	$\nu_\mu + n \to \mu^- + p + \eta^0$	0.90
23	$\nu_\mu + n \to \mu^- + \Lambda + K^+$	0.12
26	$\nu_\mu + (n\|p) \to \mu^- + (n\|p) + \text{mesons}$	1.07
31	$\nu_\mu + n \to \nu_\mu + n + \pi^0$	1.10
32	$\nu_\mu + p \to \nu_\mu + p + \pi^0$	1.67
33	$\nu_\mu + n \to \nu_\mu + p + \pi^-$	1.05
34	$\nu_\mu + p \to \nu_\mu + n + \pi^+$	0.54
36	$\nu_\mu + N \to \nu_\mu + N + \pi^0$	1.72
38	$\nu_\mu + n \to \nu_\mu + n + \gamma$	0.01
39	$\nu_\mu + p \to \nu_\mu + p + \gamma$	0.02
41	$\nu_\mu + (n\|p) \to \nu_\mu + (n\|p) + \text{multi-}\pi$	2.36
42	$\nu_\mu + n \to \nu_\mu + n + \eta^0$	0.17
43	$\nu_\mu + p \to \nu_\mu + p + \eta^0$	0.18
44	$\nu_\mu + n \to \nu_\mu + \Lambda + K^0$	0.05
45	$\nu_\mu + p \to \nu_\mu + \Lambda + K^+$	0.04
46	$\nu_\mu + (n\|p) \to \nu_\mu + (n\|p) + \text{mesons}$	0.80

The MC background predictions have large uncertainties that are propagated to the result. These uncertainties can be reduced by constraining the MC background predictions with

TABLE 4.18. Fiducial $\overline{\nu}_\mu$-induced background composition for PØD water-in MC sample for both contained and non-contained selections combined. Fractions are calculated with respect to the total water-in background.

NEUT Code	Reaction	Fraction (%)
-46	$\overline{\nu}_\mu + (n\|p) \rightarrow \overline{\nu}_\mu + (n\|p) + \text{mesons}$	0.05
-43	$\overline{\nu}_\mu + p \rightarrow \overline{\nu}_\mu + p + \eta^0$	0.01
-41	$\overline{\nu}_\mu + (n\|p) \rightarrow \overline{\nu}_\mu + (n\|p) + \text{multi-}\pi$	0.12
-36	$\overline{\nu}_\mu + N \rightarrow \overline{\nu}_\mu + N + \pi^0$	0.11
-34	$\overline{\nu}_\mu + p \rightarrow \overline{\nu}_\mu + n + \pi^+$	0.03
-33	$\overline{\nu}_\mu + n \rightarrow \overline{\nu}_\mu + p + \pi^-$	0.04
-32	$\overline{\nu}_\mu + p \rightarrow \overline{\nu}_\mu + p + \pi^0$	0.04
-31	$\overline{\nu}_\mu + n \rightarrow \overline{\nu}_\mu + n + \pi^0$	0.06
-26	$\overline{\nu}_\mu + (n\|p) \rightarrow \mu^+ + (n\|p) + \text{mesons}$	0.02
-23	$\overline{\nu}_\mu + p \rightarrow \mu^+ + \Lambda + K^0$	0.01
-22	$\overline{\nu}_\mu + p \rightarrow \mu^+ + n + \eta^0$	0.06
-21	$\overline{\nu}_\mu + (n\|p) \rightarrow \mu^+ + (n\|p) + \text{multi-}\pi$	0.54
-16	$\overline{\nu}_\mu + N \rightarrow \mu^+ + N + \pi^-$	2.07
-13	$\overline{\nu}_\mu + p \rightarrow \mu^+ + p + \pi^-$	0.74
-12	$\overline{\nu}_\mu + p \rightarrow \mu^+ + n + \pi^0$	0.35
-11	$\overline{\nu}_\mu + n \rightarrow \mu^+ + n + \pi^-$	1.46
-1	$\overline{\nu}_\mu + p \rightarrow \mu^+ + n$	0.39

data, however this was not employed in the current version of the analysis, is outside the scope of this analysis, and is discussed in Section 5.2.

4.3.1.3. *Signal Selection Efficiency.* In order to extract the total number of signal events in the data, the selected number of signal events S^{data} needs to be corrected for the selection efficiency, i.e signal events that did not pass the selection cuts need to be recovered.

TABLE 4.19. Fiducial ν_μ-induced post-FSI background after cuts composition (in terms of before-FSI NEUT modes) for PØD water-out MC sample for both contained and non-contained selections combined. Fractions are calculated with respect to the total water-out background.

NEUT mode	Reaction	Fraction (%)
1	$\nu_\mu + n \to \mu^- + p$	40.93
11	$\nu_\mu + p \to \mu^- + p + \pi^+$	11.59
12	$\nu_\mu + n \to \mu^- + p + \pi^0$	5.68
13	$\nu_\mu + n \to \mu^- + n + \pi^+$	3.93
21	$\nu_\mu + (n\|p) \to \mu^- + (n\|p) + \text{multi-}\pi$	6.42
22	$\nu_\mu + n \to \mu^- + p + \eta^0$	0.27
23	$\nu_\mu + n \to \mu^- + \Lambda + K^+$	0.15
26	$\nu_\mu + (n\|p) \to \mu^- + (n\|p) + \text{mesons}$	0.57
31	$\nu_\mu + n \to \nu_\mu + n + \pi^0$	1.11
32	$\nu_\mu + p \to \nu_\mu + p + \pi^0$	1.26
33	$\nu_\mu + n \to \nu_\mu + p + \pi^-$	1.17
34	$\nu_\mu + p \to \nu_\mu + n + \pi^+$	0.61
36	$\nu_\mu + N \to \nu_\mu + N + \pi^0$	1.59
38	$\nu_\mu + n \to \nu_\mu + n + \gamma$	0.02
41	$\nu_\mu + (n\|p) \to \nu_\mu + (n\|p) + \text{multi-}\pi$	2.09
42	$\nu_\mu + n \to \nu_\mu + n + \eta^0$	0.03
43	$\nu_\mu + p \to \nu_\mu + p + \eta^0$	0.02
44	$\nu_\mu + n \to \nu_\mu + \Lambda + K^0$	0.09
45	$\nu_\mu + p \to \nu_\mu + \Lambda + K^+$	0.03
46	$\nu_\mu + (n\|p) \to \nu_\mu + (n\|p) + \text{mesons}$	0.55

The signal selection efficiency $\epsilon_{w|a}$ is predicted by MC and can be defined for water-in and air-in samples similarly:

$$\epsilon \equiv \epsilon^{MC} = \frac{S^{sel}}{S^{gen}}, \tag{30}$$

TABLE 4.20. Fiducial $\overline{\nu}_\mu$-induced background for PØD water-out MC sample for both contained and non-contained selections combined. Fractions are calculated with respect to the total water-out background.

NEUT mode	Reaction	Fraction (%)
-36	$\overline{\nu}_\mu + N \to \overline{\nu}_\mu + N + \pi^0$	0.17
-34	$\overline{\nu}_\mu + p \to \overline{\nu}_\mu + n + \pi^+$	0.02
-33	$\overline{\nu}_\mu + n \to \overline{\nu}_\mu + p + \pi^-$	0.07
-32	$\overline{\nu}_\mu + p \to \overline{\nu}_\mu + p + \pi^0$	0.06
-31	$\overline{\nu}_\mu + n \to \overline{\nu}_\mu + n + \pi^0$	0.02
-26	$\overline{\nu}_\mu + (n\|p) \to \mu^+ + (n\|p) + \text{mesons}$	0.04
-22	$\overline{\nu}_\mu + p \to \mu^+ + n + \eta^0$	0.09
-21	$\overline{\nu}_\mu + (n\|p) \to \mu^+ + (n\|p) + \text{multi-}\pi$	0.35
-16	$\overline{\nu}_\mu + N \to \mu^+ + N + \pi^-$	2.29
-13	$\overline{\nu}_\mu + p \to \mu^+ + p + \pi^-$	0.72
-12	$\overline{\nu}_\mu + p \to \mu^+ + n + \pi^0$	0.38
-11	$\overline{\nu}_\mu + n \to \mu^+ + n + \pi^-$	2.03
-1	$\overline{\nu}_\mu + p \to \mu^+ + n$	0.46

S^{sel} is the number of selected MC signal events, and s^{gen} is the total number of generated signal events in MC the PØD fiducial volume.

The efficiency of a selection is, in general, a function of MC-truth neutrino energy E_ν, since the number of selected events S^{sel} is a function of E_ν:

$$\epsilon(E_\nu) = \frac{S^{sel}(E_\nu)}{s^{gen}} \qquad \epsilon_i = \frac{S_i^{sel}}{s^{gen}}, \tag{31}$$

where i is the MC-truth neutrino energy bin index, S_i^{sel} is the number of selected signal events in the true neutrino energy bin i. This efficiency is a function of detector response, particle detection thresholds, and cuts used. In regions where the efficiency is zero, i.e. bins with no data events, a fully model dependent efficiency correction is utilized.

For the purposes of this one-bin analysis, ϵ, a single bin efficiency correction per T2K run, i, is employed:

$$\epsilon \equiv \langle \epsilon \rangle = \frac{1}{s^{gen}} \cdot \sum_i S_i^{sel}. \tag{32}$$

It is required to be corrected by C^{sand} in order to account for the sand interference effect present in the data, but not simulated in the MC. C^{sand} is a function of the T2K beam power, hence a function of T2K Run, and the reason why each Run must have it's own ϵ correction. The efficiency-corrected number of signal events per T2K Run, s^{data}, can be obtained via

$$s^{data} = \frac{S^{data}}{C^{sand} \cdot \epsilon}, \tag{33}$$

where S^{data} is the signal after cuts, resulting from Equation 29.

MC predictions for water-in and water-out signal selection efficiencies per Run are presented in Table 4.25. Statistical and systematic uncertainties on efficiencies are discussed in Sections 4.5 and 4.6 of this dissertation.

4.3.2. Flux. The T2K flux prediction, $\Phi(E_\nu)$, is based on a FLUKA and GEANT3 MC simulation, which uses the proton beam monitor data as an input. The simulated flux is tuned or reweighted to pion and kaon production data. The details of flux simulation and subsequent reweighting are discussed in depth in the T2K flux paper [114].

In general, there are 4 types of neutrinos contributing to the T2K flux at ND280, ν_μ, $\overline{\nu}_\mu$, ν_e, and $\overline{\nu}_e$, all of which can contribute to the measurement background, but only the ν_μ part of the flux contributes to the signal.

After the background subtraction and efficiency correction, the obtained number of CC1π^+ signal events, s^{data}, is a function of incident neutrino flux, $\Phi(E_\nu)$ $\left[\frac{\nu_\mu}{cm^2}\right]$, and the signal cross

section, $\sigma(E_\nu)$. The flux prediction is quantized into discrete bins of MC-truth neutrino energy, Φ_i, and the following relationships are employed:

$$\Phi = \int \frac{\partial \Phi(E_\nu)}{\partial E_\nu} dE_\nu \approx \sum_i \frac{\Delta \Phi_i}{\Delta E_i} \Delta E_i,$$

$$\int \sigma(E_\nu) \frac{\partial \Phi(E_\nu)}{\partial E_\nu} dE_\nu \approx \sum_i \sigma_i \frac{\Delta \Phi_i}{\Delta E_i} \Delta E_i, \tag{34}$$

and Equation 26 becomes:

$$\langle \sigma_s \rangle = \frac{s^{data}}{T \cdot \Phi} = \frac{1}{T \cdot \Phi} \cdot \sum_i \sigma_i \Delta \Phi_i, \tag{35}$$

where i is the MC-truth neutrino energy bin index, σ_i is the signal cross section average value for bin i, $\Delta\Phi_i$ is the incident flux in bin i, ΔE_i is the bin i width. More details about the actual cross section calculation follow in Sections 4.3.4 through 4.3.5.

Flux tuning 11b v3.2 is used to reweight the nominal ND280 MC [146]. The flux tuning event weights are shown in Figure 4.78.

The total tuned ν_μ flux prediction for PØD water-in running periods during T2K Runs 1, 2, and 4, scaled to the corresponding data POT is shown in Figure 4.79. The above-mentioned flux prediction comes with uncertainties that arise from many different sources including but not limited to hadron production, beam alignment, horn absolute current, etc. These sources and the sizes of corresponding uncertainties are discussed in depth in the T2K flux paper [114]. The propagation of flux uncertainty through this measurement is described in details in Section 4.6.1.

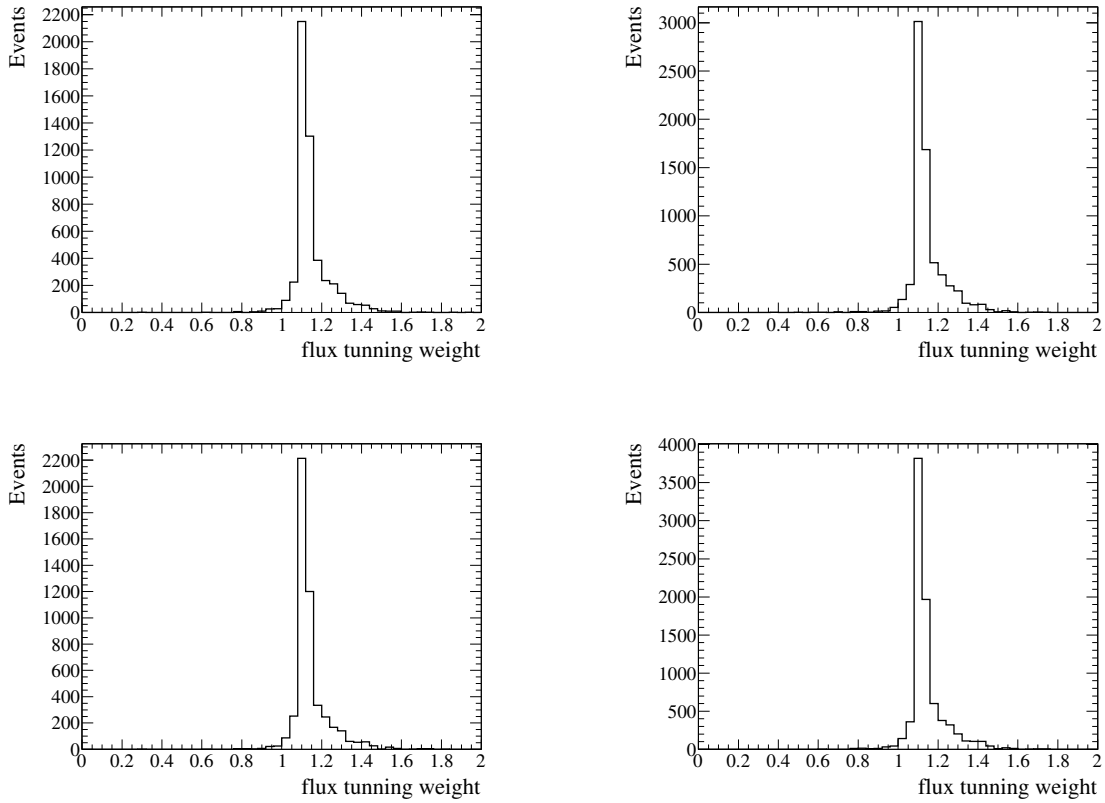

FIGURE 4.78. Flux tuning weights for events selected after cuts: Run 1 water-in (top-left), Run 2 water-in (top-right), Run 2 water-out (bottom-left), Run 3 water-out (bottom-right). Tuning weights for Run 4 water-in and water-out look similar and are not presented here.

4.3.3. INTERACTING TARGETS. The number of interacting targets, $T_{\mathrm{H_2O}}$, is taken to be the number of nucleons in water bags in the fiducial volume of the PØD and can be calculated using the mass of the water in the PØD fiducial volume shown in Table 4.21 with

$$T_{\mathrm{H_2O}} = \frac{1}{M_{\mathrm{H_2O}}} \cdot m_{\mathrm{H_2O}} \cdot (n_n + n_p) \cdot N_a = 1.15773^{30} \text{ nucleons}, \tag{36}$$

where $M_{\mathrm{H_2O}}$ is molar mass of water, $m_{\mathrm{H_2O}}$ [138] is the mass of water in the PØD fiducial volume, n_n and n_p are the numbers of neutrons and protons, respectively, per water molecule and N_a is the Avogadro's constant. The values of constants used can be found in Table 4.22.

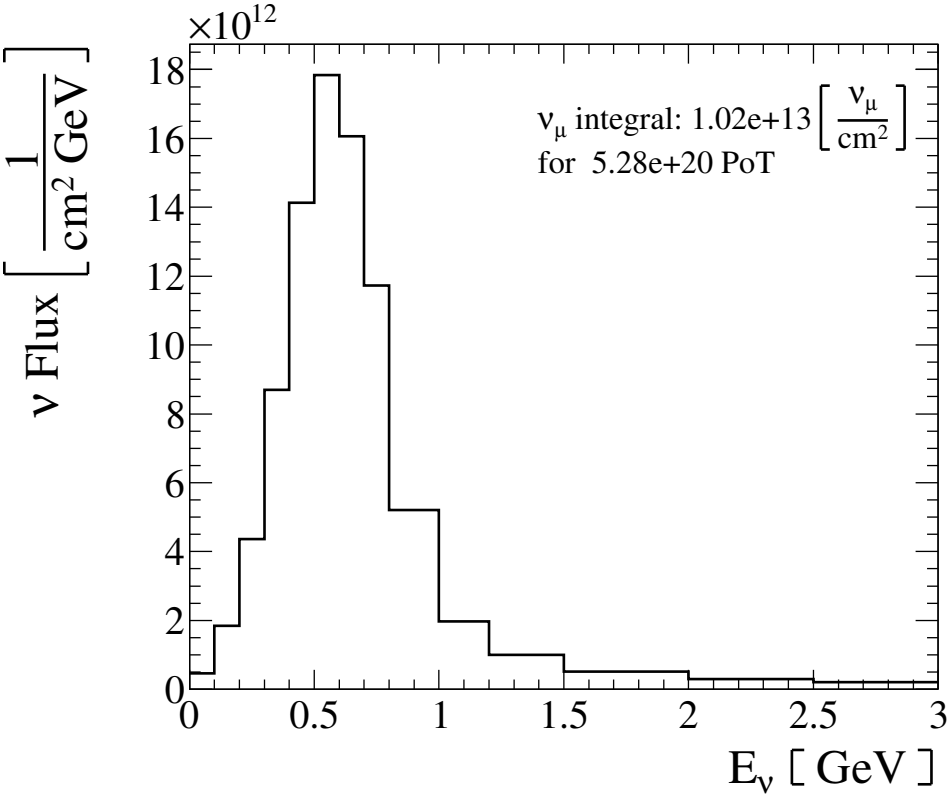

FIGURE 4.79. Tuned MC ν_μ flux prediction normalized to the combined data POT of Runs 1, 2 and 4 with the PØD detector in the water-in configuration. The PØD water-out configuration POT is not considered since there is no water present in the detector, hence no ν_μ interactions on H_2O as a target. Flux is normalized to the total PØD water-in data POT after data quality cuts, i.e. good PØD data, and no requirement on the TPC, FGD or ECALs data quality. The energy binning scheme is described in Table 4.29.

Systematic uncertainties in the mass of the PØD and their propagation through the measurement are discussed in Section 4.6.6.1.

TABLE 4.21. The fiducial mass of the PØD, m_w and m_a, for water-in and water-out configurations respectively, and m_{H_2O}, the fiducial water mass for data versus MC. Uncertainty on m_{H_2O} for data was obtained via an independent measurement and is explained in T2K-TN-073 [138].

Mass [kg]	RDP5D	MCP5E
m_w	5,480.30 ± 37.40	5,393.22 ± 0.56
m_a	3,578.30 ± 33.80	3,469.14 ± 0.55
m_{H_2O}	1,902.00 ± 16.00	1,924.08 ± 0.36

TABLE 4.22. Constants used in the calculation of T_{H_2O}

M_{H_2O}	0.01801528	$\left[\frac{kg}{mol}\right]$
N_a	$6.02214129(27) \times 10^{23}$	$[mol^{-1}]$
n_n	8	
n_p	10	

4.3.4. WATER-IN/WATER-OUT SUBTRACTION. The PØD design provides for a unique ability to add and remove water from its fiducial volume, which allows for two detector configurations, i.e. water-in (w) and water-out (a), and consequently for a cross section measurement on water, via a water-out statistical event rate subtraction.

4.3.4.1. *Advantages and Disadvantages.* The main advantage of the water-in/water-out subtraction method is the ability to measure the cross sections on a single target material, in this case water. There is also a significant reduction of systematic uncertainties, e.g. due to the unknown size of the cross section on brass, lead and other non-water materials. Since the cross sections on these targets is the same for water-in and water-out running, it allows us to simply subtract such events, and not worry about associated systematic uncertainties.

The biggest disadvantage is the increased statistical uncertainty involved in subtracting two large numbers.

Another potential disadvantage of this analysis technique is that it makes it difficult to perform a multiple-bin analysis, since the detector density is different for the two detector configurations, which leads to different detector responses for the two samples, thus the events passing the same cuts for water-in and water-out data sets, will occupy different parts of the phase space.

4.3.4.2. *Water-in Events.* In the case of water-in running signal events in the fiducial volume of the PØD can occur on scintillator, water, brass, etc. The total number of signal

events in the fiducial volume for data can be obtained via:

$$s_w = s_w^{\mathrm{H_2O}} + s_w^{scint}, \tag{37}$$

where $s_w^{\mathrm{H_2O}}$ is the total number of signal on water, s_w^{scint} is the total number of signal on scintillator, brass, etc. Later in the text s_w^{scint} will be referred to as number of signal events on scintillator for simplicity.

The purpose of this measurement is to be able to obtain $s_w^{\mathrm{H_2O}}$ which is the total number of signal events on water exclusively in data:

$$s_w^{\mathrm{H_2O}} = s_w - s_w^{scint} = \sum_i \frac{N_{w,i} - C_{w,i}^{mass} C_{w,i}^{sand} B_{w,i}}{C_{w,i}^{sand} \epsilon_{w,i}} - s_w^{scint}, \tag{38}$$

where the index i denotes PØD water-in datasets collected during T2K Runs 1, 2 and 4, with $C_{w,i}^{mass}$ and $C_{w,i}^{sand}$ calculated for each dataset. The number of signal events on scintillator, s_w^{scint}, can be expressed via:

$$s_w^{scint} = \sigma^{scint} \cdot \Phi_w \cdot T^{scint}, \tag{39}$$

where σ^{scint} is the signal cross section on scintillator, Φ_w is the integrated flux for the combined water-in running period, and T^{scint} is the number of target nucleons in the scintillator. MC predictions for the fraction of signal events after cuts occurring on various target nuclei are shown in Table 4.23.

4.3.4.3. *Water-out Events.* In the case of PØD water-out running, neutrino interactions in the fiducial volume of the PØD occur almost exclusively in scintillator, with some interactions happening on brass and other materials (Table 4.24). The number of all total signal events

TABLE 4.23. MC predictions of percentages of signal events occurring on specific targets for the PØD water-in configuration.

	Water-in Runs		
Element	1	2	4
Carbon	45.0 %	45.7 %	46.3 %
Oxygen	26.5 %	26.2 %	26.5 %
Hydrogen	20.7 %	20.0 %	19.5 %
Copper	6.5 %	7.2 %	6.6 %
Other	1.2 %	0.9 %	1.2 %

in the fiducial volume for data can be found with

$$s_a = \sum_j \frac{N_{a,j} - C^{mass}_{a,j} C^{sand}_{a,j} B_{a,j}}{C^{sand}_{a,j} \epsilon_{a,j}}, \quad s^{scint}_a = \sigma^{scint} \cdot \Phi_a \cdot T^{scint}, \quad s_a = s^{scint}_a, \tag{40}$$

where the index j denotes PØD water-out datasets collected during T2K Runs 2, 3 and 4, with each dataset having a different set of corrections, and where σ^{scint} is the signal cross section on scintillator, assumed to be the same for water-in and water-out running periods. The flux Φ_a is integrated for the water-out period, and T^{scint} is the number of target nucleons in the scintillator, which is the same for both water-in and water-out running periods.

If we take the ratio of the total number of signal events for water-in and water-out running, σ^{scint} and T^{scint} naturally cancel out and we are left with

$$\frac{s^{scint}_w}{s^{scint}_a} = \frac{\Phi_w}{\Phi_a}, \tag{41}$$

which is a ratio of integrated fluxes for water-in and water-out running periods. It can be further reduced to water-in to water-out ratio of POTs, R_p,

$$\frac{s^{scint}_w}{s^{scint}_a} = \frac{\phi_w \cdot P_w}{\phi_a \cdot P_a} = \frac{P_w}{P_a} = R_p, \tag{42}$$

if the flux per POT is the same for both cases $\phi_w = \phi_a$, which is assumed to be the case for this analysis.

MC predictions for the signal events after cuts occurring on various target nuclei are shown in Table 4.24.

TABLE 4.24. MC predictions of percentages of signal events occurring on specific targets for the PØD water-out configuration.

	Water-out Runs		
Element	2	3	4
Carbon	73.6 %	74.2 %	74.2 %
Oxygen	0.17 %	0.2 %	0.2 %
Hydrogen	13.0 %	13.5 %	13.5 %
Copper	11.4 %	10.1 %	10.1 %
Other	1.8 %	1.9 %	1.9 %

4.3.4.4. *Subtracting Events on Non-Water.* Using Equations 37 through 42 one can subtract events that are happening on non-water target materials resulting in an observed number of events that are hapenning on water exclusively:

$$s_w^{\mathrm{H_2O}} = s_w - R_p \cdot s_a = \sum_i \frac{N_{w,i} - C_{w,i}^{mass} C_{w,i}^{sand} B_{w,i}}{C_{w,i}^{sand} \epsilon_{w,i}} - R_p \sum_j \frac{N_{a,j} - C_{a,j}^{mass} C_{a,j}^{sand} B_{a,j}}{C_{a,j}^{sand} \epsilon_{a,j}}. \tag{43}$$

4.3.5. CROSS SECTION ON WATER. Finally, using Equation 43, the flux-averaged absolute CC1π^+ cross section on water, $\langle \sigma_{\nu_\mu \mathrm{CC1}\pi^+} \rangle_\Phi$, can be written as

$$\begin{aligned} \langle \sigma_{\nu_\mu \mathrm{CC1}\pi^+} \rangle_\Phi &= \frac{s^{\mathrm{H_2O}}}{\Phi_w \cdot \mathrm{T}^{\mathrm{H_2O}}} \\ &= \frac{1}{\Phi_w \cdot \mathrm{T}^{\mathrm{H_2O}}} \cdot \left(\sum_i \frac{N_{w,i} - C_{w,i}^{mass} C_{w,i}^{sand} B_{w,i}}{C_{w,i}^{sand} \epsilon_{w,i}} - R_p \sum_j \frac{N_{a,j} - C_{a,j}^{mass} C_{a,j}^{sand} B_{a,j}}{C_{a,j}^{sand} \epsilon_{a,j}}. \right), \end{aligned} \tag{44}$$

where T^{H_2O} is the number of nucleons in the water targets in the fiducial volume of the PØD. Interactions on other materials (e.g. scintillator) are not considered, since they are subtracted out in the numerator, thus the w index was dropped.

4.3.5.1. *Mock-Data Studies.* Several mock-data studies were performed and their results are presented in this Section. The first type of mock data (MD1), involved v3.2-flux-tuned MCP5E scaled to RDP5D data POT (after DQ cuts), therefore closely representing the statistical uncertainties in the data with flux-tuned mass-corrected MC central value predictions for B^{MC} and ϵ^{MC}. Using Equation 44, where N_w and N_a are MD1 numbers of events, the following cross section value was obtained for MD1:

$$\langle \sigma_{\nu_\mu \mathrm{CC1}\pi^\pm} \rangle_\Phi = 1.26 \cdot 10^{-39} \left[\frac{\mathrm{cm}^2}{\mathrm{nucleon}} \right] \pm 12.9\% \text{ (stat.)}. \tag{45}$$

This mock-data cross section is statistically compatible with the simulated MC-truth after-FSI cross section value presented in Section 1.6.4. This confirms that the cross section calculation method and the subtraction technique work and give consistent results. The methods used to obtain the statistical uncertainties and the uncertainties themselves are discussed in Section 4.5 of this dissertation.

The second type of mock data, MD2, had the same background, but the signal prediction was scaled by 0.9, therefore changing N_w and N_a. Results for MD2 give:

$$\langle \sigma_{\nu_\mu \mathrm{CC1}\pi^\pm} \rangle_\Phi = 1.13 \cdot 10^{-39} \left[\frac{\mathrm{cm}^2}{\mathrm{nucleon}} \right] \pm 13.9\% \text{ (stat.)}. \tag{46}$$

The scaling factor of 0.9 was chosen for the signal model, as the apparent size of the discrepancy between data and MC observed in several production 4 based ν_μ-induced CC inclusive analyses [139] [140].

TABLE 4.25. Mock-data (MD) types 1 and 2: N, B and ϵ for PØD water-in and water-out samples.

MD	Run #	PØD config.	N per 10^{20} POT	ϵ (%)	B per 10^{20} POT
1	1	water-in	1057.09	7.18	520.97
1	2	water-in	1086.94	7.14	531.95
1	4	water-in	1057.46	6.94	523.42
1	2	water-out	593.59	5.95	294.47
1	3	water-out	603.51	6.16	301.48
1	4	water-out	599.36	6.12	299.43
2	1	water-in	1003.48	7.18	520.97
2	2	water-in	1031.44	7.14	531.95
2	4	water-in	1004.06	6.94	523.42
2	2	water-out	563.68	5.95	294.47
2	3	water-out	573.31	6.16	301.48
2	4	water-out	569.36	6.12	299.43

4.3.5.2. *Data Results.* Using the values from Table 4.26, the data cross section on water, $\langle\sigma_{\nu_\mu \mathrm{CC1}\pi^+}\rangle_\Phi$, was obtained with Equation 44:

$$\langle\sigma_{\nu_\mu \mathrm{CC1}\pi^\pm}\rangle_\Phi = 1.10 \cdot 10^{-39} \left[\frac{\mathrm{cm}^2}{\mathrm{nucleon}}\right] \pm 14.5\% \text{ (stat.)} \tag{47}$$

The resulting cross section value is close to the MD2 value, 1.13×10^{-39} cm^2, which had the signal prediction scaled by 0.9. However the same consistency can be achieved by scaling the background prediction up by a factor of 1.1.

The propagation of statistical and systematic uncertainties associated with this results along with the background prediction normalization are discussed in Section 4.4. The significance of this result and possible ways to improve the analysis are discussed in the final chapter.

TABLE 4.26. Numbers of data events after cuts, N, normalized to 10^{20} POT. B and ϵ numbers are predicted by the MC.

Run #	PØD config.	POT	N per 10^{20} POT	ϵ (%)	B per 10^{20} POT
1	water-in	$0.296 \cdot 10^{20}$	960.7	7.18	521.0
2	water-in	$0.698 \cdot 10^{20}$	1001.6	7.14	531.9
4	water-in	$1.647 \cdot 10^{20}$	1044.4	6.94	523.4
2	water-out	$0.359 \cdot 10^{20}$	598.7	5.95	294.5
3	water-out	$1.355 \cdot 10^{20}$	554.2	6.16	301.5
4	water-out	$1.776 \cdot 10^{20}$	608.3	6.12	299.4

4.4. Propagation of Uncertainties

This Section desribes the propagation of both statistical and systematic uncertainties performed in this analysis. All of the uncertainties where propagated using one of the two approaches: analytic and/or numerical. In certain cases, where it was viable, both methods were employed for cross-checking and validation purposes.

4.4.1. Analytic Uncertainty Propagation. The total uncertainty on the cross section, $\delta\langle\sigma_{\nu_\mu \mathrm{CC1}\pi^+}\rangle_\Phi$ or $\delta\langle\sigma\rangle_\Phi$ for short, can be determined analytically, via standard uncertainty propagation valid for a function of uncorrelated variables. It can be obtained by finding the standard deviation of the cross section function $\langle\sigma_{\nu_\mu \mathrm{CC1}\pi^+}\rangle_\Phi$ described by Equation 44 resulting in:

$$\delta\langle\sigma\rangle_\Phi = \sqrt{\left(\frac{\partial\langle\sigma\rangle_\Phi}{\partial s^{\mathrm{H_2O}}}\right)^2 (\delta s^{\mathrm{H_2O}})^2 + \left(\frac{\partial\langle\sigma\rangle_\Phi}{\partial \Phi_w}\right)^2 (\delta\Phi_w)^2 + \left(\frac{\partial\langle\sigma\rangle_\Phi}{\partial \mathrm{T}_{\mathrm{H_2O}}}\right)^2 (\delta \mathrm{T}_{\mathrm{H_2O}})^2}, \tag{48}$$

where $\delta s^{\mathrm{H_2O}}$, $\delta\Phi_w$ and $\delta \mathrm{T}_{\mathrm{H_2O}}$ are the uncertainties on the number of events on water, $s^{\mathrm{H_2O}}$, integrated flux, Φ_w, and the number of interacting nucleons, $\mathrm{T}_{\mathrm{H_2O}}$, respectively, all of which are considered to be uncorrelated.

The first term in Equation 48 describes the statistical and systematic uncertainties on the number of events on water, $s^{\mathrm{H_2O}}$, while the last two terms describe uncertainties associated with the flux and the number of interacting targets, correspondingly.

The partial derivatives in Equation 48 are reduced to

$$\frac{\partial\langle\sigma\rangle_{\Phi}}{\partial s^{\mathrm{H_2O}}} = \frac{1}{\Phi_w \cdot \mathrm{T}_{\mathrm{H_2O}}}, \tag{49}$$

$$\frac{\partial\langle\sigma\rangle_{\Phi}}{\partial \Phi_w} = -\frac{s^{\mathrm{H_2O}}}{\Phi_w^2 \cdot \mathrm{T}_{\mathrm{H_2O}}}, \tag{50}$$

and

$$\frac{\partial\langle\sigma\rangle_{\Phi}}{\partial \mathrm{T}_{\mathrm{H_2O}}} = -\frac{s^{\mathrm{H_2O}}}{\Phi_w \cdot \mathrm{T}_{\mathrm{H_2O}}^2}, \tag{51}$$

yielding

$$\delta\langle\sigma\rangle_{\Phi} = \langle\sigma_{\nu_\mu}\rangle_{\Phi} \cdot \sqrt{\left(\frac{1}{s}\right)^2 \cdot (\delta s)^2 + \left(\frac{1}{\Phi_w}\right)^2 \cdot (\delta\Phi_w)^2 + \left(\frac{1}{\mathrm{T}}\right)^2 \cdot (\delta\mathrm{T})^2}, \tag{52}$$

where the $\mathrm{H_2O}$ index in $s^{\mathrm{H_2O}}$ and $\mathrm{T}_{\mathrm{H_2O}}$ was dropped for convinience.

The flux systematic uncertainty was propagated via MC reweighting, which is described in Section 4.6.1, therefore the second term in Equation 52 will be ignored for the rest of this section. The last term, which will be shown to be small compared to other sources of uncertainty, is also ignored in this section, but revisited in Section 4.2.4.1,which allows for rewriting Equation 52 in simpler form as

$$\frac{\delta\langle\sigma\rangle_{\Phi}}{\langle\sigma_{\nu_\mu}\rangle_{\Phi}} = \frac{\delta s^{\mathrm{H_2O}}}{s^{\mathrm{H_2O}}}. \tag{53}$$

The uncertainty on the number of signal events on water, $s^{\mathrm{H_2O}}$, described by Equation 43, can be expressed as

$$\delta s^{\mathrm{H_2O}} = \sqrt{(\delta s_w)^2 + R_p^2 \cdot (\delta s_a)^2 - 2 \cdot R_p \cdot \rho \cdot \delta s_w \delta s_a}, \tag{54}$$

where ρ is the water-in to water-out correlation coefficient, which can be ranging from 0, in case of statistical uncertainties, to 1 (i.e. 100% correlation). For example, ρ is 1 in case of the flux systematic uncertainty.

Combining Equations 38 through 40, δs_w and δs_a can be obtained via

$$\delta s_w = \sqrt{\sum_i \left(\left(\frac{\partial s_w}{\partial N_{w,i}} \right)^2 (\delta N_{w,i})^2 + \left(\frac{\partial s_w}{\partial B_{w,i}} \right)^2 (\delta B_{w,i})^2 + \left(\frac{\partial s_w}{\partial \epsilon_{w,i}} \right)^2 (\delta \epsilon_{w,i})^2 \right)}, \tag{55}$$

and

$$\delta s_a = \sqrt{\sum_j \left(\left(\frac{\partial s_a}{\partial N_{a,j}} \right)^2 (\delta N_{a,j})^2 + \left(\frac{\partial s_a}{\partial B_{a,j}} \right)^2 (\delta B_{a,j})^2 + \left(\frac{\partial s_a}{\partial \epsilon_{a,j}} \right)^2 (\delta \epsilon_{a,j})^2 \right)}, \tag{56}$$

where the partial derivatives are reduced to

$$\frac{\partial s_w}{\partial N_{w,i}} = \frac{1}{C_{w,i}^{sand} \epsilon_{w,i}}, \; \frac{\partial s_a}{\partial N_{a,j}} = \frac{1}{C_{a,j}^{sand} \epsilon_{a,j}}, \tag{57}$$

$$\frac{\partial s_w}{\partial B_{w,i}} = -\frac{C_{w,i}^{mass}}{\epsilon_{w,i}}, \; \frac{\partial s_a}{\partial B_{a,j}} = -\frac{C_{a,j}^{mass}}{\epsilon_{a,j}}, \tag{58}$$

and

$$\frac{\partial s_w}{\partial \epsilon_{w,i}} = -\frac{N_{w,i} - C_{w,i}^{mass} C_{w,i}^{sand} B_{w,i}}{C_{w,i}^{sand} \epsilon_{w,i}^2}, \; \frac{\partial s_a}{\partial \epsilon_{a,j}} = -\frac{N_{a,j} - C_{a,j}^{mass} C_{a,j}^{sand} B_{a,j}}{C_{a,j}^{sand} \epsilon_{a,j}^2}, \tag{59}$$

yielding

$$(\delta s_w)^2 = \sum_i \Big(\Big(\frac{1}{C^{sand}_{w,i}\epsilon_{w,i}} \Big)^2 (\delta N_{w,i})^2 + \Big(\frac{C^{mass}_{w,i}}{\epsilon_{w,i}} \Big)^2 (\delta B_{w,i})^2 + \Big(\frac{N_{w,i} - C^{mass}_{w,i} C^{sand}_{w,i} B_{w,i}}{C^{sand}_{w,i}\epsilon^2_{w,i}} \Big)^2 (\delta \epsilon_{w,i})^2 \Big) \tag{60}$$

for the uncertainty on the water-in number of signal events and

$$(\delta s_a)^2 = \sum_j \Big(\Big(\frac{1}{C^{sand}_{a,j}\epsilon_{a,j}} \Big)^2 (\delta N_{a,j})^2 + \Big(\frac{C^{mass}_{a,j}}{\epsilon_{a,j}} \Big)^2 (\delta B_{a,j})^2 + \Big(\frac{N_{a,j} - C^{mass}_{a,j} C^{sand}_{a,j} B_{a,j}}{C^{sand}_{a,j}\epsilon^2_{a,j}} \Big)^2 (\delta \epsilon_{a,j})^2 \Big) \tag{61}$$

for water-out, where $\delta N_{w|a}$ is the Poisson statistical uncertainty on number of events $N_{w|a}$ in data

$$\delta N_{w|a} = \sqrt{N_{w|a}},$$

and $\delta B_{w|a}$, $\delta \epsilon_{w|a}$ are uncertainties associated with the predicted backgrounds and selection efficiencies.

All systematic uncertainties on the numbers of water-in and water-out events are correlated to a greater or lesser extent. In case of flux, cross section and FSI model systematic uncertainties, the correlations are handled in a consistent manner through uncertainty propagation via MC reweighting, and analytic uncertainty calculations were not necessary.

Those systematics that were propagated for water-in and water-out events analytically using Equation 54, e.g. some of the detector systematics, were assumed to be either uncorrelated, 100% correlated or 100% anticorrelated, whichever gave the most conservative uncertainty. Inserting Equations 60 and 61 into Equation 54, assuming no correlations between water-in and water-out uncertainties, $\rho = 0$, and using Equation 53, the fractional

uncertainty on the cross section can be obtained via

$$
\begin{aligned}
\frac{\delta\langle\sigma\rangle_{\Phi}}{\langle\sigma_{\nu_\mu}\rangle_{\Phi}} = & \frac{1}{\sum_i \frac{N_{w,i}-C^{mass}_{w,i}C^{sand}_{w,i}B_{w,i}}{C^{sand}_{w,i}\epsilon_{w,i}} - R_p\sum_j \frac{N_{a,j}-C^{mass}_{a,j}C^{sand}_{a,j}B_{a,j}}{C^{sand}_{a,j}\epsilon_{a,j}}} \times \\
& \Big(\sum_i \Big(\Big(\frac{1}{C^{sand}_{w,i}\epsilon_{w,i}}\Big)^2 (\delta N_{w,i})^2 + \Big(\frac{C^{mass}_{w,i}}{\epsilon_{w,i}}\Big)^2 (\delta B_{w,i})^2 \\
& + \Big(\frac{N_{w,i} - C^{mass}_{w,i}C^{sand}_{w,i}B_{w,i}}{C^{sand}_{w,i}\epsilon^2_{w,i}}\Big)^2 (\delta\epsilon_{w,i})^2\Big) + R_p^2 \cdot \sum_j \Big(\Big(\frac{1}{C^{sand}_{a,j}\epsilon_{a,j}}\Big)^2 (\delta N_{a,j})^2 \\
& + \Big(\frac{C^{mass}_{a,j}}{\epsilon_{a,j}}\Big)^2 (\delta B_{a,j})^2 + \Big(\frac{N_{a,j} - C^{mass}_{a,j}C^{sand}_{a,j}B_{a,j}}{C^{sand}_{a,j}\epsilon^2_{a,j}}\Big)^2 (\delta\epsilon_{a,j})^2\Big)\Big)^{\frac{1}{2}}. \qquad (62)
\end{aligned}
$$

4.4.2. MC Uncertainties and Reweighting Methods. To propagate certain systematic uncertainties MC reweighting methods can be utilized. There were two reweighting methods used in this analysis: event-by-event reweighting, using `T2KReWeight`, and bin-by-bin reweighting when dealing with histograms. The basics of both of these methods are described in this section.

MC reweighting techniques are a common and computationally inexpensive way of propagating variations in the MC models to the final MC simulation results. They are an alternative to rerunning the entire MC simulation chain: generating the initial particle 4-vectors, passing these vectors to the detector simulation, electronic readout simulation, reconstruction, and analysis. In fact, in case of large MC simulation samples or numbers of events, and/or a large number of model parameters that need to be varied, it becomes computationally impossible to rerun the entire MC simulation chain.

The general idea behind MC reweighting methods in this analysis is that the CC1π^+ cross section can be recalculated for each variation j of the underlying models as follows

$$
\langle\sigma_{\nu_\mu}\rangle^{(j)}_{\Phi} = \frac{s^{(j)}_{\mathrm{H_2O}}}{\Phi^{(j)}_{w}\cdot \mathrm{T}_{\mathrm{H_2O}}}, \qquad (63)
$$

where in theory all three variables can be changing, but in practice, however, the number of target nucleons, T_{H_2O}, would remain unchanged when varying the flux or FSI models. The RMS deviation of the reweighted cross sections from the nominal central value can be quoted as a systematic uncertainty

$$\delta\langle\sigma\rangle_\Phi = \sqrt{\frac{1}{k}\cdot\sum_j\left(\langle\sigma_{\nu_\mu}\rangle_\Phi^{(j)} - \langle\sigma_{\nu_\mu}\rangle_\Phi^{\text{nominal}}\right)^2}, \tag{64}$$

where k is the number of necessary model variations.

The basic idea behind the event-by-event reweighting is that normalization weights corresponding to certain model parameter variations are generated for each event in the sample. Applying these weights to events, or event reweighting, is essentially simple renormalization of each individual event in the sample. Collectively the weights change the overall normalization and shape of the MC sample.

Event weights are usually a ratio of neutrino cross sections for a particular neutrino reaction. For instance, a weight for event i corresponding to model variation j is

$$w_{i,j} = \frac{\sigma_{i,j}(E,...)}{\sigma_{i,\ \text{nom}}(E,...)}. \tag{65}$$

The numerator is the cross section corresponding to the varied model, and the denominator corresponds to the nominal cross section model for a particular type of event. The event weight, $w_{i,j}$, usually depends on the neutrino energy, E_i, and other kinematic variables of event i.

Event-by-event MC reweighting was accomplished via the `T2KReWeight` library, and was used to propagate the cross section and FSI model systematic uncertanties, and is discussed in Sections 4.6.2 and 4.6.3.

The bin-by-bin reweighting method used to propagate the flux uncertainty is discussed in detail in Section 4.6.1, dedicated to the flux systematic uncertainty propagation. This bin-by-bin reweighting method developed by the author is orders of magnitude faster than the event-by-event reweighting method provided by the `T2KReWeight` library, since instead of reweighting billions of events, only a few hundred histogram bins are reweighted.

4.5. Statistical Uncertainties

The total statistical uncertainty on the cross section measurement comes from statistical uncertainties in the numbers of data events, N_w for combined T2K Runs 1, 2 and 4, and N_a for combined T2K Runs 2, 3 and 4,

$$\frac{\sqrt{N_w}}{N_w} = 1.92\%, \qquad \frac{\sqrt{N_a}}{N_a} = 2.21\%, \tag{66}$$

and statistical uncertainties in the MC predictions for backgrounds, B_w and B_a, and efficiencies, ϵ_w and ϵ_a, due to limited MC statistics. Both of the uncertainties were evaluated separately. They were computed via a method of random statistical throws, where the measured numbers of events, N_w and N_a, or B_w, B_a, ϵ_w and ϵ_a, were allowed to vary according to Poisson statistics. The results were cross-checked via a semi-analytic calculation using Equation 62.

4.5.1. Uncertainty due to Limited Data Statistics.

Using the statistical throws method, the data cross section $\langle \sigma_{\nu_\mu \mathrm{CC1}\pi^+} \rangle_\Phi^{(i)}$ was recalculated $k = 10^5$ times for each throw i via equation

$$\sigma^{(i)}_{\mathrm{CC1}\pi^+} = \frac{s^{(i)}_{\mathrm{H_2O}}}{\Phi_w \cdot T_{\mathrm{H_2O}}}, \tag{67}$$

where $s^{(i)}_{\mathrm{H_2O}}$ changes for each throw i according to the following equations

$$s^{(i)}_{\mathrm{H_2O}} = s^{(i)}_w - R_p \cdot s^{(i)}_a, \tag{68}$$

$$s^{(i)}_w = \sum_k \frac{N^{(i)}_{wk} - C^{mass}_{wk} C^{sand}_{wk} B_{wk}}{C^{sand}_{wk} \epsilon_{wk}}, \tag{69}$$

$$s^{(i)}_a = \sum_j \frac{N^{(i)}_{aj} - C^{mass}_{aj} C^{sand}_{aj} B_{aj}}{C^{sand}_{aj} \epsilon_{aj}}. \tag{70}$$

The probabilities of observing $N^{(i)}_{w|a}$ events, given measured data numbers $\langle N \rangle_{w|a}$, are described by the Poisson distribution

$$P(N^{(i)_{w|a}}) = \frac{e^{-\langle N_{w|a} \rangle} \cdot \langle N_{w|a} \rangle^{N^{(i)}_{w|a}}}{N^{(i)}_{w|a}!}, \tag{71}$$

and was implemented using the `TRandom3->Poisson()` method from the ROOT library [129].

The results of random statistical throws for data are shown in Figures 4.80 and 4.81. The fractional statistical uncertainty on the data cross section value due to limited data statistics is

$$\frac{\Delta\sigma}{\sigma} \approx \pm 15.0\% \text{ (data stat.)}, \tag{72}$$

using the throwing method and

$$\frac{\Delta\sigma}{\sigma} \approx \pm 15.0\% \text{ (data stat.)}, \tag{73}$$

for the analytic calculation using Equation 62.

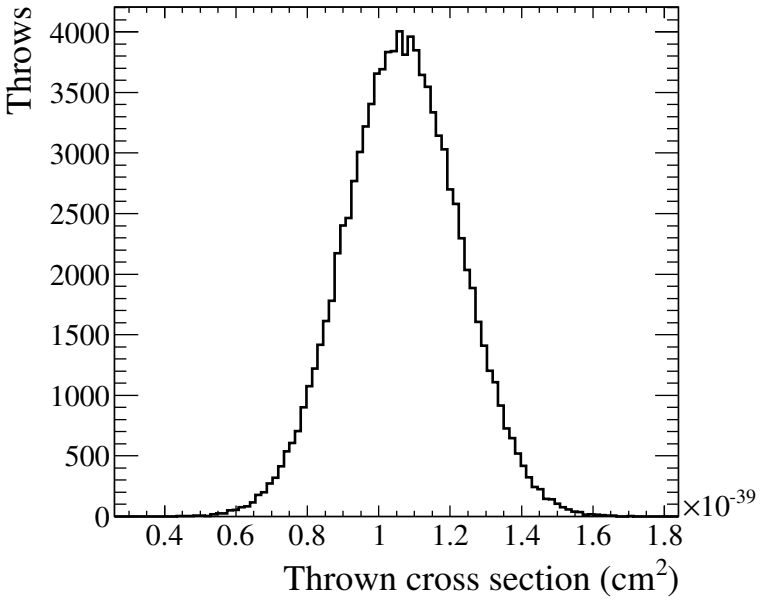

FIGURE 4.80. A histogram of thrown data cross section values, $\langle \sigma_{\nu_\mu \mathrm{CC}1\pi^+} \rangle_\Phi^{(i)}$, as a result of 100,000 statistical throws.

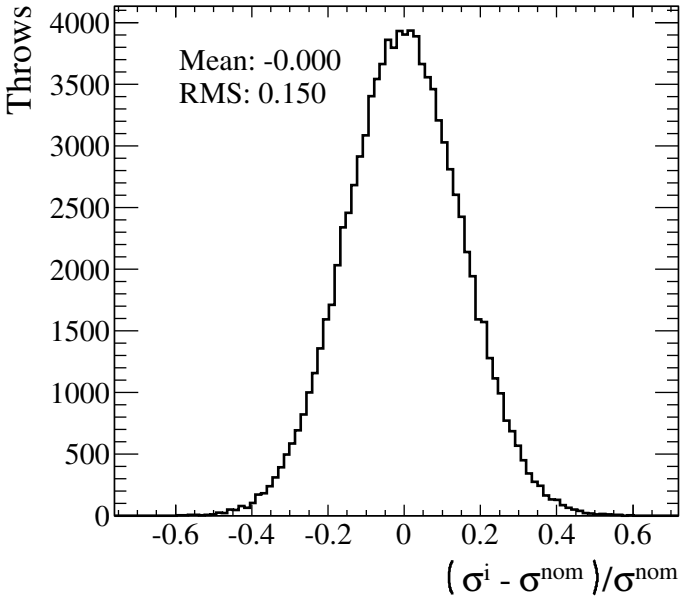

FIGURE 4.81. Fractional deviations of the thrown cross section from the nominal value, as a result of 100,000 statistical throws.

4.5.2. UNCERTAINTY DUE TO LIMITED MC STATISTICS. Using the statistical throws method again, the data cross section $\langle \sigma_{\nu_\mu \mathrm{CC}1\pi^+} \rangle_\Phi^{(i)}$ was recalculated $k = 10^5$ times for each throw i via Equation 67 where $s_{\mathrm{H_2O}}^{(i)}$ changes for each throw i according to Equation 68.

$s^{(i)}_{w|a}$ can be found via

$$s^{(i)}_{w} = \sum_{k} \frac{N_{wk} - C^{mass}_{wk} C^{sand}_{wk} B^{(i)}_{wk}}{C^{sand}_{wk} \epsilon^{(i)}_{wk}}, \tag{74}$$

$$s^{(i)}_{a} = \sum_{j} \frac{N_{aj} - C^{mass}_{aj} C^{sand}_{aj} B^{(i)}_{aj}}{C^{sand}_{aj} \epsilon^{(i)}_{aj}}, \tag{75}$$

$$\epsilon^{(i)} = \frac{S^{(i)}}{s^{gen}}, \tag{76}$$

where $B^{(i)}_{w|a}$ and $\epsilon^{(i)}_{w|a}$ MC predictions are allowed to fluctuate statistically for MC POT. The

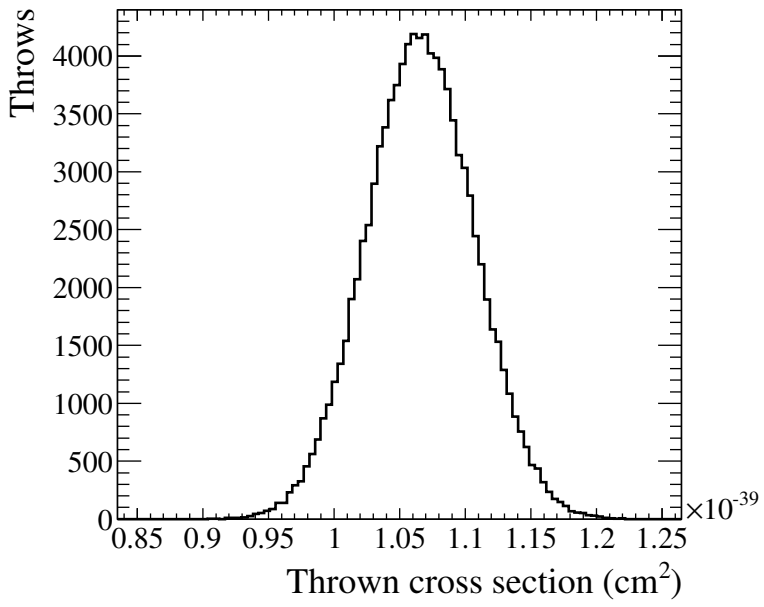

FIGURE 4.82. A histogram of thrown data cross sections, corresponding to the statistical uncertainty in MC.

probabilities of observing $B^{(i)}_{w|a}$ background events, given the MC CV numbers $\langle B \rangle_{w|a}$, are

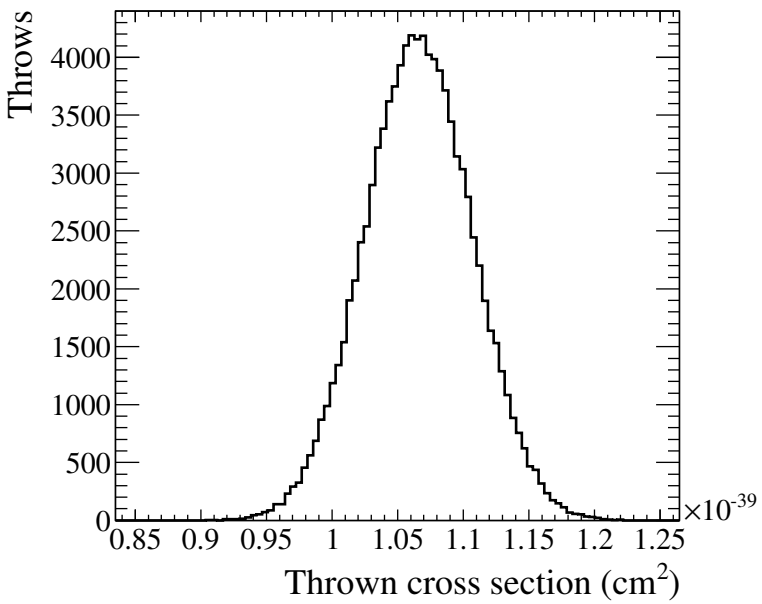

FIGURE 4.83. Fractional deviations of the thrown cross section from the nominal value, corresponding to the statistical uncertainty in MC.

described by the Poisson distribution

$$P(B^{(i)_{w|a}}) = \frac{e^{-\langle B_{w|a}\rangle} \cdot \langle B_{w|a}\rangle^{B^{(i)}_{w|a}}}{B^{(i)}_{w|a}!} \tag{77}$$

Similarly for $\epsilon^{(i)}_{w|a}$ the probability of observing a particular efficiency, is

$$P(\epsilon^{(i)_{w|a}}) = P\left(\frac{S^{(i)}}{s^{gen}}\right) = \frac{e^{-\langle \frac{S_{w|a}}{s^{gen}_{w|a}}\rangle} \cdot \langle \frac{S_{w|a}}{s^{gen}_{w|a}}\rangle^{\frac{S^{(i)}_{w|a}}{s^{gen}_{w|a}}}}{\frac{S^{(i)}_{w|a}}{s^{gen}_{w|a}}!}, \tag{78}$$

where the statistical uncertainties on $s^{gen}_{w|a}$ are considered negligible.

The effect of random statistical throws of MC backgrounds and efficiencies on the data cross section are shown in in Figures 4.82 and 4.83. The fractional statistical uncertainty on the data cross section value due to limited MC statistics, obtained via the throwing method,

is therefore

$$\frac{\Delta\sigma}{\sigma} \approx \pm 3.9\% \text{ (MC stat.)}. \tag{79}$$

4.5.3. Summary of Statistical Uncertainties. Statistical uncertainties due to limited data and MC statistics are presented in Table 4.27. Data and MC contributions added in quadrature give a total statistical uncertainty of 15.5%.

Table 4.27. Summary of data and MC statistical uncertainties for the CC1π^+ analysis.

Data	$\pm$ 15.0%
MC	$\pm$ 3.9%

4.6. Systematic Uncertainties

Consider the following quote from Barlow [147]:

> "The standard procedure for doing an analysis can be caricatured as follows
>
> (1) Devise cuts, get result.
>
> (2) Do analysis for random errors (likelihood or Poisson statistics.)
>
> (3) Make big table.
>
> (4) Alter cuts by arbitrary amounts, put in table.
>
> (5) Repeat step 4 until time/money/supervisors patience is exhausted.
>
> (6) Add variations in quadrature.
>
> (7) Quote result as systematic error.
>
> (8) If challenged, describe it as conservative.
>
> This combines evaluation of errors with checks for mistakes, in a totally inappropriate way."

There is a multitude of reasons why this approach is wrong, and some of them are discussed in [147]. For the purposes of this analysis, the main reason why this approach is incorrect, is that it allows for double-counting of uncertainties, therefore inflating the overall error. According to Barlow, if a consistency check is passed, the correct thing is to do nothing, i.e. not to add the discrepancy in quadrature with the systematic uncertainty. The condition of whether the check is passed or not is decided on a case by case basis.

Following Barlow's advice, in this analysis, the systematic uncertainty evaluations are separated from checks for mistakes where possible. Most of the designed checks were successfully passed, with data and MC being consistent within the defined norm, e.g. statistical uncertainty.

In case of some systematic effects, e.g. dE/dx energy deposition, additional studies were performed and systematic uncertainties evaluated and propagated. Identified systematic mistakes were dealt with on a case by case basis with corrections.

Systematic effects relevant to the determination of charged-current single π^+ production flux-averaged cross section on water with the PØD detector are the ones that affect the values used to determine the cross section as defined in Equation 44. Therefore we are interested in the systematic uncertainties associated with: the T2K ND280 flux prediction, MC models of neutrino cross sections, final state interactions, pion secondary interactions as well as the uncertainties related to the detector simulation. The latter include uncertainties in target mass and selection efficiency.

In other words the systematic effects of interest to this analysis include those that affect Φ, T, S, B and ϵ variables in Equation 44. Section 4.6.1 describes in detail the propagation of the flux systematic uncertainty, which is the single largest source of uncertainty in this

analysis. Uncertainty in the number of interacting targets is the actual PØD detector is small and is discussed in Section 4.6.6.1.

Systematics associated with S, B and ϵ are either related to inherent MC model uncertainties or uncertainties in the detector response. Treatment of theoretical model uncertainties is described in Section 4.6.2, 4.6.3 and 4.6.4. Detector systematic effects are discussed in Section 4.6.6.

In this single-bin analysis no explicit cuts on kinematic variants are employed nor are binned shape templates used, hence the likelihood of introducing a data vs MC bias, as a result of the analysis cuts, is small. It is also worth noting that ND280 tracker reconstruction information was not utilized in the analysis, therefore tracker-related systematics were of no relevance and also not taken into account in this analysis.

4.6.1. Flux Systematic Uncertainty. This section describes propagation of the flux systematic uncertainty through the analysis using the flux covariance matrix provided by the T2K flux group and described in the T2K flux prediction paper [114]. The reweighting procedure and its outcome are described here as well.

4.6.1.1. *Flux Covariance.* A flux covariance matrix, described in [114] that contains all of the flux uncertainty information necessary for this analysis is presented in Figure 4.84 in a form of a fractional covariance matrix for the T2K flux prediction at ND280 and SK. The ordering of the ND280 flux bins, or flux parameter bins, is shown in Table 4.28. SK flux errors occupy bins 80 - 159, but are not used in this analysis, since this analysis does not use SK data. Twenty neutrino energy bins used in the variable-size flux binning for each of the contributing neutrino types, with finer binning around the T2K flux peak and coarser at the higher energy tail, are shown in Table 4.29.

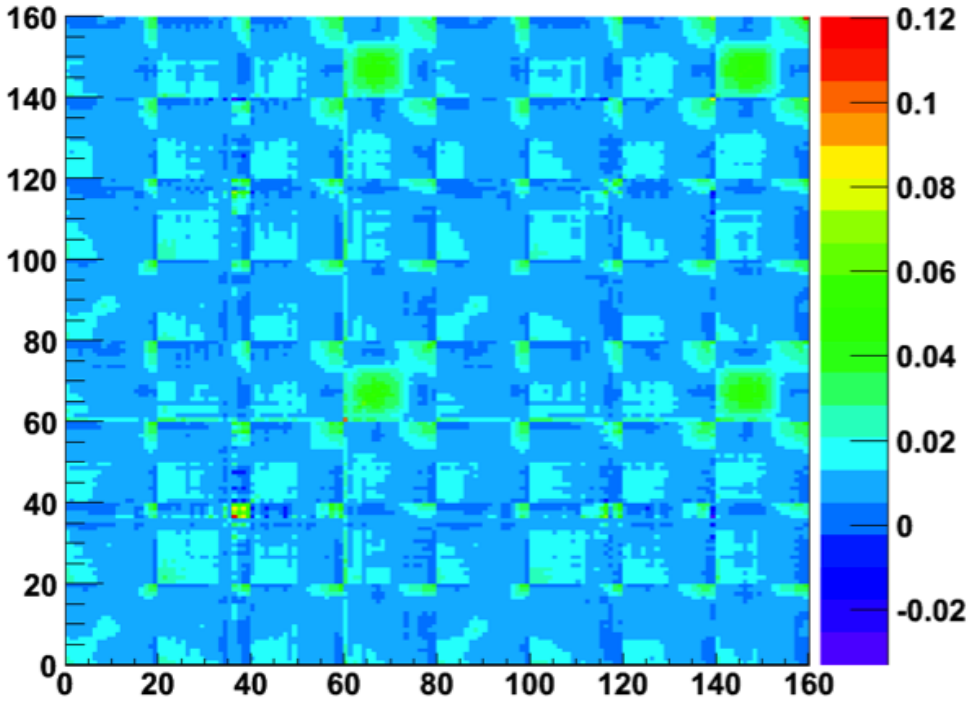

FIGURE 4.84. Fractional covariance matrix for the T2K flux prediction. This is a 160 × 160 matrix, corresponding to 160 flux parameter bins of the T2K flux prediction. The first 80 parameters correspond to the flux at ND280, the second 80 correspond to the flux at SK.

TABLE 4.28. Ordering of the flux parameter bins for the conributing neutrino types.

ν_μ	$\bar{\nu}_\mu$	ν_e	$\bar{\nu}_e$
0 - 19	20 - 39	40 - 59	60 - 79

4.6.1.2. *Introduction to MC Flux Reweighting.* To propagate the flux systematic uncertainty presented in the form of a fractional covariance matrix through the cross section measurement, a MC reweighting method is used. The reweighting method used is in theory similar to the reweighting philosophy implemented in the `T2KReWeight` library, but instead of doing event-by-event reweighting, it reweights flux, signal and background MC-truth neutrino energy histograms, which are described in Section 4.6.1.3.

TABLE 4.29. True neutrino energy bins used in the variable-size flux binning, which corresponds to the flux histogram shown in Figure 4.79.

Bin #	Low edge (GeV)	High edge (GeV)
0	0.0	0.1
1	0.1	0.2
2	0.2	0.3
3	0.3	0.4
4	0.4	0.5
5	0.5	0.6
6	0.6	0.7
7	0.7	0.8
8	0.8	1.0
9	1.0	1.2
10	1.2	1.5
11	1.5	2.0
12	2.0	2.5
13	2.5	3.0
14	3.0	3.5
15	3.5	4.0
16	4.0	5.0
17	5.0	7.0
18	7.0	10.0
19	10.0	30.0

The bin-by-bin reweighting employed for the propagation of the flux uncertainty is at least an order of $O(n-b)$ more efficient than event-by-event reweighting in both computational time and space, where n is the number of events and b is the number of flux bins. In other words, if the events can be binned in a way that is consistent with the covariance matrix describing their uncertainties, and if the number of events is a lot greater than the number of bins, then binning events once and reweighting the binned distribution bin-by-bin many times is a lot more efficient than reweighting all of the events event-by-event many times. For

this analysis $n - b \sim 1.5 \cdot 10^6$, so the improvement of the flux reweighting algorithm efficiency is very noticeable.

The MC histogram distributions that are being bin-by-bin reweighted are described in detail in the following Section 4.6.1.3. The resulting cross section distribution for all throws i, a cross section probability density function, is shown in Figure 4.91.

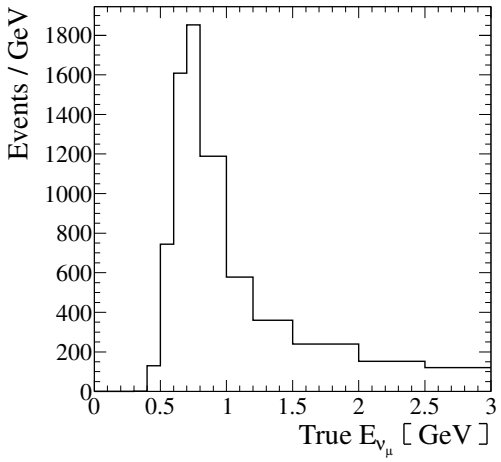

FIGURE 4.85. Selected signal histogram after analysis cuts for Run 1 + 2 + 4 PØD water-in running periods, normalized to total data POT for water-in running period after data quality cuts. Binning described in Table 4.29.

4.6.1.3. *Reweightable MC Distributions.* MC predictions of the MC-truth neutrino energy spectra of the selected signal events for each separate water-in/water-out running period, binned in the flux variable size binning, are shown in Figures 4.85 and 4.86. These distributions are subject to reweighting in the process of propagating the flux systematic uncertainty.

The selected background MC-truth neutrino energy histograms are shown in Figures 4.87 and 4.88.

4.6.1.4. *Bin-by-bin Reweighting Method.* A statistically large number of toy MC throws, N_{throws}, were generated to propagate the flux systematic uncertainty. For each throw i the flux model was randomly fluctuated within the uncertainties described by the flux covariance

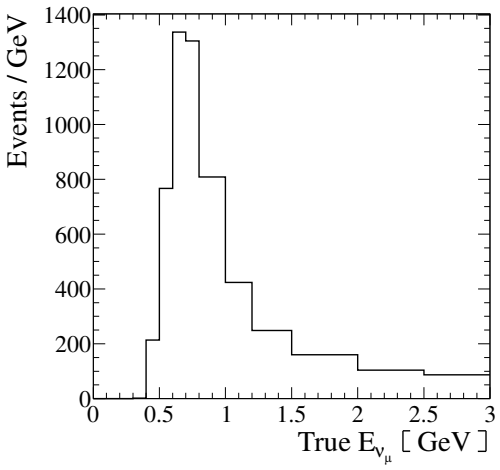

FIGURE 4.86. Selected signal histogram after analysis cuts for Run 2 + 3 + 4 PØD water-out running periods, normalized to total data POT for water-out running period after data quality cuts. Binning described in Table 4.29.

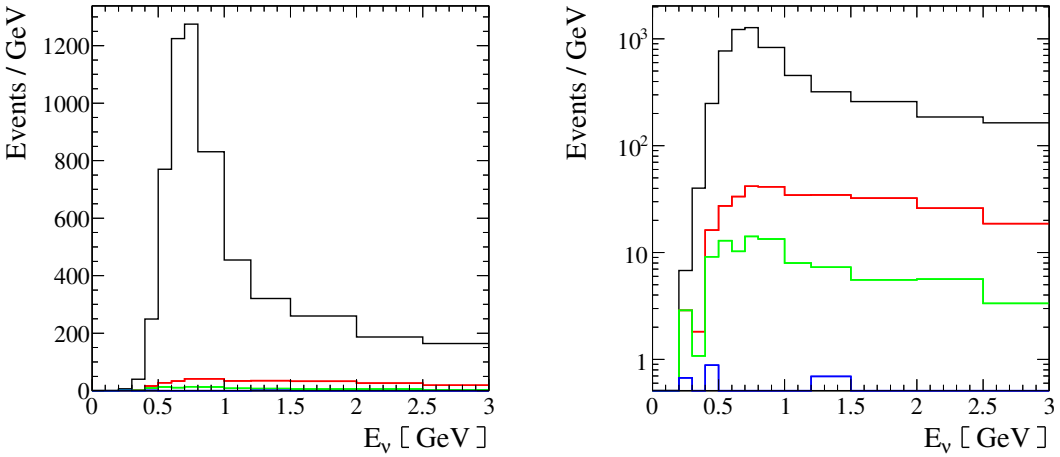

FIGURE 4.87. Four flavors of background passing the cuts: ν_μ (black), $\overline{\nu}_\mu$ (red), ν_e (green), $\overline{\nu}_e$ (blue), for Run 1 + 2 + 4 PØD water-in MC normalized to corresponding data POT after data quality cuts. The y axis on the right plot is in log scale.

matrix. Then, for each throw the flux histogram (Figure 4.79), and the signal and background histograms (Section 4.6.1.3) were reweighted bin-by-bin, using a pseudo-random vector of correlated bin normalization parameters obtained using the Cholesky-decomposed [141] fractional covariance matrix from Figure 4.84.

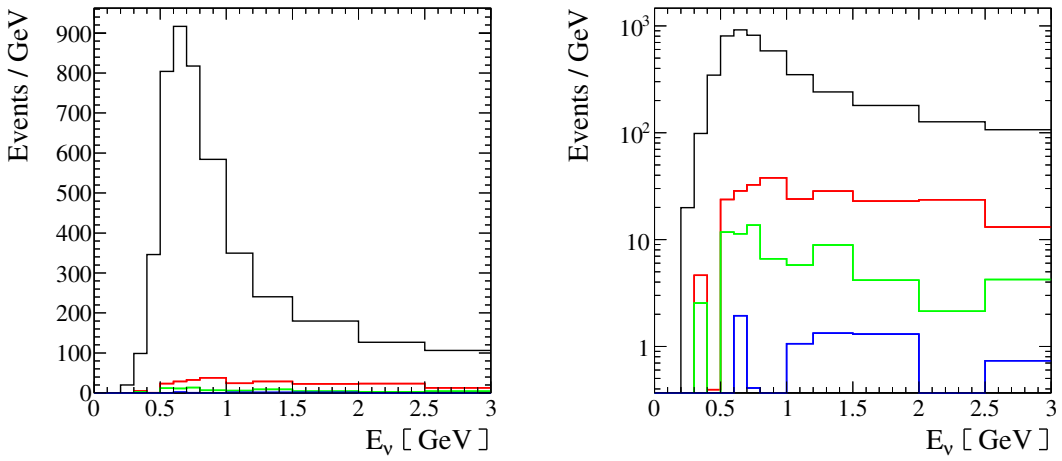

FIGURE 4.88. Four flavors of background passing the cuts: ν_μ (black), $\overline{\nu}_\mu$ (red), ν_e (green), $\overline{\nu}_e$ (blue), for Run 2 + 3 + 4 PØD water-out MC normalized to corresponding data POT after data quality cuts. The y axis on the right plot is in log scale.

The detailed procedure for determining the flux uncertainty is as follows. For each flux throw i:

- A vector of randomly fluctuated flux bin normalization parameters was obtained

$$\boldsymbol{w}^{(i)} = (w_0^{(i)}, .., w_k^{(i)}), \tag{80}$$

where $k = 80$, the number of ND280 flux parameters, and $w_b^{(i)}$ is normalization parameter for bin b. It consists of 4 parts, each corresponding to a specific neutrino flavor:

$$\boldsymbol{w}_f^{(i)} = (w_{f,0}^{(i)}, .., w_{f,k}^{(i)}), \qquad f = \{\nu_e, \nu_\mu, \bar{\nu_e}, \bar{\nu_\mu}\}, \tag{81}$$

where $k = 20$, the number of ND280 flux parameters per neutrino flavor f.

- The obtained vector of weights was used to reweight the flux, signal and background distributions described in Table 4.30. The reweighted signal and background numbers

of events for T2K Run r were calculated as weighted sum of the bin contents:

$$B_r^{(i)} = C_r^{mass} C_r^{sand} \sum_b \sum_f w_{b,f}^{(i)} B_{b,f,r}, \quad S_r^{(i)} = C_r^{mass} C_r^{sand} \sum_b w_{b,f}^{(i)} S_{b,r}, \tag{82}$$

where $B_r^{(i)}$ is the reweighted and corrected number of background and $S_r^{(i)}$ is the reweighted and corrected number of signal events after cuts, and b is the MC-truth neutrino energy bin index. $B_{b,f,r}$ and $S_{b,r}$ are bin contents of bin b of histogram of neutrino type f. Note that the signal events are all of type $f = \nu_\mu$. The reweighted and corrected signal before cuts, or generated signal, $s_{gen}^{(i)}$, needed for the effiency denominator was obtained via:

$$s_{gen,r}^{(i)} = \sum_b w_b^{(i)} s_{gen,b,r}, \quad \epsilon_r^{(i)} = \frac{S^{(i)}}{C_r^{sand} \cdot s_{gen,r}^{(i)}}, \tag{83}$$

and the reweighted integrated flux was calculated using:

$$\Phi_w^{(i)} = \sum_b w_b^{(i)} \Phi_{w,b}. \tag{84}$$

Note that all of the above quantities were reweighted for two samples, water-in and water-out, with the same random vector $w^{(i)}$.

- The efficiency-corrected numbers of signal CC1π^+ events for PØD water-in and water-out samples were obtained via the background subtraction method:

$$s_w^{(i)} = \sum_r \frac{N_{w,r} - C_{w,r}^{mass} C_{w,r}^{sand} B_{w,r}^{(i)}}{C_{w,r}^{sand} \epsilon_{w,r}^{(i)}}, \tag{85}$$

$$s_a^{(i)} = \sum_r \frac{N_{a,r} - C_{a,r}^{mass} C_{a,r}^{sand} B_{a,r}^{(i)}}{C_{a,r}^{sand} \epsilon_{a,r}^{(i)}}, \tag{86}$$

where N is the measured number of data events after selection cuts.

- Water subtraction was performed:

$$s^{(i)}_{\mathrm{H_2O}} = s^{(i)}_{w} - R_p \cdot s^{(i)}_{a}. \tag{87}$$

- Finally, the reweighted cross section on water was obtained:

$$\langle \sigma_{\nu_\mu \mathrm{CC1}\pi^+} \rangle^{(i)}_{\Phi} = \frac{s^{(i)}_{\mathrm{H_2O}}}{\Phi^{(i)}_{w} \cdot \mathrm{T}_{\mathrm{H_2O}}}. \tag{88}$$

It must be noted that just as the signal can be extracted via background subtraction (Equations 85 and 86), it can also be extracted via an alternative method called signal fraction correction, or the purity correction method:

$$s^{(i)}_{w} = \sum_r \frac{N_{w,r} C^{sand}_{w,r} p^{(i)}_{w,r}}{C^{sand}_{w,r} \epsilon^{(i)}_{w,r}}, \; s^{(i)}_{a} = \sum_r \frac{N_{a,r} C^{sand}_{a,r} p^{(i)}_{a,r}}{C^{sand}_{a,r} \epsilon^{(i)}_{a,r}}. \tag{89}$$

The purity correction method would give a smaller propagated flux uncertainty than the background subtraction method, because the purity, p, is not greatly affected by the changes in the flux normalization and shape. However, the downside of the purity correction method is that it biases the measurement towards the signal prediction in the MC (which is known to be not entirely correct), and therefore was not used to extract the final cross section in this analysis. The purity correction method was used in the flux uncertainty propagation solely for the purposes of comparison with the results of the background subtraction method.

The results of the 100,000 flux throws, for both the background subtraction method, and the purity correction method, can be seen in Figures 4.89 and 4.90. These figures show that the propagated flux uncertainty is twice as large for the background subtraction method, than it is for the purity correction method. This is due to the fact that in the background

TABLE 4.30. Histograms that are reweighted for each flux parameter throw.

Variable	Description
$B_{\nu_\mu,w,Run\ 1}$	Selected ν_μ background for Run 1 (w)
$B_{\nu_\mu,w,Run\ 2}$	Selected ν_μ background for Run 2 (w)
$B_{\nu_\mu,w,Run\ 4}$	Selected ν_μ background for Run 4 (w)
$B_{\nu_\mu,a,Run\ 2}$	Selected ν_μ background for Run 2 (a)
$B_{\nu_\mu,a,Run\ 3}$	Selected ν_μ background for Run 3 (a)
$B_{\nu_\mu,a,Run\ 4}$	Selected ν_μ background for Run 4 (a)
$B_{\overline{\nu}_\mu,w,Run\ 1}$	Selected $\overline{\nu}_\mu$ background for Run 1 (w)
$B_{\overline{\nu}_\mu,w,Run\ 2}$	Selected $\overline{\nu}_\mu$ background for Run 2 (w)
$B_{\overline{\nu}_\mu,w,Run\ 4}$	Selected $\overline{\nu}_\mu$ background for Run 4 (w)
$B_{\overline{\nu}_\mu,a,Run\ 2}$	Selected $\overline{\nu}_\mu$ background for Run 2 (a)
$B_{\overline{\nu}_\mu,a,Run\ 3}$	Selected $\overline{\nu}_\mu$ background for Run 3 (a)
$B_{\overline{\nu}_\mu,a,Run\ 4}$	Selected $\overline{\nu}_\mu$ background for Run 4 (a)
$B_{\nu_e,w,Run\ 1}$	Selected ν_e background for Run 1 (w)
$B_{\nu_e,w,Run\ 2}$	Selected ν_e background for Run 2 (w)
$B_{\nu_e,w,Run\ 4}$	Selected ν_e background for Run 4 (w)
$B_{\nu_e,a,Run\ 2}$	Selected ν_e background for Run 2 (a)
$B_{\nu_e,a,Run\ 3}$	Selected ν_e background for Run 3 (a)
$B_{\nu_e,a,Run\ 4}$	Selected ν_e background for Run 4 (a)
$B_{\overline{\nu}_e,w,Run\ 1}$	Selected $\overline{\nu}_e$ background for Run 1 (w)
$B_{\overline{\nu}_e,w,Run\ 2}$	Selected $\overline{\nu}_e$ background for Run 2 (w)
$B_{\overline{\nu}_e,w,Run\ 4}$	Selected $\overline{\nu}_e$ background for Run 4 (w)
$B_{\overline{\nu}_e,a,Run\ 2}$	Selected $\overline{\nu}_e$ background for Run 2 (a)
$B_{\overline{\nu}_e,a,Run\ 3}$	Selected $\overline{\nu}_e$ background for Run 3 (a)
$B_{\overline{\nu}_e,a,Run\ 4}$	Selected $\overline{\nu}_e$ background for Run 4 (a)
$S_{\nu_\mu,w,Run\ 1}$	Selected ν_μ signal for Run 1 (w)
$S_{\nu_\mu,w,Run\ 2}$	Selected ν_μ signal for Run 2 (w)
$S_{\nu_\mu,w,Run\ 4}$	Selected ν_μ signal for Run 4 (w)
$S_{\nu_\mu,a,Run\ 2}$	Selected ν_μ signal for Run 2 (a)
$S_{\nu_\mu,a,Run\ 3}$	Selected ν_μ signal for Run 3 (a)
$S_{\nu_\mu,a,Run\ 4}$	Selected ν_μ signal for Run 4 (a)
$s_{\nu_\mu,w,Run\ 1}$	all generated ν_μ signal for Run 1 (w)
$s_{\nu_\mu,w,Run\ 2}$	all generated ν_μ signal for Run 2 (w)
$s_{\nu_\mu,w,Run\ 4}$	all generated ν_μ signal for Run 4 (w)
$s_{\nu_\mu,a,Run\ 2}$	all generated ν_μ signal for Run 2 (a)
$s_{\nu_\mu,a,Run\ 3}$	all generated ν_μ signal for Run 3 (a)
$s_{\nu_\mu,a,Run\ 4}$	all generated ν_μ signal for Run 4 (a)
$\Phi_{\nu_\mu,w}$	ν_μ flux for the combined (w) running

subtraction method, the ∼12% flux uncertainty enters the cross section calculation twice, i.e.

through the background term, B, in the numerator, and through the flux term, Φ, in the denominator, both of which pull the cross section in the same direction.

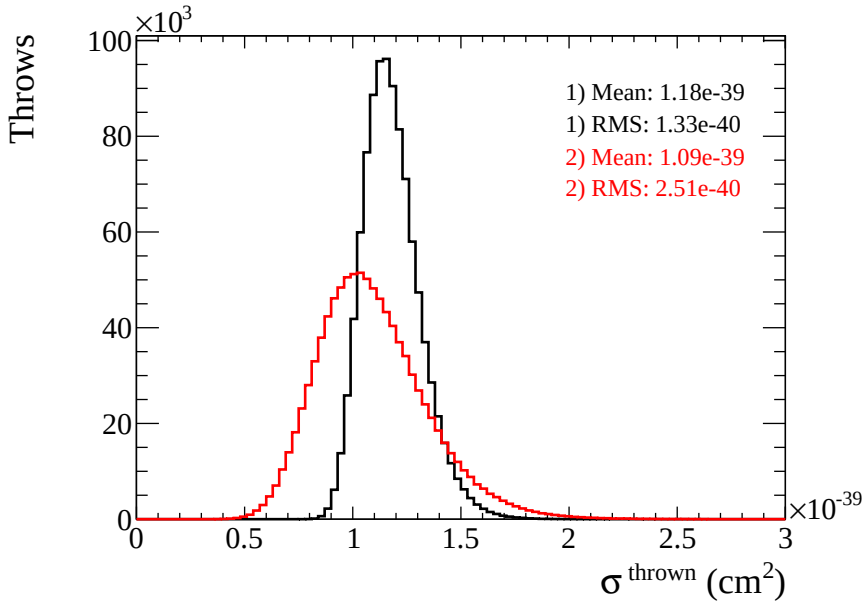

FIGURE 4.89. The recalculated data cross section for 100,000 flux throws. Shown in back is the result of the background subtraction method, and shown in red is the result of the signal fraction correction, i.e. the purity correction method.

4.6.1.5. *Propagated Flux Uncertainty.* The asymmetric flux error bars for the data cross section were evaluated at 68.2% C.L. around the central value of the $(\sigma^{thrown} - \sigma^{nominal})/\sigma^{nominal}$ distribution (Figure 4.91), where the central value is defined as the value splitting the distribution into two equal parts, such that the probability of measuring a cross section higher than the nominal is equal to that of measuring the cross section lower than the nominal. The final progagated flux systematic uncertainty is therefore

$$\frac{\delta\langle\sigma\rangle}{\langle\sigma\rangle} = ^{+25.16\%}_{-20.12\%} \tag{90}$$

This is the most dominant uncertainty in the analysis. One of the future possible improve-

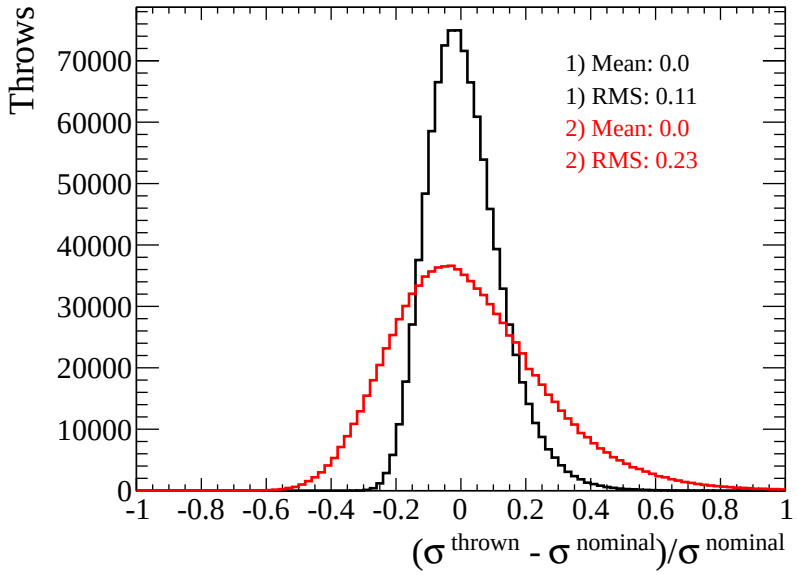

FIGURE 4.90. The deviation of the recalculated cross section from the nominal for 100,000 flux throws. Shown in back is the result of the background subtraction method, and shown in red is the result of the signal fraction correction, i.e. the purity correction method.

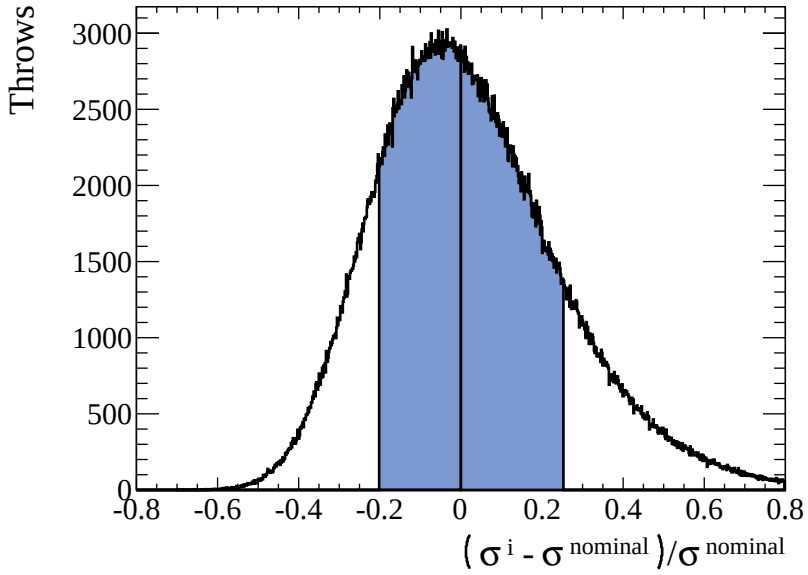

FIGURE 4.91. Asymmetric propagated flux error bars for the data cross section value at 68.2% C.L. (shaded area).

ments to this analysis would be the reduction of this uncertainty, e.g. constraining it with data-driven background fit. The flux covariance matrices for S and B predictions are shown in Appendix G.

4.6.2. Cross Section Models Uncertainties. This section describes the propagation of the systematic uncertainties of such cross section model parameters as axial mass, M_a, Fermi momentum, p_f, etc. The FSI and SI uncertainties are discussed in Sections 4.6.3 and 4.6.4.

Table 4.31. NEUT [142] and NIWG [143] parameter names and sigmas used in the analysis. $\delta\epsilon$ and δB signify whether reweighting is employed for efficiency and background correspondingly.

Parameter Name	Variable	Frac. σ	$\delta\epsilon$	δB
NEUT M_a CCQE shape	NXsec_MaCCQEshape	0.165289	yes	yes
NEUT M_a resonant shape	NXsec_MaRESshape	0.165289	yes	yes
NEUT π-less Δ decay norm.	NSystNucl_PilessDcyRES	0.2	no	yes
NIWG Δ mass mean	NIWGDeltaMass_mean	0.1	yes	yes
NIWG Δ mass width	NIWGDeltaMass_width	0.52	yes	yes
NIWG 2012a CCQE E0 norm.	NIWG2012a_ccqeE0	0.11	yes	yes
NIWG 2012a CCQE E1 norm.	NIWG2012a_ccqeE1	0.3	yes	yes
NIWG 2012a CCQE E2 norm.	NIWG2012a_ccqeE2	0.3	yes	yes
NIWG 2012a CC1π E0 norm.	NIWG2012a_cc1piE0	0.21	yes	yes
NIWG 2012a CC1π E1 norm.	NIWG2012a_cc1piE1	0.4	yes	yes
NIWG 2012a NC1π E0 norm.	NIWG2012a_nc1piE0	0.3	no	yes
NIWG 2012a NC1π^0 E0 norm.	NIWG2012a_nc1pi0E0	0.31	no	yes
NIWG 2012a CC multi-π E0 norm.	NIWG2012a_ccmultipiE0	0.25	yes	yes
NIWG 2012a CCDIS E0 norm.	NIWG2012a_ccdisE0	0.25	yes	yes
NIWG 2012a CC coherent E0 norm.	NIWG2012a_cccohE0	1	yes	yes
NIWG 2012a NC coherent E0 norm.	NIWG2012a_nccohE0	0.3	no	yes
NIWG 2012a NC other E0 norm.	NIWG2012a_ncotherE0	0.3	no	yes
NIWG 2012a ν_e-CC E0 norm.	NIWG2012a_ccnueE0	0.06	no	yes
NIWG 2012a spectral function	NIWG2012a_sf	1	yes	yes
NIWG 2012a binding energy	NIWG2012a_eb	0.36	yes	yes
NIWG 2012a Fermi momentum	NIWG2012a_pf	0.13825	yes	yes

4.6.2.1. *Cross section Model Parameters.* Various neutrino cross section model parameters (knobs) implemented in NEUT MC, and contributing to the signal and background predictions in this analysis, have systematic uncertainties associated with them (Table 4.31). The detailed description of these parameters and their reweight implementations in `T2KReWeight` can be obtained from [142] and [143]. These uncertainties were propagated through the cross section measurement via MC reweighting, with event weights generated using the `T2KReWeight` library, and the procedure to apply the weights is outlined in this section. The list of cross section model parameters shown in Table 4.31 is taken as a standard list used in the T2K oscillation analyses performed in 2012, as well as other T2K ND280 cross section analyses performed around 2012 - 2014. It must be noted that the NIWG[23] 2012a CC coherent E0 (corresponding to the 0 - 2 GeV neutrino energy bin) normalization parameter has a 100% uncertainty associated with it, which is due to the fact that the coherent single pion production data are sparse, and models are known to be flawed. It must also be noted that there is a continuous effort by the T2K NIWG group to constantly revisit the model parameters and their uncertainties, when knew knowledge of these parameters becomes available.

4.6.2.2. *MC Model Reweighting.* To propagate the cross section model systematic uncertainties a MC reweighting method was used, similar to that in [145]. The utilized reweighting method relies on the `T2KReWeight` library, where event-by-event reweighting is performed according to variations in the cross section models. The reweighted cross section for each variation i in the model was obtained using Equation 63. The cross section model parameters are assumed to be uncorrelated, which is largely true (only NC and CC coherent are assumed

[23] NIWG stands for the T2K Neutrino Interaction Working Group.

TABLE 4.32. The effect of positive 1-σ variations in the cross section model parameters on signal and background predictions. Water-in and water-out numbers are scaled to corresponding data POT, with flux tuning and a set of corrections applied.

Parameter name	s_w	s_a	s_{H_2O}	$(\sigma_i - \sigma)/\sigma$ (%)
NXSec_MaCCQEshape	18,561.5	12,258.7	6,302.7	-1.36
NXSec_MaRESshape	18,775.6	12,404.3	6,371.2	-0.29
NSystNucl_PilessDcyRES	17,706.4	11,845.7	5,860.6	-8.28
NIWG2012a_ccqeE0	18,217.7	11,986.3	6,231.3	-2.48
NIWG2012a_ccqeE1	18,371.4	12,119.9	6,251.4	-2.17
NIWG2012a_ccqeE2	18,472.3	12,198.3	6,274.0	-1.81
NIWG2012a_cc1piE0	18,257.6	12,170.1	6,087.5	-4.7
NIWG2012a_cc1piE1	18,065.0	12,102.2	5,962.8	-6.68
NIWG2012a_nc1piE0	18,659.7	12,318.3	6,341.4	-0.76
NIWG2012a_nc1pi0E0	18,563.3	12,281.2	6,282.1	-1.69
NIWG2012a_ccmultipiE0	18,253.7	12,218.3	6,035.3	-5.55
NIWG2012a_ccdisE0	18,844.0	12,444.9	6,399.1	0.145
NIWG2012a_nccohE0	18,662.7	12,311.2	6,351.5	-0.60
NIWG2012a_ncotherE0	18,493.4	12,240.1	6,253.2	-2.14
NIWG2012a_ccnueE0	18,760.5	12,394.0	6,366.5	-0.36
NIWG2012a_sf	19,404.8	12,748.5	6,656.2	4.17
NIWG2012a_eb	18,863.2	12,429.1	6,434.0	0.69
NIWG2012a_pf	18,602.5	12,318.5	6,284.0	-1.65
NIWGDeltaMass_mean	18,641.8	12,337.6	6,304.1	-1.34
NIWGDeltaMass_width	18,698.1	12,355.2	6,342.8	-0.73

to be correlated, but their overall contribution is small), therefore their individual uncertainty contributions were simply added in quadrature.

Here it must be noted that not all knobs are relevant for the signal model, i.e. after-FSI CC1π^+, therefore the signal selection efficiency, ϵ, was reweighted only for knobs that were relevant to the signal model. For instance, the π-less delta decay model knob, is not relevant

to the signal model, since our signal category by definition cannot contained pion-less delta decay events. Similarly, no NC events are ever considered to be part of signal, hence NC model variations are only applied to the background predictions, but not to the efficiency.

TABLE 4.33. The effect of negative 1-σ variations in the cross section model parameters on signal and background predictions. Water-in and water-out numbers are scaled to corresponding data POT, with flux tuning and a set of corrections applied.

Parameter name	s_w	s_a	$s_{\mathrm{H_2O}}$	$100 \cdot (\sigma_i - \sigma)/\sigma$ (%)
NXSec_MaCCQEshape	18,991.2	12,551.5	6,439.7	0.78
NXSec_MaRESshape	18,775.6	12,404.3	6,371.2	-0.28
NSystNucl_PilessDcyRES	19,843.7	12,962.5	6,881.2	7.69
NIWG2012a_ccqeE0	19,331.2	12,820.7	6,510.5	1.88
NIWG2012a_ccqeE1	19,178.3	12,687.7	6,490.6	1.57
NIWG2012a_ccqeE2	19,078.6	12,610.2	6,468.3	1.22
NIWG2012a_cc1piE0	19,177.6	12,547.8	6,629.8	3.75
NIWG2012a_cc1piE1	19,467.0	12,676.3	6,790.7	6.27
NIWG2012a_nc1piE0	18,890.8	12,490.0	6,400.8	0.17
NIWG2012a_nc1pi0E0	18,987.2	12,527.1	6,460.1	1.10
NIWG2012a_ccmultipiE0	19,290.8	12,586.1	6,704.7	4.92
NIWG2012a_ccdisE0	18,705.7	12,362.2	6,343.4	-0.72
NIWG2012a_cccohE0	24,317.8	17,623.8	6,693.9	4.76
NIWG2012a_nccohE0	18,887.8	12,497.1	6,390.7	0.01
NIWG2012a_ncotherE0	19,057.2	12,568.2	6,488.9	1.55
NIWG2012a_ccnueE0	18,790.6	12,414.6	6,376.0	-0.21
NIWG2012a_sf	18,111.8	12,037.2	6,074.6	-4.93
NIWG2012a_eb	18,690.1	12,380.8	6,309.3	-1.26
NIWG2012a_pf	18,918.1	12,475.2	6,442.9	0.83
NIWGDeltaMass_mean	18,769.0	12,215.9	6,553.1	2.55
NIWGDeltaMass_width	18,858.8	12,465.7	6,393.1	0.05

The effects of positive and negative 1-σ variations in the cross section model parameters on signal and background predictions are shown in Tables 4.32 and 4.33 respectively. The charged-current coherent single pion production normalization parameter is not included in Table 4.32, since this channel is already known to be overestimated in the implementation of the Rein-Sehgal model in the version of NEUT generator used in this analysis. Only the negative 1-σ variation is included in the cross section model uncertainty calculation.

The final cross section model systematic uncertainty obtained via Equation 91

$$\delta\langle\sigma\rangle_{\Phi} = \sqrt{\sum_{i} \left(\langle\sigma_{\nu_\mu}\rangle_{\Phi}^{(i)} - \langle\sigma_{\nu_\mu}\rangle_{\Phi}^{\text{nominal}}\right)^2}. \tag{91}$$

is therefore

$$\frac{\delta\langle\sigma\rangle}{\langle\sigma\rangle} = ^{+15.02\%}_{-16.04\%} \tag{92}$$

This uncertainty could be reduced if the efficiency of selecting signal events is increased and/or background is reduced, which is evident from equations in Section 4.4.1.

4.6.3. FSI Model Uncertainties. FSI models are one of the most revelant practical issues in the neutrino cross sections field, for different neutrino experiments show different preferences for the FSI models. For instance, the MiniBooNE single pion production data lean towards cross section models with no FSI, or FSI turned off, while MINERνA results are in good agreement with the FSI on.

In this analysis, the FSI systematic uncertainties arise from the uncertainties in the following pion/nucleon reinteraction models (implemented in NEUT), while the pion/nucleon is propagating through the initial target nucleon:

- Pion absorption;

- Charge exchange at low energies;
- Inelastic scattering at low energies;
- Pion production;
- Charge exchange at high energies;
- Inelastic scattering at high energies.

In order to propagate this uncertainty through the analysis, the well-established recipe described in T2K-TN-32 [153] and T2K-TN-131 [145] was used. In short, the `T2KReWeight` library was used to generate event weights, corresponding to variations in the FSI model parameters. Using 16 sets of FSI weights, described in Appendix D, with each set corresponding to a different "one sigma" contour in the FSI parameter space, the systematic uncertainty was calculated using Equation 64 from Section 4.4.2, where the number of model variations is equal to the number of FSI parameter sets, $k = 16$. This method assumes that FSI parameters are uncorrelated.

As aforementioned, this analysis utilizes an after-FSI signal definition, i.e. our signal category always has a single π^+ in the final state exiting the nucleus. This implies that events where a single π^+ was created in the initial state, but later got either absorbed and/or charge exchanged, will constitute a background interaction. Hence the efficiency, ϵ, is not reweighted in in the course of the FSI parameter variation study. It is only the background, B, that inherits the FSI uncertainty.

The results of the reweighting for the 16 parameter sets are shown in Table 4.34. The effect of the FSI variations on the signal and background MC-truth neutrino energy distributions is shown in Figures 4.92 and 4.93. The FSI systematic uncertainty propagated

TABLE 4.34. The results of 16 FSI parameter variations, absolute and fractional changes in the measured cross section.

Par. Set	$\delta\langle\sigma\rangle$	$\frac{\delta\langle\sigma\rangle}{\langle\sigma\rangle}$ (%)
1	$-8.17589 \cdot 10^{-42}$	-0.77
2	$-1.36631 \cdot 10^{-41}$	-1.28
3	$2.14468 \cdot 10^{-42}$	0.20
4	$-1.57513 \cdot 10^{-41}$	-1.48
5	$2.37723 \cdot 10^{-41}$	2.23
6	$-1.48963 \cdot 10^{-41}$	-1.40
7	$2.33319 \cdot 10^{-41}$	2.19
8	$-2.26562 \cdot 10^{-41}$	-2.13
9	$-1.75754 \cdot 10^{-41}$	-1.65
10	$-2.7544 \cdot 10^{-41}$	-2.58
11	$-4.68894 \cdot 10^{-42}$	-0.44
12	$-2.69471 \cdot 10^{-41}$	-2.53
13	$2.42747 \cdot 10^{-41}$	2.28
14	$-2.61469 \cdot 10^{-41}$	-2.45
15	$1.10836 \cdot 10^{-41}$	1.04
16	$-3.2231 \cdot 10^{-41}$	-3.02
RMS	$2.0312 \cdot 10^{-41}$	1.91

for this analysis is therefore:

$$\frac{\delta\langle\sigma\rangle}{\langle\sigma\rangle} = ^{+1.91\%}_{-1.91\%} \tag{93}$$

4.6.4. SI MODEL UNCERTAINTIES. The Secondary Interactions (SI) are similar to the FSI effects in terms of the physics involved, with the only significant difference being the location of reinteractions. SI occur outside the initial target nucleus, and not in the primary neutrino vertex. Pions and protons interact in the detector and can be absorbed, can change their charge (charge exchange) or can be scattered. Those interactions are not necessarily

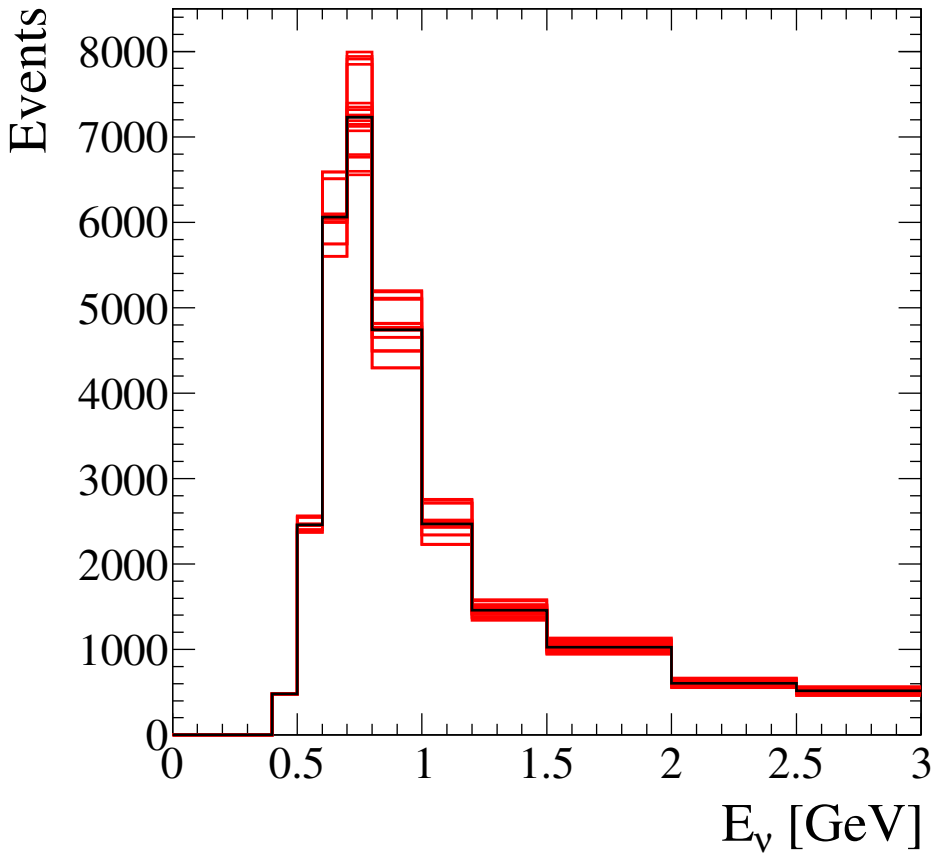

FIGURE 4.92. Variations in the MC-truth neutrino energy distributions for signal corresponding to 16 FSI parameter sets. Black histograms are the nominal distributions, red histograms are the varied distributions.

well modelled by GEANT4 for the T2K energy range (low energy). The T2K ND280 Tracker analyses have already shown some data-MC discrepancies for pion SI. To estimate the effect of pion SI data-MC differences on this analysis, the Monte Carlo simulation files were reprocessed with different models of hadronic interactions, which are recommended by the GEANT4 group for use with the high energy physics experiments:

(1) QGSP_BERT (default) - Bertini cascade model ($E \lesssim 10$ GeV), quark gluon string model ($E \gtrsim 10$ GeV);

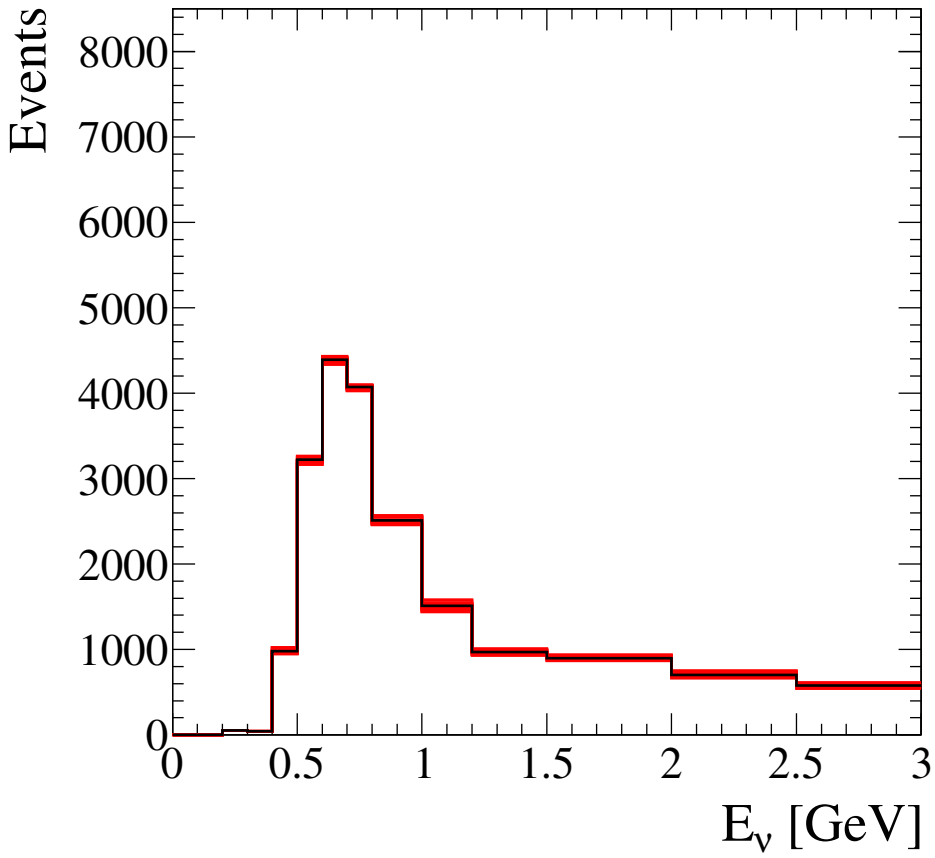

FIGURE 4.93. Variations in the MC-truth neutrino energy distributions for background corresponding to 16 FSI parameter sets. Black histograms are the nominal distributions, red histograms are the varied distributions.

(2) FTFP_BERT - Bertini cascade model ($E \lesssim 5$ GeV), FTF (FRITIOF) model ($E \gtrsim 4$ GeV);

(3) QGSP_BIC - binary cascade model ($E \lesssim 10$ GeV), quark gluon string model ($E \gtrsim 10$ GeV).

For each of these models, the number of selected signal events and number of the pion background events (background events accepted by our cuts which contain at least one pion) were calculated. The results of this study are shown in Table 4.35. After applying selection cuts, the fraction of the total background, which was the pion background, was 40.3% for

TABLE 4.35. Number of selected signal, S, and the pion background events, B, for three MCs with different models of hadronic interactions. QGSP_BERT is the nominal model for which the statistical errors have been shown. ΔS and ΔB (shown in brackets for FTFP_BERT and QGSP_BIC models) are the fractional differences from the nominal model in S and B respectively.

Model	Water-in		Water-out	
	S (ΔS)	B (ΔB)	S (ΔS)	B (ΔB)
QGSP_BERT	$1013 \pm 3.1\%$	$379 \pm 5.1\%$	$664 \pm 3.9\%$	$209 \pm 6.9\%$
FTFP_BERT	943 (-6.91%)	397 (+4.75%)	631 (-4.97%)	221 (+5.74%)
QGSP_BIC	1027 (+1.38%)	356 (-6.07%)	662 (-0.30%)	224 (+7.18%)

water-in and 39% for water-out. These fractions were multiplied by the absolute values of the largest fractional differences ΔB between the models from the Table 4.35. This gave a 2.4% background error for water-in and 2.8% for water-out. Efficiency uncertainties have been taken directly as the absolute values of the largest fractional differences ΔS from the Table 4.35: 6.9% (water-in) and 5% (water-out). An analytic formula to propagate these uncertainties into the final uncertainty on $s_{\mathrm{H_2O}}$ and cross section was used. Assuming correlated water-in and water-out uncertainties, the total SI uncertainty of 10.15% on the cross section was obtained. SI uncertainty is assumed to be uncorrelated with the FSI, which is extremely conservative. This possibly contributes to an inflation of the total systematic uncertainty, however at present there is no established good way of determining how correlated the SI and FSI are in the PØD detector.

4.6.5. SUMMARY OF MODEL UNCERTAINTIES. The various model systematic uncertainties are summarized in Table 4.36. The total model systematic uncertainty, with all the uncorrelated uncertainties added in quadrature, is therefore:

$$\frac{\delta\langle\sigma\rangle}{\langle\sigma\rangle} = ^{+31.03\%}_{-27.69\%} \tag{94}$$

TABLE 4.36. Summary of physics models' systematic uncertainties for the CC1π^+ analysis.

	+1-σ (%)	-1-σ (%)
Flux	25.16	20.12
Cross section	15.02	16.04
FSI	1.91	1.91
SI	10.15	10.15

4.6.6. DETECTOR SYSTEMATIC UNCERTAINTIES. This section describes the study of the PØD detector systematic effects and the associated uncertainties. Most of the detector systematic studies presented here were carried out together by T. Wachala and the author with some of the studies adopted from the other T2K analyses, e.g. the NCE analysis [90].

4.6.6.1. *PØD Fiducial Water Mass.* The uncertainty on the mass of water in the fiducial volume of the PØD detector was obtained via an independent measurement and is described in detail in the PØD geometry T2K internal document [138]. In short, the measurement of the incoming water flow rate into the PØD detector was performed while the PØD water targets were filled. The uncertainty in that measurement was less than 0.84% of the total water mass, and this number is added in quadrature with the rest of the systematics. The uncertainty of the MC detector mass, which comes from the uncertainties in the densities of the simulated materials, is less than 0.03% for both water-in and water-out PØD configurations, which is negligible compared to other sources of systematic uncertainty, and therefore can be safely ignored.

4.6.6.2. *Out-of-Fiducial Volume Background.* The main contribution to the out-of-fiducial (OOF) background in this analysis comes from the neutrino interactions inside the PØD, but outside of the fiducial volume. These types of events occur mostly in the volume immediately outside the fiducial volume, but inside the PØD, that is within the water target (25 cm

buffer from the edges in x and y) and in the Central and Upstream ECALs (Figures 4.94 and 4.95). If the rate of the interactions in the side buffer and ECALs differs between data and

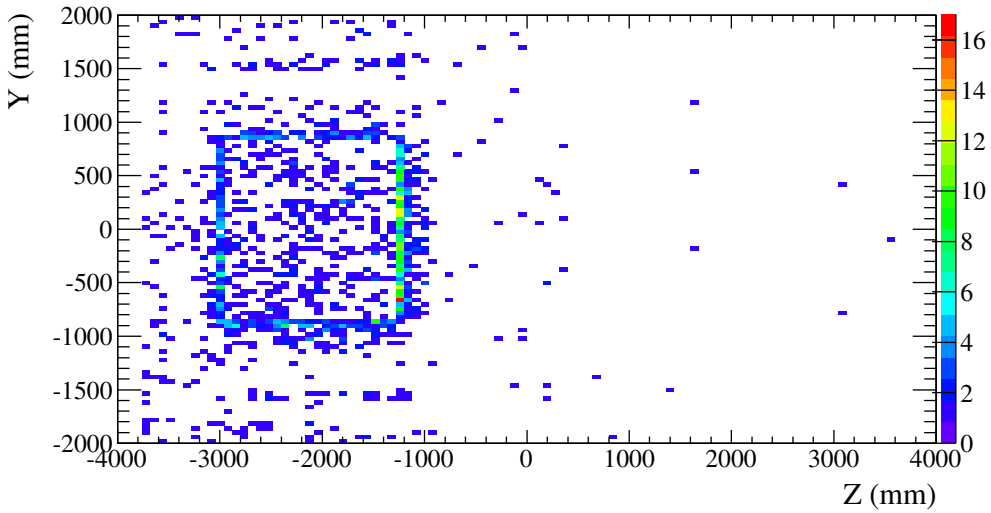

FIGURE 4.94. y-z view of the MC-truth vertices for OOF backgrounds for water-in MC.

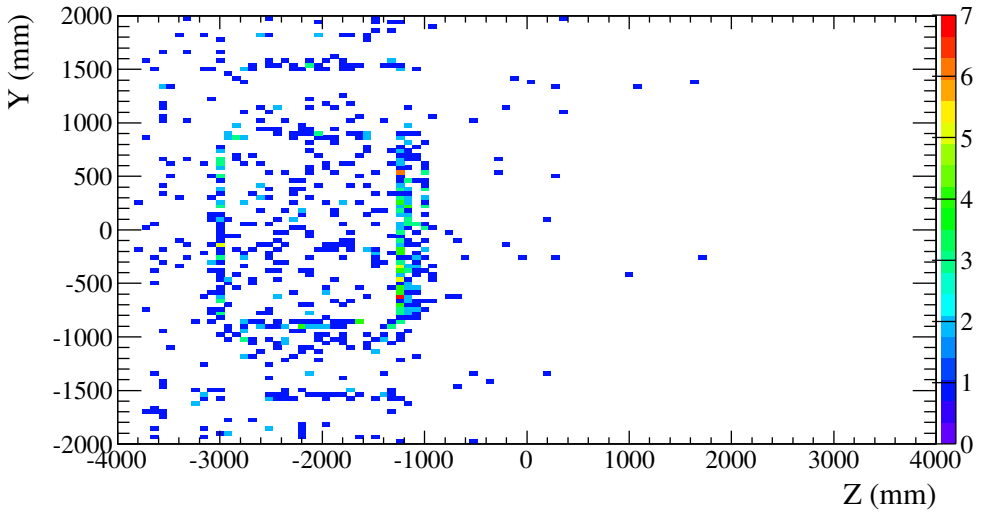

FIGURE 4.95. y-z view of the MC-truth vertices for OOF backgrounds for water-out MC.

Monte Carlo it will introduce a systematic bias in the calculated cross section. To evaluate the effect of the potential data-Monte Carlo difference in OOF background event rates, a dedicated event selection (OOF background enriched side-band sample) was prepared. The

two-track sample cuts as described in the Section 4.2.2.2 and 4.2.2.3 were implemented, but with an "inverted" definition of the PØD fiducial volume. The starting point of the muon candidate track had to be located in the PØD but outside of the standard fiducial volume defined in Section 4.2.2.1. Then the sample was divided into three sub-samples with events originating in USECal, Water Target buffer and CECal. Data/MC event rate ratios for each of the sub-samples were calculated. The sand muon MC was included in the selection. Flux tuning, mass and sand muon pileup corrections were applied. The results of this OOF background-enriched side-band selection are shown in Table 4.37.

It is clear that the absolute scale of the OOF background in MC does not represent well this type of background in the data, and therefore this MC background prediction needs to be corrected. One possible explanation for this data versus MC discrepancy is an incorrect cross section normalization for lead, which is present in the ECals. The cross section on lead has not yet been measured, so it is unclear if the absolute normalization of this cross section in the model is correct. Another possible source of data-MC discrepancy is sand-muon-induced interactions in the magnet that enter the PØD from the sides. It has been shown in the PØD-based NCE analysis [90] that the neutron background coming from the magnet and entering the PØD is not well simulated in the MC. Data/MC ratios from Table 4.37 have

TABLE 4.37. Data/MC ratios for the two-track OOF background-enriched selection. Uncertainties quoted are purely statistical. The numbers are used as multiplicative correction factors for different categories of OOF background in the OOF systematic uncertainty calculation.

Upstream ECal		Water target		Central ECal	
water-in	water-out	water-in	water-out	water-in	water-out
1.263 ± 0.057	0.964 ± 0.033	0.978 ± 0.066	0.933 ± 0.060	0.858 ± 0.108	0.823 ± 0.090

been taken, for the purpose of the OOF background uncertainty study, as multiplicative correction factors for the predicted OOF backgrounds.

To propagate the data-MC differences in OOF background into the final cross section uncertainty, 10,000 toy Monte Carlos for both water-in and water-out sets were generated. For each toy experiment every OOF background event has been classified using MC truth information by whether it happened in Upstream ECal, Water Target buffer, Central ECal or outside the PØD. Next, the event was weighted with the appropriate correction factor (data/MC ratio) from Table 4.37, which was randomly fluctuated according to Gaussian statistics with the sigma given by the data/MC ratio error from the same table. If an event appeared to be in the outside-of-PØD category, a factor of 1.0 with 0.2 error was used (motivated by the external studies of the interactions in SMRD and ECAL). Weights for water-in and water-out events were fluctuated indepedently. This is equivalent to uncorrelated water-in and water-out errors. The water-in and water-out uncertainties were treated as uncorrelated because of the lack of knowledge on the exact correlations for OOF background errors. However, it is very likely that they are highly correlated, which means that treating them as uncorrelated is conservative. For each of the toy MCs the number of selected background events for water-in and water-out was recalculated as well as the final number of signal events on water after subtraction.

The distributions of the selected background events for water-in and water-out are shown in Figures 4.96 and 4.97. The fractional differences from the nominal number of selected events on water after subtraction are shown in Figure 4.98. The RMS of this distribution, which is 2.7%, was taken as a systematic uncertainty on the CC1π^+ cross section.

4.6.6.3. *dE/dx Particle ID.* The dE/dx cut, which allows for the μ^-/π^+ vs p discrimination in order to primarily reject the CCQE background, is the last cut in the selection procedure. Discrepancies between the MC simulation of the deposited charge and the actual deposited charge in data can lead to a selection bias in the dE/dx PID method.

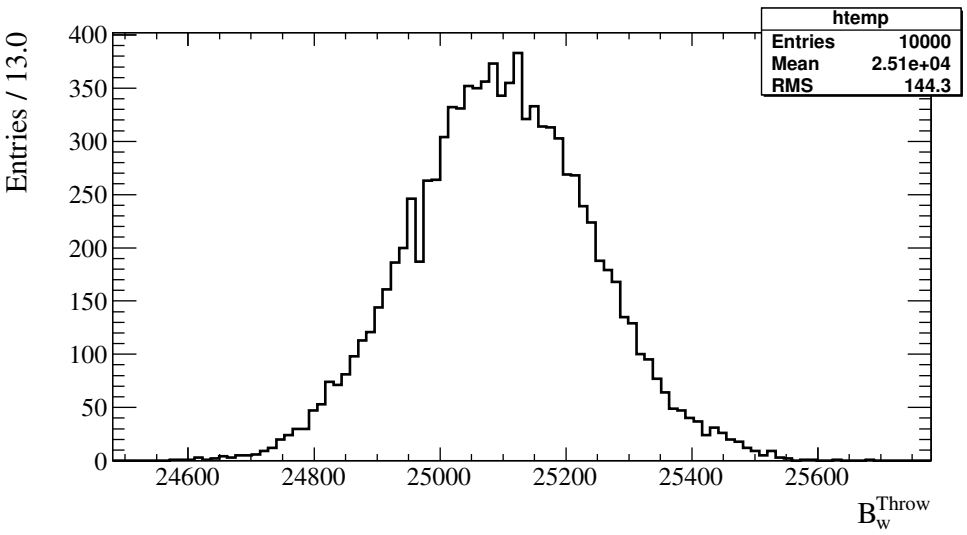

FIGURE 4.96. Number of thrown background events, B_w^{throw}, for 10,000 toy MC throws for the water-in sample for the out-of-fiducial volume background systematics study.

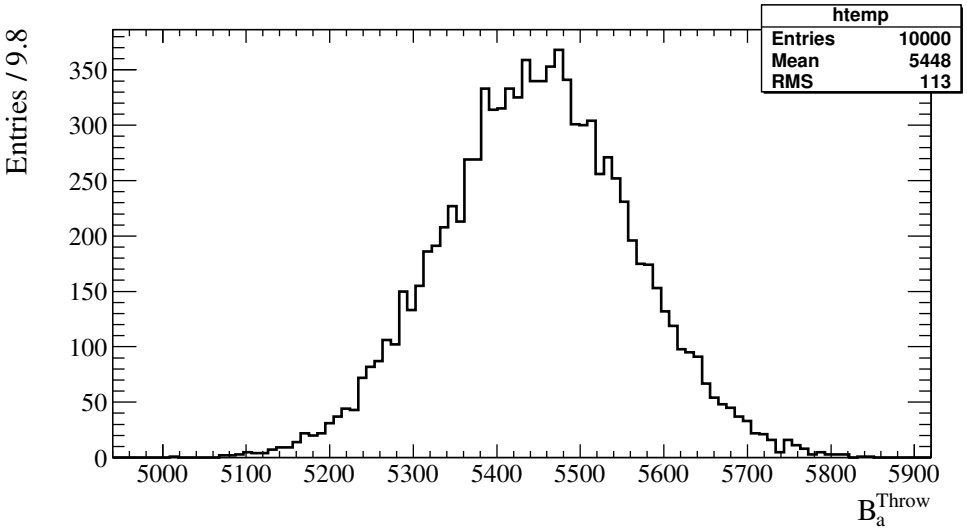

FIGURE 4.97. Number of thrown background events, B_a^{throw}, for 10,000 toy MC throws for the water-out sample for the out-of-fiducial volume background systematics study.

The standard dE/dx PID algorithm uses constants (means and sigmas) provided by the fits to the stopping sand muons in data. In this study, the dE/dx PID cut optimization was repeated using the same PID algorithm, but with constants taken from the fits to the sand muon MC, as opposed to the data. This method will expose any data versus MC

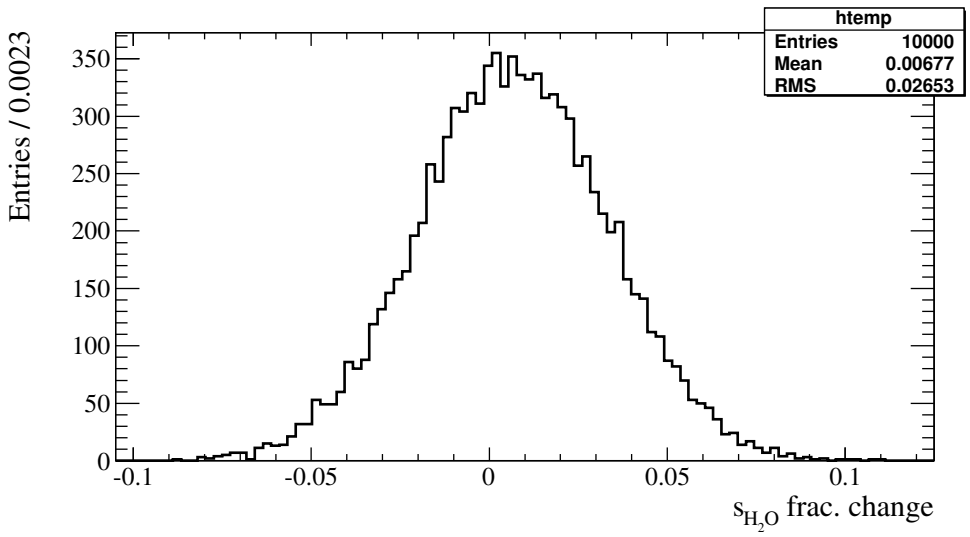

FIGURE 4.98. Fractional difference between number of selected events on water for different number of out-of-fiducial events.

discrepancies associated with the dE/dx PID cut. To evaluate the differences between the two, the PID cut was varied between optimal values for the data-driven (called nominal from now on) algorithm and the MC-driven algorithm.

The dE/dx cut values were varied between 13.9 and 15.3 for Kalman tracks and 4.3 and 4.7 for parametric tracks. These cut ranges were made substaintially big to cover the entire region of interest, i.e. the region between the two peaks in the dE/dx distributions. For every water-in cut value, a water-out one was varied independently within the limits mentioned above. This is equivalent to uncorrelated water-in and water-out uncertainties, and gives a conservative measure of the uncertainty. For each of the PID cut variations, the number of selected events on water after the water subtraction was recalculated for both the nominal and MC-driven PIDs (Figure 4.99).

The fractional difference in the number of events on water between the nominal (data-driven) and MC-driven PIDs is shown in Figure 4.100. The RMS and the mean of the distribution in Figure 4.100 added in quadrature give 2.1%. This value is taken as a conservative systematic uncertainty on the cross section value, and comfortably covers the

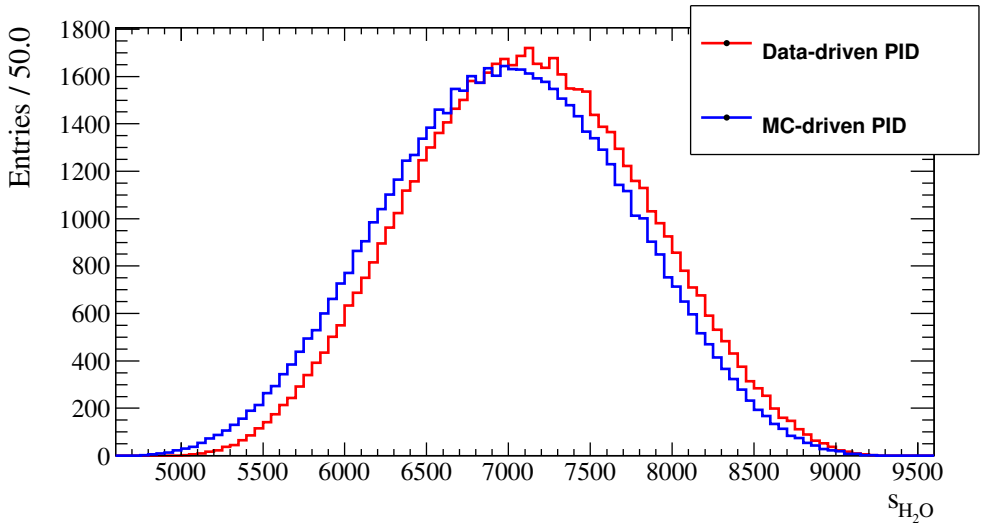

FIGURE 4.99. Number of selected events on water for nominal and MC-driven dE/dx PID.

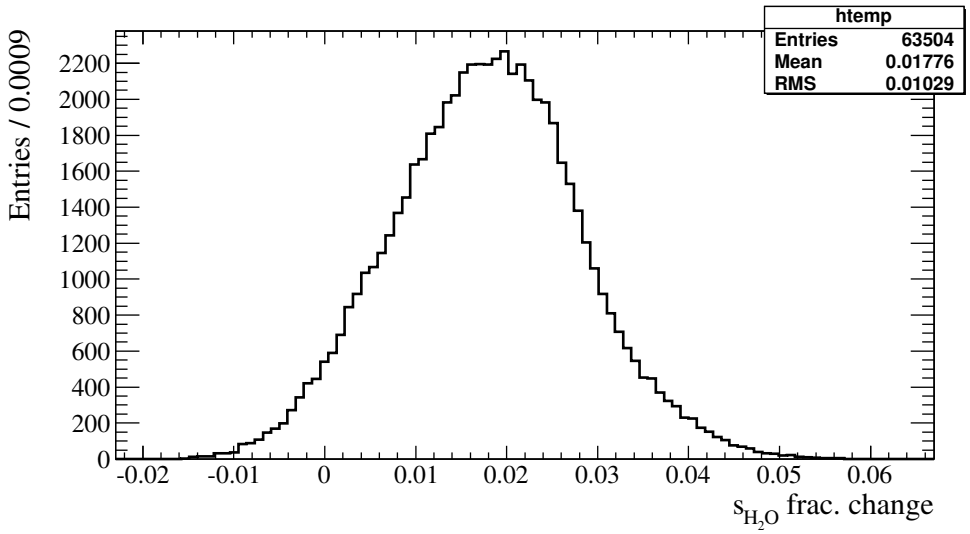

FIGURE 4.100. Fractional difference between number of selected events on water for data-driven and MC-driven dE/dx PID.

dE/dx PID data-MC discrepancy. In future productions of MC simulations it would be necessary to tune the MC energy deposition calibration to better fit the data in order to resolve this issue properly.

4.6.6.4. *Michel Electron Finding Efficiency.* In order to check for possible disagreement between data and MC in the efficiency of finding delayed (Michel electron) hit clusters in the PØD, the following strategy was adopted from the PØD NCE analysis [90].

The side-band samples of data and MC used for this study were sand muons entering the PØD from the upstream face and stopping in the water target or Central ECAL. Selecting sand muons that stop in the PØD allows for the detection of Michel clusters and for the calculation of the Michel cluster finding efficiency.

Every event was required to have exactly one track in the PØD, which starts in its upstream face and stops in the water target or Central ECAL. To get the cleanest possible set of muons, a dE/dx PID was applied to all selected tracks to require every track to be compatible with the μ^-/π^+ dE/dx pull values for muons ($pull < 13.0$ for Kalman tracks and $pull < 2.0$ for parametric tracks).

Using this selection of stopping sand muons, the fraction of events where the reconstruction has found at least one Michel cluster was calculated. The results of this study are shown in Table 4.38.

TABLE 4.38. Fraction of events with at least one Michel cluster in the PØD for stopping sand muons samples.

	water-in	water-out
Data	0.4538 ± 0.0042	0.5201 ± 0.0052
MC	0.4353 ± 0.0017	0.4741 ± 0.0025
(Data-MC)/Data	0.0043 ± 0.0014	0.097 ± 0.017

The following strategy was used to propagate the uncertainty into the final cross section result. For the water-in sample the number of the signal events accepted by the Michel cut in the selection procedure was varied by $\pm 1\sigma$. The number of the pion background events (background events with pions leaving the target nucleus) accepted by the Michel cut was

shifted by $\pm 1\sigma$ simultaneously with the signal shift. For the water-out sample the same procedure was performed as for the water-in, but independently (assuming uncorrelated errors).

Finally, the number of selected events on water (after water subtraction) and fractional difference from the nominal $s_{\mathrm{H_2O}}$ was recalculated. The largest fractional difference, 2.95%, was taken as the systematic uncertainty on the cross section.

4.6.6.5. *Fiducial Volume.* To check the stability of the result for different fiducial volume definitions the following strategy common to most PØD-based analyses are used.

The x-y, z upstream and z downstream fiducial volume boundaries were changed from the nominal values in the steps (σ) equal to the vertex resolution: 33 mm in x-y and 20 mm in z. The effects of the changes in the fiducial volume for data vs MC water-in and water-out samples were investigated.

The vertex resolutions along the ND280 x, y and z axes were obtained using MC water-in and water-out samples with one reconstructed vertex in the PØD fiducial volume with no restrictions on event multiplicity. The disctributions of the difference between MC-truth and reconstructed vertex positions, i.e. x and y vertex resolutions, can be found in Figures 4.101 and 4.102. The x and y boundaries were varied simultaneously by $\pm 2\sigma,\ \pm 1\sigma,\ 0\sigma$. The z upstream boundary was varied by $-1\sigma,\ 0\sigma,\ +1\sigma,\ +2\sigma$ and the z downstream boundary was varied by $-2\sigma,\ -1\sigma,\ 0\sigma,\ +1\sigma$. In the case of z boundary changes, the ECAL regions (-2σ in z upstream and $+2\sigma$ in z downstream case) were avoided, where there are materials with different properties (lead, etc.) than the materials present in the water targets.

All possible combinations of the variations of the boundaries were checked. Tables F.1, F.2 and F.3 in Appendix F lists all 80 parameter sets used.

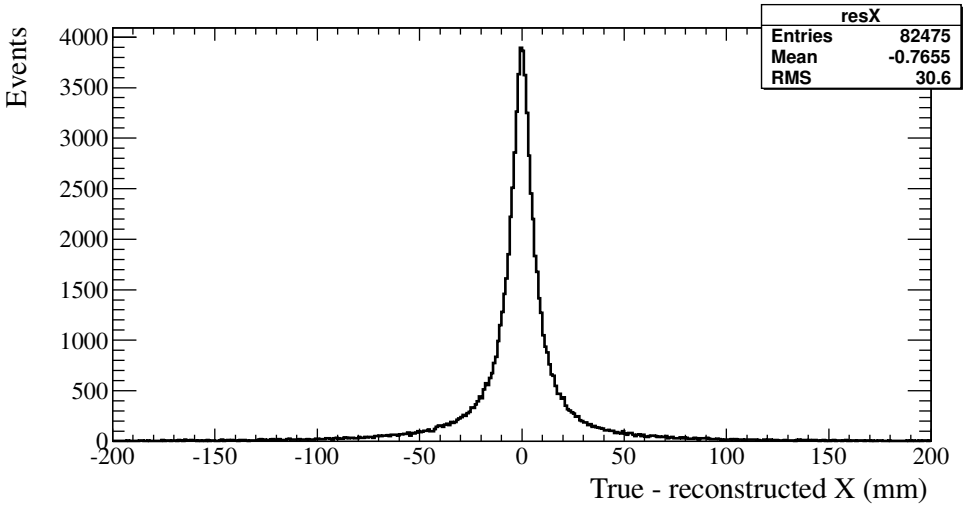

FIGURE 4.101. Difference between the MC-truth and reconstructed vertex position in x for the water-in MC sample.

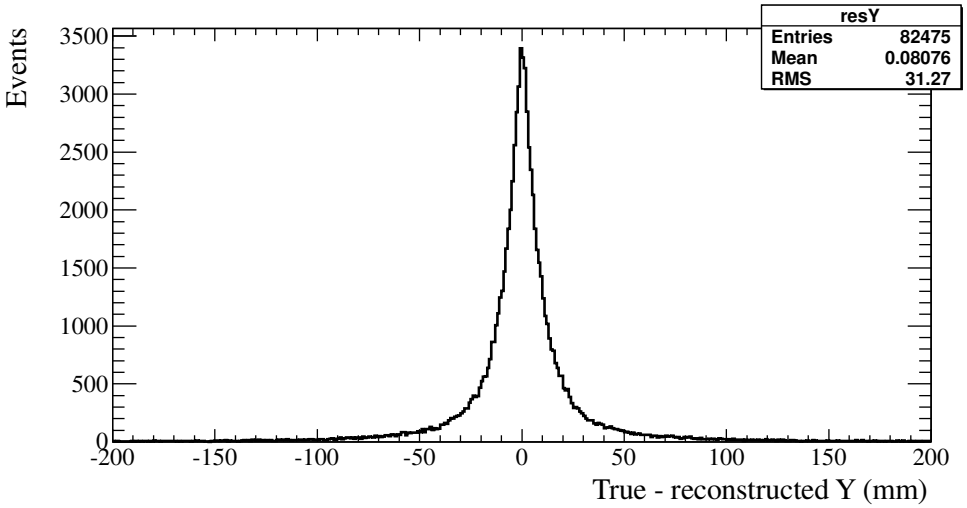

FIGURE 4.102. Difference between MC-truth and reconstructed vertex position in y for the water-in MC sample.

For each combination of variations the difference from the nominal number of events for data and MC was calculated. In the next step the difference between data and MC fractional differences was found. Figures 4.103 and 4.104 show the results of these studies for 80 fiducial volume variations of the water-in and water-out samples. The maximum of the differences between data and MC was measured to be 0.6% for water-in and 1% for water-out. To propagate the differences into the uncertainty on $s_{\mathrm{H_2O}}$, the analytic formula (Equation 54)

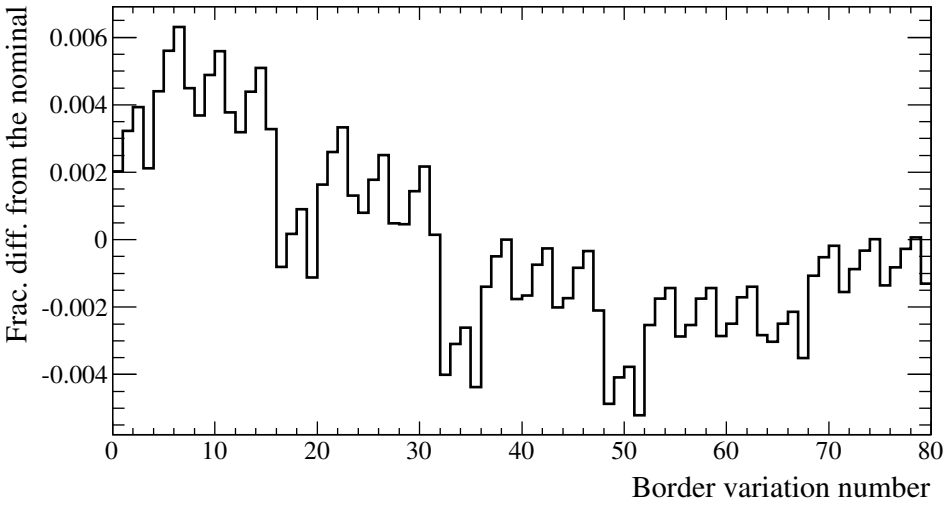

FIGURE 4.103. Difference of MC and data fractional differences for different fiducial volume variations for the water-in sample.

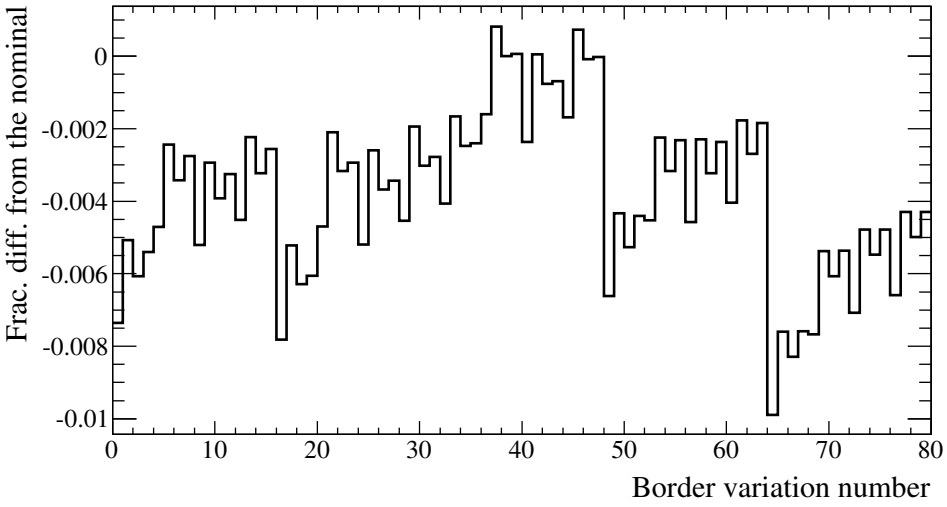

FIGURE 4.104. Difference of MC and data fractional differences for different fiducial volume variations for the water-out sample.

was used. Data-MC differences induced by the effects on the fiducial volume boundaries affect both background estimation as well as the signal selection efficiency. The water-in and water-out maximum differences were taken as the errors on the backgrounds as well as on the efficiencies. Fiducial volume uncertainties between water-in and water-out were assumed to

be correlated, since the shape of the vertex distributions does not depend on whether water is in the PØD or not. The final uncertainty on the cross section value is taken as 2.88%.

4.6.6.6. *PØD Reconstruction Algorithms.* To check for the discrepancies between data and MC in PØD event reconstruction a study was performed in which the subsets of data and MC were reprocessed with different values of the tracking parameters. The road-following (tracking) parameters were varied independently with the steps of σ within $\pm 2\sigma$ boundaries. The parameters, their nominal values and steps are listed below:

(1) Width - road width, nominal value = 80 mm, $\sigma = 20$ mm;

(2) Layer - acceptable track-hit gap, nominal value = 2, $\sigma = 1$;

(3) Angle - angular road width (in radians), nominal value = 0.55, $\sigma = 0.1375$.

The analysis event selection code was run over the reprocessed data and MC sets for the same parameter variations. Afterwards, the fractional differences from the nominal numbers of selected events in both data and MC were calculated for each of the parameters variations. Maximum data-MC differences were 1.1% for the water-in number of selected events, and 3.6% for water-out

Figures 4.105 and 4.106 shows the plots of the difference of the fractional differences between data and MC for all studied parameters variations.

To propagate the differences into the uncertainty on the number of selected events on water, the analytic formula presented in Equation 54 was used. Differences in the PØD reconstruction affect both backgrounds and the efficiency, therefore the water-in and water-out maximum differences were quoted as the errors on both the backgrounds and on the efficiencies. Tracking in the PØD relies on hits in the detector and there are no detector hits in the water target for the water-in mode. Therefore, water-in and water-out uncertainties for

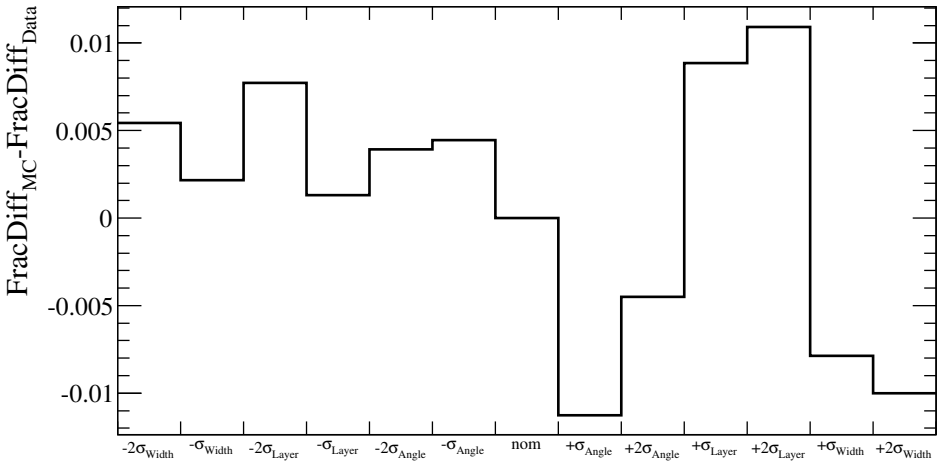

FIGURE 4.105. Difference between the fractional differences in data and Monte Carlo due to p0dRecon tracking parameter variations for the water-in sample.

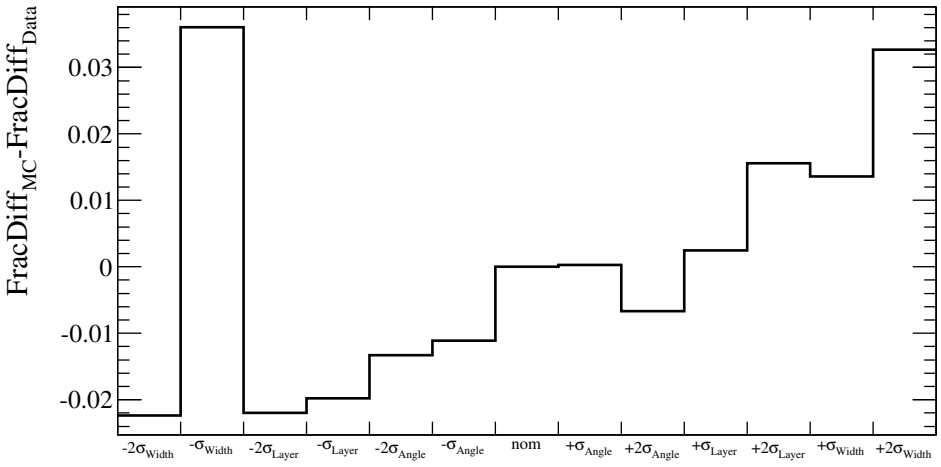

FIGURE 4.106. Difference between the fractional differences in data and Monte Carlo due to p0dRecon tracking parameter variations for the water-out sample.

PØD reconstruction were assumed to be correlated. The final PØD reconstruction uncertainty is quoted as 0.25%.

4.6.6.7. *Sand Muons.* To properly treat the sand muon background, however small it is, external studies performed by Justyna Lagoda were used in this analysis. These studies show that the data/MC ratio for PØD through-going sand muons is 1.084 ± 0.002 [137]. This ratio

is used as a correction for the Monte Carlo sand muon background prediction. To propagate the uncertainty into final cross section result, a 0.2% systematic uncertainty on the efficiency prediction was assigned.

The sand muon fractions of the total background were calculated using Table 4.10. The simulation of sand muons does not depend on whether the water is in the PØD or not. Therefore, it was assumed that the water-in and water-out uncertainties related to sand muons are correlated. Using the analytic formula for the uncertainty propagation (Equation 54), the uncertainty of 3% on s_{H_2O} was obtained.

4.6.6.8. *Other Uncertainties.* The beam power is measured by 5 current transformers (CTs) with an accuracy of 2% [114], however in this analysis this uncertainty, i.e. the POT uncertainty, is folded into the flux uncertainty, which is discussed in Section 4.6.1.

A mistake in PØD data quality flags for Run 3b, when RMM2 was noisy during three ND280 runs - 8350, 8351, and 8359, was identified at the time of finishing this analysis, potentially resulting in a $\sim 1\%$ effect. This number was added in quadrature with the rest of the systematic uncertainties.

During the course of this analysis it was discovered that for less than 0.01% of the events, the reconstructed vertex in the PØD was not properly matched to a simulated MC vertex in the `NRooTrackerVtx` data structure. This effect is tiny compared to other sources of uncertainty, and, therefore, was safe to ignore in this analysis.

4.6.7. Summary of Detector Systematic Uncertainties. A summary of all the detector-related systematic uncertainties and data corrections is shown in Table 4.39. The total detector systematic uncertainty was calculated by adding all the contributions in quadrature, and is quoted as 6.14%.

TABLE 4.39. Summary of detector-related systematic uncertainties for CC1π^+ analysis.

	Sys. Uncertainty	Correction
OOF Background	± 2.7%	no
dE/dx PID	± 2.1%	no
Michel electron	± 2.95%	no
Fiducial volume	± 2.88%	no
PØD reconstruction	± 0.25%	no
Sand muons	± 3%	yes
Other	± 1%	no

4.7. RESULTS

This CC1π^+ analysis used the data collected during T2K Runs 1 - 4 (2010 - 2014) with PØD water-in POT of 2.64×10^{20} and water-out POT of 3.71×10^{20}. Analysis cuts were developed to obtain two CC1π^+ event sub-selections with a focus on contained and partially contained events.

The two selections, developed in this analysis, have a good combined phase space coverage, and an efficiency of 6 - 7% with ∼50% (60%) purity for NEUT (GENIE) for both PØD water-in and water-out samples. A statistical water-in/water-out event rate subtraction technique was used to obtain a CC1π^+ cross section on water as an exclusive target. This is the first measurement of this channel on water as a target.

The cross section obtained for the MD1 mock data (MC scaled to data POT) shown in Equation 45 in Section 4.3.5 was compared against the MC-truth flux-averaged cross section prediction, calculated using an independent method outlined in Appendix D. The agreement between the cross sections is well within the statistical uncertainties, which therefore validates the water subtraction, and the cross section calculation methods. The MC-truth cross section calculation method was independently cross-checked using the before-FSI cross sections

extracted directly from NEUT event generator [152], and good agreement was observed for the case of the oxygen target (no direct benchmark for the cross section on H_2O currently exists).

A data cross section of the ν_μ-induced charged-current single π^+ production channel on water as a target with the full uncertainty was extracted:

$$\langle \sigma_{\nu_\mu \mathrm{CC1}\pi^+} \rangle_\Phi = (1.10 \cdot 10^{-39}) \, {}^{+35.27\%}_{-32.38\%} \, \frac{\mathrm{cm}^2}{\mathrm{nucleon}}$$

$$\left(\begin{array}{ccc} {}^{+15.49\%}_{-15.49\%} \text{ (stat.)} & {}^{+25.16\%}_{-20.12\%} \text{ (flux)} & {}^{+15.02\%}_{-16.04\%} \text{ (xsec)} \\ {}^{+1.91\%}_{-1.91\%} \text{ (FSI)} & {}^{+10.15\%}_{-10.15\%} \text{ (SI)} & {}^{+6.14\%}_{-6.14\%} \text{ (det.)} \end{array} \right),$$

where the result is provided in the form of a single neutrino energy bin cross section integrated over the entire T2K flux (0 - 30 GeV). 2,703 (2,187) data events were selected after analysis cuts with 1,387.2 (1,046.0) predicted background events for water-in (water-out) PØD detector configurations.

In the NEUT water-in (water-out) sample the selected CC1π^+ events have the neutrino energy in the range of 391 MeV - 17.3 GeV (380 MeV - 14.2 GeV). For the GENIE water-in (water-out) sample the selected CC1π^+ events have the neutrino energy in the 403 MeV - 17.3 GeV (395 MeV - 17.3 GeV). In the NEUT water-in (water-out) sample, the mean energy of selected signal events is 1.85 GeV (1.73 GeV), and peak energy is 810 MeV (630 MeV). For the GENIE water-in (water-out) MC, 1.85 GeV (1.76 GeV) is the mean selected signal energy, and 744 MeV (768 MeV) is the peak selected signal energy. Overall, there is measurable disagreement between NEUT and GENIE CC1π^+ models, and further studies are necessary to resolve it.

The data result uncertainty is dominated by flux and cross section models uncertainties, and is consistent with the NEUT-based MC prediction of $1.26 \cdot 10^{-39}$ cm^2. Limited statistics

is the third largest source of the result uncertainty. A comparison of the measured data cross section with the NEUT and GENIE predictions is shown in Figure 4.107. The measurement

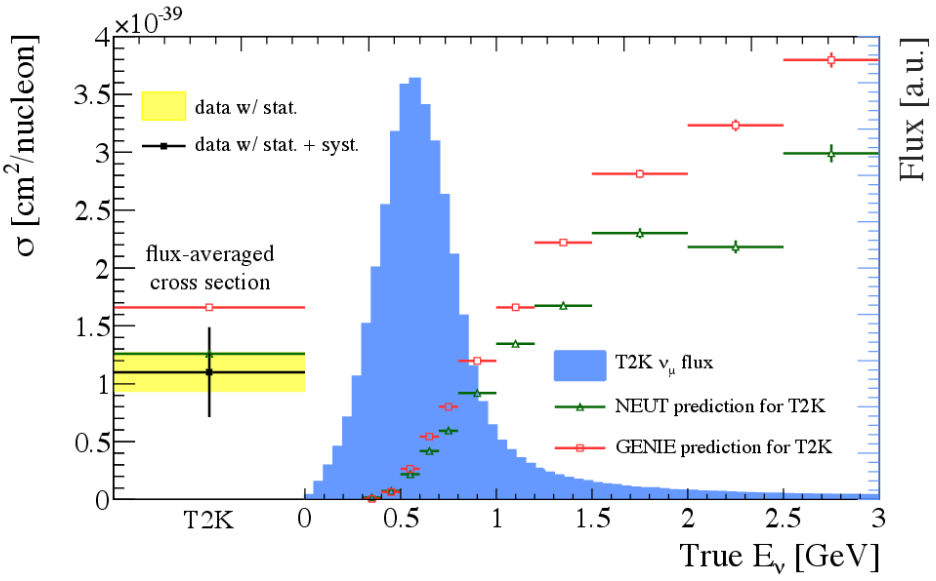

FIGURE 4.107. The PØD-based flux-averaged CC1π^+ cross section on water is shown on the left, together with the single-bin NEUT and GENIE CC1π^+ predictions. Data are shown as black dots, NEUT as green triangles, and GENIE as red squares. T2K ND280 ν_μ area normalized flux is shown as a blue histogram starting at 0 GeV neutrino energy. The binned differential NEUT and GENIE predictions are shown as well.

prefers a lower cross section value than that predicted by the model, but it agrees with both NEUT and GENIE predictions within the uncertanties of the measurement. It is particularly close to the cross section obtained for MD2 mock data, which has the signal prediction scaled by 0.9. The implications and the importance of this result are discussed in the last chapter of this dissertation. Possible future improvements to this measurement are also covered in the last chapter.

CHAPTER 5

Discussion of the Result

5.1. Conclusions

The CC1π^+ cross section on water measured in this analysis is the first measurement of this channel on water as a target. All the previous measurements (ANL, BNL, MiniBooNE etc.) were performed on different targets. It is also a first attempt at measuring the CC1π^+ channel at low neutrino energies, below 1 GeV where data are sparse, with an off-axis neutrino beam.

In this analysis the maximum signal selection efficiency of 8% is obtained at $\sim$800 MeV neutrino energy, and an efficiency of 4 - 8% is predicted for the 400 - 800 MeV range. The low selection efficiency is driven by several factors, including but not limited to PØD detector resolution and reconstruction thresholds, limitations of the PØD event reconstruction software, vast amounts of backgrounds that need to be rejected etc. Also, the single-track and more-than-two-tracks topologies were ignored in this analysis, which leads to a lower overall efficiency. Analysis improvements that may increase the selection efficiency are discussed in Section 5.2.

It is also important to note that the selection efficiency is predicted by MC, and is applied as a single correction factor, and therefore corrects the selected events in the regions were there are no PØD data, e.g. below the CC1π^+ event reconstruction threshold ($E_\nu <\sim 400$ MeV). As a consequence, the measured cross section depends heavily on the implementation of the models in NEUT. For a different generator, e.g. GENIE, the final cross section measurement would be different. The issue of model dependency and ways of mitigating it are discussed in Section 5.2.

The CC1π^+ result presented in this dissertation favors the NEUT model with FSI, which is similar to the MINERνA measurement [92], but different from the MiniBooNE measurement [91] (MiniBooNE result favors the model with no FSI). Interestingly, there are significant discrepancies in both normalization and shape between the MiniBooNE and MINERνA measurements, which are not well understood.

The data presented in this work provide new information about the neutrino-induced single pion production and can be used to place additional constraints on the FSI part of the model, and on coherent pion production. The data are consistent with the NEUT MC predicted value, considering the full uncertainty range, statistical and systematic sources added in quadrature. The data are in better agreement with the NEUT MC prediction, whereas the GENIE MC seems to overpredict the level of the data, which is similar to the observation made in the MINERVA CC1π^+ analysis.

The measurement is dominated by model systematic uncertainties, of which the flux and cross section models are the two largest contributors. The statistical uncertainty, which can be improved with more data, is the third largest uncertainty source.

5.2. Future Work

There are a number of possible improvements that can be made to the PØD-based CC1π^+ measurement, some of which are underway. The final goal of the CC1π^+ research group at Colorado State University, who are extending this analysis, is to publish a differential CC1π^+ cross section on water. In order to achieve this goal, several important steps need to be taken.

One of the highest priority items is to increase the CC1π^+ selection efficiency. This can be achieved in a number of ways:

- expanding the event selection to include other event topologies;

- developing a different event selection using multi-variate analysis techniques to take advantage of less obvious patterns;
- improving event reconstruction performance (p0dRecon), for example dealing with various event mis-reconstruction modes.

Expanding the selection to include one and three track events can potentially increase the number of selected signal events by a factor of two, however in both of these event categories, CC1π^+ is not the dominant channel, and rejecting the background channels is going to be challenging. A multi-variate analysis approach and expanding the selection to include more event topologies are being actively investigated by the CSU group.

Another natural improvement to this analysis would be the reduction of systematic uncertainties. To achieve that, it is possible to perform data-driven background fits using orthogonal datasets (side-band samples), in order to reduce the uncertainty associated with the background normalizations (Appendix E). Potential sideband samples include one-track events, since this topology is dominated by CCQE, two-track events with an inverted dE/dx and Michel cuts, three track events etc. This work has already been started by the members of the CSU group and preliminary estimates show that the total systematic uncertainty could be reduced from $\sim$35% to 10-20%, which would constitute more precise knowledge of this channel than is currenly used in the T2K oscillations analyses.

More data and MC are needed in order to reduce the statistical uncertainties, and Figure 5.1 shows the prediction of the future statistical uncertainty as a function of water-in and water-out POT. From this figure it can be seen that the statistical uncertainty could be reduced to less than 5%, for instance, if there is a factor of six more water-in POT, and factor of six more water-out POT, than used for the current measurement.

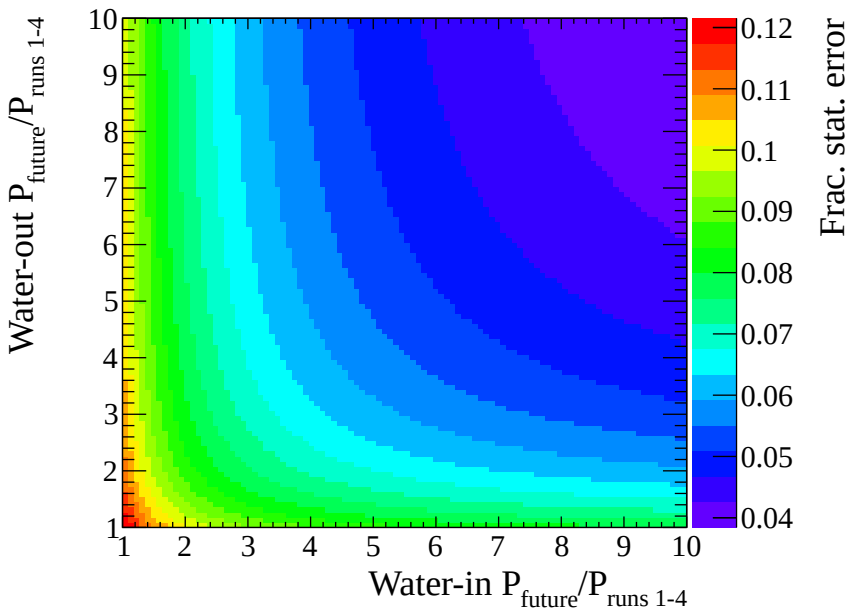

FIGURE 5.1. Future statistical uncertainty predicted for this measurement assuming that signal and background fractions remain the same. P_{future} is future POT, $P_{Runs\ 1-4}$ is the POT for Runs 1-4.

In order to obtain a differential cross section, and to reconstruct the neutrino energy of CC1π^+ events, the momentum of muons, pions and protons would have to be measured. There is some promising progress being made with respect to that. In the NCE analysis [90], which explores the one-track event topology, the momentum of the protons is well reconstructed. However, momentum reconstruction becomes a difficult task in the case of more complicated event topologies, e.g. two or three track events. This is especially the case for low energy pions, because of the hadronic rescattering, which makes them look more like showers than tracks.

A differential cross section measurement would also require a binned efficiency prediction, e.g. ϵ as a function of π^+ momentum and angle, which could allow for a less model dependent measurement. For example, the future differential measurement could focus exclusively on the parts of phase space where there are enough data present, and make no attempts at efficiency correcting the bins where there are none.

The CC1π^+ measurement on water described in this document represents the first steps towards a differential cross section measurement of the CC1π^+ channel with the PØD detector of the T2K near detector complex. Some of the analysis improvements described in this section have already been started by the CSU group, and the next iteration of this analysis will be published in the near future.

References

[1] W. Pauli, Open letter to the group of radioactive people at the Gauverein meeting in Tbingen, Zurich (1930)

[2] M.F. L'Annunziata, Radioactivity, Elsevier, p. 100, ISBN 978-0-444-52715-8 (2007)

[3] F. Reines, C.L. Cowan, Jr, Nature **178** (4531), pp. 446-449 (1956)

[4] G. Danby, J.-M. Gaillard, K. Goulianos, L. M. Lederman, N. B. Mistry, M. Schwartz, J. Steinberger, Phys. Rev. Lett. **9**, pp. 36-44 (1962)

[5] M.L. Perl, G. Abrams, A. Boyarski, M. Breidenbach, D. Briggs, F. Bulos, W. Chinowsky, J.Dakin *et al.*, Phys. Rev. Lett. **35** (22), pp. 1489-1492 (1975)

[6] K. Kodama *et al.* (DONUT Collaboration), Phys. Lett. **B504** (3), pp. 218-224 (2001)

[7] S.J. Barish *et al.*, Phys. Rev. **D16**, 3103 (1977)

[8] G. Radecky *et al.*, Phys. Rev. **D25**, 1161 (1982)

[9] C. Wilkinson *et al.*, `arXiv:1411.4482v1 [hep-ex]` (2014)

[10] K.M. Graczyk, D. Kielczewska, P. Przewlocki, J.T. Sobczyk, Phys. Rev. **D80**, 093001, `arXiv:0908.2175 [hep-ph]` (2009)

[11] K.M. Graczyk, J. Zmuda, J.T. Sobczyk, `arXiv:1407.5445 [hep-ph]` (2014)

[12] S.J. Barish *et al.*, Phys. Rev. **D19**, 2521 (1979)

[13] N.J. Baker *et al.*, Phys. Rev. **D23**, 2499 (1981); G. Fanourakis, *et al.* Phys. Rev. **D21**, 562 (1980)

[14] N.J. Baker *et al.*, Phys. Rev. **D25**, 617 (1982)

[15] R. Davis, D. S. Harmer, K. C. Hoffman, Phys. Rev. Lett. **20**, 1205 (1968)

[16] R. Davis, Phys. Rev. Lett. **12**, 303 (1964)

[17] The Super-Kamiokande Collaboration, Phys. Lett. **B433** (1998)

[18] Q. Ahmad *et al.*, Phys. Rev. Lett. **87** (7), 071301 (2001)

[19] J. Beringer *et al.* (Particle Data Group), Phys. Rev. **D86**, 010001 (2014)

[20] V. Gribov, B. Pontecorvo, Phys. Lett. **B28** (7), pp. 493-496 (1969)

[21] L. Wolfenstein, Phys. Rev. **D17** (9), 2369 (1978)

[22] A. Y. Smirnov. `arXiv:hep-ph/0305106` (2003)

[23] Parke S. J, FERMILAB-CONF-86-130-T, C86-07-16 (1986)

[24] K. Eguchi *et al.* (KamLAND Collaboration), Phys. Rev. Lett. **90** (2), 021802021807. `arXiv:hep-ex/0212021` (2003)

[25] MINOS Collaboration, `http://www-numi.fnal.gov/collab/`

[26] NOνA Neutrino Experiment, `http://www-nova.fnal.gov/`

[27] MINERνA Experiment, `http://minerva.fnal.gov/`

[28] T2K Experiment, `http://t2k-experiment.org/`

[29] LBNE Experiment, `http://lbne.fnal.gov/`

[30] K. Abe *et al.*, `arXiv:1109.3262 [hep-ex]` (2011)

[31] F. P. An *et al.* (Daya Bay Collaboration), Phys. Rev. Lett. **108** (17) (2012)

[32] J. K. Ahn *et al.* (RENO collaboration), `arXiv:1204.0626v2 [hep-ex]` (2012)

[33] K. Zuber, Neutrino Physics, 2nd ed. ISBN 978-1-4200-6471-1 (2011)

[34] S. Bilenky, Introduction to the Physics of Massive and Mixed Neutrinos, ISBN 978-3-642-14042-6 (2010)

[35] The Fourth family of quarks and leptons: second international symposium, ISBN 0-89766-581-3, ISBN 0-89766-582-1 (1989)

[36] M. Goldhaber, L. Grodzins, A.W. Sunyar, Phys. Rev. **109** (3), pp. 1015-1017 (1958)

[37] P. Alspector *et al.*, Phys. Rev. Lett. **36** (15), pp. 837 - 840 (1976)

[38] G. R. Kalbfleisch *et al.*, Phys. Rev. Lett. **43** (19), pp. 1361 - 1364 (1979)

[39] K. Hirata *et al.*, Phys. Rev. Lett. **58** (14), pp. 1490 - 1493 (1987)

[40] R. M. Bionta *et al.*, Phys. Rev. Lett. **58** (14), pp. 1494 - 1496 (1987)

[41] M.J. Longo, Phys. Rev. **D236** (10), pp. 3276 - 3277 (1987)

[42] L. Stodolsky, Phys. Lett. **B201** (3), pp. 353 - 354 (1988).

[43] MINOS Collaboration, Phys. Rev. **D76** (7), arXiv:0706.0437 [hep-ex] (2007)

[44] OPERA Collaboration, Journal of High Energy Physics 2012 (10), p. 93. arXiv:1109.4897v4 (2012)

[45] ICARUS Collaboration, Phys. Lett. **B713** (1), pp. 17 - 22. arXiv:1203.3433 (2012)

[46] Borexino Collaboration, Phys. Lett. B 716 (35), pp. 401 - 405, arXiv:1207.6860 (2012)

[47] LVD and OPERA Collaboration, The European Physical Journal Plus **127** (6), p. 71, arXiv:1206.2488 (2012)

[48] OPERA Collaboration, arXiv:1109.4897v1 (2011)

[49] CMS Collaboration, Phys. Lett. **B716** (1), pp. 30 - 61, arXiv:1207.7235 (2012)

[50] ATLAS Collaboration, Phys. Lett. **B716** (1), pp. 129, arXiv:1207.7214 (2012)

[51] T. Yanagida, Progress of Theoretical Physics **64** (3), pp. 1103 - 1105 (1980)

[52] R. N. Mohapatra, G. Senjanovic, Phys. Rev. Lett. **44** (14), pp. 912 - 915 (1980)

[53] J. Schechter, J.W.F. Valle, Phys. Rev. **22** (9), pp. 2227 - 2235 (1980)

[54] P. Hut, K.A. Olive, Phys. Lett. **B87** (12), pp. 144 - 146 (1979)

[55] A. Goobar, S. Hannestad, E. Mrtsell, H. Tu, Journal of Cosmology and Astroparticle Physics **606** (6), p. 19, arXiv:astro-ph/0602155 (2006)

[56] V.N. Aseev *et al.*, Phys. Rev. **D84**, 112003 (2011)

[57] S. Yasumi *et al.*, Phys. Lett. **B334**, pp. 229 - 233 (1994)

[58] K.A. Assamagan *et al.*, Phys. Rev. **D53**, 6065 (1996)

[59] R. Barate *et al.*, European Physics Journal **C2**, 395 (1998)

[60] E. Giusarma *et al.*, Phys. Rev. **D88**, 063515 (2013)

[61] K.A. Olive *et al.* (Particle Data Group), Chin. Phys. C38, 090001, http://pdg.lbl.gov/2014/listings/rpp2014-list-neutrino-prop.pdf (2014)

[62] R. Davis *et al.*, Phys. Rev. Lett. **20** (21), pp. 1205 - 1209 (1968)

[63] Q.R. Ahmad *et al.* (SNO Collaboration), Phys. Rev. Lett. **87** (7), 071301 (2001)

[64] Y. Fukudae *et al.* (Super-Kamiokande Collaboration), Phys. Rev. Lett. **81** (8), pp. 1562 - 1567 (1998)

[65] F. P. An *et al.* (Daya Bay Collaboration), Phys. Rev. Lett. **108** (17), 1803 (2012)

[66] K. Abe *et al.* (T2K Collaboration), Phys. Rev. Lett. **107**, 041801 (2011)

[67] K. Abe *et al.* (T2K Collaboration), Phys. Rev. **D85**, 031103(R) (2012)

[68] M.H. Ahn *et al.* (K2K Collaboration), Phys. Rev. **D74** (7), 072003, arXiv:hep-ex/0606032 (2006)

[69] D.G. Michael *et al.*, Phys. Rev. Lett. **97** (19), 191801, arXiv:hep-ex/0607088 (2006)

[70] K.A. Olive *et al.* (Particle Data Group), Chin. Phys. **C38**, 090001, http://pdg.lbl.gov/2014/reviews/rpp2014-rev-neutrino-mixing.pdf (2014)

[71] Z. Maki, M. Nakagawa, S. Sakata, Progress of Theoretical Physics, Volume 28, Issue 5, pp. 870-880 (1962)

[72] D. Griffiths, Introduction to Elementary Particles, 2nd ed. ISBN 978-3-527-40601-2 (2012)

[73] K.A. Olive *et al.* (Particle Data Group), Chin. Phys. C38, 090001, http://pdg.lbl.gov/2014/reviews/rpp2014-rev-nu-cross sections.pdf (2014)

[74] J.A. Formaggio, G.P. Zeller. Rev. Mod. Phys. 84, 1307 (2012)

[75] M. Tzanov *et al.*, Phys. Rev. **D74**, 012008 (2006)

[76] C. Anderson *et al.*, Phys. Rev. Lett. **108**, 161802 (2012)

[77] K. Abe *et al.*, Phys. Rev. **D87**, 092003 (2013)

[78] A. Kayis-Topaksu *et al.*, Nucl. Phys. **B798**, 1 (2008)

[79] O. Samoylov *et al.*, Nucl. Phys. **B876**, 339 (2013)

[80] D. Allasia *et al.*, Nucl. Phys. **B343**, 285 (1990)

[81] T. Kitagaki *et al.*, Phys. Rev. **D28**, 436 (1983)

[82] S. Bonetti *et al.*, Nuovo Cimento **A38**, 260 (1977); N.Armenise *et al.*, Nucl. Phys. *B152*, 365 (1979)

[83] D. Casper, Nucl. Phys. (Proc. Supp.) **112**, 161 (2002), default v3 NUANCE

[84] R. Tacik, AIP Conf. Proc. **1405**, 229 (2011); S. Boyd *et al.*, AIP Conf. Proc. **1189**, 60 (2009)

[85] Y. Hayato, Acta Physica Polonica **B**, Vol. 40 (2009)

[86] C. Andreoupoulos *et al.* (GENIE Collaboration), Acta Physica Polonica **B**, Vol. 40 (2009)

[87] H. Gallagher, Nucl. Phys. B - Proc. Supp., Volume 112, p. 188-194 (2002)

[88] L.A. Ahrens *et al.*, Phys. Rev. **D35**, 785 (1987)

[89] A.A. Aguilar-Arevalo *et al.* (MiniBooNE Collaboration), Phys. Rev. **D82**, 092005 (2010)

[90] D. Ruterbories, Ph.D. thesis, `http://inspirehep.net/record/1321638` (2014)

[91] A.A. Aguilar-Arevalo *et al.* (MiniBooNE Collaboration), Phys. Rev. **D83**, 052007 (2011)

[92] B. Eberly *et al.* (MINERνA Collaboration), `arXiv:1406.6415v2 [hep-ex]` (2014)

[93] A. Higuera *et al.* (MINERνA Collaboration), `arXiv:1409.3835v4 [hep-ex]` (2014)

[94] J.T. Sobczyk, J. Zmuda, `arXiv:1410.7788v3 [nucl-th]` (2015)

[95] A.A. Aguilar-Arevalo *et al.* (MiniBooNE Collaboration), Phys. Rev. **D83**, 052009 (2011)

[96] J. A. Formaggio, Rev. Mod. Phys. **84**, pp. 13071341 (2012)

[97] GEANT 4, `http://geant4.cern.ch`

[98] D. Rein and L. Sehgal, Annals of Physics **133**, pp. 79-153 (1981)

[99] R.P. Feynman, M. Kislinger, F. Ravndal, Phys. Rev. **D3**, pp. 27062732 (1971)

[100] C. Berger and L. Sehgal, Phys.Rev. **D76**, 113004, arXiv:0709.4378 [hep-ph] (2007)

[101] K. M. Graczyk and J. T. Sobczyk, Phys. Rev. **D77**, 053001, arXiv:0707.3561 [hep-ph] (2008)

[102] T. Leitner, O. Buss, U. Mosel, and L. Alvarez-Ruso, PoS NUFACT08, 009, arXiv:0809.3986 [nucl-th] (2008)

[103] JLab, https://hallcweb.jlab.org/resdata/database/jlabh2.txt

[104] K. Kuzmin *et al.*, Mod. Phys. Lett. **A19** (2004)

[105] S. Nakamura, H. Kamano, T. S. H. Lee, and T. Sato, arXiv:1303.4152 [hep-ph] (2013)

[106] H. Kamano, S. Nakamura, T.-S. Lee, and T. Sato, Phys. Rev. **D86**, 097503, arXiv:1207.5724 [nucl-th] (2012)

[107] T2K collaboration, T2K letter of intent, JPARC PAC, (2007)

[108] K. Abe *et al.* (T2K Collaboration), arXiv:1502.01550v1 (2015)

[109] Y.Abe *et al.*, Phys. Rev. Lett. **108**, 131801 (2012)

[110] F. An *et al.*, Phys. Rev. Lett. **108**, 171803 (2012)

[111] J. Ahn *et al.*, Phys. Rev. Lett. **108**, 191802 (2012)

[112] K. Abe *et al.* (T2K Collaboration), arXiv:1106.1238 [physics.ins-det] (2011)

[113] JPARC public page, http://j-parc.jp

[114] K. Abe *et al.* (T2K Collaboration), Phys. Rev. **D87**, 012001 (2013)

[115] A.K. Ichikawa *et al.*, Nucl. Instrum. Meth. **A690**, pp. 27-33, ISSN 0168-9002, http://dx.doi.org/10.1016/j.nima.2012.06.045 (2012)

[116] K. Abe *et al.* (T2K Collaboration), Phys. Rev. **D87**, 092003 (2013)

[117] K. Abe *et al.* (T2K Collaboration), Phys. Rev. **D90**, 072012 (2014)

[118] K. Abe *et al.* (T2K Collaboration), Phys. Rev. Lett. **113**, 241803 (2014)

[119] K. Abe *et al.* (T2K Collaboration), Phys. Rev. **D90**, 052010 (2014)

[120] Super-Kamiokande webpage, `http://www-sk.icrr.u-tokyo.ac.jp`

[121] K. Abe *et al.* (Super-Kamiokande Collaboration), Phys. Rev. **D90**, 072005 (2014)

[122] K. Abe *et al.*, Nucl. Instrum. Meth. **A694**, pp. 211 - 223 (2012)

[123] ND280 public page, `http://nd280.org`

[124] P.-A. Amaudruz *et al.*, Nucl. Instrum. Meth. **A696**, pp. 1-31, ISSN 0168-9002, `http://dx.doi.org/10.1016/j.nima.2012.08.020` (2012)

[125] N. Abgrall *et al.*, Nucl. Instrum. Meth. **A637**, Issue 1, pp. 25-46, ISSN 0168-9002, `http://dx.doi.org/10.1016/j.nima.2011.02.036` (2011)

[126] S. Aoki *et al.*, Nucl. Instrum. Meth. **A698**, pp. 135-146 (2013)

[127] S. Assylbekov *et al.*, Nucl. Instrum. Meth. **A686**, pp. 48-63 (2012)

[128] D. Allan *et al.*, JINST 8 P10019, `doi:10.1088/1748-0221/8/10/P10019` (2012)

[129] ROOT data analysis framework, `http://root.cern.ch/`

[130] MIDAS wiki page, `https://midas.triumf.ca/`

[131] K. Connolly, Ph.D. thesis, Univ. of Washington,
`http://www.t2k.org/docs/thesis/043` (2014)

[132] I. Taylor, Ph.D. thesis, Univ. of London,
`http://www.t2k.org/docs/thesis/001` (2009)

[133] L. Trung, Ph.D. thesis, University of Stony Brook,
`http://www.t2k.org/docs/thesis/002` (2010)

[134] MINOS Collaboration, `arXiv:hep-ex/0204021v1` (2002)

[135] A. Hillairet *et al.*, T2K Internal Technical Note, T2K-TN-72 (2013)

[136] S. Assylbekov, T. Wachala, R.J. Wilson, T2K Internal Technical Note, T2K-TN-136 (2014)

[137] C. Bojechko *et al.*, T2K Internal Technical Note, T2K-TN-152, v4.2 (2013)

[138] K. Gilje, T2K Internal Technical Note, T2K-TN-73, v3.1 (2013)

[139] M. Ravonel *et al.*, T2K Internal Technical Note, T2K-TN-117, v7 (2013)

[140] T. Campbell *et al.*, T2K Internal Technical Note, T2K-TN-80, v4 (2013)

[141] Cholesky factorization, N.J. Higham (originator), Encyclopedia of Mathematics, Springer, ISBN 978-1-55608-010-4

[142] P. De Perio *et al.*, T2K Internal Technical Note, T2K-TN-108 (2012)

[143] P. De Perio *et al.*, T2K Internal Technical Note, T2K-TN-113 (2012)

[144] G. Lopez *et al.*, T2K Internal Technical Note, T2K-TN-56 (2011)

[145] D. Ruterbories, T2K Internal Technical Note, T2K-TN-131 (2012)

[146] K. Suzuki, `http://www.t2k.org/beam/NuFlux/FluxRelease/11brelease`

[147] R. Barlow, `arXiv:hep-ex/0207026` (2002)

[148] J. Orear, Notes on statistics for physicists, UCRL-8417,
`http://nedwww.ipac.caltech.edu/level5/Sept01/Orear/frames.html`

[149] R. Bevington, Data reduction and analysis for the physical sciences, McGraw Hill (1969)

[150] M. Hartz, T2K Internal Technical Note, T2K-TN-145 (2013)

[151] M. Hartz, T2K Internal Technical Note, T2K-TN-172 (2013)

[152] P. De Perio, NEUT v5.0.7 Cross Sections,
`http://www.t2k.org/asg/xsec/niwgdocs/neut/neut_xsecs/`

[153] P. de Perio, T2K Internal Technical Note, T2K-TN-32 v1.0 (2010)

APPENDIX A

Non-ν_μ Backgrounds After Cuts

The non-ν_μ background contamination after analysis cuts is small compared to ν_μ backgrounds, and it therefore does not affect the analysis results. Tables A.1, A.2, A.3 and A.4 show the exact numbers for non-ν_μ background as predicted by NEUT MC for water-in and water-out PØD configurations.

Table A.1. Fiducial ν_e-induced background for PØD water-in NEUT MC sample for both contained and non-contained selections combined. Fractions are calculated with respect to the total water-in background.

NEUT Code	Reaction	Fraction (%)
1	$\nu_e + n \to e^- + p$	0.25
11	$\nu_e + p \to e^- + p + \pi^+$	0.44
12	$\nu_e + n \to e^- + p + \pi^0$	0.03
13	$\nu_e + n \to e^- + n + \pi^+$	0.13
16	$\nu_e + N \to e^- + N + \pi^+$	0.12
21	$\nu_e + (n\|p) \to e^- + (n\|p) + \text{multi-}\pi$	0.11
23	$\nu_e + n \to e^- + \Lambda + K^+$	0.00
26	$\nu_e + (n\|p) \to e^- + (n\|p) + \text{mesons}$	0.04
31	$\nu_e + n \to \nu_e + n + \pi^0$	0.02
32	$\nu_e + p \to \nu_e + p + \pi^0$	0.07
33	$\nu_e + n \to \nu_e + p + \pi^-$	0.03
34	$\nu_e + p \to \nu_e + n + \pi^+$	0.03
36	$\nu_e + N \to \nu_e + N + \pi^0$	0.01
41	$\nu_e + (n\|p) \to \nu_e + (n\|p) + \text{multi-}\pi$	0.07
42	$\nu_e + n \to \nu_e + n + \eta^0$	0.01
43	$\nu_e + p \to \nu_e + p + \eta^0$	0.01
46	$\nu_e + (n\|p) \to \nu_e + (n\|p) + \text{mesons}$	0.02

TABLE A.2. Fiducial $\overline{\nu}_e$-induced background composition for PØD water-in MC sample for both contained and non-contained selections combined. Fractions are calculated with respect to the total water-in background.

NEUT Code	Reaction	Fraction (%)
-41	$\overline{\nu}_e + (n\|p) \rightarrow \overline{\nu}_e + (n\|p) + \text{multi-}\pi$	0.01
-36	$\overline{\nu}_e + N \rightarrow \overline{\nu}_e + N + \pi^0$	0.00
-34	$\overline{\nu}_e + p \rightarrow \overline{\nu}_e + n + \pi^+$	0.00
-31	$\overline{\nu}_e + n \rightarrow \overline{\nu}_e + n + \pi^0$	0.00
-26	$\overline{\nu}_e + (n\|p) \rightarrow e^+ + (n\|p) + \text{mesons}$	0.00
-21	$\overline{\nu}_e + (n\|p) \rightarrow e^+ + (n\|p) + \text{multi-}\pi$	0.01
-16	$\overline{\nu}_e + N \rightarrow e^+ + N + \pi^-$	0.02
-13	$\overline{\nu}_e + p \rightarrow e^+ + p + \pi^-$	0.02
-12	$\overline{\nu}_e + p \rightarrow e^+ + n + \pi^0$	0.00
-11	$\overline{\nu}_e + n \rightarrow e^+ + n + \pi^-$	0.02
-1	$\overline{\nu}_e + p \rightarrow e^+ + n$	0.00

TABLE A.3. Fiducial ν_e-induced background composition for PØD water-out MC sample for both contained and non-contained selections combined. Fractions are calculated with respect to the total water-out background.

NEUT Code	Reaction	Fraction (%)
1	$\nu_e + n \rightarrow e^- + p$	0.22
11	$\nu_e + p \rightarrow e^- + p + \pi^+$	0.29
12	$\nu_e + n \rightarrow e^- + p + \pi^0$	0.07
13	$\nu_e + n \rightarrow e^- + n + \pi^+$	0.18
16	$\nu_e + N \rightarrow e^- + N + \pi^+$	0.22
22	$\nu_e + n \rightarrow e^- + p + \eta^0$	0.05
32	$\nu_e + p \rightarrow \nu_e + p + \pi^0$	0.02
33	$\nu_e + n \rightarrow \nu_e + p + \pi^-$	0.03
34	$\nu_e + p \rightarrow \nu_e + n + \pi^+$	0.03
36	$\nu_e + N \rightarrow \nu_e + N + \pi^0$	0.03
41	$\nu_e + (n\|p) \rightarrow \nu_e + (n\|p) + \text{multi-}\pi$	0.08
46	$\nu_e + (n\|p) \rightarrow \nu_e + (n\|p) + \text{mesons}$	0.09

TABLE A.4. Fiducial $\overline{\nu}_e$-induced background composition for PØD water-out MC sample for both contained and non-contained selections combined. Fractions are calculated with respect to the total water-out background.

NEUT Code	Reaction	Fraction (%)
-43	$\overline{\nu}_e + p \rightarrow \overline{\nu}_e + p + \eta^0$	0.02
-41	$\overline{\nu}_e + (n\|p) \rightarrow \overline{\nu}_e + (n\|p) + \text{multi-}\pi$	0.02
-16	$\overline{\nu}_e + N \rightarrow e^+ + N + \pi^-$	0.06
-13	$\overline{\nu}_e + p \rightarrow e^+ + p + \pi^-$	0.02
-12	$\overline{\nu}_e + p \rightarrow e^+ + n + \pi^0$	0.04

APPENDIX B

GENIE Selection

In this appendix, the results of the event selection using the GENIE MC samples are presented.

Table B.1 summarizes the entire event selection (Selections One and Two combined) for the predictions of the GENIE simulation for water-in and water-out modes (scaled to data POT). B is the number of background events predicted by GENIE MC, and ϵ and p are the

Table B.1. Summary of event selection for both sub-selections. No flux tuning and no corrections have been applied. Quantities are calculated using GENIE Monte Carlo simulation.

	B	ϵ	p
water-in	1,084.0	7.0%	60.4%
water-out	849.0	5.9%	59.5%

efficiency and purity of the event selection.

Comparing the GENIE-based selection performance numbers from Table B.1 and NEUT numbers from Table 4.10, it is clear that GENIE predicts less background for both water-in - 1,084.02 (1208.03 for NEUT), and water-out - 848.97 (931.98 for NEUT). The purity of the selection is higher for GENIE: 60.35% (50.79% for NEUT) and 59.46% (50.97% for NEUT). The efficiencies of the selection are comparable between GENIE and NEUT.

The efficiency of the selection as a function of muon candidate MC-truth kinematic properties (momentum and angle with respect to the z axis) and pion candidate MC-truth kinematic properties is shown in Figures B.1, B.2, B.3, and B.4.

Efficiency distributions for GENIE in Figures B.1, B.2, B.3, and B.4 have similar shapes to the distributions for NEUT (Figures 4.56, 4.57, 4.58, and 4.59).

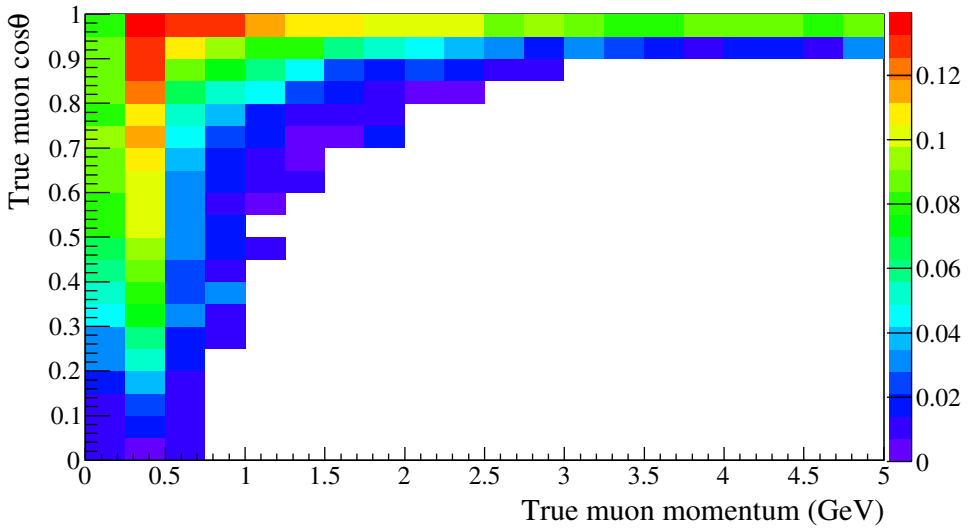

FIGURE B.1. Overall efficiency of both selections combined as a function of the MC-truth muon candidate momentum and cos(θ) for GENIE water-in MC.

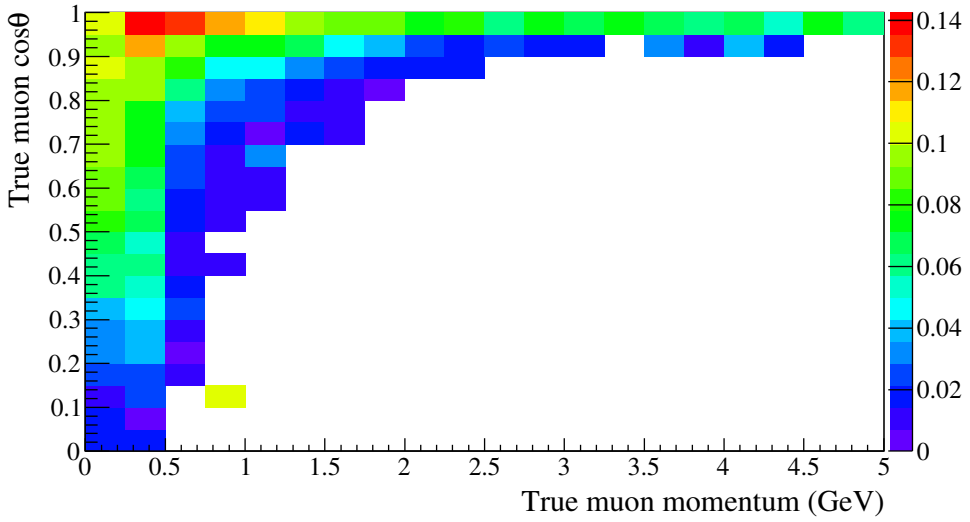

FIGURE B.2. Overall efficiency of both selections combined as a function of the MC-truth muon candidate momentum and cos(θ) for GENIE water-out MC.

The efficiency as a function of MC-truth neutrino energy is shown in Figures B.5, and B.6. The efficiencies as a function of MC-truth neutrino energy for GENIE (Figures B.5, and Figures B.6) also have very similar shape to the NEUT-based distributions (Figures 4.60, and 4.61).

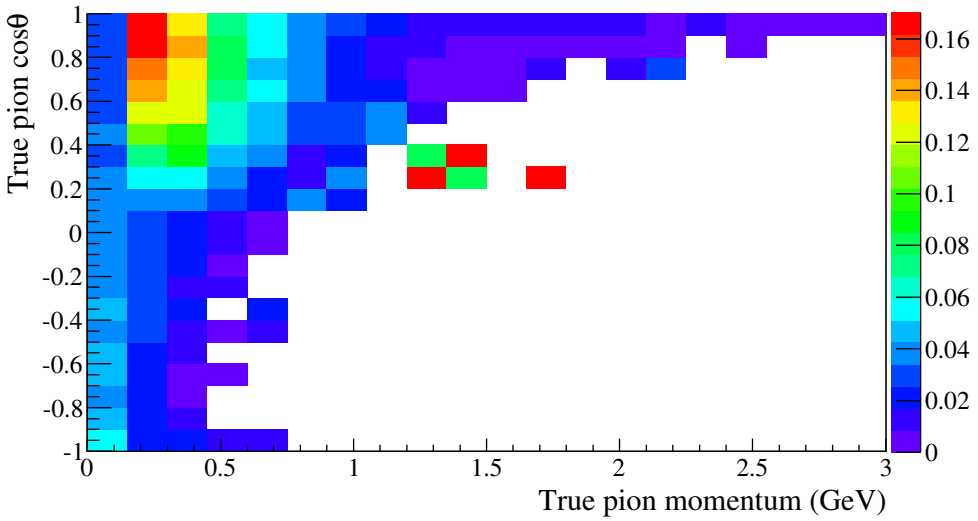

FIGURE B.3. Overall efficiency of both selections combined as a function of the MC-truth pion candidate momentum and cos(θ) for GENIE water-in MC.

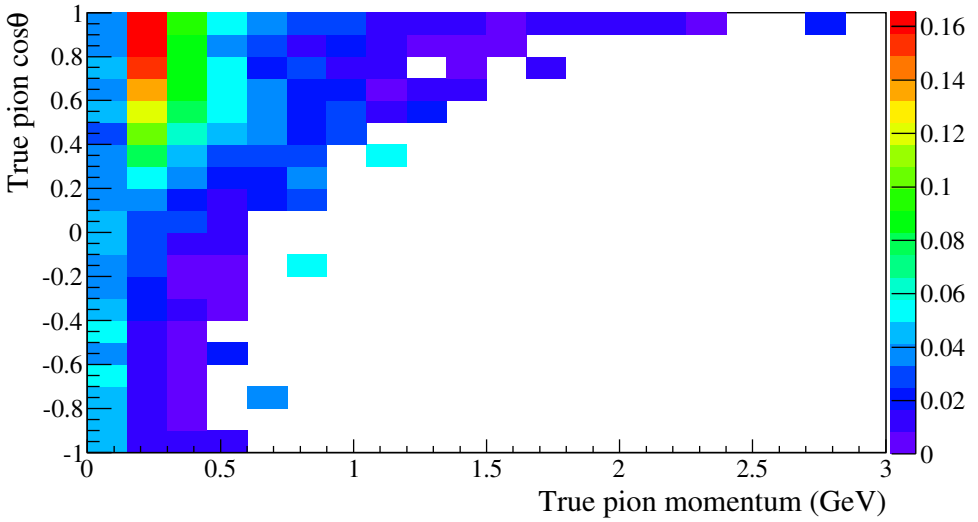

FIGURE B.4. Overall efficiency of both selections combined as a function of the MC-truth pion candidate momentum and cos(θ) for GENIE water-out MC.

The rest of the figures in this appendix show the comparisons of the reconstructed kinematic variables for data and GENIE MC for both selections, i.e. Selections One and Two. MC is always normalized to corresponding data POT with flux tuning 11b v3.2 and all corrections applied, unless otherwise stated.

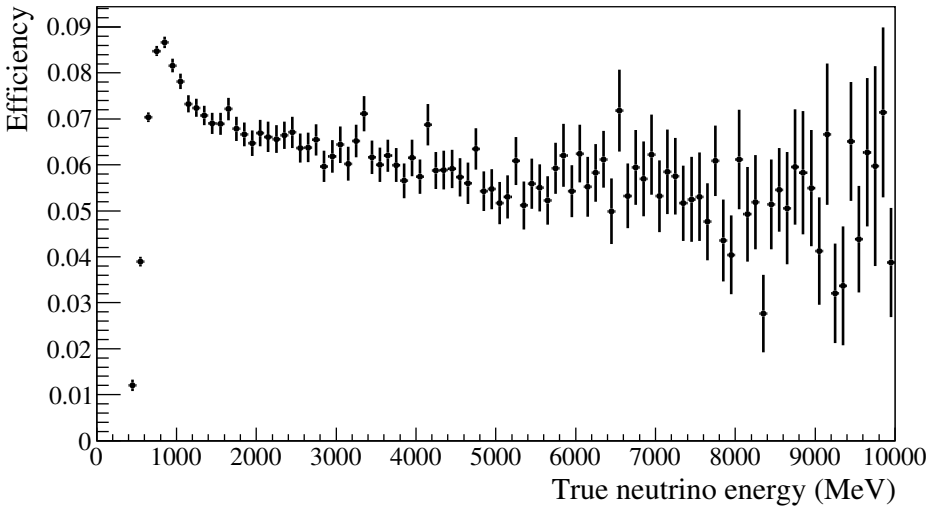

FIGURE B.5. Overall efficiency as a function of MC-truth neutrino energy for the water-in GENIE MC.

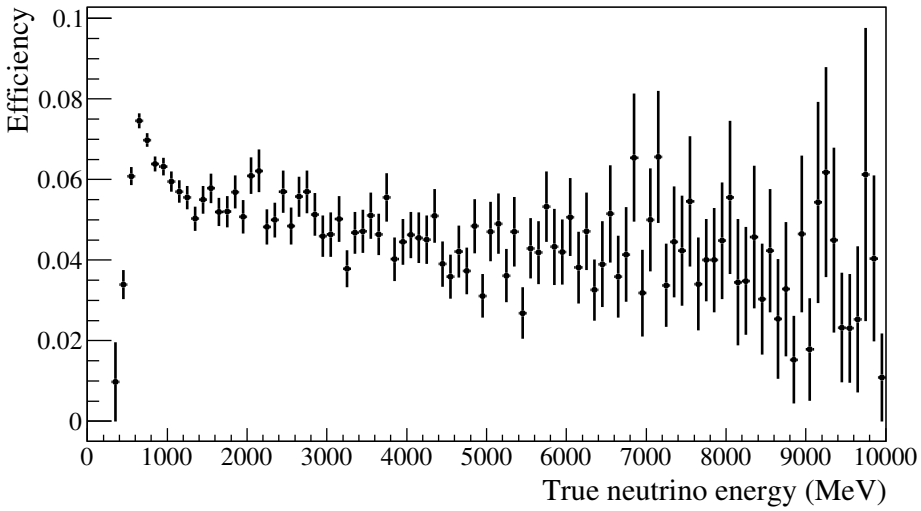

FIGURE B.6. Overall efficiency as a function of MC-truth neutrino energy for the water-out GENIE MC.

Figures B.7, B.8, B.9, and B.10 show kinematic distributions of the μ^- candidate tracks for Selection One. Figures B.11, B.12, B.13, and B.14, show kinematic distributions of the π^+ candidate tracks for Selection One.

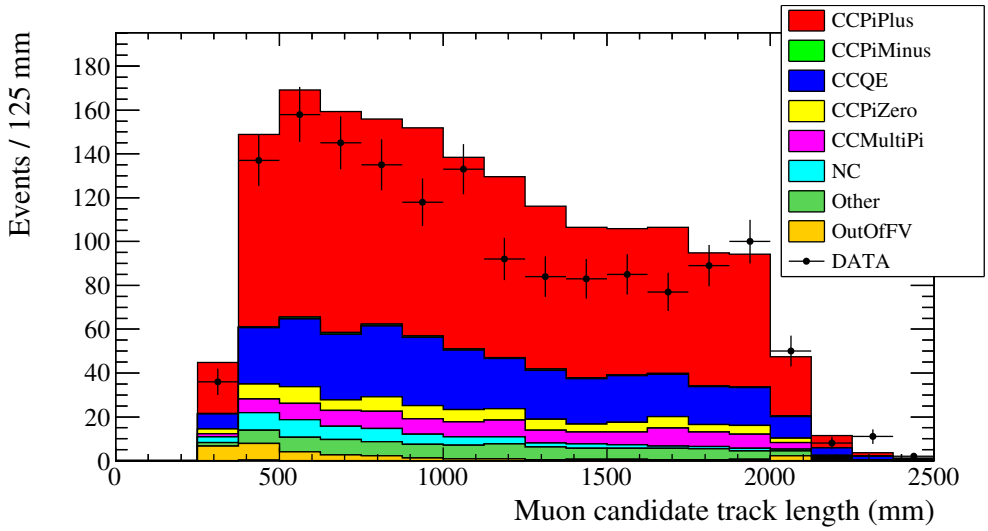

FIGURE B.7. Muon candidate track length after Selection One for water-in data and GENIE MC.

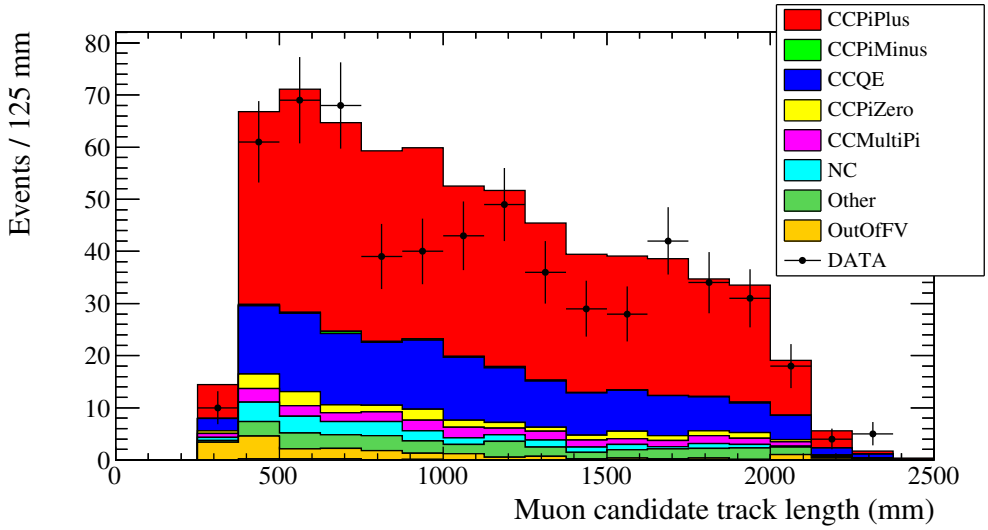

FIGURE B.8. Muon candidate track length after Selection One for water-out data and GENIE MC.

Figures B.15, B.16, B.17, and B.18 show kinematic distributions of the μ^- candidate tracks for Selection Two. Figures B.19, B.20, B.21, and B.22, show kinematic distributions of the π^+ candidate tracks for Selection Two.

From these data-MC comparison plots it can be seen that the GENIE predictions tend to be higher than the data points. This is the opposite to what was seen for NEUT. The

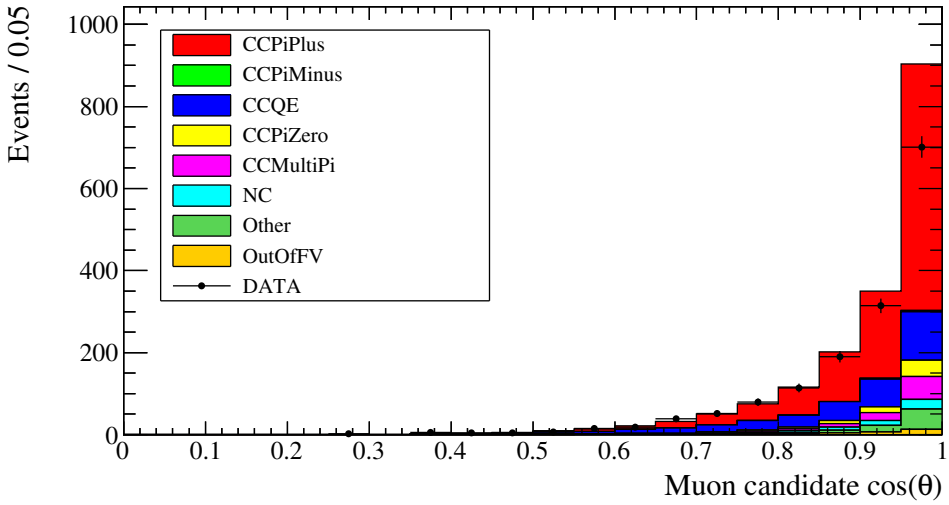

FIGURE B.9. Muon candidate track $\cos(\theta)$ after Selection One for water-in data and GENIE MC.

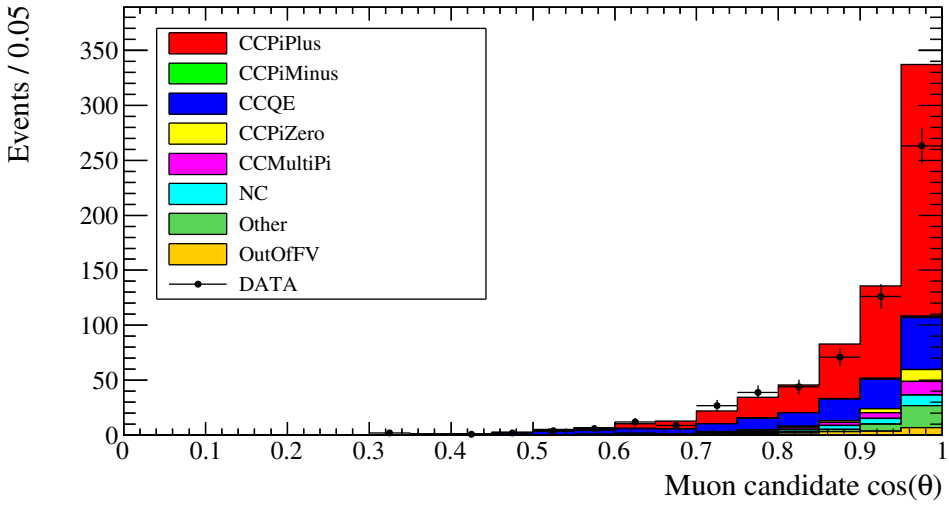

FIGURE B.10. Muon candidate track $\cos(\theta)$ after Selection One for water-out data and GENIE MC.

agreement in shape between data and the GENIE MC is relatively good, and comparable to the one for NEUT.

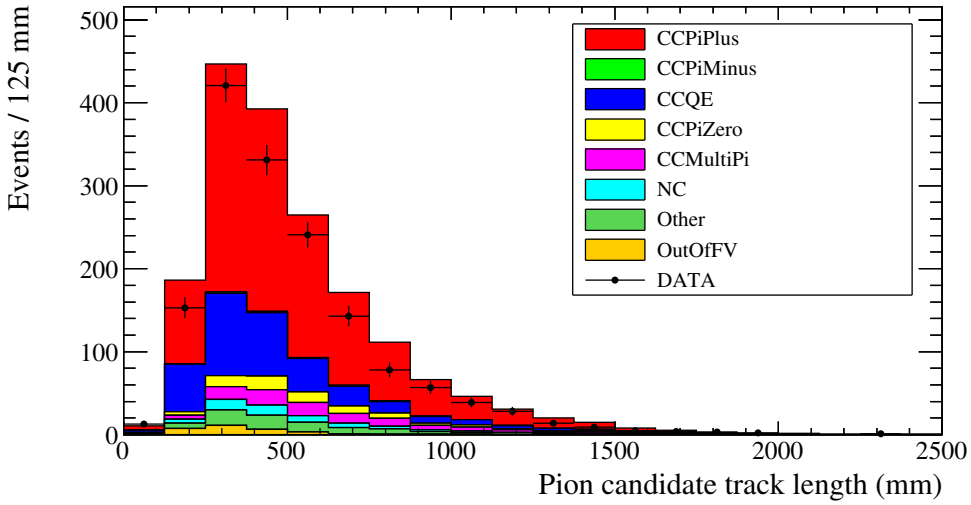

FIGURE B.11. Pion candidate track length after Selection One for water-in data and GENIE MC.

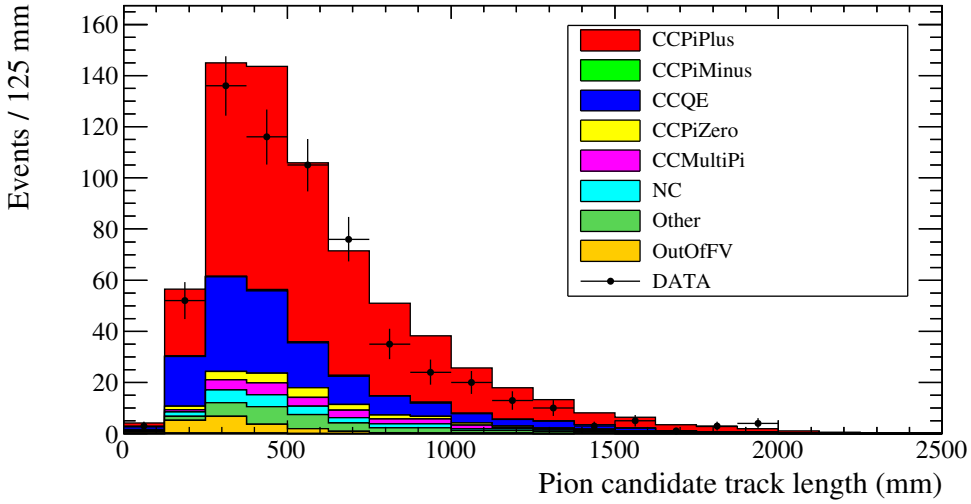

FIGURE B.12. Pion candidate track length after Selection One for water-out data and GENIE MC.

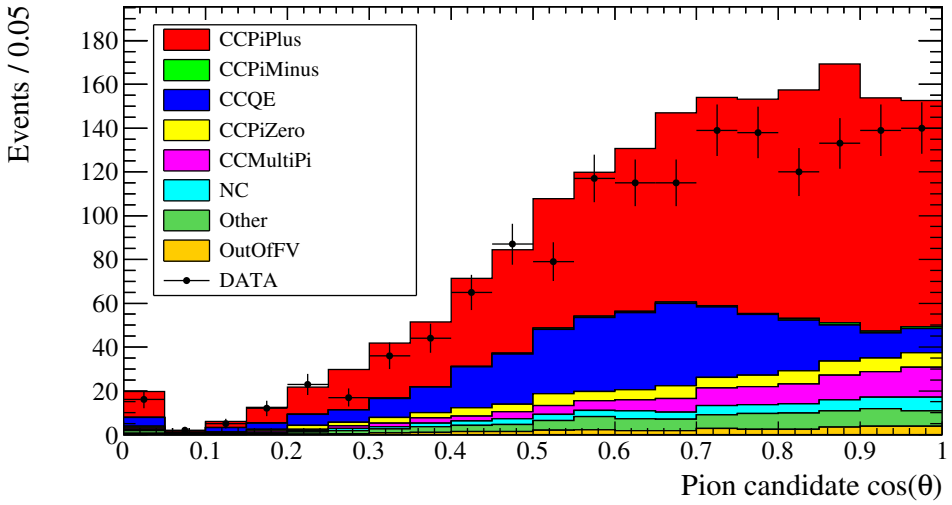

FIGURE B.13. Pion candidate track $\cos(\theta)$ after Selection One for water-in data and GENIE MC.

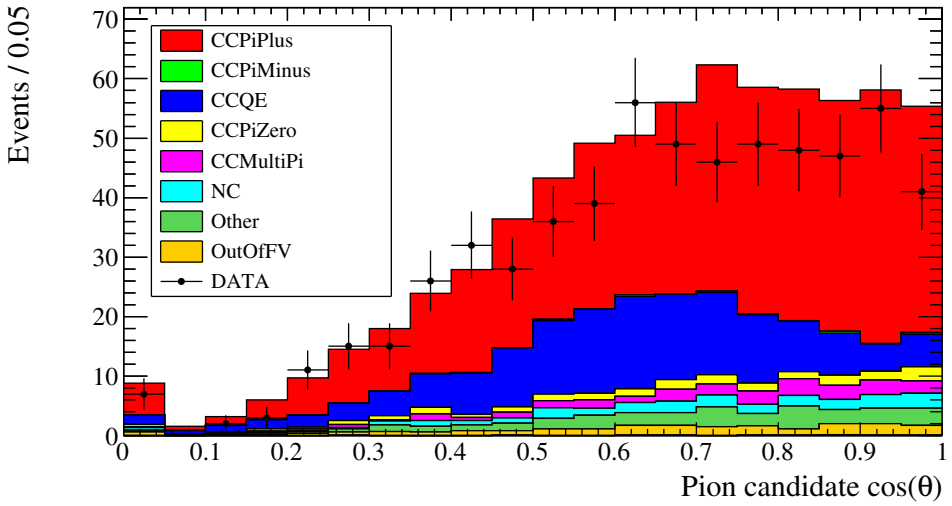

FIGURE B.14. Pion candidate track $\cos(\theta)$ after Selection One for water-out data and GENIE MC.

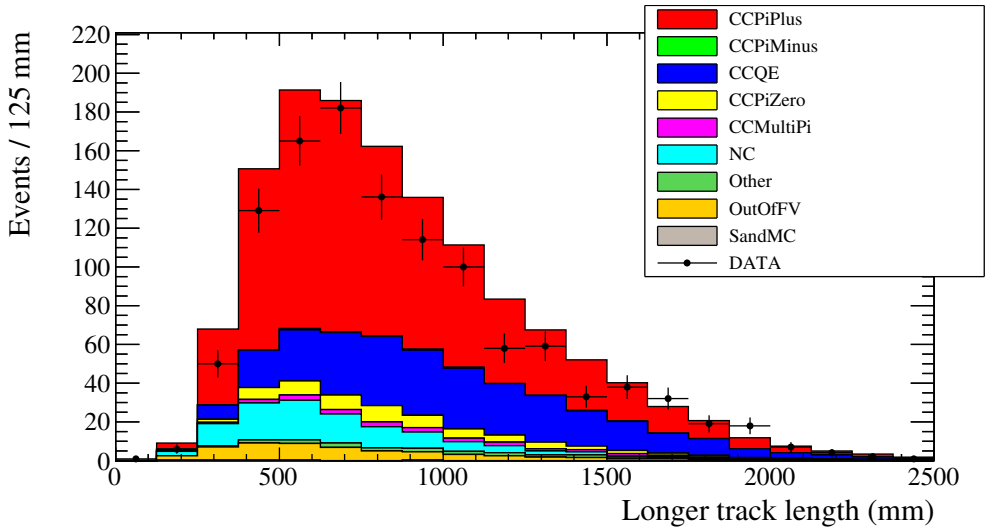

FIGURE B.15. Track length of the longer track after Selection Two for water-in data and GENIE MC.

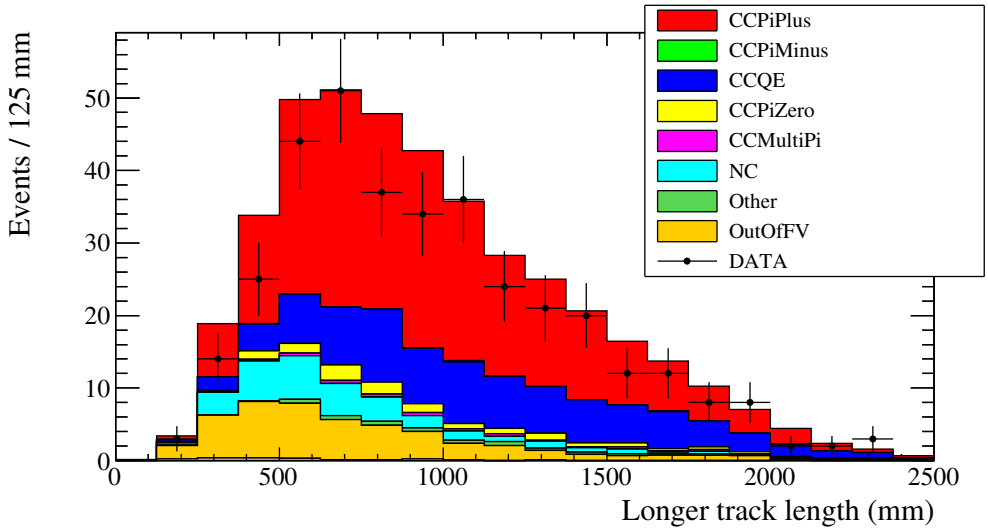

FIGURE B.16. Track length of the longer track after Selection Two for water-out data and GENIE MC.

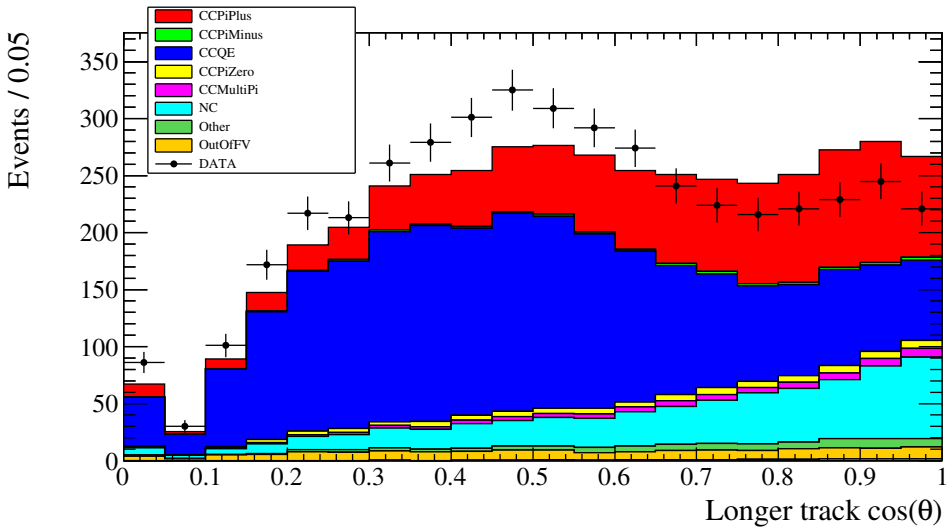

FIGURE B.17. Track $\cos(\theta)$ of the longer track after Selection Two for water-in data and GENIE MC.

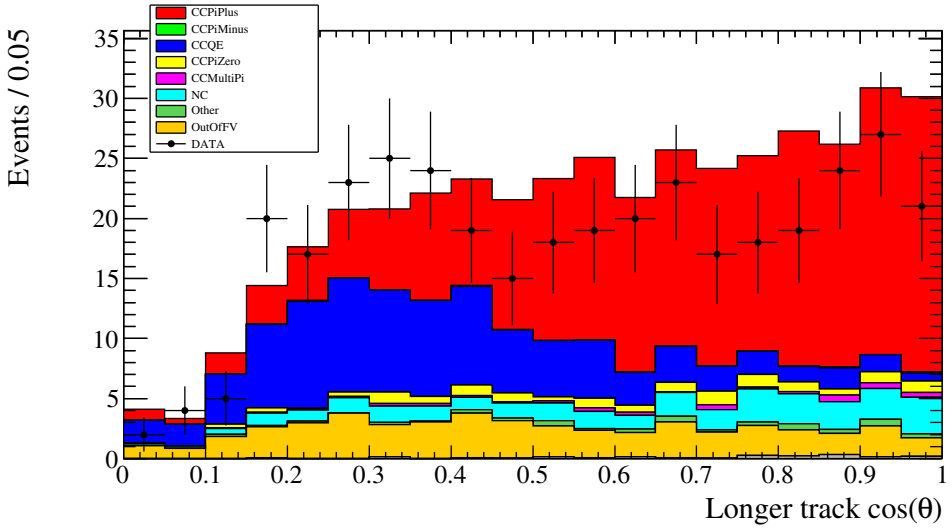

FIGURE B.18. Track $\cos(\theta)$ of the longer track after Selection Two for water-out data and GENIE MC.

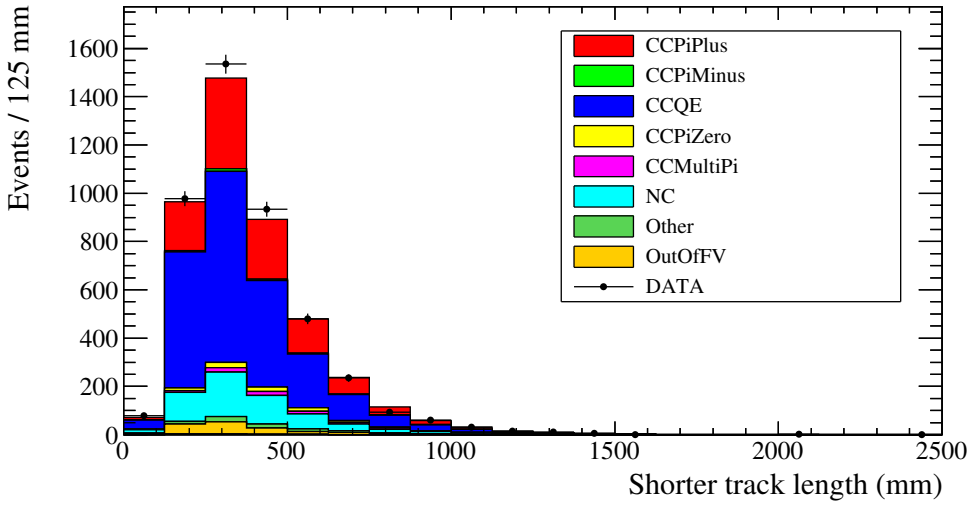

FIGURE B.19. Track length of the shorter track after Selection Two for water-in data and GENIE MC.

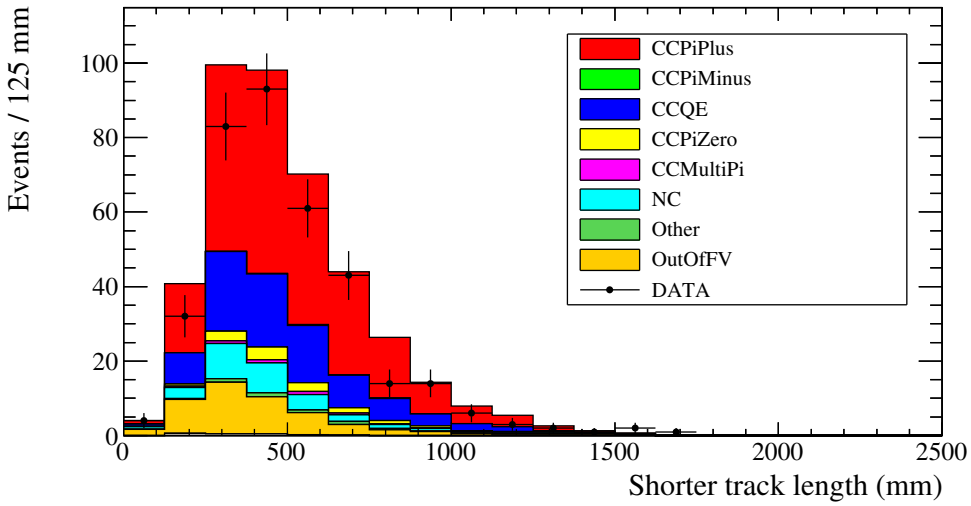

FIGURE B.20. Track length of the shorter track after Selection Two for water-out data and GENIE MC.

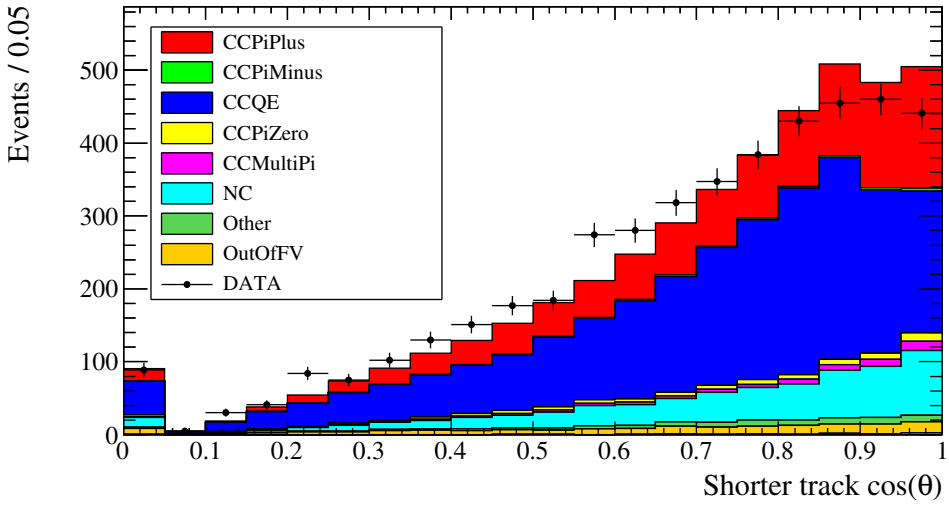

FIGURE B.21. Track $\cos(\theta)$ of the shorter track after Selection Two for water-in data and GENIE MC.

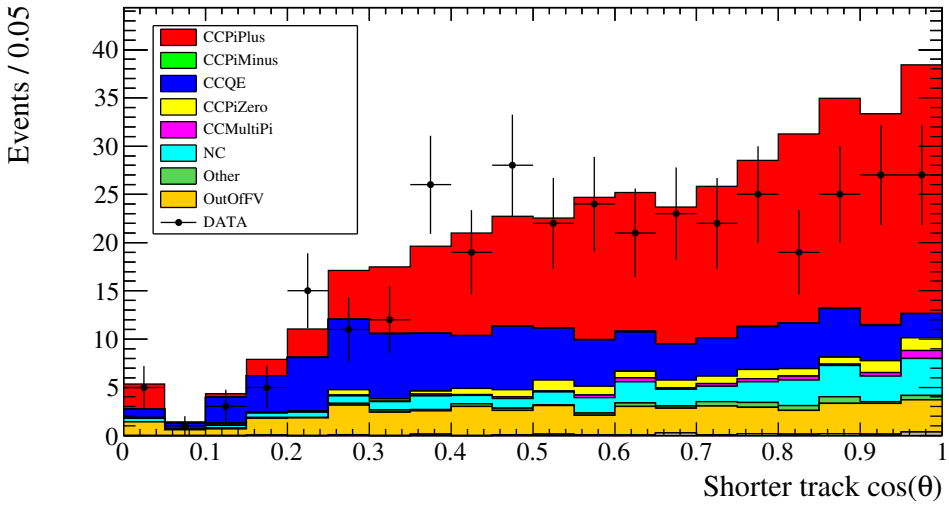

FIGURE B.22. Track $\cos(\theta)$ of the shorter track after Selection Two for water-out data and GENIE MC.

APPENDIX C

MC Flux-averaged Cross Section Calculation Method

In this appendix the recipe used to calculate the MC-truth cross section is discussed. The MC-truth NEUT single bin flux-averaged absolute CC1π^+ cross section on water can be obtained via

$$\langle\sigma\rangle_{flux}^{MC-truth} = \frac{s^{\mathrm{H_2O},\ MC-truth}}{\Phi_w^{MC-truth} \cdot \mathrm{T}^{\mathrm{H_2O},\ MC-truth}} = \frac{s_w^{MC-truth} - R_p^{MC-truth} \cdot s_a^{MC-truth}}{\Phi_w^{MC-truth} \cdot \mathrm{T}^{\mathrm{H_2O},\ MC-truth}},$$

where all the MC-truth variables were calculated using NEUT MC considering all the MC signal neutrino interactions in the fiducial volume of the PØD for MC POTs. $s^{\mathrm{H_2O},\ MC-truth}$ is the MC signal on water as a target after statistical water-in water-out subtraction, $\mathrm{T}^{\mathrm{H_2O},\ MC-truth}$ is the MC number of targets as calculated using the MC detector fiducial mass, as opposed to the real detector mass in data, $\Phi_w^{MC-truth}$ is the integrated flux normalized to MC water-in POT, $s_w^{MC-truth}$ is the signal number of events in water-in MC in the fiducial volume for water-in MC POT, $s_a^{MC-truth}$ is the signal number of events in water-out MC in the fiducial volume for water-out MC POT, and $R_p^{MC-truth}$ is the POT ratio of water-in MC to water-out MC.

The results of these calculation for NEUT were cross-checked against an independent calculation performed by Patrick De Perio [152] and were found to be in good agreement.

APPENDIX D

NEUT FSI Parameter Sets

The NEUT FSI parameter sets used in the propagation of the FSI systematic uncertainty are shown in Table D.1. The FSI parameters are assumed to be uncorrelated. Each FSI set corresponds to a different "one sigma" contour in the FSI parameter space.

Table D.1. 16 NEUT FSI parameter sets, used in the propagation of the FSI systematic uncertainty.

Par. Set	FSIQE	FSIQEH	FSIINEL	FSIABS	FSICX	FSICXH
1	0.6	1.1	1.5	0.7	0.5	2.3
2	0.6	1.1	1.5	0.7	1.6	2.3
3	0.7	1.1	1.5	1.6	0.4	2.3
4	0.7	1.1	1.5	1.6	1.6	2.3
5	1.4	1.1	1.5	0.6	0.6	2.3
6	1.3	1.1	1.5	0.7	1.6	2.3
7	1.5	1.1	1.5	1.5	0.4	2.3
8	1.6	1.1	1.5	1.6	1.6	2.3
9	0.6	2.3	0.5	0.7	0.5	1.3
10	0.6	2.3	0.5	0.7	1.6	1.3
11	0.7	2.3	0.5	1.6	0.4	1.3
12	0.7	2.3	0.5	1.6	1.6	1.3
13	1.4	2.3	0.5	0.6	0.6	1.3
14	1.3	2.3	0.5	0.7	1.6	1.3
15	1.5	2.3	0.5	1.5	0.4	1.3
16	1.6	2.3	0.5	1.6	1.6	1.3

APPENDIX E

Checking the Backgrounds

In this appendix a potential recipe to check the consistency on the MC background predictions, both absolute scales of separate background modes and corresponding systematic uncertainties, is discussed. The background is to be considered self-consistent if its MC prediction agrees with the data within the statistical and systematic uncertainties, e.g. within 1-σ, for background-enriched sideband samples. In case the background prediction does not agree with the data, it can be renormalized and in case of sufficient statistics a better constraint could be put upon it.

In general, the total background B^{MC} is a sum of fiducial and out-of-fiducial backgrounds,

$$B = B_F + B_{OOF}, \tag{95}$$

both of which can be separated into constituent sources via

$$B_F = B_F^{\nu_\mu} + B_F^{\overline{\nu}_\mu} + B_F^{\nu_e} + B_F^{\overline{\nu}_e}. \tag{96}$$

and

$$B_{OOF} = B_{OOF}^{\nu_\mu} + B_{OOF}^{\overline{\nu}_\mu} + B_{OOF}^{\nu_e} + B_{OOF}^{\overline{\nu}_e}, \tag{97}$$

where we dropped the $w|a$ index for convenience. $B_F^{\nu_\mu}$ amounts to the largest single contribution, 84.24% of total background for water-in and 77.39% for water-out and can be expressed via

$$B_F^{\nu_\mu} = B_{F,1}^{\nu_\mu} + B_{F,11}^{\nu_\mu} + B_{F,21}^{\nu_\mu} + B_{F,12}^{\nu_\mu} + B_{F,13}^{\nu_\mu} + B_{F,NC}^{\nu_\mu}, \tag{98}$$

where $B^{\nu_\mu}_{F,1-21}$ are backgrounds due to individual CC NEUT reaction modes, in decreasing order, contributing 73.76% of the background, and $B^{\nu_\mu}_{F,NC}$ is the combined NC background, 10.48% of the total background for water-in MC sample. The before-FSI CCQE component, $B^{\nu_\mu}_{F,1}$, contributes 38.6% of total background for water-in and 40.9% for water-out, which can be seen from Tables 4.17 and 4.19.

The total uncertainty on the background can be found with

$$\frac{\delta B}{B} = \sqrt{\left(\frac{\delta B_F}{B}\right)^2 + \left(\frac{\delta B_{OOF}}{B}\right)^2}, \tag{99}$$

where $\frac{\delta B_F}{B}$ and $\frac{\delta B_{OOF}}{B}$ can be found similarly

$$\frac{\delta B_F}{B} = \sqrt{\left(\frac{\delta B^{\nu_\mu}_F}{B}\right)^2 + \left(\frac{\delta B^{\overline{\nu}_\mu}_F}{B}\right)^2 + \left(\frac{\delta B^{\nu_e}_F}{B}\right)^2 + \left(\frac{\delta B^{\overline{\nu}_e}_F}{B}\right)^2}, \tag{100}$$

$$\frac{\delta B_{OOF}}{B} = \sqrt{\left(\frac{\delta B^{\nu_\mu}_{OOF}}{B}\right)^2 + \left(\frac{\delta B^{\overline{\nu}_\mu}_{OOF}}{B}\right)^2 + \left(\frac{\delta B^{\nu_e}_{OOF}}{B}\right)^2 + \left(\frac{\delta B^{\overline{\nu}_e}_{OOF}}{B}\right)^2}, \tag{101}$$

and

$$\delta B^{\nu_\mu}_F = \sqrt{\left(\delta B^{\nu_\mu}_{F,1}\right)^2 + \left(\delta B^{\nu_\mu}_{F,11}\right)^2 + \left(\delta B^{\nu_\mu}_{F,21}\right)^2 + \left(\delta B^{\nu_\mu}_{F,12}\right)^2 + \left(\delta B^{\nu_\mu}_{F,13}\right)^2 + \left(\delta B^{\nu_\mu}_{F,NC}\right)^2}. \tag{102}$$

Using specific background-enriched sideband samples, e.g. $B^{\nu_\mu}_{F,CCQE}$ enriched 1-track or 2-track samples, which constrain the dominant background, the number of CCQE background events can be extracted via,

$$B^{\nu_\mu}_{F,CCQE} = N^{MC} - N^{non-CCQE}, \tag{103}$$

where N^{MC} is the total number of events in the sideband, defined by specific cuts, and $N^{non-CCQE}$ are all non-$B^{\nu_\mu}_{F,CCQE}$ events.

Equation 103 can be rewritten using the total number of events in the sideband sample for data, N^{Data},

$$B^{\nu_\mu}_{F,CCQE} = R_N \cdot N^{MC} - N^{non-CCQE}, \tag{104}$$

where

$$R_N = \frac{N^{Data}}{N^{MC}} \tag{105}$$

is the background scaling factor.

The uncertainty on the CCQE background could be recalculated using

$$\delta B^{\nu_\mu}_{F,CCQE} = \sqrt{\left(N^{Data}\right)^2 \left(\delta R_N\right)^2 + R_N^2 \left(\delta N^{Data}\right)^2 + \left(\delta N^{non-CCQE}\right)^2} \tag{106}$$

and potentialy reduced, given enough statistics in the sideband.

APPENDIX F

Fiducial Cut Variations

Table F.1. Sets 0 through 30 of x/y, z upstream, and z downstream trims in mm used in fiducial volume systematics evaluation.

Parameter set	x/y trim	z upstream trim	z downstream trim
0	-66	-20	-40
1	-66	-20	-20
2	-66	-20	0
3	-66	-20	20
4	-66	0	-40
5	-66	0	-20
6	-66	0	0
7	-66	0	20
8	-66	20	-40
9	-66	20	-20
10	-66	20	0
11	-66	20	20
12	-66	40	-40
13	-66	40	-20
14	-66	40	0
15	-66	40	20
16	-33	-20	-40
17	-33	-20	-20
18	-33	-20	0
19	-33	-20	20
20	-33	0	-40
21	-33	0	-20
22	-33	0	0
23	-33	0	20
24	-33	20	-40
25	-33	20	-20
26	-33	20	0
27	-33	20	20
28	-33	40	-40
29	-33	40	-20
30	-33	40	0

TABLE F.2. Sets 31 through 60 of x/y, z upstream, and z downstream trims in mm used in fiducial volume systematics evaluation.

Parameter set	x/y trim	z upstream trim	z downstream trim
31	-33	40	20
32	0	-20	-40
33	0	-20	-20
34	0	-20	0
35	0	-20	20
36	0	0	-40
37	0	0	-20
38	0	0	0
39	0	0	20
40	0	20	-40
41	0	20	-20
42	0	20	0
43	0	20	20
44	0	40	-40
45	0	40	-20
46	0	40	0
47	0	40	20
48	33	-20	-40
49	33	-20	-20
50	33	-20	0
51	33	-20	20
52	33	0	-40
53	33	0	-20
54	33	0	0
55	33	0	20
56	33	20	-40
57	33	20	-20
58	33	20	0
59	33	20	20
60	33	40	-40

TABLE F.3. Sets 61 - 79 of x/y, z upstream and z downstream trims in mm used in fiducial volume systematics evaluation.

Parameter set	x/y trim	z upstream trim	z downstream trim
61	33	40	-20
62	33	40	0
63	33	40	20
64	66	-20	-40
65	66	-20	-20
66	66	-20	0
67	66	-20	20
68	66	0	-40
69	66	0	-20
70	66	0	0
71	66	0	20
72	66	20	-40
73	66	20	-20
74	66	20	0
75	66	20	20
76	66	40	-40
77	66	40	-20
78	66	40	0
79	66	40	20

APPENDIX G

Flux Covariance Matrices for S and B

The after-cuts signal and background covariance matrices showing the effect of the flux uncertainties are presented in this section.

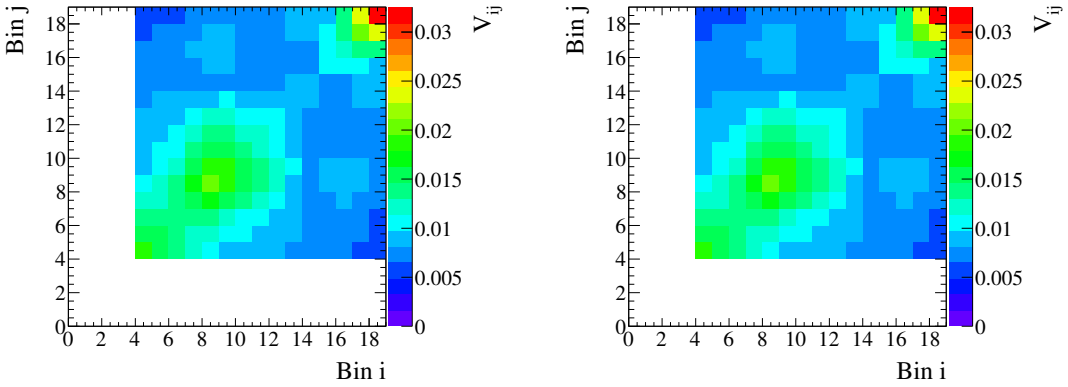

Figure G.1. Fractional 20 × 20 flux covariance matrix for signal events passing the cuts during water-in running, for Run 1 (left) and Run 2 (right). Bins 0 to 3 are empty, since they do not contain any signal events.

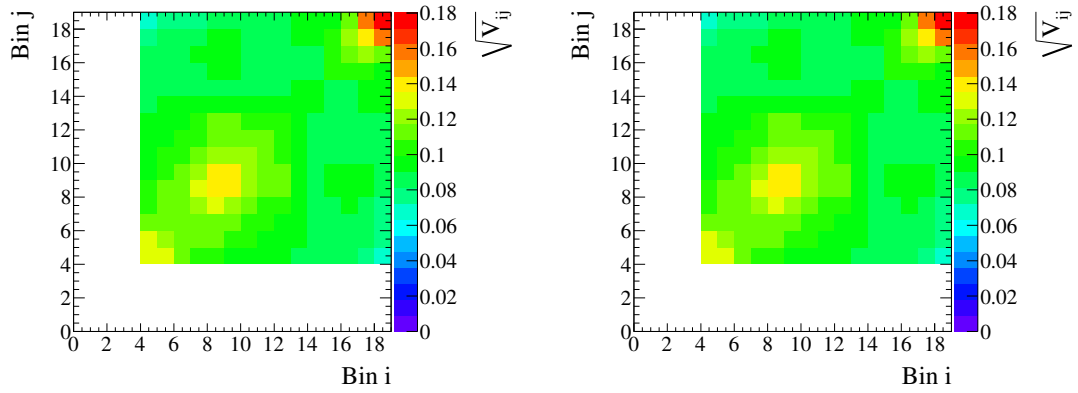

Figure G.2. Fractional 20 × 20 flux error matrix for signal events passing the cuts during water-in running, for Run 1 (left) and Run 2 (right). Bins 0 to 3 are empty, since they do not contain any signal events.

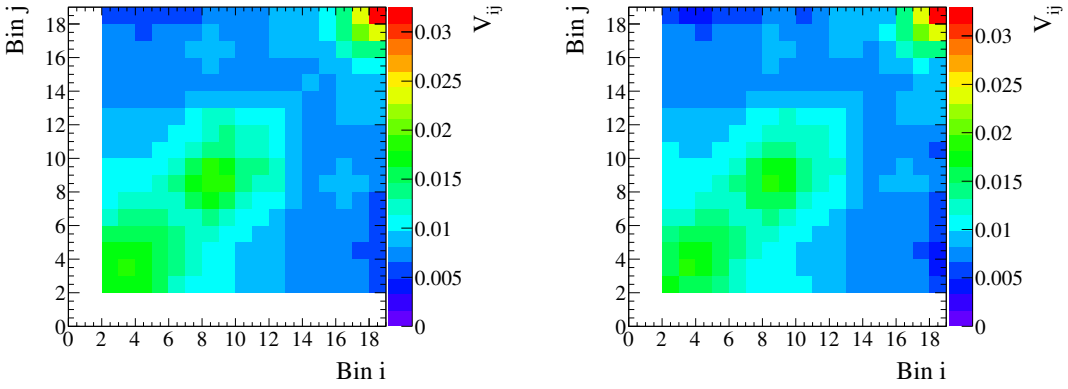

FIGURE G.3. Fractional 20 × 20 flux covariance matrix for background events passing the cuts during water-in running, for Run 1 (left) and Run 2 (right). Bins 0 and 1 are empty since they don't contain any background events.

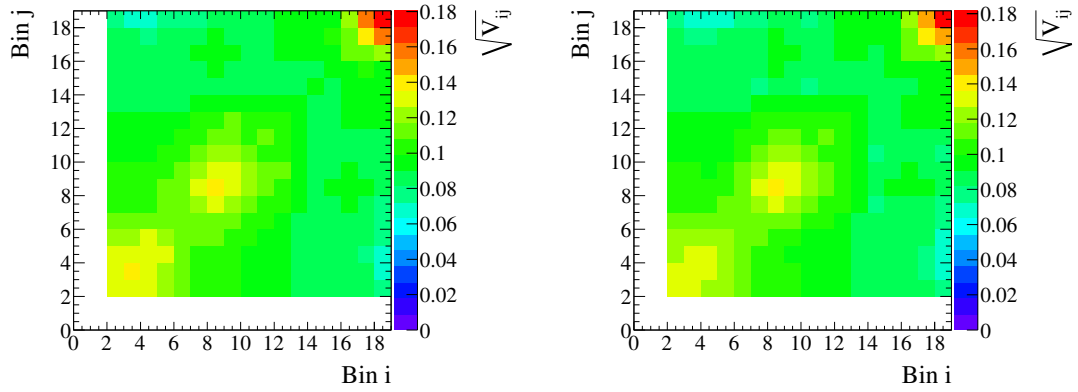

FIGURE G.4. Fractional 20 × 20 flux error matrix for background events passing the cuts during water-in running, for Run 1 (left) and Run 2 (right). Bins 0 and 1 are empty since they don't contain any background events.

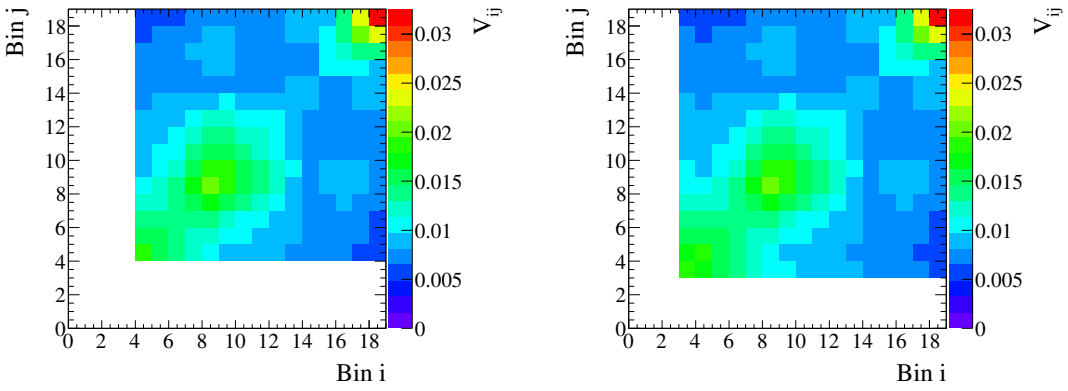

FIGURE G.5. Fractional 20 × 20 flux covariance matrix for signal events passing the cuts during water-out running, for Run 2 (left) and Run 3 (right). Bins 0 to 3 are empty, since they do not contain any signal events.

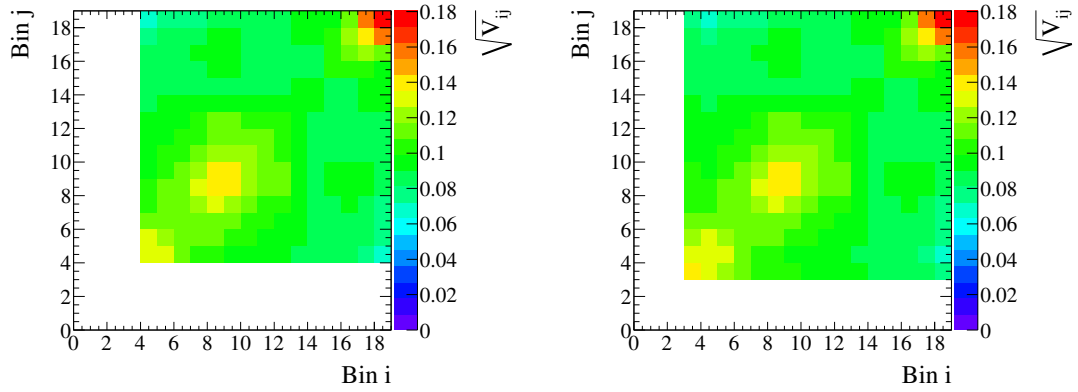

FIGURE G.6. Fractional 20 × 20 flux error matrix for signal events passing the cuts during water-out running, for Run 2 (left) and Run 3 (right). Bins 0 to 3 are empty, since they do not contain any signal events.

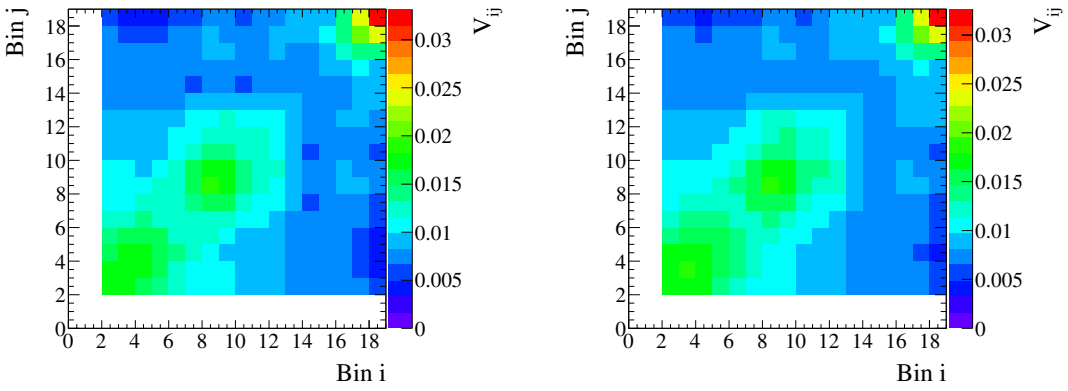

FIGURE G.7. Fractional 20 × 20 flux covariance matrix for background events passing the cuts during water-out running, for Run 2 (left) and Run 3 (right). Bins 0 and 1 are empty since they don't contain any background events.

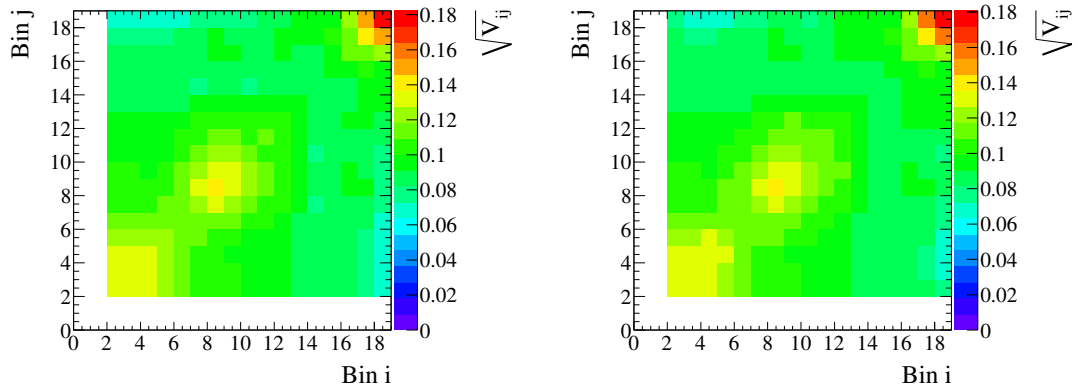

FIGURE G.8. Fractional 20 × 20 flux error matrix for background events passing the cuts during water-out running, for Run 2 (left) and Run 3 (right). Bins 0 and 1 are empty since they don't contain any background events.